



udp UNIVERSIDAD
DIEGO PORTALES

**A LARGE MULTI-WAVELENGTH STUDY OF
LOCAL
ACTIVE GALACTIC
NUCLEI**

**THIS THESIS IS PRESENTED BY
KRITI KAMAL GUPTA**

**TO THE
INSTITUTO DE ESTUDIOS ASTROFÍSICOS,
FACULTAD DE INGENIERÍA Y CIENCIAS**

To qualify for the Doctorate Degree in Astrophysics.

Supervisor: Dr. Claudio Ricci Cherubini

UNIVERSIDAD DIEGO PORTALES

Santiago, Chile

2023

© 2023, Kriti Kamal Gupta

All rights reserved by the thesis author, unless otherwise stated.

Total or partial reproduction, by any means or procedure, is authorized for academic purposes only, provided the content of the thesis is not changed in any way and a complete bibliographic reference is made to the original source, including the bibliographical citations of the present document and its author.

Acta de Deliberación Defensa de Tesis Doctoral

En Santiago, a 31 de mayo de 2023, el Tribunal de Defensa de Tesis Doctoral compuesto por el profesor Claudio Ricci (UDP), Dr. Roberto Assef (UDP), Dr. Benny Trakhtenbrot (Tel Aviv University, Israel), Dra. Shobita Satyapal (George Mason University, EE.UU.) y Dr. Mike Koss (Eureka Scientific, EE. UU.), sobre la base del texto del proyecto, la exposición del doctorando y sus respuestas a las intervenciones de los miembros del tribunal ha resuelto aprobar la tesis doctoral *A LARGE MULTI-WAVELENGTH STUDY OF LOCAL ACTIVE GALACTIC NUCLEI* del doctorando KRITI KAMAL GUPTA. Actuó como ministro de fe el Dr. Manuel Aravena.

Los miembros del Tribunal y el ministro de fe firman para constancia.



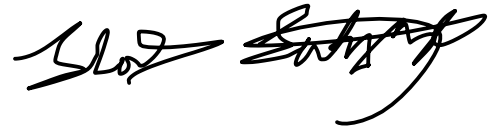
Claudio Ricci
Supervisor, UDP



Roberto Assef, UDP



Benny Trakhtenbrot
Tel Aviv University, Israel



Shobita Satyapal
George Mason University, EEUU



Mike Koss
Eureka Scientific, EEUU



Manuel Aravena
Ministro de fe

*To ma and papa,
it's all because of you...*

Perhaps the reason this night looks so beautiful,
is not because of these stars or lights,
but because of us...
- Mikrokosmos

Acknowledgement

Working on this thesis has been an experience in itself. While I was writing it, I couldn't help but revisit the last four years of my life and it made me realize, how this document is more than just a physical requirement to get my doctorate. In some sense, it is also an account of a time in my life that taught me a lot and changed me the most (in a good way). And this would not have been possible without the people in my life who helped me through it and kept me going.

First and foremost, I would like to convey my heartfelt gratitude to my supervisor, Dr. Claudio Ricci, for giving me the opportunity to do my Ph.D. with him. Honestly, I could not have asked for a more helpful, reliable, considerate, and motivating person to guide me through this challenging journey. Thank you Claudio for choosing me to be your first Ph.D. student, for introducing me to the interesting and mysterious world of AGN, and for trusting me enough to assign me to this project. I really appreciate all the advice you gave me and am thankful for your guidance throughout the course of my Ph.D. There were times, that I hope you know, I could not have moved forward without your encouragement and support. Thank you for being my inspiration and driving force.

I would like to take this opportunity to thank each and every member of the Núcleo de Astronomía at UDP, for providing me with an amazing work environment and for making my stay in Santiago an incredible experience. Thanks to you, coming to the university never felt like a chore and instead, I used to look forward to meeting you all at the office. Thank you Paula for always being available to chat about literally anything. I loved the wide range of our conversations, from discussing possible research projects we could work on, to talking about huskies and taking crazy pictures together. Thanks to José for always being a little goofy whenever we met. To Tom for making me laugh with his impressions, no matter the time and place. Thank you Lucas, for all your efforts so I could arrive and stay in Chile without any issues, and for organizing those barbeque parties. Thank you Manuel for your little jokes that never failed to bring a smile to my face and to Roberto for always being there to save the day.

Thank you Alice for being a fellow swimming and diving enthusiast and Erika for sharing my musical taste.

I am also thankful to some of the friends I made over the last couple of years for all the quality time we spent together. Thanks to Anya and Cristina for taking me around the city when I first arrived and for introducing me to some of my now favorite cuisines. Thanks to Drew and Tanio for some of the most fun outings and hikes. And thank you Dejene, Alessia, Alejandra, Grace, George, Prachi, Matthew, and Camilla for all the good times and for just being there.

I want to express my most sincere gratitude to my parents, the two people without whom none of this would have been possible. Thank you Mataji and Pappa, for this amazing life, for believing in me, and for giving me the freedom to follow my dreams.

And finally, I have to thank the one person who has always been there for me, no matter what. My rock, my soulmate, my sister. Didi, thank you for putting up with me all these years, for understanding me when no one else does, and for reaching out to me or waiting for me to reach you.

마지막으로, 김남준, 김석진, 민윤기, 정호석, 박지민, 김태형, 전정국, 그리고 방탄소년단, 나는 당신을 많이 사랑해. 너무, 너무 사랑하고 진짜 보고싶어서요. 정말유. 많이, 많이 감사하고 감사합니다. 아포방포. 보라해.

Abstract

Galaxies are one of the main components of our Universe and a majority of their visible light comes from the stars they are made up of. However, there exists a small percentage of galaxies that emit enormous amounts of energy which cannot be attributed solely to their stellar population. These galaxies host unusually bright nuclei that can sometimes outshine the rest of the galaxy by several orders of magnitudes. Additionally, the strong emission originating at the center of these galaxies is spread over the entire electromagnetic spectrum. Such galaxies with exceptionally bright nuclei are called active galaxies or Active Galactic Nuclei (AGN).

All AGN harbor a supermassive black hole (SMBH) at their center, that grows in mass by accreting material from its surroundings. In the process, the in-falling matter transfers a fraction of its rest mass energy into radiation, which is predominately responsible for the large luminosities of AGN. The majority of the energy output of AGN is observed in the optical, ultraviolet (UV), and X-rays, along with significant emission in the infrared and, for some sources, radio. This multi-wavelength emission of AGN is attributed to its different components, with the accretion disk producing mainly optical/UV photons and the X-rays being generated in a hot plasma close to the central SMBH. In this context, an in-depth study of the spectral energy distribution (SED) of AGN can prove extremely useful to understand these extraordinary objects.

The primary objective of this thesis is to investigate the multi-wavelength emission properties of AGN present in the local Universe, with the aim to improve our understanding of AGN accretion physics and to obtain fundamental insights into the ongoing processes in their innermost regions. The first part of this thesis deals with exploring the X-ray properties of obscured AGN. We used a sample of 386 hard-X-ray-selected *Swift*/BAT AGN to study how the Thomson-scattered X-ray radiation in these sources relates to the physical properties of AGN. We obtained a negative correlation of the fraction of scattered radiation (f_{scatt}) with the X-ray column density (N_{H}). Using spectral simulations, we verified that this correlation was

not an outcome of degeneracy between the parameters. We show that this correlation could either be due to the dependence of the Thomson cross-section on the inclination angle, or it could indicate that more obscured sources are surrounded by tori with higher covering factors, causing a decrease in the fraction of scattered radiation allowed to escape. We also found a positive correlation between f_{scatt} and the ratio of [O III] $\lambda 5007$ to X-ray luminosity, enabling us to determine the region where this scattered radiation originates, i.e. the narrow-line region.

In the second part of this thesis, we present a broadband SED study of unobscured AGN focused on examining the optical/UV and X-ray emission of nearby AGN. We used the 70-month *Swift*/BAT catalog consisting of hard-X-ray-selected sources to obtain an unbiased sample of AGN, appropriate to carry out a comprehensive analysis of AGN SEDs. We compiled simultaneous optical, UV, and X-ray data of 236 unobscured AGN and constructed their optical-to-X-ray SEDs, after removing any contamination due to the host galaxy and accounting for dust extinction. We employed a multi-temperature disk model to fit the optical/UV part of the SED and used X-ray models describing the primary as well as reprocessed X-ray emission to fit the X-ray spectra. Based on the SED fitting, we estimated important quantities including optical-to-X-ray spectral index (α_{ox}), bolometric corrections (κ_{bol}), bolometric luminosity (L_{bol}), and Eddington ratio (λ_{Edd}) for our source sample. We reported optical/UV bolometric correction factors in the six *Swift*/UVOT filters, at 4400 Å, and for the entire optical/UV energy range. We also calculated soft and hard-X-ray bolometric corrections in the 2 – 10 keV and 14 – 195 keV energy bands, respectively. These corrections are useful to convert luminosities at specific wavelengths (L_{λ}) into L_{bol} when multi-wavelength data is not accessible. For the same reason, we have also presented a correlation between κ_{bol} and α_{ox} .

Finally, we have discussed in detail how the 2 – 10 keV X-ray bolometric correction (κ_{2-10}) evolves with various AGN properties like luminosity, black hole mass, and Eddington ratio. Some of our main findings are: (i) κ_{2-10} does not show any dependence on the intrinsic 2 – 10 keV luminosity (L_{2-10}), suggesting that L_{bol} scales linearly with L_{2-10} . (ii) A positive correlation exists between κ_{2-10} and L_{bol} , implying a dominant contribution of the optical/UV

luminosity to the total bolometric luminosity. (iii) The correlation between κ_{2-10} and L_{bol} disappears at low Eddington ratios ($\lambda_{\text{Edd}} < 0.01$), indicating a possible change in AGN accretion around these values. Numerous studies on accretion disk models have previously suggested that the accretion rate of an AGN can influence the type of accretion flow, with the standard disk model failing at lower accretion rates and being replaced by advection-dominated accretion flows. Based on our results, we cannot comment on how the accretion flow occurs in these sources, but we could argue that it changes around $\lambda_{\text{Edd}} = 0.01$. We also conclusively state that the Eddington ratio of an AGN is the primary regulator of its accretion physics and emission properties.

Contents

Acknowledgement	ix
Abstract	xi
List of Figures	xix
List of Tables	xxxiii
1 Active Galactic Nuclei: An Overview	1
1.1 Structure of AGN	1
1.1.1 Central Supermassive Black Hole	1
1.1.2 Accretion Disk	3
1.1.3 X-Ray Corona	6
1.1.4 Broad-Line Region	7
1.1.5 Narrow-Line Region	7
1.1.6 Dusty Torus	8
1.1.7 Relativistic Jets	9
1.2 AGN Unification Model	10
1.3 AGN Emission	10
1.3.1 Optical/UV	10
1.3.2 X-Rays	11
1.4 Focus and Outline of the Thesis	14

2	Scattered X-Ray Radiation in Obscured AGN	17
2.1	Introduction	18
2.2	Sample and Data	21
2.2.1	X-Ray Data	21
2.2.2	Optical Data	23
2.3	The Correlation Between Scattering Fraction and Column Density	24
2.3.1	Testing Parameter Degeneracies	32
2.4	The Correlation Between Scattering Fraction and $L_{[\text{OIII}]} / L_X$, $L_{[\text{OIII}]}^{\text{corr}} / L_X$ and $L_{[\text{OII}]} / L_X$	36
2.5	The Relation Between Scattering Fraction and M_{BH} , L_X and λ_{Edd}	39
2.6	Discussion	41
2.6.1	The Effect of Inclination Angle and Torus Covering Factor on Scattering Fraction	41
2.6.2	X-ray Scattering in the Narrow-Line Region	44
2.6.3	The Role of Eddington Ratio	46
2.7	Summary and Conclusion	47
	Appendix	49
	A: The $f_{\text{scatt}} - N_{\text{H}}$ Correlation with Different Cuts	49
	B: X-ray Spectral Simulations	50
	C: Aperture Effects on $[\text{OIII}] \lambda 5007$ Measurements	51
3	Optical-to-X-ray SEDs of Unobscured AGN	53
3.1	Introduction	53
3.2	Sample	60
3.3	Data Reduction	65
3.3.1	<i>Swift</i> /UVOT	65
3.3.2	<i>Swift</i> /XRT	66

3.4	X-Ray Spectral Fitting	70
3.5	GALFIT Analysis	74
3.5.1	Light Profiles used in GALFIT	75
3.5.2	GALFIT Fitting Procedure	77
3.5.3	Corrections to GALFIT-estimated PSF Magnitudes	81
3.6	Broadband SED Fitting	85
3.7	Summary	92
	Appendix	93
	A: GALFIT Simulations	93
	B: Comparison with the HST	96
4	Optical, UV and X-ray Emission Properties of Unobscured AGN	103
4.1	Median SED Models	104
4.2	Optical/UV Disk Emission	106
4.2.1	Disk Temperature and Normalization	106
4.2.2	Host Galaxy Dust Extinction	108
4.3	Optical-to-X-ray Spectral Index (α_{ox})	112
4.4	X-Ray Bolometric Corrections	117
4.5	Optical/UV Bolometric Corrections	118
4.6	Summary and Conclusion	121
5	2 – 10 keV X-Ray Bolometric Correction for Unobscured AGN	125
5.1	The Correlation of κ_{2-10} with Luminosity	125
5.1.1	κ_{2-10} vs L_{2-10}	126
5.1.2	κ_{2-10} vs L_{bol}	127
5.2	The Correlation of κ_{2-10} with Eddington Ratio and Black Hole Mass	132
5.2.1	κ_{2-10} vs λ_{Edd}	132

5.2.2	κ_{2-10} vs M_{BH}	134
5.3	Summary and Conclusion	135
6	Concluding Remarks	137
6.1	Key Findings	138
6.2	Future Prospects	140
Appendix A: Broadband SED Fits		141
Appendix B: Long Tables		219
Bibliography		248

List of Figures

1.1	A detailed schematic of an AGN at the center of a massive galaxy, showing an inside-out view of the different components of the AGN: starting with a central supermassive black hole, a corona of hot electrons, an accretion disk, a region of fast-moving gas producing broad-emission lines, a dusty, torus-like structure surrounding the entire system, a distant region of slower-moving gas producing narrow-emission lines, and a powerful radio jet. Image credit: Roen Kelly. . .	2
1.2	Light curves for Mrk 335 showing (from top to bottom) the continuum and the broad emission line features (He II and H β) that are used for reverberation mapping techniques to estimate black hole mass and the size of the BLR (Section 1.1.4). The vertical lines have been shifted by the measured He II and H β lag values (2.7 days and 13.9 days, respectively) to aid the eye in identifying the correct lag values for each emission line. Figure from Grier et al. (2012)	4
1.3	Different accretion disk models to describe accretion flow into the central SMBH: (a) The standard Shakura & Sunyaev disk model and (b) The ADAFs model for sub-Eddington accretion.	6
1.4	Composite AGN spectrum showing broad emission lines, such as Ly α , H α , Mg II, and C IV. Power-law fits to the estimated continuum flux are shown as dashed lines. Figure from Vanden Berk et al. (2001)	8

1.5	A schematic of the dusty torus showing the effect of its covering factor and composition on the level of obscuration observed in the line-of-sight (also see Section 1.2). The left part presents the average torus properties of an unbiased Compton-thin AGN sample, while the right part illustrates the AGN line-of-sight column density (N_{H}) distribution derived from the torus average column density distribution when a clumpy torus is considered. Figure from Zhao et al. (2021)	9
1.6	An illustration of the AGN unification model, which proposes that the difference in the properties of type I and type II AGN is due to their different viewing angles with respect to the obscuring torus. Image credit: Aurore Simonnet. . .	11
1.7	Broadband spectral energy distribution (SED) of a radio-loud (top) and radio-quiet (bottom) AGN showing their multi-wavelength emission from radio up to X-rays, originating in different parts of the AGN. Figure from Shang et al. (2011) . . .	12
1.8	(a) Illustration of an AGN showing the primary X-ray emission arising from the corona and being reprocessed by the surrounding structure. (b) A typical X-ray spectrum of an AGN with various features corresponding to the primary and reprocessed emission. Figure from Ricci Ph.D. 2011.	13

2.1	Scattering fraction vs column density: The plot shows the scattering fraction and the column density values (from R17) for our sample of 386 obscured AGN in the background as grey open circles (upper limits as downward arrows and best-fit values with error bars showing errors at 90% confidence level). Black circles with error bars correspond to the survival analysis (SA) results for each $\log N_{\text{H}}$ bin (f_{scatt} median calculated using the 50th percentile and the 1σ uncertainty calculated using the 16th and 84th percentile). Blue circles with error bars (1σ) depict the results obtained from 10,000 Monte Carlo (MC) simulations. The solid red line is the linear regression obtained from the data points excluding upper limits, while the dashed red line is the linear regression calculated using MC simulations. 2 sources in our sample have $\log(N_{\text{H}}/\text{cm}^{-2}) > 25$, but for display purpose only they are plotted at $\log(N_{\text{H}}/\text{cm}^{-2}) = 25$. The plot clearly shows a negative correlation between f_{scatt} and $\log N_{\text{H}}$. Correlation parameters for the two methods are given in Table 2.1.	25
-----	--	----

2.2	Scattering fraction vs column density for objects corresponding to two bins in: (a) Top panel: intrinsic 14–195 keV luminosity (L_{14-195}), (b) Middle panel: black hole mass (M_{BH}), and (c) Bottom panel: Eddington ratio (λ_{Edd}). The linear regression line as well as the median f_{scatt} and $\log N_{\text{H}}$ values with 1σ uncertainty for each $\log N_{\text{H}}$ bin are calculated using MC simulations. The plots show a distinct negative correlation between scattering fraction and column density. The correlation parameters are given in Table 2.2.	28
-----	---	----

2.3 (a) Distribution in values of the slope of the correlation between scattering fraction and column density. (b) Distribution in the probability of the null hypothesis for the correlation between scattering fraction and column density. The distribution obtained from the XSPEC simulations is shown in grey, with the median slope marked by a dashed grey line (in the left panel). The value obtained from the data (excluding upper limits) is shown as a dashed black line. The median value obtained from MC simulations (including upper limits) is shown by a dashed blue line with the shaded blue region showing the possible range of values. The difference in the values obtained from the XSPEC simulations and the data/MC simulations, for the slope of the correlation and the probability of the null hypothesis, shows that any degeneracy between the parameters (f_{scatt} and $\log N_{\text{H}}$) does not produce an artificial correlation. 32

2.4 Scattering fraction vs (a) $L_{[\text{OIII}]} / L_{2-10}$, (b) $L_{[\text{OIII}]} / L_{14-195}$, (c) $L_{[\text{OIII}]^{\text{corr}}} / L_{2-10}$, (d) $L_{[\text{OIII}]^{\text{corr}}} / L_{14-195}$, (e) $L_{[\text{OII}]} / L_{12-10}$, and (f) $L_{[\text{OIII}]} / L_{14-195}$. Our data is shown as grey open circles in the background (upper limits as downward arrows and best-fit values with error bars showing errors at 90% confidence level). The black and blue circles with error bars correspond to the median and 1σ uncertainty in f_{scatt} calculated using SA and MC simulations, respectively. The solid red linear regression line is obtained from the data by excluding upper limits, while the dashed red regression line is obtained from MC simulations. The plots show a positive correlation between f_{scatt} and $L_{[\text{OIII}]} / L_{\text{X}}$, $L_{[\text{OIII}]^{\text{corr}}} / L_{\text{X}}$ and $L_{[\text{OII}]} / L_{\text{X}}$. Correlation parameters are presented in Table 2.1. 37

2.5	(a) Scattering fraction vs intrinsic 14–195 keV luminosity. (b) Scattering fraction vs black hole mass. (c) Scattering fraction vs Eddington ratio. Our data is shown as grey open circles in the background (upper limits as downward arrows and best-fit values with error bars showing error at 90% confidence level). The black and blue circles with error bars correspond to the median and 1σ uncertainty in f_{scatt} calculated using SA and MC simulations, respectively. The solid red line (only in the bottom panel) depicts the linear regression fit to the data, excluding upper limits. The dashed red line (only in the bottom panel) is the regression fit obtained from MC simulations. The plots show no correlation between f_{scatt} and L_{14-195} (r -value = 0.081) and M_{BH} (r -value = 0.071). A weak negative correlation is detected between f_{scatt} and λ_{Edd} . Correlation parameters are reported in Table 2.1.	40
-----	--	----

2.6	Schematic representation of an AGN showing a particular structure and geometry of the torus (also see Figure 4[b] of Ramos Almeida & Ricci 2017). The inclination angle is measured from the normal to the accretion disk and relative to the observer. The intrinsic column density of the obscuring torus increases with inclination. The torus covering factor is determined from the fraction of sources within a specific column density range (details are given in Ricci et al. 2015 and Ramos Almeida & Ricci 2017).	42
-----	--	----

2.7	(a) Scattering fraction vs column density with an uppercut on f_{scatt} at 5% (blue) and 10% (black). The grey open circles in the background show the data points (with error bars showing errors at 90% confidence level) for objects with $f_{\text{scatt}} < 10\%$. The black and blue circles are the median and uncertainty (1σ) in f_{scatt} and $\log N_{\text{H}}$ calculated using MC simulations for each $\log N_{\text{H}}$ bin and both the linear regression lines are also obtained using the same method. (b) Scattering fraction vs column density for objects with > 200 counts. The data points for these objects are shown as grey open circles in the background (error bars show values in the 90% confidence level). The black circles correspond to the median and uncertainty (1σ) in f_{scatt} and $\log N_{\text{H}}$ calculated using MC simulations for each $\log N_{\text{H}}$ bin, while the black line is the linear regression line obtained using the same method.	50
2.8	(a) An example of a simulated spectrum created using XSPEC. The model used to simulate and fit the spectrum is shown in red. The text box shows the best-fit values obtained for the various free parameters, while the bottom panel shows the fit residuals. (b) An example of a correlation between the simulated values of scattering fraction and column density obtained from XSPEC simulations. The black line shows the linear regression fit to the simulated dataset.	51
2.9	(a) The ratio of observed [O III] $\lambda 5007$ luminosity to intrinsic X-ray luminosity vs redshift. (b) The ratio of observed [O III] $\lambda 5007$ luminosity to intrinsic X-ray luminosity vs physical slit size (kpc) used for [O III] $\lambda 5007$ measurements. The blue and black lines show the linear regression fit to our data for intrinsic X-ray luminosity in the 2–10 keV and 14–195 keV energy bands, respectively. The shaded regions show uncertainty in the regression lines. The lack of correlation in both cases (r -value = 0.087 and 0.077, respectively) suggests that the [O III] $\lambda 5007$ measurements are not significantly affected by the aperture size of the sources.	52

3.1	A schematic representation of the spectral energy distribution (SED) of an unobscured AGN. The colored curves depict the main physical components of AGN emission, while the SED of a star-forming galaxy is shown in grey. Figure from Harrison (2014)	54
3.2	Several multi-wavelength SED studies of AGN have shown that the X-ray bolometric corrections correlate strongly with the bolometric luminosity and the Eddington ratio. Whereas, optical bolometric correction remains constant with these properties. Here we show results from some of these studies. Figure from Duras et al. (2020)	59
3.3	Distribution plots of the (a) black hole mass, (b) $2 - 10$ keV intrinsic, X-ray luminosity, and (c) redshift of the total sample of unobscured <i>Swift</i> /BAT AGN (in grey) and our final sample of 236 unobscured AGN (dashed green histogram). The figures show that our sample covers the parameter space probed by the complete sample of unobscured <i>Swift</i> /BAT AGN, in terms of redshift, black hole mass, and luminosity.	63
3.4	Pipeline estimated flux distribution for the 6 <i>Swift</i> /UVOT filters.	68
3.5	Pipeline estimated AB Magnitude distribution for the 6 <i>Swift</i> /UVOT filters.	68
3.6	(a) Distribution of the best-fit values of photon index (Γ) obtained after the $0.3 - 10$ keV X-ray spectral fitting (Section 3.4). The vertical line marks the median value of $\Gamma = 1.77$. (b) Histogram of the intrinsic $2 - 10$ keV flux for our AGN sample.	73
3.7	A comparison between the $2 - 10$ keV intrinsic fluxes calculated from this work and those obtained by R17 following a detailed broadband X-ray spectral analysis. The black line shows the linear regression fit, while the red dashed line is $x = y$	73

3.8	A few examples of source image fitting with GALFIT using a sky + PSF + Sérsic profile (Section 3.5): (a) SWIFTJ2226.8+3628 and (b) SWIFTJ0640.4-2554. In each panel, the left image is the source image, the middle one is the model, and the right one is the fit-residual. We show the fit in all six <i>Swift</i> /UVOT filters from top to bottom in order (U, V, B, UVW1, UVW2, and UVM2).	79
3.9	A few examples of source image fitting with GALFIT using a sky + PSF profile for high redshift sources: (a) SWIFTJ1723.2+3418 and (b) SWIFTJ1421.4+4747. We corrected the GALFIT-estimated fluxes for such sources (Section 3.5.3) as GALFIT was unable to fit a Sérsic profile to these sources and hence, missed some AGN flux. In each panel, the left image is the source image, the middle one is the model, and the right one is the fit-residual. We show the fit in all six <i>Swift</i> /UVOT filters from top to bottom in order (U, V, B, UVW1, UVW2, and UVM2).	80
3.10	Plots showing the difference in the PSF magnitudes estimated by GALFIT and the actual magnitude of the star used to replicate the AGN at the center of the simulated type I AGN population (ΔM_{filter}) vs the AGN light ratio ($R_{\text{light}}^{\text{filter}}$) for all six <i>Swift</i> /UVOT filters, (a) UVW1, (b) UVW2, (c) UVM2, (d) U, (e) V, and (f) B, based on simulations (described in Appendix 3.7). The plots also show the best-fit function and their equations for both cases: when a Sérsic profile fit was obtained (in red) and when a fit with a Sérsic profile fit was not possible (in green). The equations mentioned in each figure were then used to calculate the corresponding corrections to improve the PSF magnitudes estimated by GALFIT during the source image decomposition to compute the AGN light devoid of host galaxy contamination.	83

3.11	A distribution in the value of the maximum disk temperature as obtained after fitting the optical/UV SEDs of our source sample with a dust-extinction corrected thermal disk model (described in Section 3.6). The median value of kT_{max} from this distribution is 2.7 eV. This value was used to improve the optical/UV SED fits for sources whose disk temperatures could not be constrained.	88
3.12	A few examples of the optical-to-X-ray SED fits. From top to bottom, the fits are for sources: SWIFTJ0208.2+4452, SWIFTJ0630.7+6342, and SWIFTJ1421.4+4747. The left panel shows the counts in the optical/UV filters (black points) and the 0.3 – 10 keV X-ray spectrum (cyan points). It also shows the fit obtained using the optical/UV disk model including dust extinction (in red) and the X-ray model (in blue), along with the fit residuals. The right panel shows the best-fit SED model for each source.	90
3.13	A few examples of the optical-to-X-ray SED fits. From top to bottom, the fits are for sources: SWIFTJ0002.5+0323, SWIFTJ0654.6+0700, and SWIFTJ1316.9-7155. The left panel shows the counts in the optical/UV filters (black points) and the 0.3 – 10 keV X-ray spectrum (cyan points). It also shows the fit obtained using the optical/UV disk model including dust extinction (in red) and the X-ray model (in blue), along with the fit residuals. The right panel shows the best-fit SED model for each source.	91
3.14	Comparing the expected AGN (star) flux to the PSF flux estimated by GALFIT for the three UV filters. The star symbols show the best-fit results without a Sérsic profile, while the circle symbols show the results when the fitting with a Sérsic profile does not converge but we still obtain better constraints on the PSF profile compared to the fit without a Sérsic profile. The $x = y$ line is shown in red. The color bar indicates the AGN light ratio.	99

3.15 (a) Comparing the expected AGN (star) flux to the PSF flux estimated by GALFIT for UVOT filter UVW1. (b) The same plot as (a) but in different redshift bins. The $x = y$ line is shown in red. The color bar indicates the AGN light ratio.	99
3.16 (a) Comparing the expected AGN (star) flux to the PSF flux estimated by GALFIT for UVOT filter UVW2. (b) The same plot as (a) but in different redshift bins. The $x = y$ line is shown in red. The color bar indicates the AGN light ratio.	100
3.17 (a) Comparing the expected AGN (star) flux to the PSF flux estimated by GALFIT for UVOT filter UVM2. (b) The same plot as (a) but in different redshift bins. The $x = y$ line is shown in red. The color bar indicates the AGN light ratio.	100
3.18 Comparing the expected AGN (star) flux to the PSF flux estimated by GALFIT for filters (top to bottom) UVW1, UVW2, and UVM2. The three subplots in each figure show the three different morphologies considered and the different symbols correspond to the redshift range. The $x = y$ line is shown in red. The color bar indicates the AGN light ratio.	101
3.19 Plot showing the source magnitudes in the faintest optical band against the brightest UV band. It is evident from this figure that the AGN in our sample are brighter in the optical when compared to the UV and even the faintest optical band is brighter than the brightest UV band. Therefore, based on the GALFIT simulations carried out in the UV band to calculate the correction factors for GALFIT-estimated PSF magnitudes and fluxes, only the faintest and farthest sources need to be corrected in the optical as well. The $x = y$ line is shown in red.	102

4.1	Rest frame optical-to-X-ray best-fit SED models (a) with absorption and (b) without absorption, for the 236 unobscured, nearby AGN in our sample (in grey). The median SED model is shown as the black solid line.	104
4.2	The absorption corrected, median SED (normalized at 1 eV) in bins of (a) 2–10 keV X-ray luminosity, (b) bolometric luminosity, (c) black hole mass, and (d) Eddington ratio. The black solid curve shows the lower value bin and the red dashed curve is the higher value bin, for each panel.	105
4.3	The maximum disk temperature (kT_{max}) as a function of (a) the redshift of the source, and (b) the disk normalization (K_{uvo}). The black solid line shows the best-fit relation.	107
4.4	The maximum disk temperature (kT_{max}) as a function of (a) the bolometric luminosity, and (b) the Eddington ratio. The black solid line shows the best-fit relation.	108
4.5	(a) Distribution of $E(B-V)_{\text{HG}}$, that quantifies the intrinsic dust extinction of the AGN emission in the optical/UV due to the host galaxy. (b) $E(B-V)_{\text{HG}}$ as a function of the redshift. The black solid line shows the best-fit relation. . . .	109
4.6	The host galaxy dust extinction in the optical/UV [$E(B-V)_{\text{HG}}$] as a function of the X-ray column density (N_{H}). The black line shows the weak correlation between the two quantities.	109
4.7	The monochromatic luminosity at 2500 Å vs the monochromatic luminosity at 2 keV. The best-fit relation from our work is shown as a black solid line, while the grey-shaded region shows the one-sigma confidence interval for the best fit. We also show the relation reported by Steffen et al. (2006), Lusso et al. (2010), and Lusso & Risaliti (2016) as a blue dash-dotted line, red dashed line, and green dotted line, respectively.	113

4.8	(a) A distribution plot of the optical-to-X-ray spectral index (α_{ox}) for our sample of hard-X-ray-selected nearby, unobscured AGN. (b) A plot showing α_{ox} as a function of redshift, but we do not find any significant correlation between the two parameters (black solid line shows the best-fit relation).	113
4.9	α_{ox} as a function of the rest-frame monochromatic luminosity at (a) 2500 Å (UV) and (b) 2 keV (X-ray). We find a tight anti-correlation between α_{ox} and $L_{2500\text{Å}}$ (shown as the black solid line in the left panel) but no significant relation with $L_{2\text{keV}}$ (shown as a black solid line in the right panel), as confirmed by previous works. For comparison, we also plot the best-fit relations from Steffen et al. (2006) ; blue dash-dotted line) and Lusso et al. (2010) ; red dashed line). The grey-shaded region shows the one-sigma confidence interval for our best-fit relation.	114
4.10	(a) α_{ox} as a function of Eddington ratio. We find a weak anti-correlation between the two parameters (black solid line), unlike the strong anti-correlation reported by Lusso et al. (2010) ; red dashed line). (b) α_{ox} as a function of bolometric luminosity. We find a significant anti-correlation between the two quantities (see Table 4.3). The black solid line shows the best-fit relation.	115
4.11	Plot of the 2 – 10 keV bolometric correction (κ_{2-10}) against α_{ox} . The black solid line shows the best-fit relation we obtained, which is in good agreement with the one estimated by Lusso et al. (2010) ; red dashed line).	116
4.12	(a) A distribution plot of the soft X-ray bolometric correction (κ_{2-10}) for our sample of hard-X-ray-selected nearby, unobscured AGN. (b) A plot showing how κ_{2-10} evolves with redshift, and we do not find any significant dependence of κ_{2-10} on redshift (black solid line shows the best-fit relation).	117
4.13	Plot of the 14 – 195 keV bolometric correction (κ_{14-195}) against (a) L_{14-195} and (b) λ_{Edd} . The black solid line shows the best-fit relation we obtained.	118

4.14	4400 Å bolometric correction as a function of (a) the 4400 Å monochromatic luminosity and (b) the bolometric luminosity. We find a very weak correlation in both cases (Section 4.5, Table 4.4) shown as the black line. Hence, we show the best fit with a constant value as well (red dashed line). For both cases, we obtain a value of $\kappa_{4400\text{\AA}} = 7.9 \pm 0.3$	119
5.1	(a) κ_{2-10} as a function of L_{2-10} . The data points from this work are shown in the background as grey circles. The red points show the binned data and the black line is the best linear fit relation. (b) κ_{2-10} as a function of L_{2-10} in bins of (from top to bottom) L_{bol} , M_{BH} , and λ_{Edd} . The black points represent the lower-value bin and the blue points correspond to the higher-value bin in each panel.	126
5.2	(a) κ_{2-10} as a function of L_{bol} . The data points from this work are shown in the background as grey circles. The red points show the binned data and the black line is the best-fit relation. (b) Comparison plot of the relation between κ_{2-10} and L_{bol} from various works. The black points show the binned data from this work along with the best-fit relation as the black solid line. The green dashed line is the best-fit relation from Duras et al. (2020) and the blue dash-dotted line shows the result of Lusso et al. (2012)	127
5.3	(a) κ_{2-10} as a function of L_{bol} in bins of (from top to bottom) L_{2-10} , M_{BH} , and λ_{Edd} . The black points represent the lower-value bin and the blue points correspond to the higher-value bin in each panel. (b) κ_{2-10} as a function of L_{bol} in 3 bins of λ_{Edd} . The lowest bin of $\lambda_{\text{Edd}} < 0.01$ is shown as black diamonds, the $0.01 < \lambda_{\text{Edd}} < 0.1$ bin is shown as blue circles, and the highest $\lambda_{\text{Edd}} > 0.1$ bin is shown by red squares.	129

5.4	The absorption corrected median SED (normalized at 1eV) in three bins of Eddington ratio. The black solid curve shows the lowest value bin, the red dashed curve is the intermediate value bin and the blue dash-dotted curve is the highest value bin.	130
5.5	(a) κ_{2-10} as a function of the λ_{Edd} . The data points from this work are shown in the background as grey circles. The red points show the binned data and the black line is our best linear fit relation. (b) Comparison plot of the relation between κ_{2-10} and λ_{Edd} from various works. The black points show the binned data from this work along with the best-fit relation as the black solid line. The green dashed line is the best-fit relation from Duras et al. (2020) and the blue dash-dotted line shows the result of Lusso et al. (2012) . (c) κ_{2-10} as a function of the λ_{Edd} in bins of (from top to bottom) L_{2-10} , L_{bol} , and M_{BH} . The black points represent the lower-value bin and the blue points correspond to the higher-value bin in each panel.	133
5.6	(a) κ_{2-10} as a function of the M_{BH} . The data points from this work are shown in the background as grey circles. The red points show the binned data and the black line is our best linear fit relation. For comparison, we also show the best-fit relation from Duras et al. (2020) as a green dashed line. (b) κ_{2-10} as a function of the M_{BH} in bins of (from top to bottom) L_{2-10} , L_{bol} , and λ_{Edd} . The black points represent the lower-value bin and the blue points correspond to the higher-value bin in each panel.	134
1	Continued from Figure 3.13, showing broadband SED fits, best-fit SED models, and fit residuals for all the sources in our sample.	141

List of Tables

2.1	Correlation results for Figure 2.1 (Section 2.3), Figure 2.4 (Section 2.4), and Figure 2.5c (Section 2.5).	29
2.2	Correlation results from MC simulations for Figure 2.2 (Section 2.3). . .	30
3.1	Characteristics of <i>Swift</i> /UVOT Filters. The central wavelength corresponds to the mid-point between the wavelengths at the FWHM. The zeropoint magnitude indicates the magnitude of a source producing one count per second. The counts to flux conversion factor, when multiplied with the count rate, gives the flux (F_λ) in $\text{erg s}^{-1} \text{cm}^{-2} \text{\AA}^{-1}$	62
3.2	The list of sources in our sample, along with their BAT and Swift IDs, counterpart names, coordinates (in degrees, J2000), redshifts, luminosity distances in Mpc (Koss et al. 2022b), and X-ray column density values from R17. The full version of this table is given in the appendix (Table 1).	64
3.3	The list of observation IDs of the observations used for each source, along with their exposure times with <i>Swift</i> /UVOT and <i>Swift</i> /XRT, and the available <i>Swift</i> /UVOT filters.	67
3.4	List of source fluxes as calculated by the <i>Swift</i> /UVOT command <code>uvotsource</code> via 5 arcsecs aperture photometry, along with statistical errors (Section 3.3.1). Flux units: $10^{-15} \text{erg cm}^{-2} \text{s}^{-1} \text{\AA}^{-1}$	69

3.5	Results of the X-ray spectral fitting (Section 3.4), with best-fit values of the photon index, the $2 - 10$ keV intrinsic fluxes with errors, and the model used to attain the best fit (described in detail in R17). Flux units: $10^{-12} \text{ erg cm}^{-2} \text{ s}^{-1}$	72
3.6	List of AGN fluxes (corrected) as estimated by GALFIT image decomposition (Section 3.5). The last column shows, in the form of flags, if the GALFIT-estimated flux was corrected (c) and if the UVOT pipeline estimated flux was used (for any of the filters) to create the final SEDs (p). Flux units: $10^{-15} \text{ erg cm}^{-2} \text{ s}^{-1} \text{ \AA}^{-1}$	84
3.7	Results of the optical/UV SED fitting (Section 3.6), with the best-fit values of the disk temperature (kT_{max} in eV), the extinction due to the host galaxy $E(B - V)_{\text{HG}}$, and the total, intrinsic optical/UV flux (from $10^{-7} - 100$ keV) with errors. The last column shows, in the form of flags, if the disk temperature was fixed to its median value of 2.7 eV (t) and if the host galaxy extinction was fixed to 0.0 or was constrained as an upper limit during the fitting (e). Flux units: $10^{-11} \text{ erg cm}^{-2} \text{ s}^{-1}$	89
3.8	List of source magnitudes as calculated by the <i>Swift</i> /UVOT command <code>uvotsource</code> via 5 arcsecs aperture photometry, along with statistical errors (Section 3.3.1).	97
3.9	List of AGN magnitudes (corrected) as estimated by GALFIT image decomposition (Section 3.5). The last column shows in the form of flags if the GALFIT-estimated magnitude was corrected (c) and if the UVOT pipeline estimated magnitude was used (for any of the filters) to create the final SEDs (p).	98
4.1	Correlation results for Figures 4.3, 4.4, 4.5, and 4.6, described in Section 4.2.	110

4.2	List of outputs from the broadband SED fitting, including the 2500 Å, 2 keV, and the bolometric luminosities in units of $\log(L/\text{erg s}^{-1})$. We also present the black hole masses (M_{BH}) of our sources as estimated by Mejía-Restrepo et al. (2022) in units of $\log(M_{\text{BH}}/M_{\odot})$. Finally, we list the estimated value of the optical-to-X-ray spectral indices (α_{ox} ; Section 4.3), the soft X-ray (κ_{2-10} ; Section 4.4) and 4400 Å optical bolometric corrections ($\kappa_{4400\text{Å}}$; Section 4.5), and the Eddington ratios (λ_{Edd} in log). The full version of this table is given in the appendix (Table 2).	111
4.3	Correlation results for Figures 4.7, 4.8, 4.9, 4.10, and 4.11, described in Section 4.3.	116
4.4	Correlation results for Figures 4.13a and 4.14, described in Sections 4.4 and 4.5.	120
4.5	A list of the estimated values of the optical, UV, and hard X-ray bolometric corrections (described in Sections 4.4 and 4.5).	121
4.6	Median values of the optical/UV bolometric corrections with respective uncertainties (Section 4.5).	122
5.1	Correlation results for Figures 5.1a, 5.2a, 5.5a, and 5.6a, described in Sections 5.1 and 5.2.	131
1	Full version of Table 3.2.	219
2	Full version of Table 4.2.	234

Chapter 1

Active Galactic Nuclei: An Overview

Our universe consists of many extremely energetic phenomena, and Active Galactic Nuclei (AGN) are definitely one of them. The large amounts of energy emitted by AGN (up to $L \sim 10^{15} L_{\odot}$) make them one of the most luminous sources ever known. Moreover, they emit radiation over the entire electromagnetic spectrum, from the lowest energy (radio; $\lambda \sim 10$ cm) to the highest energy (gamma rays; $E \sim \text{few MeV}$), making them some of the most interesting objects to be ever discovered.

In the following sections, we will give a brief overview of the structure of an AGN (Section 1.1), their unification model (Section 1.2), and their multi-wavelength emission (Section 1.3).

1.1 Structure of AGN

AGN are believed to be constituted of various components, that occupy different physical scales (see Figure 1.1) and are responsible for emitting radiation at different wavelengths (also see Section 1.3).

1.1.1 Central Supermassive Black Hole

At the center of the AGN resides a supermassive black hole (SMBH), the main engine of the system. Although the SMBH does not emit any electromagnetic radiation of its own, thanks to its strong gravitational force due to all of its mass ($\sim 10^5 - 10^{10} M_{\odot}$) being contained at a

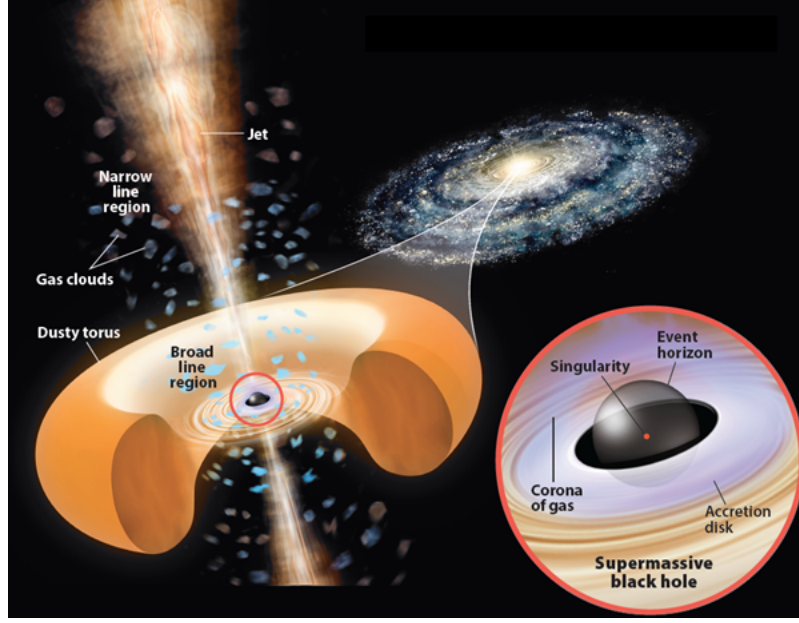


Figure 1.1: A detailed schematic of an AGN at the center of a massive galaxy, showing an inside-out view of the different components of the AGN: starting with a central supermassive black hole, a corona of hot electrons, an accretion disk, a region of fast-moving gas producing broad-emission lines, a dusty, torus-like structure surrounding the entire system, a distant region of slower-moving gas producing narrow-emission lines, and a powerful radio jet. Image credit: Roen Kelly.

singular point (called the singularity), it accretes surrounding material onto itself and this infalling material emits the majority of radiation coming from the AGN. Any material within a distance of the Schwarzschild radius (r_s ; marking the event horizon) from the point of singularity is bound to fall into the central black hole. The Schwarzschild radius corresponds to the distance at which even light is unable to escape the gravitational pull of the black hole and is defined as:

$$r_s = 2r_g, \text{ where } r_g = \frac{GM_{\text{BH}}}{c^2} \quad (1.1)$$

Here, G is the gravitational constant, c is the speed of light, and M_{BH} is the mass of the central black hole. To estimate the mass of the SMBH in AGN, a bunch of different techniques are used:

- In the presence of broad emission lines in the AGN spectra, the width of these lines is used to estimate the black hole mass (M_{BH}) assuming that the motion of the gas forming

this broad line region (BLR) is virialized. Hence, using the following relation:

$$\frac{v_{\text{BLR}}^2}{r_{\text{BLR}}} = \frac{GM_{\text{BH}}}{r_{\text{BLR}}^2} \quad (1.2)$$

one can calculate M_{BH} if the size (r_{BLR}) of the BLR is known. Thanks to reverberation mapping experiments, based on the observed lag between the emission lines and the continuum emission (see Figure 1.2), empirical relations between the size of the BLR and the accretion luminosity have been devised (e.g., [Kaspi et al. 2000, 2005](#); [Bentz et al. 2009, 2015](#)). These relations can then be used to estimate the size of the BLR and in turn the black hole mass.

- The most commonly used emission lines in this technique are the broad $\text{H}\alpha$ and $\text{H}\beta$. For sources with broad $\text{H}\alpha$, the following relation presented by [Greene & Ho \(2005\)](#) can be employed:

$$M_{\text{BH}}(\text{H}\alpha) = 1.3 \times 10^6 \left(\frac{L_{\text{H}\alpha}}{10^{42} \text{ erg s}^{-1}} \right)^{0.57} \times \left[\frac{\text{FWHM}(\text{H}\alpha)}{10^3 \text{ km s}^{-1}} \right]^{2.06} M_{\odot} \quad (1.3)$$

For sources with broad $\text{H}\beta$, the following relation prescribed by [Trakhtenbrot & Netzer \(2012\)](#) can be used:

$$M_{\text{BH}}(\text{H}\beta) = 1.05 \times 10^8 \left(\frac{L_{5100}}{10^{46} \text{ erg s}^{-1}} \right)^{0.65} \times \left[\frac{\text{FWHM}(\text{H}\beta)}{10^3 \text{ km s}^{-1}} \right]^2 M_{\odot} \quad (1.4)$$

- In the case of higher redshift sources, other emission lines like $\text{Mg II } \lambda 2798$ or $\text{C IV } \lambda 1549$ are used (e.g., [Vestergaard & Peterson 2006](#); [Trakhtenbrot & Netzer 2012](#)).
- In the absence of broad emission lines in the AGN spectra, M_{BH} can be estimated using the correlation between the black hole mass and the host galaxy stellar velocity dispersion (σ_*), as described by [Kormendy & Ho \(2013\)](#):

$$\log \left(\frac{M_{\text{BH}}}{M_{\odot}} \right) = 4.38 \times \log \left(\frac{\sigma_*}{200 \text{ km s}^{-1}} \right) + 8.49 \quad (1.5)$$

1.1.2 Accretion Disk

The primary source of emission in AGN is the conversion of gravitational energy into electromagnetic radiation. The material surrounding the SMBH loses its angular momentum as it

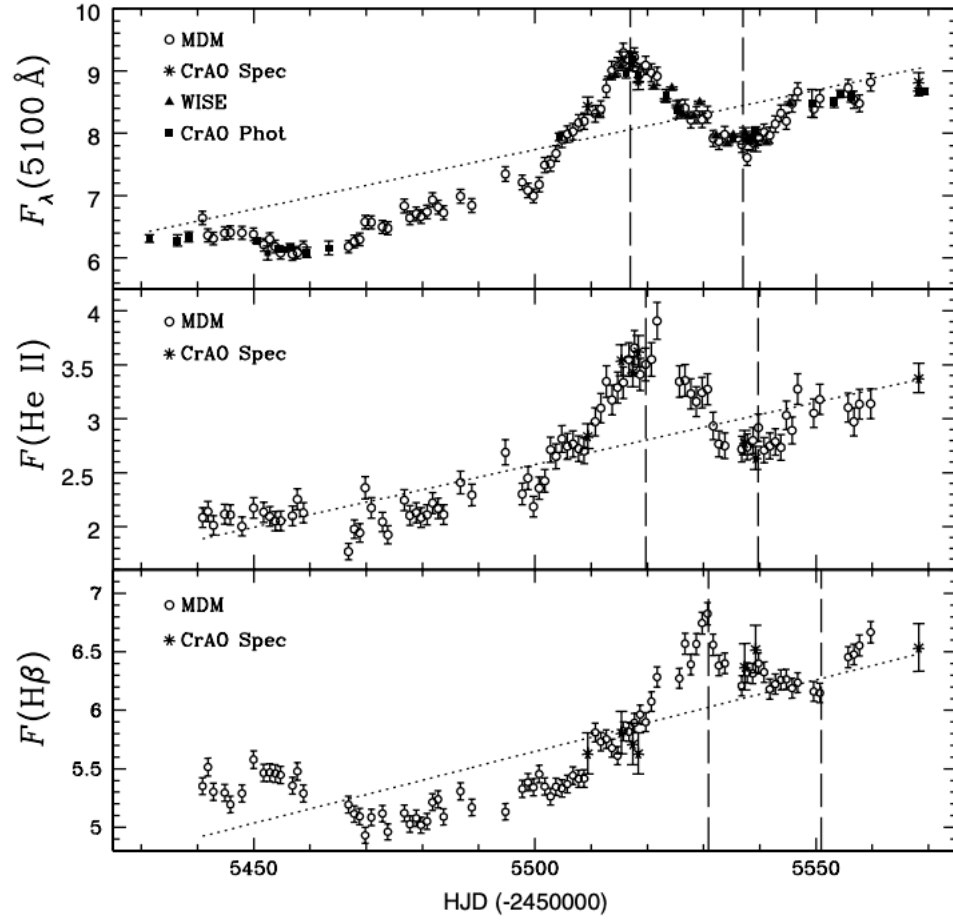


Figure 1.2: Light curves for Mrk 335 showing (from top to bottom) the continuum and the broad emission line features (He II and H β) that are used for reverberation mapping techniques to estimate black hole mass and the size of the BLR (Section 1.1.4). The vertical lines have been shifted by the measured He II and H β lag values (2.7 days and 13.9 days, respectively) to aid the eye in identifying the correct lag values for each emission line. Figure from [Grier et al. \(2012\)](#).

spirals inwards in the form of an accretion disk, and is eventually accreted by the black hole. The rest mass energy of this in-falling material is converted into radiation (mainly in the optical and UV) with efficiency η , such that:

$$L_{\text{bol}} = \eta \dot{M} c^2 \quad (1.6)$$

where L_{bol} is the total accretion luminosity of the AGN and \dot{M} is the mass inflow rate or the accretion rate of the AGN. Additionally, an important quantity called the Eddington luminosity (L_{Edd}) is defined as the luminosity at the Eddington limit when the radiation pressure balances the gravitational force, assuming a spherically symmetric system and a fully ionized medium. For such a scenario, the luminosity is given as:

$$L_{\text{Edd}} = \frac{4\pi G M_{\text{BH}} m_p c}{\sigma_T} \approx 1.5 \times 10^{38} \frac{M_{\text{BH}}}{M_{\odot}} \text{ erg s}^{-1} \quad (1.7)$$

Here, m_p is the mass of a proton and σ_T is the Thomson cross-section. For a disk emitting at the Eddington luminosity, the corresponding accretion rate can be given as:

$$\dot{M}_{\text{Edd}} = \frac{L_{\text{Edd}}}{\eta c^2} \quad (1.8)$$

And finally, we can introduce the term ‘‘Eddington ratio’’ (λ_{Edd}), which by definition is the ratio of the bolometric luminosity and the Eddington luminosity of the AGN, and is commonly used as a proxy for the accretion rate of the AGN:

$$\lambda_{\text{Edd}} = \frac{L_{\text{bol}}}{L_{\text{Edd}}} \quad (1.9)$$

Different accretion flow models (Figure 1.3) can be used to describe this mass accretion onto the central SMBH in AGN (see Beloborodov 1999 for a review).

- The standard accretion disk model (see Figure 1.3a) assumes a geometrically thin and optically thick geometry for the disk (e.g., Shakura & Sunyaev 1973), with a temperature gradient (the innermost regions being the hottest) and emission that replicates a system consisting of multiple blackbody components. The spin of the black hole (a_*) plays an important role here, as it affects the location of the innermost stable circular orbit (ISCO) or the marginally stable orbit ($r_{\text{ms}} = 6r_g$ for a non-rotating black hole), in turn affecting the efficiency of the mass-to-energy conversion (e.g., Novikov & Thorne 1973). The

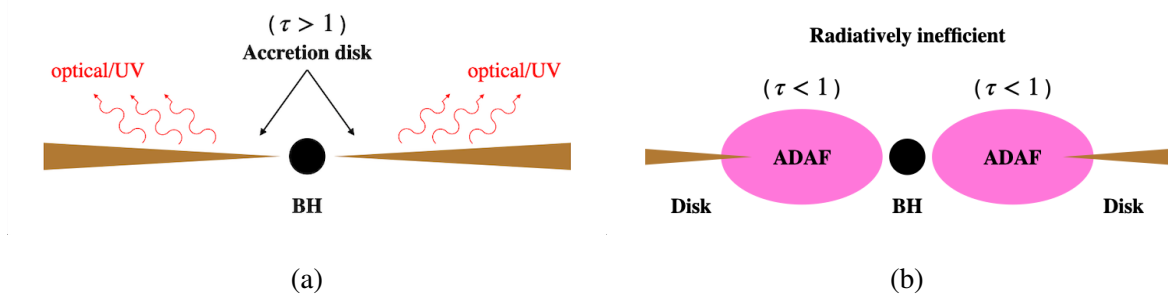


Figure 1.3: Different accretion disk models to describe accretion flow into the central SMBH: (a) The standard [Shakura & Sunyaev](#) disk model and (b) The ADAFs model for sub-Eddington accretion.

highest efficiency is achieved for a maximally rotating black hole, with the stable orbit extending much closer to the black hole up to $r_{\text{ms}} = r_g/2$.

- The slim disk or the optically thick advection-dominated accretion flow (ADAF) model, another example of the cold accretion flow, is used to describe mass accretion onto a SMBH when the accretion rate of the AGN exceeds \dot{M}_{Edd} . In this case of Super-Eddington accretion, the gas becomes too optically thick to radiate the trapped energy which eventually flows into the black hole via advection (e.g., [Katz 1977](#); [Begelman 1978](#); [Abramowicz et al. 1988](#)). As a result, the mass-to-radiation efficiency factor for this model is much lower.
- In the case of quiescent SMBHs, with sub-Eddington accretion rates, radiatively inefficient, optically thin ADAFs (see Figure 1.3b) provide a thermally stable solution for a possible mode of the accretion flow (e.g., [Ichimaru 1977](#); [Narayan & Yi 1994](#)). The viscous energy of the low-density gas, unable to be dissipated as radiation on accretion timescales, goes into heating the accretion flow, hence making the disk geometrically thick (e.g., [Yuan & Narayan 2014](#)).

1.1.3 X-Ray Corona

Following the energy radiated by the accretion disk, primarily at optical and UV wavelengths, the second main contributor to AGN emission is the high-energy radiation originating at scales much closer to the SMBH. While the accretion disk can extend upto a few $100r_g$ from the

center, based on the variability timescales of the X-ray emission, it is believed to be produced at much smaller scales of ~ 5 to $10r_g$. It has now been accepted that this X-ray emission is due to the Comptonization of the optical/UV seed photon from the disk by a plasma of hot electrons called the corona (e.g., [Haardt & Maraschi 1991](#)). The lower energy disk photons are up-scattered by the high energy electrons in the corona up to X-ray energies, limited by the temperature of the corona.

1.1.4 Broad-Line Region

Beyond the accretion disk, the AGN is surrounded by fast-rotating gas, gravitationally bound and photoionized by the central SMBH. This region is the source of the broad-emission lines seen in the AGN spectra and hence, is called the broad line region (BLR; [Peterson 2006](#)). The Doppler width of the emission lines corresponds to the high velocity of the gas in this region, reaching values of ~ 5000 to $10,000 \text{ km s}^{-1}$. The distance of the BLR from the central SMBH is estimated using reverberation mapping to range from 0.01 to 1 pc. The most prominent and commonly observed broad-emission lines in an AGN spectrum are the hydrogen Balmer-series lines ($H\alpha \lambda 6563$, $H\beta \lambda 4861$, and $H\gamma \lambda 4340$), the hydrogen Ly $\alpha \lambda 1216$ and other lines like $Mg \text{ II } \lambda 2798$, $[C \text{ III}] \lambda 1909$, and $C \text{ IV } \lambda 1549$ (Figure 1.4).

1.1.5 Narrow-Line Region

Contrary to the BLR, the narrow-line region (NLR) has a much lower electron density making it favorable for forbidden transitions (for e.g., $[O \text{ III}] \lambda 4959$, $[O \text{ III}] \lambda 5007$, $[N \text{ II}] \lambda 6584$, $[S \text{ II}] \lambda 6717$, etc.). The widths of the narrow-emission lines indicate gas velocities in the range of 200 to 1000 km s^{-1} . Thanks to its spatial extension of a few 100 pcs up to $\sim \text{kpc}$ s, the NLR can be easily resolved using ground-based facilities and hence, is the most extensively studied part of the AGN (e.g., [Kraemer & Crenshaw 2000](#)). Various standard line ratios and diagnostic diagrams are used to better understand the physical conditions of the NLR. For example, the ratio of Balmer lines (Balmer decrement) can be used to correct for reddening. Due to a weaker radiation field, this region can also contain some dust, unlike the BLR.

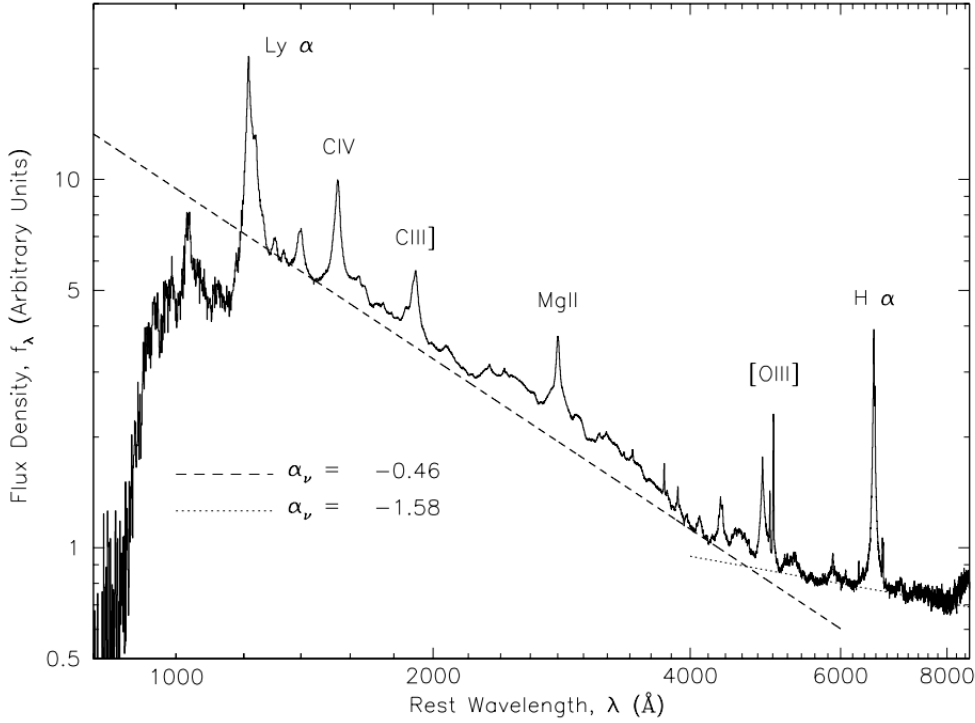


Figure 1.4: Composite AGN spectrum showing broad emission lines, such as $\text{Ly}\alpha$, $\text{H}\alpha$, Mg II , and C IV . Power-law fits to the estimated continuum flux are shown as dashed lines. Figure from [Vanden Berk et al. \(2001\)](#).

1.1.6 Dusty Torus

The entire AGN structure including the central SMBH, the accretion disk, and the BLR, is surrounded by a geometrically and optically thick, torus-like structure made up of dust and molecular gas, referred to as the “dusty torus” or the “obscuring torus” (e.g., [Urry & Padovani 1995](#)). The inner radius of this dusty torus is marked by the dust sublimation radius and its radial extent ranges from ~ 0.1 to 100 pcs. The torus is responsible for reprocessing part of the optical/UV emission from the disk and re-emitting in the infrared (IR). Different models have been proposed to describe the geometry and composition of the torus. While the simplest models assume a continuous density distribution throughout the torus, more complicated clumpy torus models with high-density clumps embedded in a lower-density smooth dusty medium have also been proposed (e.g., [Krolik & Begelman 1988](#); [Nenkova et al. 2002](#)). An important property of the dusty torus is its covering factor, which quantifies what fraction of the AGN

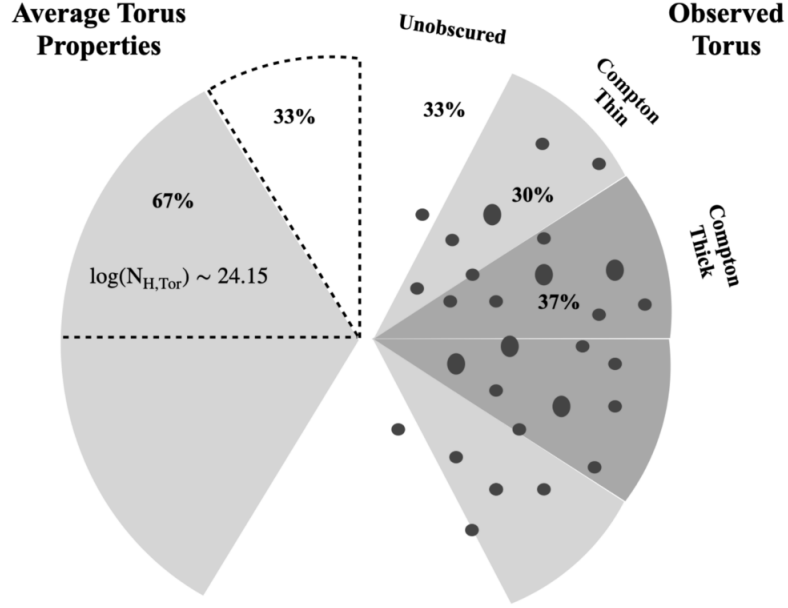


Figure 1.5: A schematic of the dusty torus showing the effect of its covering factor and composition on the level of obscuration observed in the line-of-sight (also see Section 1.2). The left part presents the average torus properties of an unbiased Compton-thin AGN sample, while the right part illustrates the AGN line-of-sight column density (N_{H}) distribution derived from the torus average column density distribution when a clumpy torus is considered. Figure from Zhao et al. (2021).

sky is covered by the torus and therefore, how much of the original emission from the accretion disk is obscured (Figure 1.5).

1.1.7 Relativistic Jets

The low energy part of AGN emission is dominated by relativistic radio jets. These are highly-collimated streams of fast-moving particles ejected perpendicular to the accretion disk, from regions close to the central SMBH. The jets can extend from a few parsecs to more than 100 kpc when they are the strongest (in about 10% AGN). They mainly emit non-thermal radiation via synchrotron (e.g., Maraschi et al. 1992) and inverse-Compton scattering processes (e.g., Blandford & Königl 1979).

1.2 AGN Unification Model

Based on their observable properties at different wavelengths, AGN have been classified into numerous classes. A few examples include classifications based on: (i) strength of radio emission (radio-quiet and radio-loud; [Kellermann et al. 1989](#)), (ii) optical emission line ratios (type 1, 1.2, 1.5, 1.8, 1.9, and 2), (iii) presence or absence of broad emission lines (type I and type II; [Osterbrock 1978](#)), etc. The primary premise of the AGN unification model is that the differences observed in the properties of various types of AGN are not due to an intrinsic difference in the structure or the physical processes in play, but rather due to orientation (e.g., [Antonucci 1993](#); [Urry & Padovani 1995](#)). Depending on the viewing angle of the AGN, due to the presence of the dusty torus (Section 1.1.6), specific components or features get obscured and are not observed. In this respect, the broad classification of AGN into type I and type II, where the former's spectrum contains both broad and narrow emission lines, while the latter is missing broad lines, can be explained as an effect of the observer's line of sight being obscured by the dusty toroidal structure surrounding the inner regions of the AGN (e.g., [Antonucci & Miller 1985](#)). As shown in Figure 1.6, the unification model proposes that type II AGN are viewed edge-on, hence the absence of broad emission lines in their spectrum due to the obscuration of the BLR, whereas type I AGN are viewed face-on without any disruption by the torus and hence we get a direct, unobscured view of the BLR.

1.3 AGN Emission

AGN are mainly characterized by the large amounts of energy emitted by them, which is also spread over multiple wavelengths. In this section, we will focus on discussing the two major contributors to these high luminosities produced by AGN.

1.3.1 Optical/UV

As mentioned in Section 1.1.2, AGN grow by accreting the material in their surroundings in the form of a disk and in the process emit radiation at optical and UV energies. This thermal emission produced due to the conversion of the gravitational energy of the in-falling material

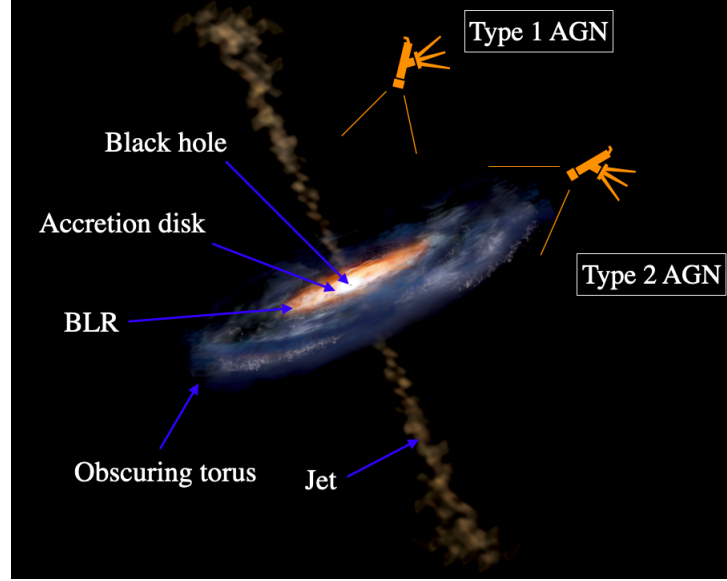


Figure 1.6: An illustration of the AGN unification model, which proposes that the difference in the properties of type I and type II AGN is due to their different viewing angles with respect to the obscuring torus. Image credit: Aurore Simonnet.

into radiation is believed to constitute a significant fraction ($> 50\%$) of an AGN's total luminosity. In the spectral energy distribution (SED) of AGN, this translates to a broad hump-like feature, commonly called the big blue bump (BBB), extending over the optical and UV regimes (e.g., [Shang et al. 2005](#)). In most cases, this emission can be modeled using multi-temperature blackbodies. The optical/UV emission of AGN is most of the time contaminated by stellar emission from the host galaxy, more so in the case of type II AGN. Additionally, it is also affected by extinction due to the dust present in the host galaxy. Therefore, when studying or modeling the optical/UV part of AGN SEDs, these effects due to host galaxy contamination and dust extinction have to be specially considered in the analysis.

1.3.2 X-Rays

X-rays are the second largest contributor to AGN emission, especially in type I AGN with minimum obscuration due to the dusty torus in the line of sight. X-rays are believed to be produced close to the central SMBH via Comptonization of the optical/UV photons from the accretion disk by a plasma of hot electrons (Section 1.1.3). This primary X-ray emission

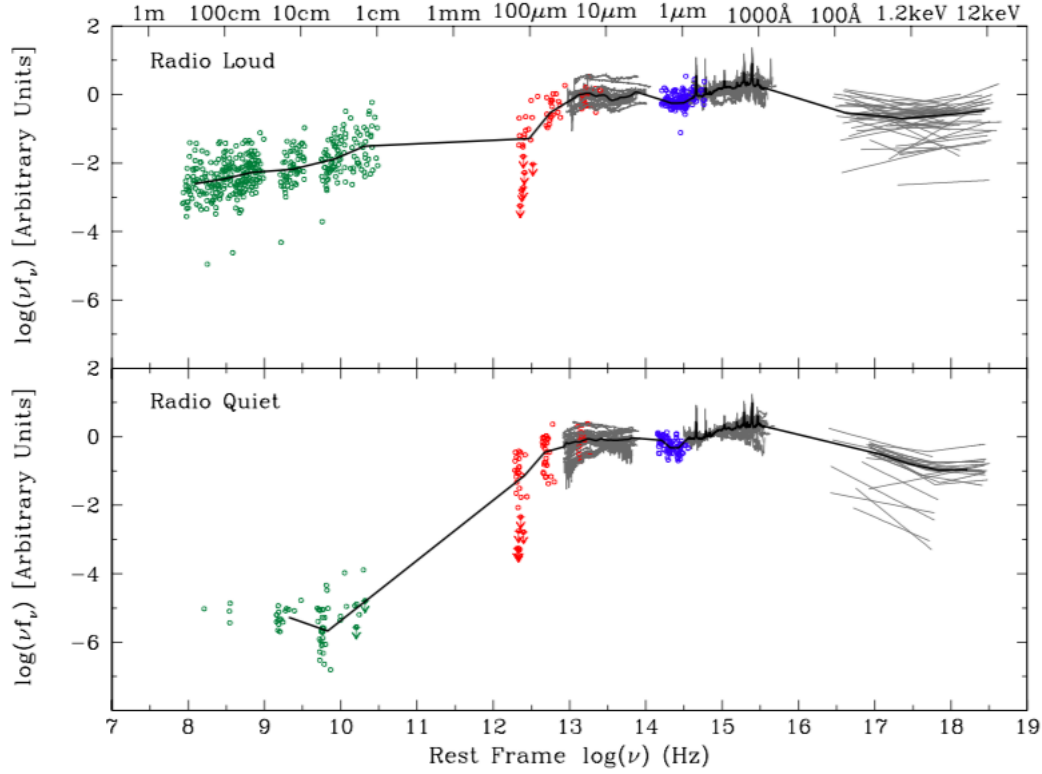


Figure 1.7: Broadband spectral energy distribution (SED) of a radio-loud (top) and radio-quiet (bottom) AGN showing their multi-wavelength emission from radio up to X-rays, originating in different parts of the AGN. Figure from [Shang et al. \(2011\)](#).

appears in the X-ray spectrum of AGN in the form of a continuum with a high energy cutoff ($E_{\text{cut}} \sim \text{few } 100 \text{ keV}$), most probably related to the cut-off in the energy distribution of the electrons in the corona responsible for up-scattering the seed photons from the disk to emit X-rays. The X-ray continuum can be modeled by a power law:

$$F(E) = kE^{-\Gamma} \text{ photons s}^{-1} \text{ cm}^{-2} \text{ keV}^{-1} \quad (1.10)$$

where, k is the normalization, and Γ is the photon index (related to the spectral index α as $\Gamma = 1 + \alpha$). Multiple studies of large samples of AGN have narrowed down the value of Γ in the range of 1.8 to 2.0 (e.g., [Nandra & Pounds 1994](#); [Beckmann et al. 2009](#); [Ricci et al. 2017a](#)).

Secondary X-ray emission can also arise in AGN due to reprocessing of the primary X-ray emission by the neutral and ionized circumnuclear material from possibly the accretion

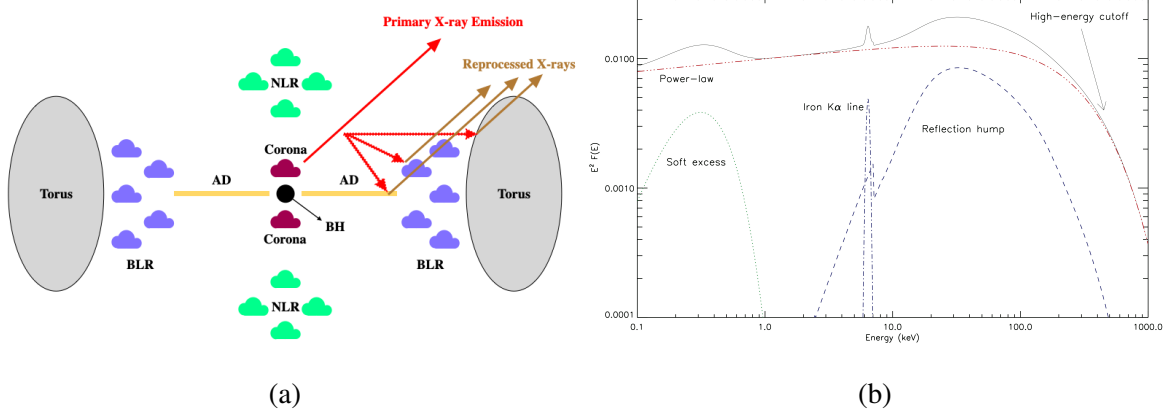


Figure 1.8: (a) Illustration of an AGN showing the primary X-ray emission arising from the corona and being reprocessed by the surrounding structure. (b) A typical X-ray spectrum of an AGN with various features corresponding to the primary and reprocessed emission. Figure from Ricci Ph.D. 2011.

disk and/or the molecular torus (see Figure 1.8a). Different features in the broadband X-ray spectrum correspond to this reprocessed emission, such as the reflection or “Compton” hump peaking around 30 keV and the fluorescent Fe K α line at 6.4 keV (Figure 1.8b). Strong absorption features are also visible at softer X-rays ($E < 10$ keV) in the case of obscured sources.

Considering the variations in the X-ray spectra of AGN due to their different levels of obscuration, AGN are classified into two types: (i) obscured and (ii) unobscured, based on their line-of-sight column density (N_H). Unobscured AGN are characterized by $\log(N_H/\text{cm}^{-2}) < 22$ while obscured AGN have $\log(N_H/\text{cm}^{-2}) > 22$. Generally, the optical and X-ray classification of AGN show good agreement, with type I AGN being unobscured and type II AGN showing evidence of obscuration. Additionally, AGN with $\log(N_H/\text{cm}^{-2}) > 24$ are specifically classified into a separate class of Compton-thick sources due to the high degrees of suppression of the primary emission (especially at energies < 10 keV) due to photoelectric absorption and Compton scattering by the surrounding material. The X-ray spectrum of these AGN is dominated by the reprocessed emission. Thanks to their high penetration power and least host-galaxy contamination, hard X-rays ($E > 10$ keV) are ideal to detect obscured as well Compton-thick AGN, as well as to probe the innermost regions of AGN. X-rays are also useful to study the composition and structure of the obscuring torus as they are much less affected by dust as compared to optical/UV.

1.4 Focus and Outline of the Thesis

This thesis focuses on studying the multi-wavelength properties of nearby AGN to better understand the physical processes at play in the inner regions of AGN. To do so, we use an almost complete and unbiased sample of hard-X-ray-selected AGN in the local universe ($z < 0.1$) and utilize their high-quality data in the optical, UV, and X-rays to get fundamental insights into the accretion properties of AGN. The primary source of all this data is the *Neil Gehrels Swift Observatory*, which is a three-telescope space observatory of NASA, with a Burst Alert Telescope (BAT) for detecting bright X-ray sources in the hard-X-rays (14 – 195 keV), and an X-ray telescope (XRT), and Ultraviolet/Optical Telescope (UVOT) for follow-up observations.

The first part of the thesis focuses on obscured AGN and using scattered X-rays radiation to better understand the structure and geometry of the dusty torus. In the second part, we shift our attention to the unobscured AGN class to: (i) present a large, comprehensive, multi-wavelength study of broadband AGN SEDs using simultaneous optical, UV, and X-ray data, (ii) estimate important quantities like intrinsic luminosities in multiple wavebands, bolometric luminosities, and Eddington ratios for our sample, (iii) provide bolometric corrections at several energies, that can be used to convert corresponding luminosities into bolometric luminosities without the need of the much more expensive and time-consuming multi-wavelength data, and finally (iv) determine the main parameter regulating and influencing AGN accretion and emission. The outline of the thesis is as follows:

In Chapter 2, we present our study of a sample of ~ 390 obscured AGN in the local universe to explore the characteristics of Thomson-scattered X-ray radiation. We inspect possible correlations of the fraction of scattered radiation with other physical properties of AGN and also try to locate the region of its origin. This study has been published as [Gupta et al. \(2021\)](#).

Chapter 3 reports the step-by-step procedure followed to create optical-to-X-ray SEDs for a sample of ~ 240 unobscured AGN. It explains in detail how we handled host galaxy contamination and galactic dust extinction to construct clean AGN SEDs. It also describes the models employed to fit the SEDs and other technical aspects of the whole analysis.

In Chapter 4, we discuss some important outcomes of our broadband SED fitting, in terms of measurements of bolometric luminosity, optical-to-X-ray spectral index, and optical/UV

bolometric corrections in 8 different energy bands. We report the median values for all bolometric corrections and also discuss some significant relations between these quantities and their implications. The main findings of this work will be reported in Gupta et al. (2023a, in prep.).

Chapter 5 is dedicated to the 2 – 10 keV X-ray bolometric correction and its correlations with quantities like bolometric luminosity, black hole mass, and Eddington ratio. Here, we also try to determine, based on our results, the main parameter controlling the bolometric correction factors. These results will be presented in Gupta et al. (2023b, in prep.).

And finally, in Chapter 6, we summarize the main findings of this thesis and discuss some important conclusions and future prospects of this work.

Chapter 2

Scattered X-Ray Radiation in Obscured AGN

AGN are generally surrounded by large amounts of gas and dust. This surrounding material reprocesses the primary X-ray emission produced close to the SMBH and gives rise to several components in the broadband X-ray spectra of AGN, including a power law possibly associated with Thomson-scattered radiation. In this chapter, we study the properties of this scattered component for a sample of 386 hard-X-ray-selected, nearby ($z \sim 0.03$) obscured AGN from the 70-month *Swift*/BAT catalog. We investigate how the fraction of Thomson-scattered radiation correlates with different physical properties of AGN, such as line-of-sight column density, X-ray luminosity, black hole mass, and Eddington ratio. We find a significant negative correlation between the scattering fraction and the column density. Based on a large number of spectral simulations, we exclude the possibility that this anti-correlation is due to degeneracies between the parameters. The negative correlation also persists when considering different ranges of luminosity, black hole mass, and Eddington ratio. We discuss how this correlation might be either due to the angle dependence of the Thomson cross-section or to more obscured sources having a higher covering factor of the torus. We also find a positive correlation between the scattering fraction and the ratio of [O III] $\lambda 5007$ to X-ray luminosity. This result is consistent with previous studies and suggests that the Thomson-scattered component is associated with the narrow-line region.

2.1 Introduction

Studies have shown that a majority of AGN are obscured (e.g., [Maiolino et al. 1998](#); [Risaliti et al. 1999](#); [Ricci et al. 2015](#); [Marchesi et al. 2018](#)) and are thus difficult to account for based on optical or UV surveys. These obscured AGN are believed to contribute significantly to the cosmic X-ray background (CXB; e.g., [Comastri et al. 1995](#); [Ueda et al. 2003](#); [Gilli et al. 2007](#); [Ueda et al. 2014](#); [Ananna et al. 2020](#)). Therefore, the study of obscured SMBHs is essential to improve our understanding of the entire AGN population and their evolution. This can be done by making use of a characteristic feature of AGN, which is their strong X-ray emission, which is produced by the Comptonization of optical and UV photons in a corona of hot electrons located close to the SMBH (e.g., [Haardt & Maraschi 1991](#)). This energetic radiation, and in particular that emitted in the hard-X-ray band ($E > 10$ keV), can be used to find obscured AGN, and to study their properties, because: (a) they are significantly less absorption-biased than lower-energy X-rays, hence can penetrate large column densities (N_{H}), up to Compton-thick values ($N_{\text{H}} > 10^{24} \text{ cm}^{-2}$; see Figure 1 of [Ricci et al. 2015](#)) and (b) they are substantially less contaminated by the light associated with the host galaxy than softer X-rays.

The broadband X-ray spectra of AGN have already been analyzed in great detail in many previous studies (e.g., [Dadina 2007](#); [Winter et al. 2009](#); [Koss et al. 2016](#); [Ricci et al. 2017a](#)). Typically, in unobscured AGN, the spectrum is dominated by a primary X-ray continuum associated with radiation produced by the corona (e.g., [Dadina 2008](#); [Beckmann et al. 2009](#)). Apart from this, the spectrum also shows several distinctive features that can be attributed to the absorption and reprocessing of the primary X-ray radiation by the circumnuclear material. For example, for column densities above 10^{22} cm^{-2} , the primary X-ray continuum is significantly suppressed due to photoelectric absorption. Signatures of reprocessed X-ray radiation by the circumnuclear material are also seen in the X-ray spectrum in the form of a broad “Compton hump” peaking around 30 keV (e.g., [Lightman & White 1988](#); [Ghisellini et al. 1994](#); [Krolik et al. 1994](#)) and a fluorescent Fe K α line at 6.4 keV (e.g., [Fabian et al. 2000](#); [Yaqoob & Padmanabhan 2004](#); [Shu et al. 2010](#); [Fukazawa et al. 2011](#); [Ricci et al. 2014](#)). These features provide important information about the geometry, as well as the physical properties of the circumnuclear material (e.g., [George & Fabian 1991](#); [Matt et al. 1991](#); [Ponti et al. 2013](#)).

When the X-ray continuum is obscured ($N_{\text{H}} \gtrsim 10^{22} \text{ cm}^{-2}$), a component possibly related to Thomson scattering of the X-ray continuum by circumnuclear photoionized gas also becomes visible. This component is believed to be produced in the Compton-thin circumnuclear material and is observed as a weak, unabsorbed, power-law continuum emerging at energies lower than the photoelectric cutoff. The scattered X-ray radiation can help us to understand the effects of obscuration and can shed light on the structure of the inner regions of AGN. The parameter generally used to study the scattered radiation in AGN is the “scattering fraction” (f_{scatt} ; e.g., [Turner et al. 1997](#); [Cappi et al. 2006](#); [Ueda et al. 2007](#); [Winter et al. 2009](#); [Yamada et al. 2020](#)). This parameter denotes the fraction of radiation scattered with respect to the primary X-ray emission of the AGN. Its intensity depends on both the covering angle of the surrounding torus and the amount of gas available for scattering (e.g., [Levenson et al. 2002](#); [Eguchi et al. 2009](#)).

Using broadband X-ray observations of hard-X-ray-selected AGN, [Ueda et al. \(2007\)](#) discovered a new type of AGN with extremely low values of scattering fraction ($f_{\text{scatt}} < 0.5\%$). They concluded that either the central SMBH in these sources is buried in a geometrically-thick torus with a small opening angle, or the amount of gas available for scattering is exceptionally low, or both. [Noguchi et al. \(2009\)](#) later presented an improved sample of these ‘buried’ AGN, and investigated their multi-wavelength properties ([Noguchi et al. 2010](#)), finding that these objects also tend to have lower values of the ratio of [O III] $\lambda 5007$ to X-ray luminosity ($L_{[\text{O III}]} / L_{\text{X}}$). They interpreted this as evidence of these AGN having a small opening angle of the torus that collimates the narrow-line region (NLR), a result further supported by [Ueda et al. \(2015\)](#) and [Kawamuro et al. \(2016\)](#). Studies have already shown that the soft X-ray ($E < 10 \text{ keV}$) emission in obscured sources can extend up to hundreds of parsecs (e.g., [Sako et al. 2000](#); [Young et al. 2001](#); [Greene et al. 2014](#)) and has a morphology similar to that of the optical NLR, as traced by the [O III] $\lambda 5007$ emission (e.g., [Bianchi et al. 2006](#); [Dadina et al. 2010](#); [Bianchi et al. 2010](#); [Gómez-Guijarro et al. 2017](#); [Fabbiano et al. 2018](#)). The detailed analysis of high-resolution X-ray spectra of obscured AGN (e.g., NGC 1068 by [Kinkhabwala et al. 2002](#) and [Brinkman et al. 2002](#); Mrk 3 by [Sako et al. 2000](#)) showed that the $< 3\text{--}4 \text{ keV}$ range is dominated by photoionization lines. This points towards both the soft X-ray and the optical emission lines being produced in the photoionized gas of the NLR. As a result, low values of $L_{[\text{O III}]} / L_{\text{X}}$ for buried AGN suggest that the possible locus of Thomson scattering of X-ray radiation is also

in the NLR. However, [Ichikawa et al. \(2012\)](#), who presented a mid- to far-infrared study of a sample of local AGN, attributed the low scattering values of AGN to strong starburst activities of the host galaxy. On the other hand, [Hönig et al. \(2014\)](#) found that objects with low scattering fractions reside in high-inclination galaxies or merger systems. Therefore, they concluded that the low values of f_{scatt} are related to the obscuration of scattered emission due to host galactic gas and dust.

This work aims to study the properties of Thomson-scattered radiation in a sample of hard-X-ray-selected AGN and to constrain the possible region of origin of this radiation. The objects in our sample were detected by the Burst Alert Telescope (BAT: [Barthelmy et al. 2005](#); [Krimm et al. 2013](#)) on board the NASA mission, *Neil Gehrels Swift Observatory* ([Gehrels et al. 2004](#)). BAT operates in the 14–195 keV energy band and is therefore sensitive to heavily obscured AGN. Since 2005, BAT has been continuously surveying the entire sky and has proved very useful to study AGN in the local Universe ($z < 0.1$). The BAT AGN Spectroscopic Survey (BASS¹) has provided high-quality multi-wavelength data for the BAT AGN, including black hole mass measurements ([Koss et al. 2017](#)), X-ray spectroscopy and modeling ([Ricci et al. 2017a](#)), near-infrared (NIR; 1–2.4 μ) spectra and modeling ([Lamperti et al. 2017](#)), NIR AO imaging ([Koss et al. 2018](#)), extensive continuum modeling of the far-infrared emission ([Ichikawa et al. 2019a](#)), radio emission ([Smith et al. 2020](#)), and molecular gas measurements ([Koss et al. 2020](#)). From this data, numerous correlations have been found such as between X-ray emission and high ionization optical lines (e.g., [Berney et al. 2015](#)) and outflows (e.g., [Rojas et al. 2020](#)) with the Eddington ratio being a key parameter in these trends (e.g. [Ricci et al. 2017b](#); [Oh et al. 2017](#); [Ricci et al. 2018](#)).

We use the 70-month *Swift*/BAT catalog ([Baumgartner et al. 2013](#)), with revised counterpart classifications from [Ricci et al. \(2017a\)](#), to understand the properties of scattered X-ray radiation in nearby obscured AGN and how it relates with the physical properties of AGN. To do so, we study possible correlations between scattering fraction and other physical properties of accreting SMBHs, such as their column density (N_{H}), X-ray luminosity (L_{X}), black hole mass (M_{BH}), and Eddington ratio (λ_{Edd}). We also investigate the dependence of f_{scatt} on the ratio of [O III] $\lambda 5007$ luminosity to X-ray luminosity ($L_{[\text{O III}]}/L_{\text{X}}$), as well as the ratio of [O II]

¹www.bass-survey.com

$\lambda 3727$ luminosity to X-ray luminosity ($L_{[\text{OII}]} / L_X$).

The structure of this chapter is as follows. In Section 2.2 we describe the sample used in this work, while in Section 2.3 we present the correlation we found between scattering fraction and column density. In Section 2.3.1, we simulate and fit spectra for a dummy population of obscured AGN, to verify that the correlation found in this section is intrinsic to our sample, and not due to parameter degeneracy. The correlations with $L_{[\text{OIII}]} / L_X$ and $L_{[\text{OII}]} / L_X$ are discussed in Section 2.4, while potential correlations with black hole mass, X-ray luminosity, and Eddington ratio are investigated in Section 2.5. Finally, we discuss and summarize our findings in Sections 2.6 and 2.7. Throughout the work, we assume a cosmological model with $H_0 = 70 \text{ km s}^{-1} \text{ Mpc}^{-1}$, $\Omega_M = 0.3$, and $\Omega_\Lambda = 0.7$.

2.2 Sample and Data

We use here the 70-month *Swift*/BAT catalog, which includes 838 hard-X-ray-selected, nearby (median redshift = 0.037) AGN. Of these, 386 ($\sim 53\%$) sources are classified as obscured AGN based on strong intrinsic absorption required in the initial absorbed power-law fits to their X-ray spectra (Ricci et al. 2017a; see Section 2.2.1). The line-of-sight column densities (N_H) of these sources lie in the range $10^{21.5} \text{ cm}^{-2}$ to 10^{25} cm^{-2} . Our analysis focuses on these obscured sources, which show features of Thomson-scattered radiation in their X-ray spectra. Of these, nine sources are flagged as blazars by Ricci et al. (2017a; see also Paliya et al. 2019). However, they are included in the analysis as their X-ray spectra showed signatures of reprocessed X-ray emission (Ricci et al. 2017a). The various parameters used in our work have been obtained from the optical (Section 2.2.2) and X-ray spectroscopic analysis (Section 2.2.1) of these sources, carried out as part of the first data release (DR1) of BASS (e.g., Koss et al. 2017; Ricci et al. 2017a).

2.2.1 X-Ray Data

The *Swift*/BAT AGN have been extensively followed up by X-ray observatories covering the 0.3–10 keV energy range. By combining observations from *XMM-Newton* (Jansen et al. 2001), *Swift*/XRT (Burrows et al. 2005), *ASCA* (Tanaka et al. 1994), *Chandra* (Weisskopf et al. 2000)

and *Suzaku* (Mitsuda et al. 2007) in the soft X-ray band ($E < 10$ keV), together with the *Swift*/BAT data, Ricci et al. (2017a; hereafter R17) carried out a detailed broadband X-ray (0.3–150 keV) spectral analysis of all 838 AGN from the 70-month *Swift*/BAT catalog, using XSPEC (Arnaud 1996; see Section 2.3.1). Firstly, they fitted the X-ray spectra of all sources using a simple power-law model, including Galactic absorption along the line of sight ($\text{TBABS}_{\text{Gal}} \cdot [\text{ZPOW}]$ in XSPEC). The residuals from these fits were then visually inspected to check for signatures of absorption from neutral matter to classify the sources as obscured or unobscured. After this preliminary exercise, 24 different spectral models were used for the X-ray spectral fitting.

The sample of 386 obscured, non-blazar AGN were fitted using nine models (B1 to B9; see R17 for more details) of increasing complexity. The different components included in these models are: (1) an X-ray continuum with a high energy cutoff (CUTOFFPL) representing the primary X-ray emission from the corona, (2) absorption of the X-ray radiation by neutral material via photoelectric absorption (ZPHABS) and Compton scattering (CABS), (3) reflection of the primary X-ray continuum by optically thick, neutral circumnuclear material (PEXRAV ; Magdziarz & Zdziarski 1995), and (4) Thomson scattering of part of the primary X-ray radiation by Compton-thin circumnuclear material.

For 272/386 (70%) obscured sources, model B1 was sufficient and hence adopted by R17 for the spectral fitting. This model consisted of an absorbed primary X-ray continuum, along with an unobscured reflection component and a Thomson-scattered component. For the latter, a cutoff power law was used, with values of the free parameters (photon index $[\Gamma]$, cutoff energy $[E_C]$, normalization $[K]$) set to be the same as those of the primary X-ray continuum. A multiplicative constant corresponding to the scattering fraction (f_{scatt}) was added to this component, as a free parameter, to renormalize the flux. For the remaining objects, model B1 was modified by adding multiple collisionally ionized plasma components or partially covering absorbers, as and when such a modified model improved the fit significantly.

The best-fit values of all free parameters in different models, employed for the spectral fitting of the AGN sources, are reported by R17. They also provide absorption-corrected fluxes of the primary continuum emission in the 2–10 keV, 14–150 keV, and 14–195 keV energy bands (F_{2-10} , F_{14-150} , and F_{14-195} , respectively) for all obscured sources. The main spectral param-

eters used in our analysis, such as f_{scatt} , N_{H} , and F_{X} , have all been obtained from their fitting analysis. Best-fit values of column densities, along with upper and lower bounds (of 90% confidence level), are available for all 386 obscured sources. In the case of the scattering fraction, best-fit values along with upper and lower errors (at 90% confidence level) are available for 250/386 ($\sim 65\%$) objects, while for the rest (136/386 $\sim 35\%$), upper limits are provided. We also calculate the intrinsic (i.e., absorption-corrected and k-corrected) luminosities for the obscured sources in the 2–10 keV, 14–150 keV, and 14–195 keV energy bands (L_{2-10} , L_{14-150} , and L_{14-195} , respectively). Spectroscopic redshifts and corresponding distance values are available for 382/386 ($\sim 99\%$) sources, and therefore, we can calculate the intrinsic luminosity for these 382 sources.

2.2.2 Optical Data

Koss et al. (2017; BASS DR1 and 2022a; BASS DR2) analysed the optical spectra of the 838 hard-X-ray-selected AGN in the 70-month *Swift*/BAT catalog. They performed multiple spectral measurements to understand the general properties of *Swift*/BAT AGN, such as broad and narrow emission-line diagnostics to classify these AGN. They also fitted the host galaxies using stellar templates to calculate their stellar velocity dispersions. They presented the fluxes and strengths of optical emission lines, as well as black hole mass estimates and accretion rates, for both obscured and unobscured AGN in their sample. Out of the 386 sources in our sample, reliable black hole mass estimates that we adopt in this work are available for 273 ($\sim 71\%$) sources. For 261/273 ($\sim 96\%$) sources, the black hole masses have been derived from the correlation between the black hole mass and the stellar velocity dispersion of the host galaxy given by Kormendy & Ho (2013). For the remaining (12/273 $\sim 4\%$) sources, we use black hole mass values from the literature. We calculate the Eddington ratio (λ_{Edd}) for these 273 sources by incorporating their black hole masses and the 2–10 keV bolometric correction ($L_{\text{bol}} = 20 \times L_{2-10}$) following Vasudevan et al. (2009):

$$\lambda_{\text{Edd}} = \left[\frac{20 \times L_{2-10} (\text{erg s}^{-1})}{1.5 \times 10^{38} \times M_{\text{BH}} (M_{\odot})} \right]. \quad (2.1)$$

To include the effects of using more advanced bolometric corrections in our work, we repeat part of the analysis described in Section 2.5 with Eddington ratio-dependent bolometric cor-

rections (Vasudevan & Fabian 2009) and obtain similar results.

Finally, in our analysis, we use the emission line measurements presented by Koss et al. (2017) and Oh et al. (2022) using the spectral line fitting codes described by Sarzi et al. (2006) and improved by Oh et al. (2011, 2015). We adopt a Gaussian amplitude-to-noise ratio (A/N) of 3 as the threshold for reliable line measurements and hence, do not include line strengths with $A/N < 3$ in our analysis. We use the observed fluxes of the [O II] $\lambda 3727$ line to calculate the observed [O II] $\lambda 3727$ luminosity ($L_{[\text{O II}]}$) for 295/386 ($\sim 76\%$) sources. We also use equivalent widths and observed fluxes of the [O III] $\lambda 5007$ line for 359/386 ($\sim 93\%$) sources and fluxes of the narrow H α and H β lines for 318/386 ($\sim 82\%$) sources and calculate the corresponding observed [O III] $\lambda 5007$ luminosity ($L_{[\text{O III}]}$) as well as the extinction-corrected [O III] $\lambda 5007$ luminosity ($L_{[\text{O III}]}^{\text{corr}}$) using the Balmer decrement, as described in Ueda et al. (2015).

2.3 The Correlation Between Scattering Fraction and Column Density

We study here the relation between the fraction of Thomson-scattered X-ray radiation and the line-of-sight column density of AGN. In Figure 2.1, we plot the scattering fraction as a function of column density (in grey) for the 386 obscured sources in our sample. The figure clearly shows a negative correlation between these parameters, which we quantify by fitting a linear regression line (in red) to the data points. We initially excluded the upper limits while calculating the regression line here since they can affect our results considerably if not handled properly. However, we do include them in later parts of this analysis to properly quantify their contribution to the correlation. We use the `linregress`² correlation function of the `scipy.stats` module in Python to fit the data with linear regression. This function minimizes the sum of squares of the difference between the actual data points and that predicted by the regression model. Throughout this work, we use this technique to fit linear regression lines to our data. The slope and intercept of the linear regression line, Pearson’s correlation coefficient, and the probability of the data arising from an underlying uncorrelated distribution (null hypothesis) are

²<https://docs.scipy.org/doc/scipy/reference/generated/scipy.stats.linregress.html>

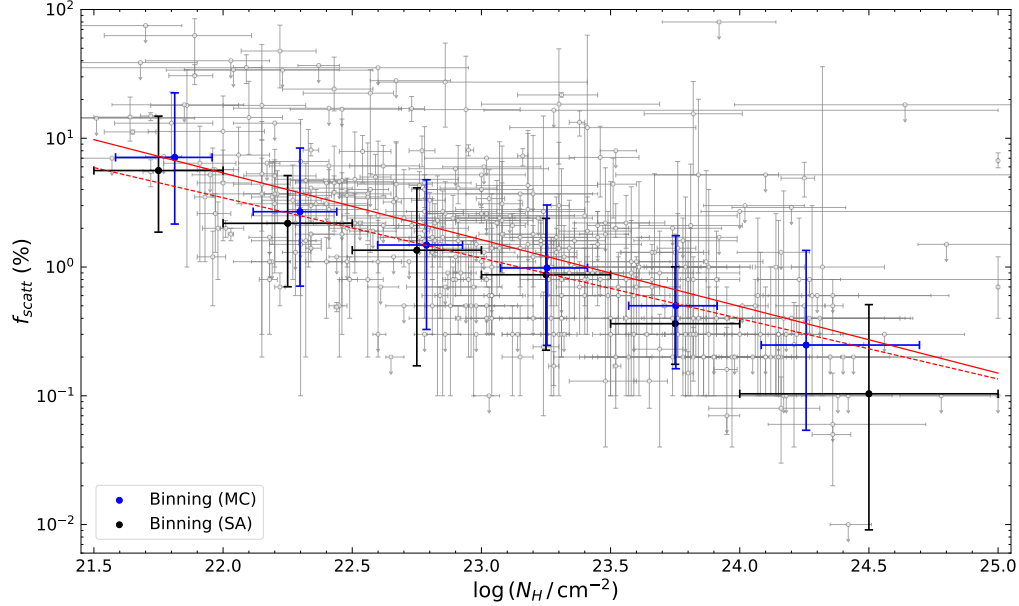


Figure 2.1: Scattering fraction vs column density: The plot shows the scattering fraction and the column density values (from R17) for our sample of 386 obscured AGN in the background as grey open circles (upper limits as downward arrows and best-fit values with error bars showing errors at 90% confidence level). Black circles with error bars correspond to the survival analysis (SA) results for each $\log N_{\text{H}}$ bin (f_{scatt} median calculated using the 50th percentile and the 1σ uncertainty calculated using the 16th and 84th percentile). Blue circles with error bars (1σ) depict the results obtained from 10,000 Monte Carlo (MC) simulations. The solid red line is the linear regression obtained from the data points excluding upper limits, while the dashed red line is the linear regression calculated using MC simulations. 2 sources in our sample have $\log(N_{\text{H}}/\text{cm}^{-2}) > 25$, but for display purpose only they are plotted at $\log(N_{\text{H}}/\text{cm}^{-2}) = 25$. The plot clearly shows a negative correlation between f_{scatt} and $\log N_{\text{H}}$. Correlation parameters for the two methods are given in Table 2.1.

reported in Table 2.1. To better visualize the decrease of the scattering fraction as the column density increases, we divide the column density into six bins (of width $\log[N_{\text{H}}/\text{cm}^{-2}] = 0.5$, except for the last one) and plot the median of the scattering fraction, along with the standard error (in black), for each bin. The median and error in f_{scatt} in each $\log N_{\text{H}}$ bin are calculated using survival analysis (SA; e.g., Feigelson & Nelson 1985; Shimizu et al. 2017) to include the contributions from the upper limits. The median f_{scatt} is calculated using the 50th percentile, and the uncertainties for each bin are calculated with respect to the median value in that bin using the 16th and 84th percentile. For $\log N_{\text{H}}$, we simply plot the midpoint of each bin with error bars = 0.5 (= 1 for the last bin).

The SA approach efficiently includes the upper limits in f_{scatt} while calculating its median value in specified bins of column density. However, it does not take into account the errors in f_{scatt} and $\log N_{\text{H}}$. In order to include these errors in our analysis, we make use of Monte Carlo (MC) simulations. To apply this technique, we handled the best-fit values with errors and upper limits separately, as discussed below:

1. **Best-Fit Values with Errors:** We created an asymmetric Gaussian distribution (normalized) to simulate the values of parameters f_{scatt} and $\log N_{\text{H}}$. We used an asymmetric distribution because the upper and lower errors in both parameters can be unequal. To create this distribution, we first assumed two different symmetric Gaussian distributions with the mean of both Gaussians equal to the best-fit value of the parameter, whereas the standard deviation (1σ) was chosen to be $\frac{\text{Upper Error}}{1.64}$ and $\frac{\text{Lower Error}}{1.64}$ for the first and second Gaussian, respectively. The errors were divided by 1.64 because they are 2σ errors. The final Gaussian was obtained by combining these two Gaussian distributions, such that the probability distribution of values greater than the mean is governed by the first Gaussian, while the probability distribution of values lower than the mean is decided by the second Gaussian. Hence, corresponding to each source with a best-fit f_{scatt} and $\log N_{\text{H}}$ value, we created two asymmetric Gaussians depicting the probability distribution functions of f_{scatt} and $\log N_{\text{H}}$, by incorporating their best-fit values as well as their upper and lower errors.

2. **Best-Fit Upper Limits:** Throughout our analysis, upper limits are only present for scat-

tering fraction. In this particular case, we employed a normalized uniform distribution to describe the probability distribution of f_{scatt} . The distribution, used for each source with an upper limit, ranges from 0 to the corresponding upper limit value of f_{scatt} , with each value in the distribution assigned equal probability.

After finalizing the probability distribution functions for both parameters (f_{scatt} and $\log N_{\text{H}}$), we performed 10,000 runs of MC simulations. In each run, a random value of the scattering fraction and column density was taken for each source from the probability distributions described above. In the case of the column density, values greater than $\log(N_{\text{H}}/\text{cm}^{-2}) = 26$ were not permitted in the simulations, and for the scattering fraction, negative values were not considered. Thus, we end up with 10,000 simulated values of the scattering fraction and column density for each of the 386 sources. Next, we bin the 3,860,000 simulated column density values into six separate bins (similar to the $\log N_{\text{H}}$ bins created for SA) and calculate the median column density for each bin. Values of $\log(N_{\text{H}}/\text{cm}^{-2}) > 25$ are included in the last bin. Similarly, the corresponding simulated values of f_{scatt} are also binned, and the median value of f_{scatt} in each bin is calculated. The standard error in each bin is calculated using the 16th and 84th percentile, as was done during the SA method. MC results are shown in blue in Figure 2.1. As evident from the figure, median and error values from SA and MC simulations are completely consistent within their error bars. Although, median f_{scatt} values calculated using SA are slightly lower than those calculated from MC simulations. However, unlike SA, MC simulations include the already calculated uncertainties in both parameters (reported by R17) and thus give better estimates of the final median and error in each column density bin.

We also used the simulated values of scattering fraction and column density to better quantify the correlation found between them. For each run of the MC simulations, we fitted a linear regression line to the simulated data and obtained the regression parameters such as slope, intercept, correlation coefficient, and the probability of the null hypothesis. The final slope, intercept, and Pearson's correlation coefficient (reported in Table 2.1) are calculated from the median of these 10,000 values, and the corresponding regression line is shown as a dashed red line in Figure 2.1. Compared to the linear regression line fitted initially to the data after excluding the upper limits, the regression line found through MC simulations is more accurate since these simulations are a better representation of the range of values that the scattering fraction

and the column density could take for each source. Hence, the corresponding regression parameters better define the observed negative correlation between f_{scatt} and $\log N_{\text{H}}$. To confirm the reliability of this correlation, we examined the probability distribution of the linear regression obtained from MC simulations. As shown in Table 2.1, for the correlation between scattering fraction and column density, we obtain a probability $= 1.5 \times 10^{-25}$ for the null hypothesis. Such a low p -value further confirms the significance of the inverse correlation obtained. We also fitted various higher-degree polynomial regressions to the data points shown in Figure 2.1 but did not find any significant improvement in the chi-square values as compared to the one for the linear regression fit.

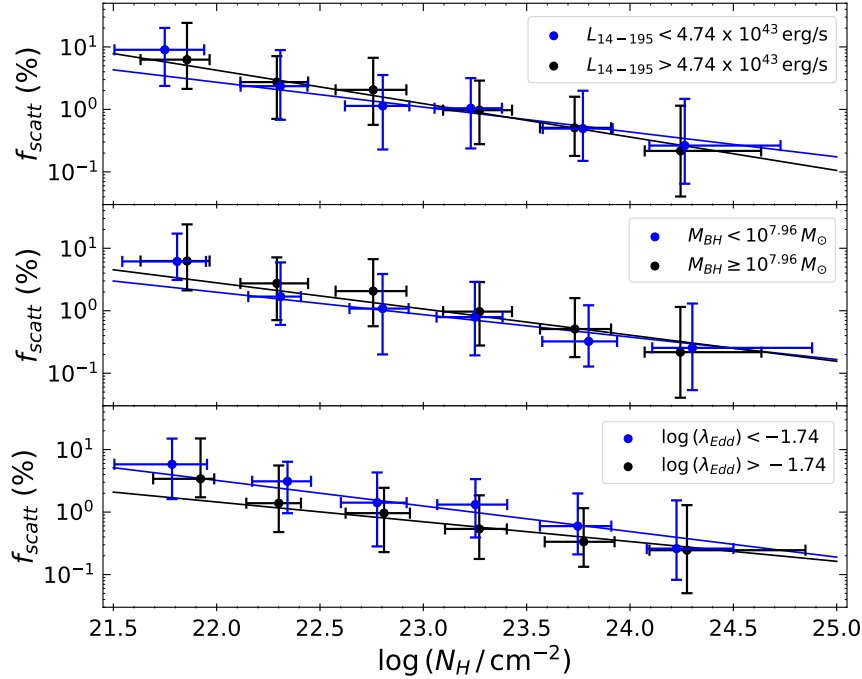


Figure 2.2: Scattering fraction vs column density for objects corresponding to two bins in: (a) Top panel: intrinsic 14–195 keV luminosity (L_{14-195}), (b) Middle panel: black hole mass (M_{BH}), and (c) Bottom panel: Eddington ratio (λ_{Edd}). The linear regression line as well as the median f_{scatt} and $\log N_{\text{H}}$ values with 1σ uncertainty for each $\log N_{\text{H}}$ bin are calculated using MC simulations. The plots show a distinct negative correlation between scattering fraction and column density. The correlation parameters are given in Table 2.2.

Table 2.1: Correlation results for Figure 2.1 (Section 2.3), Figure 2.4 (Section 2.4), and Figure 2.5c (Section 2.5).

Parameter (in log) (vs f_{scatt})	Slope ^a		Intercept ^a		R-Value ^b		P-Value ^c	
	Data ^d	MC ^e	Data ^d	MC ^e	Data ^d	MC ^e	Data ^d	MC ^e
N_{H}	-0.52 ± 0.04	-0.47 ± 0.03	12.1 ± 1.0	10.9 ± 0.7	-0.63	-0.50	1.9×10^{-28}	1.5×10^{-25}
$L_{[\text{OIII}]} / L_{2-10}$	0.26 ± 0.05	0.33 ± 0.02	0.76 ± 0.11	0.79 ± 0.06	0.35	0.36	2.5×10^{-8}	2.8×10^{-12}
$L_{[\text{OIII}]} / L_{14-195}$	0.22 ± 0.05	0.27 ± 0.02	0.75 ± 0.15	0.76 ± 0.07	0.27	0.28	2.0×10^{-5}	9.0×10^{-8}
$L_{[\text{OIII}]}^{\text{corr}} / L_{2-10}$	0.27 ± 0.05	0.36 ± 0.03	0.65 ± 0.10	0.70 ± 0.05	0.33	0.34	4.9×10^{-7}	3.2×10^{-10}
$L_{[\text{OIII}]}^{\text{corr}} / L_{14-195}$	0.20 ± 0.06	0.27 ± 0.03	0.62 ± 0.14	0.66 ± 0.07	0.23	0.24	6.0×10^{-4}	1.4×10^{-5}
$L_{[\text{OII}]} / L_{2-10}$	0.31 ± 0.05	0.40 ± 0.03	1.01 ± 0.16	1.12 ± 0.08	0.39	0.38	1.4×10^{-8}	1.8×10^{-11}
$L_{[\text{OII}]} / L_{14-195}$	0.26 ± 0.06	0.33 ± 0.03	0.97 ± 0.20	1.08 ± 0.10	0.29	0.29	2.7×10^{-5}	4.4×10^{-7}
λ_{Edd}	-0.14 ± 0.05	-0.16 ± 0.02	-0.22 ± 0.09	-0.40 ± 0.05	-0.23	-0.20	2.1×10^{-3}	1.1×10^{-3}

^a Of the linear regression line.^b The Pearson's correlation coefficient.^c The probability of the data set appearing if the null hypothesis is correct.^d Excluding upper limits.^e Monte Carlo simulations.

Table 2.2: Correlation results from MC simulations for Figure 2.2 (Section 2.3).

Parameter	Number of Sources	Bin	Slope ^a	Intercept ^a	R-Value ^b	P-Value ^c
L_{14-195}	191/382	$< 4.74 \times 10^{43} \text{ erg/s}$	-0.40 ± 0.04	9.2 ± 0.9	-0.43 ± 0.04	8.5×10^{-10}
	191/382	$> 4.74 \times 10^{43} \text{ erg/s}$	-0.54 ± 0.04	12.4 ± 0.9	-0.57 ± 0.04	1.2×10^{-17}
M_{BH}	136/273	$< 10^{7.96} M_{\odot}$	-0.36 ± 0.05	8.2 ± 1.1	-0.42 ± 0.05	4.6×10^{-7}
	137/273	$\geq 10^{7.96} M_{\odot}$	-0.42 ± 0.05	9.7 ± 1.2	-0.43 ± 0.05	1.2×10^{-7}
λ_{Edd}	136/273	$< 10^{-1.74}$	-0.41 ± 0.05	9.5 ± 1.2	-0.42 ± 0.05	2.8×10^{-7}
	137/273	$> 10^{-1.74}$	-0.32 ± 0.05	7.1 ± 1.1	-0.38 ± 0.05	5.7×10^{-6}

^a Of the linear regression line.^b The Pearson's correlation coefficient.^c The probability of the data set appearing if the null hypothesis is correct.

We also check if the correlation we found between scattering fraction and column density holds for objects in different ranges of L_{14-195} , M_{BH} , and λ_{Edd} in our sample. By specifying certain constraints on these physical properties of AGN, we aim to investigate how these external factors modify the correlation we found. To do so, we create two bins for each of these three parameters, as follows: (a) $L_{14-195} < 4.74 \times 10^{43}$ erg/s and $> 4.74 \times 10^{43}$ erg/s, (b) $M_{\text{BH}} < 10^{7.96} M_{\odot}$ and $\geq 10^{7.96} M_{\odot}$ and (c) $\log(\lambda_{\text{Edd}}) < -1.74$ and > -1.74 . These ranges were determined from the median values of these parameters. In Figure 2.2, we show the linear regression line obtained using MC simulations for each of these intervals. We also show the median and uncertainty in the values of scattering fraction and column density for each bin calculated using MC simulations. The correlation parameters for these fits and the number of sources in each parameter window are reported in Table 2.2. Very low values of probability (of the null hypothesis) establish the significance of the negative correlation between f_{scatt} and $\log N_{\text{H}}$ even when different conditions related to the physical properties of the accreting system are considered. Therefore, we can conclude that X-ray luminosity, black hole mass, and Eddington rate do not affect the negative correlation we found.

The X-ray spectra of 75/386 ($\sim 19\%$) sources in our sample were also fitted using torus models (see R17 for details). We have verified that including f_{scatt} and $\log N_{\text{H}}$ values obtained from those fittings in our original data does not affect the anti-correlation found between these parameters. One should note that scattering fraction values $\geq 5\% - 10\%$ can arise due to a partial covering absorber instead of Thomson scattering. To exclude their contributions, we apply an uppercut on the value of scattering fraction at 5% and 10%. In Appendix 2.7, we show that applying such a criterion does not modify the correlation significantly (Figure 2.7a). The correlation we found may be biased by the typically low count rates of sources with high column densities. To make sure that these sources do not regulate the observed trend, we impose a lower limit on the number of counts per source at 200 counts. Figure 2.7b in Appendix 2.7 shows that, even after removing the sources with low counts, we recover the same correlation between f_{scatt} and $\log N_{\text{H}}$, using MC simulations.

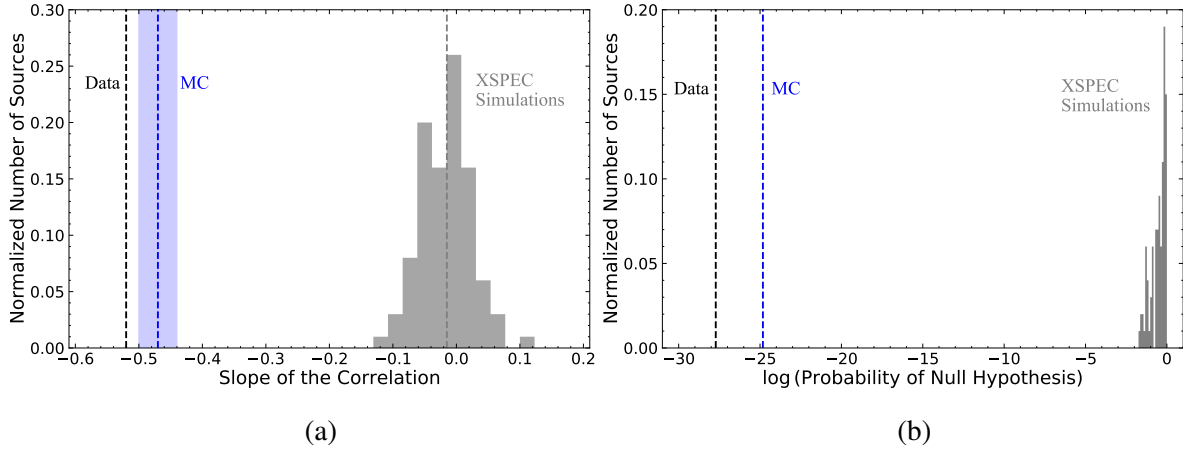


Figure 2.3: (a) Distribution in values of the slope of the correlation between scattering fraction and column density. (b) Distribution in the probability of the null hypothesis for the correlation between scattering fraction and column density. The distribution obtained from the XSPEC simulations is shown in grey, with the median slope marked by a dashed grey line (in the left panel). The value obtained from the data (excluding upper limits) is shown as a dashed black line. The median value obtained from MC simulations (including upper limits) is shown by a dashed blue line with the shaded blue region showing the possible range of values. The difference in the values obtained from the XSPEC simulations and the data/MC simulations, for the slope of the correlation and the probability of the null hypothesis, shows that any degeneracy between the parameters (f_{scatt} and $\log N_{\text{H}}$) does not produce an artificial correlation.

2.3.1 Testing Parameter Degeneracies

An important step in our analysis is to check if the correlation we found is due to degeneracy between the two spectral parameters of interest, f_{scatt} and $\log N_{\text{H}}$. Hence, in this section, we perform simulations to check for the degeneracy between the scattering fraction and the column density. We simulated 100 dummy populations of obscured AGN, with the same size as our sample, which corresponds to more than 38,000 simulations, using a predefined model to describe the X-ray spectrum of an AGN. The model was decided based on its ability to provide a statistically significant fit to the X-ray spectra of the majority of sources in our sample. We used the same model to fit the simulated spectra and obtain simulated values of the parameters column density and scattering fraction. These two parameters were then plotted against each other to check if they show any inherent correlation and degeneracy.

The X-ray spectra are simulated using the `FAKEIT` command in XSPEC v12.10.1f (Arnaud 1996). As input, this command requires a background file, a response matrix file (RMF), and an auxiliary response file (ARF). For our analysis, we use the *XMM-Newton*/EPIC-pn background, RMF, and ARF files. As a test, we repeat a set of simulations with *Swift*/XRT background and response files and obtain similar results. We also redo the simulations with multiple sets of background and response files to accommodate any changes due to source positioning in the field of view and obtain similar results as when we use a single set of background and response files. `FAKEIT` also needs an exposure time, which we randomly select from the distribution of the actual exposure times of the 386 sources in our sample. Finally, the `FAKEIT` command requires us to specify a model that will be used to generate fake spectra. For our simulations, we use the model B1 from R17 (described in detail in Section 2.2.1), which was used to fit the X-ray spectra of 272/386 ($\sim 71\%$) sources of our sample (see R17 for details). In XSPEC terminology, the model is defined by the following expression:

$$\text{ZPHABS} \times \text{CABS} \times \text{CUTOFFPL} + \text{PEXRAV} + \text{constant} \times \text{CUTOFFPL}$$

The various parameters in the model, their priors, and the conditions applied to them are explained in detail here:

- Scattering fraction (f_{scatt}): This parameter is represented by the *constant* term in the model. Its input value is selected randomly from a uniform distribution ranging from 0.1% to 5%.
- Column density (N_{H}): This parameter appears twice in the model (in components `ZPHABS` and `CABS`) and its value in these two components is tied. The default range acceptable for this parameter in the model needs to be modified to $0.1 < N_{\text{H}}/10^{22} \text{ cm}^{-2} < 1000$ to describe the obscured AGN in our sample. The input value of this parameter is randomly selected from a uniform distribution of values between 10^{22} cm^{-2} and $10^{24.5} \text{ cm}^{-2}$.
- Photon index (Γ): This parameter appears three times in the model (in the two power-laws and the `PEXRAV` component), and its value in all three components is tied. The input value of Γ is selected randomly from a Gaussian distribution centered around 1.8, with a standard deviation of 0.2 (Ricci et al. 2017a).

- High energy cutoff (E_C): This parameter also appears in the same three components as Γ , and its input value is selected randomly from a Gaussian distribution centered around 210 keV, with a standard deviation of 40 keV (Ricci et al. 2018). The value of this parameter for the three components is tied and not allowed to vary.
- Normalization (K): This parameter appears in the same three components as Γ and E_C , and its value in the three components is tied. It is calculated from flux values in the 2–10 keV band. Once the normalization values corresponding to all sources in our sample are calculated, the input value of this parameter in the model is selected randomly from the distribution of those values.
- Reflection parameter (R): The default range acceptable for this parameter is set to $-1 < R < 0$, and its value is not allowed to vary. The input value is selected randomly from a Gaussian distribution centered around -0.4, with a standard deviation of 0.1 (Ricci et al. 2017a). The reflection parameter and luminosity could be anti-correlated (e.g. Zappacosta et al. 2018) with a preference for luminous AGN to have low to null reflection parameter (e.g. Vignali et al. 1999; Reeves & Turner 2000; Page et al. 2005). Furthermore, Ricci et al. (2011) found different levels of reflection as a function of AGN type. However, we do not consider any such correlation between R and K or R and N_H in these simulations.
- All the remaining parameters, such as redshift, iron abundance, and inclination angle, are set to their default values and not allowed to vary during the fitting process.

After feeding the model and the input values of all parameters to the software, we simulated 100 spectra each for all sources (total 38,600 spectra). All spectra were rebinned to have at least 20 counts per bin to use chi-squared statistics. We only generated the spectra in the 0.3–10 keV interval, matching the energy range covered by *XMM-Newton*/EPIC-pn. All spectra were then fitted using the model defined above to obtain the best-fit values of all free parameters. For each set of simulated data, we then checked for the presence of a correlation between f_{scatt} and $\log N_H$ with a linear fit, as it was done in Section 2.3 for our sample. To do so, we create a distribution of the slopes of the linear regression lines for all 100 f_{scatt} vs $\log N_H$ plots, as

shown in Figure 2.3a. The figure clearly shows a large difference between the slopes obtained from the data/MC simulations and the XSPEC simulations. Hence, we can safely infer from this distribution that the negative correlation we found between the scattering fraction and the column density for our sample of obscured AGN is not due to parameter degeneracy. We also show the probability distribution of the null hypothesis in Figure 2.3b, which reinforces the validity of the inverse correlation we found. To confirm that these simulations do not miss sources with low f_{scatt} and low $\log N_{\text{H}}$ values, that are otherwise not present in the original data (as visible in Figure 2.1), we looked at the ratio of simulated f_{scatt} to input f_{scatt} as a function of input $\log N_{\text{H}}$. The plot did not show any trend, hence, proving the ability of these simulations to recover such sources. An example of a simulated spectrum, along with the model used and the residuals after the fit, is shown in Figure 2.8a in Appendix 2.7. We also show an example of a simulated correlation between scattering fraction and column density values obtained from these simulations in Figure 2.8b in Appendix 2.7.

One should note that the scattered X-ray radiation could be absorbed by the host galaxy. To take this into account, we repeat a set of XSPEC simulations with a modified model including an absorbed scattered component. The column density of the absorbing material is assumed to be randomly distributed between 10^{19} cm^{-2} and 10^{21} cm^{-2} . The simulated spectral parameters, column density, and scattering fraction, hence obtained, do not appear to be correlated, thus confirming the lack of degeneracy between them. Since, throughout our simulations, we use the same model to create and fit the spectra, the validity of our approach to look for degeneracies may be debated. Therefore, we repeat a set of XSPEC simulations using two models, one to create the spectra and another to fit them. We employ the `RXTorus`³ model developed by Paltani & Ricci (2017) to simulate the fake spectra and the model B1 from R17 to fit them. Since we want to simulate the X-ray spectra of obscured sources, we assume an input value of 80° for the viewing angle (where 0° is face-on), and the ratio of the inner-to-outer radius of the torus is assumed to be 0.5. The input value of the equatorial column density is randomly selected from a uniform distribution of values between 10^{22} cm^{-2} to $10^{24.5} \text{ cm}^{-2}$ and is connected to the line of sight column density via the inclination angle and the torus covering fraction. All the other parameters and their priors are the same as model B1 (described earlier). The resultant

³<https://www.astro.unige.ch/reflex/xspec-models>

simulated parameters ($\log N_H$ and f_{scatt}) are then checked for any correlation using a linear regression fit, and we obtain a slope = 0.1 ± 0.04 . Hence, we can conclusively confirm the absence of parameter degeneracy and the validity of the anti-correlation between the scattering fraction and column density.

2.4 The Correlation Between Scattering Fraction and $L_{[\text{OIII}]} / L_X$,

$L_{[\text{OIII}]}^{\text{corr}} / L_X$ and $L_{[\text{OII}]} / L_X$

Having confirmed the negative correlation between the scattering fraction and the column density for our sample of obscured AGN, we now investigate if the scattering fraction relates with the ratio of [O III] $\lambda 5007$ to X-ray luminosity ($L_{[\text{OIII}]} / L_X$). In the case of buried AGN with extremely low scattering fractions ($< 0.5\%$), several studies have shown that these sources exhibit relatively lower values of $L_{[\text{OIII}]} / L_X$ (e.g., [Noguchi et al. 2010](#); [Ueda et al. 2015](#)). As a further test, we also check for possible correlations between f_{scatt} and the ratio of [O II] $\lambda 3727$ to X-ray luminosity ($L_{[\text{OII}]} / L_X$), another tracer of the NLR. For our analysis, we adopt the observed [O II] $\lambda 3727$ luminosity ($L_{[\text{OII}]}$) and the observed as well as extinction-corrected [O III] $\lambda 5007$ luminosity ($L_{[\text{OIII}]}$ and $L_{[\text{OIII}]}^{\text{corr}}$, respectively). For L_X , we use the intrinsic X-ray luminosity in the 2–10 keV and the 14–195 keV energy bands. Although, L_{2-10} and L_{14-195} are related quantities, L_{2-10} can be strongly affected by high column densities. Therefore, we include the luminosity in the harder energy band (14–195 keV) because it is less biased by high column densities in our sample.

Figure 2.4a shows f_{scatt} as a function of $L_{[\text{OIII}]} / L_{2-10}$ for 359 sources (in grey) for which we have the $L_{[\text{OIII}]}$ and L_{2-10} measurements. Similar to the procedure followed in section 2.3, we initially fit a linear regression line (in red) to all data points, excluding the upper limits. This fitting suggests that there might be a positive correlation between f_{scatt} and $L_{[\text{OIII}]} / L_{2-10}$ that needs to be analyzed in more detail. To do so, we divide the data into six bins of $L_{[\text{OIII}]} / L_{2-10}$, such that each bin contains at least 20 sources. The median and standard error of f_{scatt} in each bin (shown in black), after including the upper limits, is calculated using the SA method. For the x-axis, we just plot the midpoint of each bin with error bars = 0.25 or 0.5, depending on the

2.4. The Correlation Between Scattering Fraction and $L_{\text{[OIII]}}/L_X$, $L_{\text{[OIII]}}^{\text{corr}}/L_X$ and $L_{\text{[OII]}}/L_X$

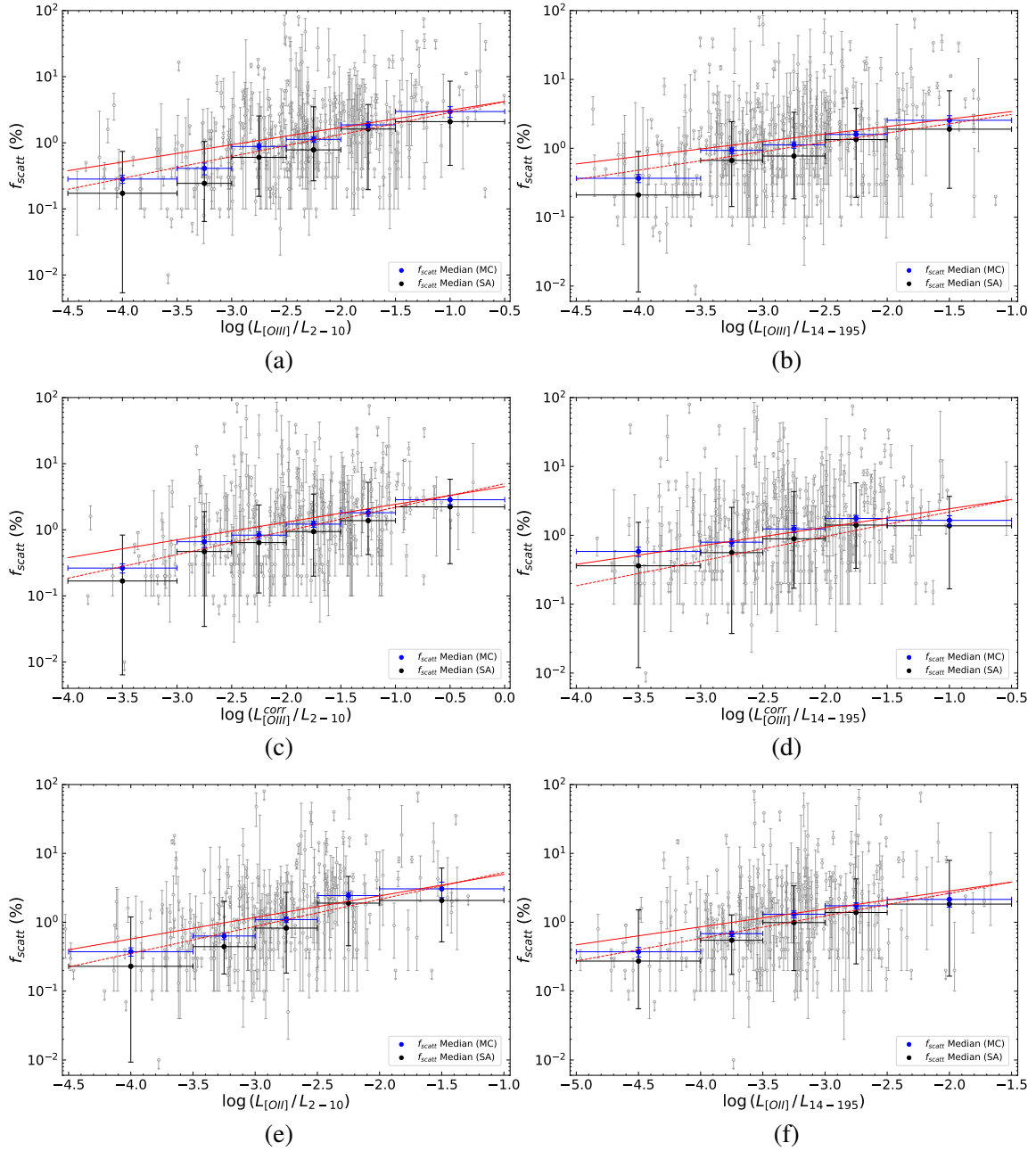


Figure 2.4: Scattering fraction vs (a) $L_{\text{[OIII]}}/L_{2-10}$, (b) $L_{\text{[OIII]}}/L_{14-195}$, (c) $L_{\text{[OIII]}}^{\text{corr}}/L_{2-10}$, (d) $L_{\text{[OIII]}}^{\text{corr}}/L_{14-195}$, (e) $L_{\text{[OII]}}/L_{12-10}$, and (f) $L_{\text{[OIII]}}/L_{14-195}$. Our data is shown as grey open circles in the background (upper limits as downward arrows and best-fit values with error bars showing errors at 90% confidence level). The black and blue circles with error bars correspond to the median and 1σ uncertainty in f_{scatt} calculated using SA and MC simulations, respectively. The solid red linear regression line is obtained from the data by excluding upper limits, while the dashed red regression line is obtained from MC simulations. The plots show a positive correlation between f_{scatt} and $L_{\text{[OIII]}}/L_X$, $L_{\text{[OIII]}}^{\text{corr}}/L_X$ and $L_{\text{[OII]}}/L_X$. Correlation parameters are presented in Table 2.1.

size of the bin. Furthermore, for better estimates of the median and standard deviation in f_{scatt} in each bin, we use MC simulations. As described in detail in Section 2.3, these simulations include the already calculated errors in the parameters to generate their probability distribution functions. However, it is important to note that we do not have error estimates for $L_{[\text{O III}]} / L_{2-10}$. Therefore, in this case, we only created these probability distributions for f_{scatt} . Whereas, for $L_{[\text{O III}]} / L_{2-10}$, we just represent the midpoints and the size of each bin, as done for the SA method. Following the procedure in Section 2.3, we obtained 10,000 values of scattering fraction for each source. For each run, depending on the $L_{[\text{O III}]} / L_{2-10}$ bins, we classify the f_{scatt} values and calculate their median in each bin. The resulting median of each bin is the average of all 10,000 medians in that bin. The error in f_{scatt} in each bin is the standard deviation in the median values with respect to the final median (shown in blue). Therefore, these errors calculated from MC simulations are significantly smaller (by a factor of \sqrt{N} , where N is the sample size in each bin) compared to those calculated from SA. Apart from this, the results from the two methods are consistent with each other. We also show the linear regression line calculated from the MC simulations (as a dashed line) in Figure 2.4a. All the correlation parameters are reported in Table 2.1.

In a similar manner as described above, the correlation between scattering fraction and $L_{[\text{O III}]} / L_{14-195}$ is also inspected and is shown in Figure 2.4b. It is clear from both plots (Figure 2.4a and 2.4b) that scattering fraction correlates with $L_{[\text{O III}]} / L_X$ (where, $X = 2-10$ and $14-195$). The significance of these two correlations is determined from their low p -values ($\approx 10^{-12}$ for $L_{[\text{O III}]} / L_{2-10}$ and $\approx 10^{-8}$ for $L_{[\text{O III}]} / L_{14-195}$). We also explore if this correlation persists when we correct the $[\text{O III}] \lambda 5007$ luminosities for reddening from the Balmer decrement (e.g., Ueda et al. 2015). The relation between the scattering fraction and $L_{[\text{O III}]}^{\text{corr}} / L_X$ for 318 sources is shown in Figure 2.4c and 2.4d. The figures show a positive correlation similar to the one found between the scattering fraction and the ratio of the observed $[\text{O III}] \lambda 5007$ to X-ray luminosity. The null hypothesis probabilities for the correlation between f_{scatt} and $L_{[\text{O III}]}^{\text{corr}} / L_X$ are quite low ($\approx 10^{-10}$ for $X = 2-10$ and $\approx 10^{-5}$ for $X = 14-195$; see Table 2.1). Thereby, highlighting the significance of the positive correlation between these two parameters. Finally, we examine the dependence of scattering fraction on the ratio of the observed $[\text{O II}] \lambda 3727$ to X-ray luminosity for 295 sources in our sample for which we could simultaneously get values of the observed

[O II] $\lambda 3727$ luminosity and the intrinsic X-ray luminosity in the 2–10 and 14–195 keV bands. (Figure 2.4e and 2.4f). As reported in Table 2.1, the correlations observed in this case have slightly higher slopes compared to those with $L_{[\text{O III}]} / L_{\text{X}}$. However, for both sets of correlations we obtain similar p -values ($< 10^{-3}$), which confirms their significance.

For the three sets of correlations evaluated in this section, it is worth noting that not always the narrow emission lines, such as [O II] $\lambda 3727$, [O III] $\lambda 5007$, H α and H β can be ascribed solely to the AGN. In some AGN hosts, there might be a non-negligible contribution from star formation that cannot be ignored (e.g., Maddox 2018). To solve this issue, we checked the emission-line classification of all sources in our sample from Koss et al. (2017). We used the [O III] $\lambda 5007$ /H β versus [N II] $\lambda 6583$ /H α and [S II] $\lambda 6717$ /H α classifications of Veilleux & Osterbrock (1987), revised by Kewley et al. (2006), to determine which sources lie in the star-forming regions of these line diagnostics diagrams. After removing those sources ($\sim 15\%$), we recovered all the positive correlations between f_{scatt} and $L_{[\text{O III}]} / L_{\text{X}}$, $L_{[\text{O III}]}^{\text{corr}} / L_{\text{X}}$, and $L_{[\text{O II}]} / L_{\text{X}}$.

2.5 The Relation Between Scattering Fraction and M_{BH} , L_{X} and λ_{Edd}

In this section, we investigate how the scattering fraction evolves with different physical properties of AGN, such as X-ray luminosity, black hole mass, and Eddington ratio (Equation 2.1). We have already seen that the correlation between scattering fraction and column density is not affected by any of these parameters. However, we want to check if the fraction of Thomson-scattered radiation is influenced by these properties. In Figure 2.5a, we show the scattering fraction as a function of the intrinsic 14–195 keV luminosity (L_{14-195}), for 382 sources (in grey). Following the procedure described in Section 2.4, we have divided the x-axis into six logarithmic bins of L_{14-195} and plotted the median and error in f_{scatt} , calculated using SA (in black) and MC simulations (in blue), for each bin. The plot shows no correlation (p -value = 0.11) between f_{scatt} and L_{14-195} . Figure 2.5b shows scattering fraction as a function of black hole mass for 273 sources, for which we used black hole mass estimates from the BASS DR2 (Section 2.2.2). The plot clearly shows a lack of correlation between f_{scatt} and M_{BH} (p -value =

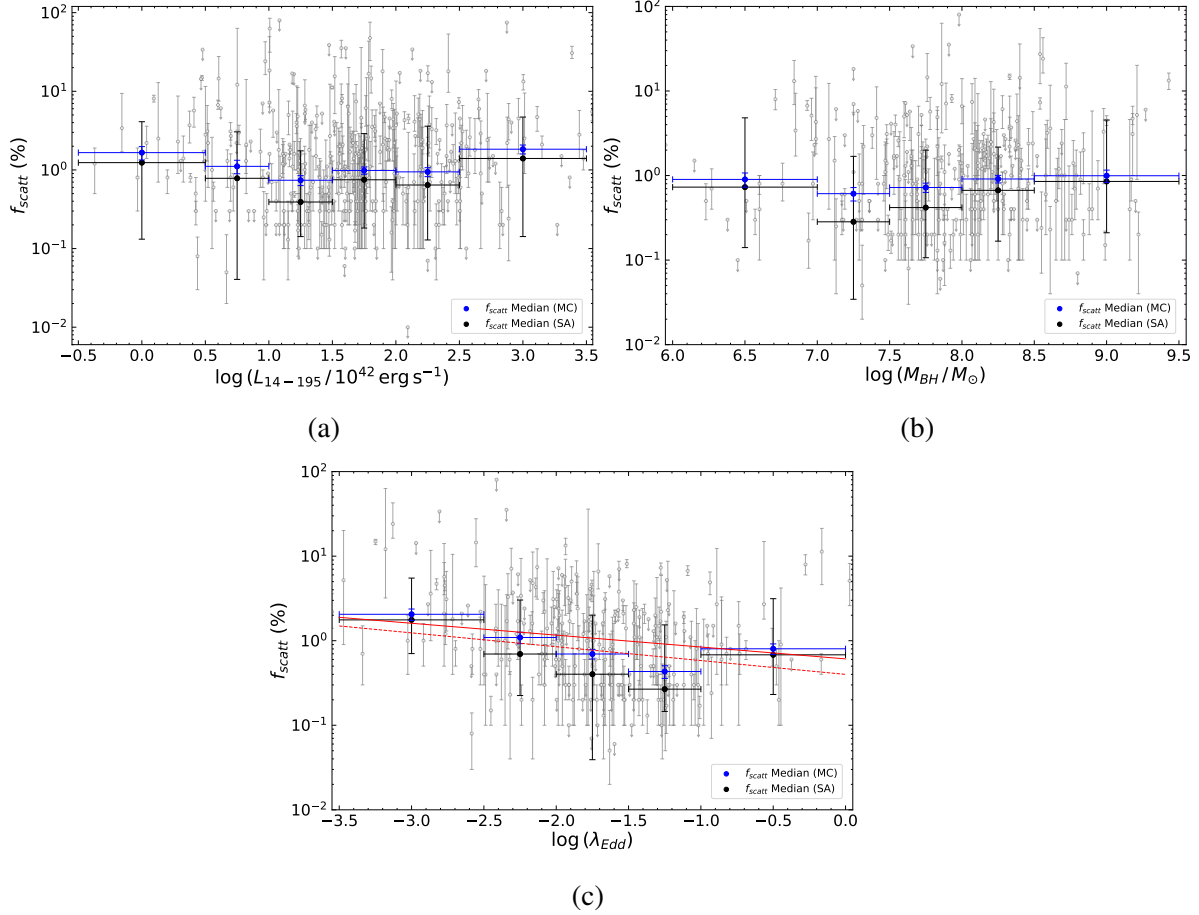


Figure 2.5: (a) Scattering fraction vs intrinsic 14–195 keV luminosity. (b) Scattering fraction vs black hole mass. (c) Scattering fraction vs Eddington ratio. Our data is shown as grey open circles in the background (upper limits as downward arrows and best-fit values with error bars showing error at 90% confidence level). The black and blue circles with error bars correspond to the median and 1σ uncertainty in f_{scatt} calculated using SA and MC simulations, respectively. The solid red line (only in the bottom panel) depicts the linear regression fit to the data, excluding upper limits. The dashed red line (only in the bottom panel) is the regression fit obtained from MC simulations. The plots show no correlation between f_{scatt} and L_{14-195} (r -value = 0.081) and M_{BH} (r -value = 0.071). A weak negative correlation is detected between f_{scatt} and λ_{Edd} . Correlation parameters are reported in Table 2.1.

0.24).

Finally, we plot the scattering fraction as a function of the Eddington ratio for 273 sources in our sample (Figure 2.5c). The Eddington ratio for these sources is calculated from Equation 2.1, using the 2–10 keV bolometric correction from Vasudevan et al. (2009) and the black hole masses. We find a weak negative correlation between f_{scatt} and λ_{Edd} (p -value ≈ 0.001). Similar to the methods employed previously, we fit two linear regression lines to the data, one excluding the upper limits in f_{scatt} and the other including upper limits and errors in f_{scatt} using MC simulations. We have reported the regression parameters calculated from both methods in Table 2.1. Vasudevan & Fabian (2009) showed that bolometric correction factors could be a function of the Eddington ratio. However, the correlation we found between f_{scatt} and λ_{Edd} does not change if we take into account such dependence.

2.6 Discussion

In the previous sections, we found various correlations between the scattering fraction and some physical properties of AGN, such as the line-of-sight column density, the ratio of the observed and extinction-corrected [O III] $\lambda 5007$ luminosity to X-ray luminosity, the ratio of the observed [O II] $\lambda 3727$ luminosity to X-ray luminosity, and Eddington ratio. In the following, we explore various interpretations of these correlations. In Section 2.6.1, we discuss two possible reasons behind the negative correlation between f_{scatt} and $\log N_{\text{H}}$. In Section 2.6.2, we discuss the dependence of f_{scatt} on $L_{[\text{O III}]} / L_{\text{X}}$ and other similar relations. We also explain how these correlations could shed light on the possible locus of Thomson scattering. And finally, in Section 2.6.3, we discuss the weak negative correlation between f_{scatt} and λ_{Edd} .

2.6.1 The Effect of Inclination Angle and Torus Covering Factor on Scattering Fraction

For our sample of 386 hard-X-ray-selected, nearby, obscured AGN from the 70-month *Swift*/BAT catalog, we find a negative correlation between the scattering fraction and the column density (Section 2.3 and Figure 2.1). This trend is consistently observed even when we consider

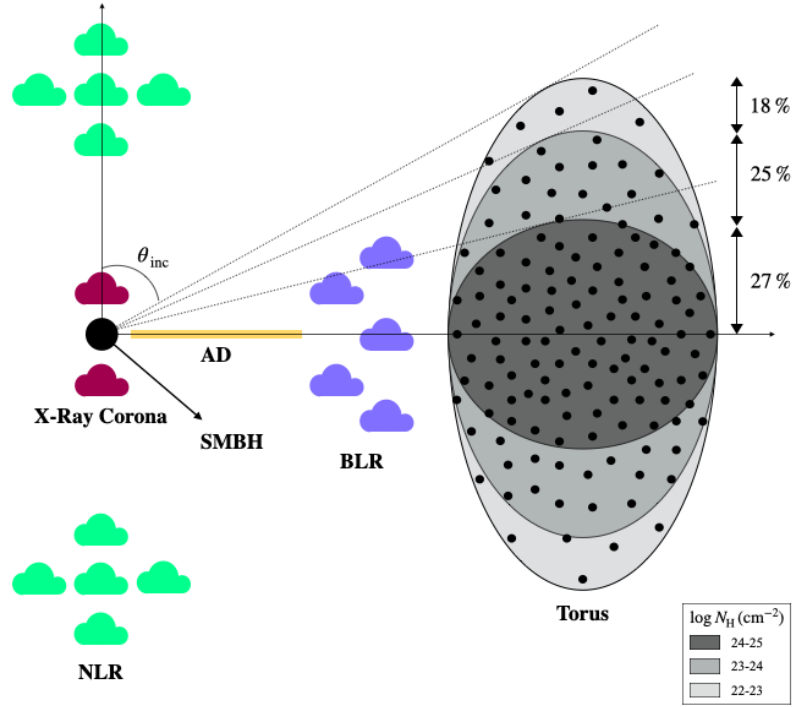


Figure 2.6: Schematic representation of an AGN showing a particular structure and geometry of the torus (also see Figure 4[b] of [Ramos Almeida & Ricci 2017](#)). The inclination angle is measured from the normal to the accretion disk and relative to the observer. The intrinsic column density of the obscuring torus increases with inclination. The torus covering factor is determined from the fraction of sources within a specific column density range (details are given in [Ricci et al. 2015](#) and [Ramos Almeida & Ricci 2017](#)).

splitting the sample into different ranges of some of the fundamental parameters of accreting SMBHs, such as their X-ray luminosity, black hole mass, and Eddington ratio (Figure 2.2). We exclude the possibility that this correlation is due to the degeneracy between different spectral parameters by simulating dummy populations of obscured AGN (Section 2.3.1). We fitted all 38,600 simulated spectra and explored possible correlations between f_{scatt} and N_{H} . The slope and probability distributions (Figure 2.3) confirm the absence of any correlation between the simulated values, thereby implying that the correlation we found is intrinsic. Very high values of scattering fraction ($\geq 5\% - 10\%$) can be either due to partially covering absorbers or due to significant contributions from radio jets (see [Ricci et al. 2017a](#) for a discussion). Therefore, we also check and confirm the existence of this correlation when an uppercut at $f_{\text{scatt}} = 5\%$

and 10% is applied (Figure 2.7a). We also verify that this trend is not due to sources with low counts: by considering a lower limit of 200 counts per source, we recover the same correlation we find for the complete sample (Figure 2.7b).

We can, therefore, confirm the existence of a significant negative correlation (p -value $\approx 10^{-25}$) between the scattering fraction and the column density. We can also infer from our analysis that the dependence of the scattering fraction on the column density is not, in any way, affected by the X-ray luminosity of the accreting system, the mass of the central SMBH, or the Eddington ratio (Table 2.2). This implies that the main parameter driving the correlation is indeed the column density. To explain this inverse correlation between the scattering fraction and column density, we discuss here two possible explanations: (a) the inclination angle dependence of the Thomson cross-section and (b) the covering factor of the surrounding torus of AGN.

Inclination Angle

To comprehend the reason behind the anti-correlation between scattering fraction and column density, we first consider the inclination angle dependence of the Thomson cross-section. The cross-section of Thomson scattering has a cosine square dependence on the inclination angle (e.g., Rybicki & Lightman 1986). We also assume an average AGN model where the torus geometries and properties are similar for all sources, and the only parameter changing between the different sources is the inclination angle. A schematic of the assumed structure of the torus is shown in Figure 2.6, where the column density increases with the inclination angle. We can also predict the covering factor (f_{cov}) of different layers of the torus, based on the fraction of sources with line-of-sight column density in a specific range, following statistical arguments given by Ricci et al. (2015) and Ramos Almeida & Ricci (2017). We start with a covering factor of 70% for the torus, corresponding to a column density of $10^{22.5 \pm 0.5} \text{ cm}^{-2}$ and calculate the inclination angle (θ_{inc}) to be approximately 46° (where, $\theta_{\text{inc}} = \cos^{-1} f_{\text{cov}}$). As we consider higher values for the column density of the obscurer, at $10^{23.5 \pm 0.5} \text{ cm}^{-2}$ and $10^{24.5 \pm 0.5} \text{ cm}^{-2}$, the covering factor of the torus relative to that column density reduces to 52% and 27%. Therefore, the viewing angles corresponding to those column densities increase to 59° and 74° . Since the fraction of Thomson-scattered radiation (denoted by f_{scatt}) will be

proportional to the cross-section of Thomson scattering ($[\frac{d\sigma}{d\Omega}]_{\text{unpol}} = \frac{r_o^2}{2} \times [1 + \cos^2\theta_{\text{inc}}]$, where $r_o = e^2/mc^2$), we used $\cos^2\theta_{\text{inc}}$ as a proxy for the scattering fraction and plotted it against the column density of the torus. We obtained an inverse correlation between these parameters with a slope $= -0.42 \pm 0.07$. This slope is consistent with what we found from our data using the MC simulations (-0.47 ± 0.03). Hence, we can conclude that the observed trend could be explained by the inclination angle dependence of the Thomson cross-section. Some studies have shown that the equivalent width of the [O III] $\lambda 5007$ line could be an indicator of inclination (e.g., Risaliti et al. 2011; Bisogni et al. 2017; Vietri et al. 2018). As a further test, we checked for a possible relation between the scattering fraction and the equivalent width of the [O III] $\lambda 5007$ line and did not find them to be correlated with each other.

Torus Covering Factor

Another possible explanation for the anti-correlation between f_{scatt} and $\log N_{\text{H}}$ could be that sources with high column densities tend to have, on average, a higher covering factor of the torus (e.g., Ricci et al. 2011; Elitzur 2012; Mateos et al. 2016; Tanimoto et al. 2018; Panagiotou & Walter 2019). This would reduce the fraction of Thomson-scattered radiation and result in lower values of scattering fraction. This interpretation also puts into perspective the conclusions made for the population of buried AGN identified by Ueda et al. (2007). They suggested that one of the plausible explanations for such low values of scattering fraction ($< 0.5\%$) would be the presence of an obscuring torus with a very high covering factor. However, we also need to keep in mind the inherent degeneracy between the torus covering factor and the amount of material available for Thomson scattering. Due to this degeneracy, a low scattering fraction can also arise due to the deficiency of circumnuclear material needed for the scattering to occur (e.g., Ueda et al. 2007).

2.6.2 X-ray Scattering in the Narrow-Line Region

In Section 2.4, we detect a positive correlation between the scattering fraction and the ratio of the observed [O III] $\lambda 5007$ luminosity to the intrinsic X-ray luminosity (Figure 2.4a and 2.4b). This correlation also persists when the [O III] $\lambda 5007$ luminosity is corrected for extinction (Fig-

ure 2.4c and 2.4d). Therefore, suggesting that the soft scattered X-ray radiation observed in obscured AGN may originate in the narrow-line region (NLR). It is well-established that emission lines present in the soft X-ray spectrum of obscured AGN are produced in a gas photoionized by the central active nucleus, rather than a collisionally ionized gas (e.g., Kinkhabwala et al. 2002; Schurch et al. 2004; Guainazzi & Bianchi 2007; Bianchi et al. 2010; Nucita et al. 2010; Braito et al. 2017). We also know that the NLR is composed of material produced by photoionization, based on which, Bianchi et al. (2006) conducted a high-resolution spectral analysis of a sample of Seyfert 2 galaxies and found a striking similarity in the extension and the overall morphology of the soft X-ray and the [O III] $\lambda 5007$ emission. They showed, using photoionization models, that it is possible to have a gas photoionized by the central AGN, extending over hundreds of parsec and producing both the [O III] $\lambda 5007$ and the soft X-ray emission. The correlation we found further supports the claim that the soft X-rays and the [O III] $\lambda 5007$ emission are produced by the same gas, i.e., the NLR. This correlation is also in agreement with previous results in the literature that found low values of $L_{[\text{O III}]} / L_X$ for sources with very low scattering fractions (e.g., Noguchi et al. 2010; Ueda et al. 2015).

Compared to $L_{[\text{O III}]} / L_X$ (slope = 0.33 ± 0.02), we recover a slightly steeper correlation (slope = 0.40 ± 0.03) when we consider $L_{[\text{O II}]} / L_X$ (Figure 2.4e and 2.4f). An even steeper dependence (slope = 0.98) is quoted by Kawamuro et al. (2016) for the ratio of [O IV] $\lambda 24.89\mu$ luminosity to 10–50 keV X-ray luminosity. Considering the fact that the [O IV] $\lambda 24.89\mu$ emission is less extinct by dust, compared to the [O III] $\lambda 5007$ emission, it is expected that the scattering fraction correlates more with its ratio to the X-ray luminosity. Consequently, the various correlations of f_{scatt} with ratios of optical line luminosities to X-ray luminosity further strengthen our conclusion that Thomson scattering occurs in the NLR. We also investigated if the correlations we found are affected by the different aperture sizes of the sources in our sample (Appendix 2.7). To do so, we checked if the $L_{[\text{O III}]} / L_X$ correlates with the redshift or the physical width of the slits used for [O III] $\lambda 5007$ measurements (reported by Koss et al. 2017 and Oh et al. 2022). As shown in Figure 2.9 in Appendix 2.7, we do not find any significant correlation between $L_{[\text{O III}]} / L_X$ and redshift or $L_{[\text{O III}]} / L_X$ and slit sizes. Therefore, we can exclude any aperture effects on the trends we observe. As the column density is much better constrained compared to the scattering fraction, we also checked if the ratio of the [O III]

$\lambda 5007$ to X-ray luminosity is correlated with the column density. However, we only obtain a very weak negative correlation between $\log N_{\text{H}}$ and $L_{[\text{O III}]} / L_{\text{X}}$, with a slope = -0.20 ± 0.01 and p -value = 1.1×10^{-4} for the 2–10 keV band, and a slope = -0.12 ± 0.01 and p -value = 2.0×10^{-2} for the 14–195 keV range. This weak correlation disappears when we consider two bins in f_{scatt} around median $f_{\text{scatt}} = 1.3$. Hence, we can conclude that the ratio of the [O III] $\lambda 5007$ to X-ray luminosity is indeed correlated with the scattering fraction and not with the column density.

The scatter visible in all plots of Figure 2.4 could be attributed to different variability timescales of the X-rays and the optical emission lines (e.g., Mushotzky et al. 1993; Schawinski et al. 2015; Oh et al. 2017; Ichikawa et al. 2019b). This correlation between scattering fraction and [O III] $\lambda 5007$ to X-ray luminosity ratio could be useful in removing the large scatter in the L_{X} versus $L_{[\text{O III}]}$ relation (e.g., Ueda et al. 2015). Figure 2.4a shows that the ratio of the optical to X-ray bolometric corrections could change by a factor of ~ 1000 since a change in scattering fraction from 0.1% to 5% causes a variation of almost three orders of magnitude in $L_{[\text{O III}]} / L_{\text{X}}$. As we show in Section 2.4 and 2.5, it is $L_{[\text{O III}]}$ which changes with f_{scatt} and not L_{X} , therefore, the ratio between the [O III] $\lambda 5007$ and the X-ray bolometric corrections for different objects could vary depending on their scattering fractions. However, exploring these effects in detail is beyond the scope of this work. Finally, given the fact that low f_{scatt} AGN, which have higher column densities, have typically low ionized optical line luminosity with respect to the X-ray luminosity, we would expect optical surveys, which rely on narrow emission lines to identify obscured AGN, could miss a significant fraction of the population of heavily obscured AGN.

2.6.3 The Role of Eddington Ratio

For our sample, we find a weak negative correlation between the scattering fraction and the Eddington ratio (Section 2.5 and Figure 2.5c). A possible interpretation of this correlation can be acquired from the inverse correlation between f_{scatt} and $\log N_{\text{H}}$. We discuss in Section 2.6.1 that the low scattering fractions could be, at least in part, due to a higher covering factor of the torus. This would imply that sources with high accretion rates having lower scattering fractions tend to be surrounded by a thicker torus. A similar argument was proposed by Noguchi et al.

(2010), who also found the Eddington ratio to be anti-correlated with the scattering fraction. Another potential explanation of this inverse correlation is explored by Ricci et al. (2017b), who presented a negative correlation between the covering factor of the Compton-thin material and λ_{Edd} . As a result, we would expect the scattering fraction to also decrease with increasing accretion rates since Thomson scattering occurs in the Compton-thin circumnuclear material. This explanation is supported by the idea that the amount of material surrounding an AGN is regulated by the radiation pressure (e.g., Fabian et al. 2006; Fabian et al. 2008; Fabian et al. 2009). Hence, it is possible that more rapidly accreting AGN tend to have a lower fraction of Thomson-scattered radiation, either due to removal of Compton-thin circumnuclear material by radiation pressure or due to a geometrically thick torus.

2.7 Summary and Conclusion

In this work, we used the 70-month *Swift*/BAT catalog to study the properties of Thomson-scattered X-ray radiation in a sample of 386 hard-X-ray-selected, obscured AGN in the local Universe. We used X-ray spectral parameters reported by Ricci et al. (2017a), black hole masses estimated by Koss et al. (2017, 2022b), and narrow-line fluxes calculated by Oh et al. (2022) to investigate possible correlations between the fraction of Thomson-scattered radiation and other physical properties of SMBHs, such as the line-of-sight column density, X-ray luminosity, black hole mass, Eddington ratio, [O III] $\lambda 5007$ to X-ray luminosity ratio, and [O II] $\lambda 3727$ to X-ray luminosity ratio. Here, we summarize our main findings:

- We found a significant negative correlation between the scattering fraction and the column density (see Section 2.3 and Figure 2.1), with a slope = -0.47 ± 0.03 (Table 2.1). We excluded the possibility that this correlation is due to sources with lower counts (Figure 2.7b) or due to partially covering absorbers ($f_{\text{scat}} \geq 5\% - 10\%$; Figure 2.7a). We also verified that the correlation persists when considering different bins of X-ray luminosity, black hole mass, and accretion rate (Figure 2.2 and Table 2.2).
- To confirm that the correlation we found is intrinsic to our sample and not due to degeneracy between the parameters, we simulated and fitted more than 38,000 obscured

AGN spectra (see Section 2.3.1 and Figure 2.8a). We then checked for possible correlations between the simulated parameters. The probability and slope distribution plots (Figure 2.3) demonstrate that parameter degeneracy is not responsible for the observed trend (Figure 2.8b).

- To understand the physical mechanism responsible for the anti-correlation between scattering fraction and column density, we discussed two possible explanations. First, we considered the inclination angle dependence of the Thomson cross-section and assumed a certain average geometry of the circumnuclear material for all AGN (see Figure 2.6 and Section 2.6). Based on these assumptions, we were able to explain the trend we observe. A second explanation for this trend is that, in general, sources with high line-of-sight column densities tend to have higher covering factors of the surrounding torus. As a result, the amount of Thomson-scattered radiation could decrease, in turn reducing the scattering fraction for these sources.
- We found a positive correlation between the scattering fraction and the ratio of $[\text{O III}] \lambda 5007$ to X-ray luminosity (see Section 2.4 and Figure 2.4), with a slope $= 0.33 \pm 0.02$ (0.27 ± 0.02) for the intrinsic 2–10 (14–195) keV X-ray luminosity. A similar, but slightly steeper, correlation was observed for the ratio of $[\text{O II}] \lambda 3727$ to X-ray luminosity. Both the trends suggest that Thomson-scattered radiation could originate in the same region responsible for the optical $[\text{O III}] \lambda 5007$ and $[\text{O II}] \lambda 3727$ emission, i.e., the NLR. This conclusion is also supported by several previous studies (e.g., Bianchi et al. 2006; Ueda et al. 2015; Kawamuro et al. 2016).
- We did not find any dependence of the fraction of Thomson-scattered radiation on the X-ray luminosity or black hole mass of the AGN. However, we detected a weak negative correlation between scattering fraction and Eddington ratio (see Section 2.5 and Figure 2.5) with a slope $= -0.16 \pm 0.02$. This relation could imply that rapidly growing SMBHs are either surrounded by a thicker torus (Noguchi et al. 2010) or have radiatively driven away the Compton-thin material needed for scattering (Ricci et al. 2017b).

Acknowledgements

We would like to thank the anonymous referee for the prompt and constructive report that strengthened this work. We thank Matthew Temple for his valuable comments. This work made use of data from the NASA/IPAC Infrared Science Archive and NASA/IPAC Extragalactic Database (NED), which are operated by the Jet Propulsion Laboratory, California Institute of Technology, under contract with the National Aeronautics and Space Administration. This research has made use of data and/or software provided by the High Energy Astrophysics Science Archive Research Center (HEASARC), which is a service of the Astrophysics Science Division at NASA/GSFC and the High Energy Astrophysics Division of the Smithsonian Astrophysical Observatory. K.K.G. was supported by a 2018 grant from the ESO-Government of Chile Joint Committee. We acknowledge support from Fondecyt Iniciacion grant 11190831 (CR), ANID grants CATA-Basal AFB-170002 (FEB), FONDECYT Regular 1190818 and 1200495 (FEB), and Millennium Science Initiative ICN12_009 (FEB). MK acknowledges support from NASA through ADAP award 80NSSC19K0749. KO acknowledges support from the National Research Foundation of Korea (NRF-2020R1C1C1005462). EP acknowledges financial support under ASI/INAF contract 2017-14-H.0.

Appendix

A: The $f_{\text{scatt}} - N_{\text{H}}$ Correlation with Different Cuts

High values of scattering fraction ($\geq 5\% - 10\%$) in obscured AGN can be attributed to partially covering absorbers or to jet emission (Ricci et al. 2017a). To assure that these sources do not affect our analysis, we apply an uppercut on the values of scattering fraction at 5% and 10% and hence drop 67 and 38 sources, respectively. We plot the remaining sources as a function of column density in Figure 2.7a. Using MC simulations (see Section 2.3), we calculate the correlation parameters and obtain a linear regression line with a slope $= -0.40 \pm 0.03$ for both cases and $p\text{-value} = 6.5 \times 10^{-17}$ (2.5×10^{-19}), for the 5% (10%) cut on f_{scatt} . As evident from the plot, we find a trend similar to the one we obtain for the entire sample.

To verify that the anti-correlation we find between scattering fraction and column density

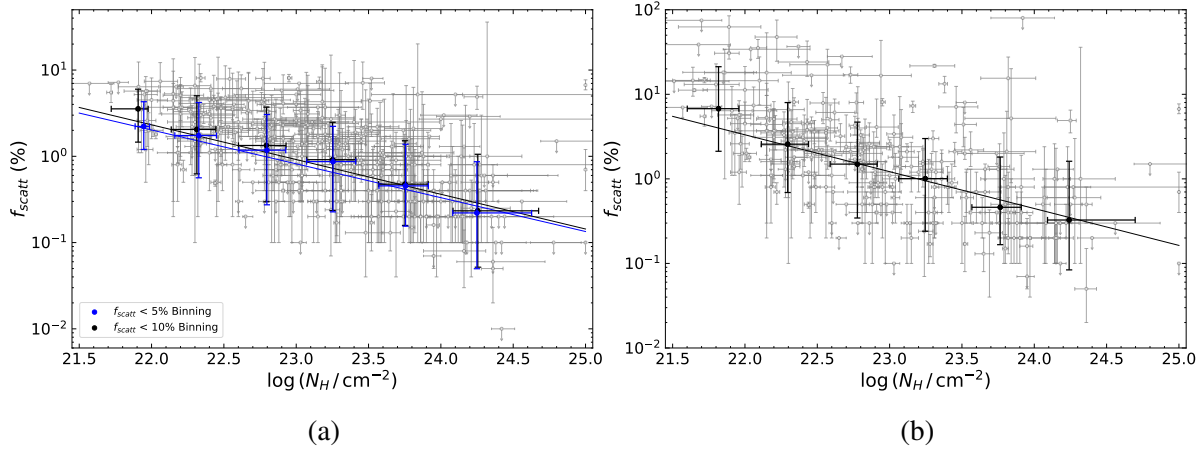


Figure 2.7: (a) Scattering fraction vs column density with an uppercut on f_{scatt} at 5% (blue) and 10% (black). The grey open circles in the background show the data points (with error bars showing errors at 90% confidence level) for objects with $f_{\text{scatt}} < 10\%$. The black and blue circles are the median and uncertainty (1σ) in f_{scatt} and $\log N_{\text{H}}$ calculated using MC simulations for each $\log N_{\text{H}}$ bin and both the linear regression lines are also obtained using the same method. (b) Scattering fraction vs column density for objects with > 200 counts. The data points for these objects are shown as grey open circles in the background (error bars show values in the 90% confidence level). The black circles correspond to the median and uncertainty (1σ) in f_{scatt} and $\log N_{\text{H}}$ calculated using MC simulations for each $\log N_{\text{H}}$ bin, while the black line is the linear regression line obtained using the same method.

is not due to sources with low counts, we apply a cut at 200 counts per source on our sample. It implies removing 136 sources from our original sample of 386 sources. We use MC simulations to quantify the dependence of f_{scatt} on $\log N_{\text{H}}$ for the modified sample. Figure 2.7b demonstrates that these sources do not affect the original correlation, as we recover a similar correlation with a linear regression slope = 0.44 ± 0.03 and $p\text{-value} = 7.0 \times 10^{-16}$.

B: X-ray Spectral Simulations

We ran multiple spectral simulations to exclude the possibility that the inverse correlation we find between the fraction of Thomson-scattered radiation and the line-of-sight column density is due to the degeneracy between these parameters (discussed in Section 2.3.1). In Figure 2.8a, we show an example of a simulated spectrum, along with the model used for simulating and

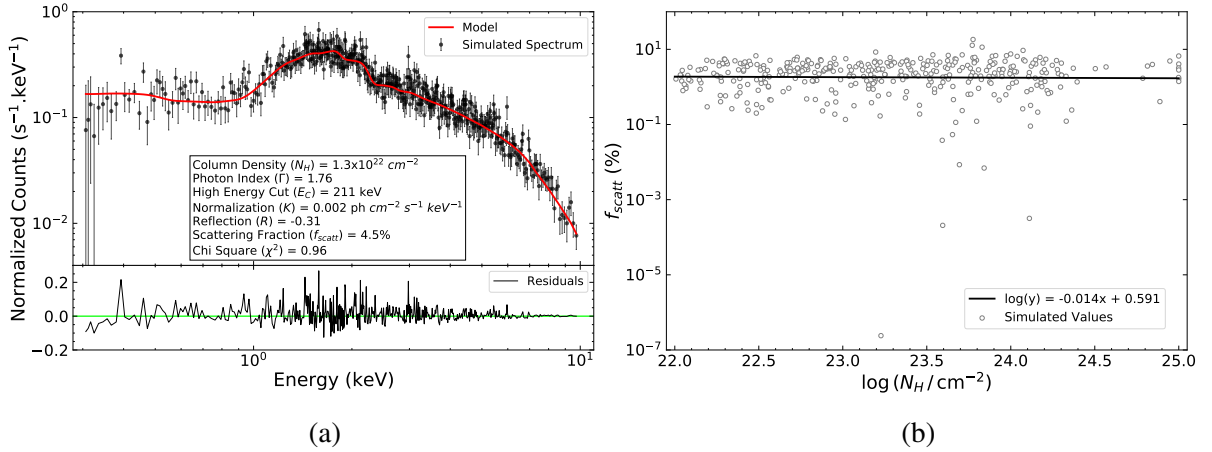


Figure 2.8: (a) An example of a simulated spectrum created using XSPEC. The model used to simulate and fit the spectrum is shown in red. The text box shows the best-fit values obtained for the various free parameters, while the bottom panel shows the fit residuals. (b) An example of a correlation between the simulated values of scattering fraction and column density obtained from XSPEC simulations. The black line shows the linear regression fit to the simulated dataset.

fitting it and the residuals after the fitting. We also show in Figure 2.8b a correlation between the set of simulated parameters.

C: Aperture Effects on [O III] $\lambda 5007$ Measurements

We have adopted observed flux measurements of the [O III] $\lambda 5007$ emission line in our analysis. To eliminate possible aperture effects on these measurements, we investigated potential correlations between the ratio of observed [O III] $\lambda 5007$ to intrinsic X-ray luminosity and the redshift (Figure 2.9a). We find a linear regression with slope = 0.14 ± 0.10 for both energy bands and p -value = 0.18 (0.13), for 2–10 keV (14–195 keV) X-ray luminosity. We also checked, in Figure 2.9b, if $L_{[\text{O III}]} / L_X$ correlates with the physical size of the slits used for the [O III] $\lambda 5007$ measurements (reported in Koss et al. 2017 and 2022b). We obtain a linear regression line with slope = 0.13 ± 0.09 (0.12 ± 0.09) for 2–10 keV (14–195 keV) X-ray luminosity and p -value = 0.16 for both cases. Based on these results, we can conclude that no significant correlation exists between the parameters, and we can exclude aperture effects from our analysis.

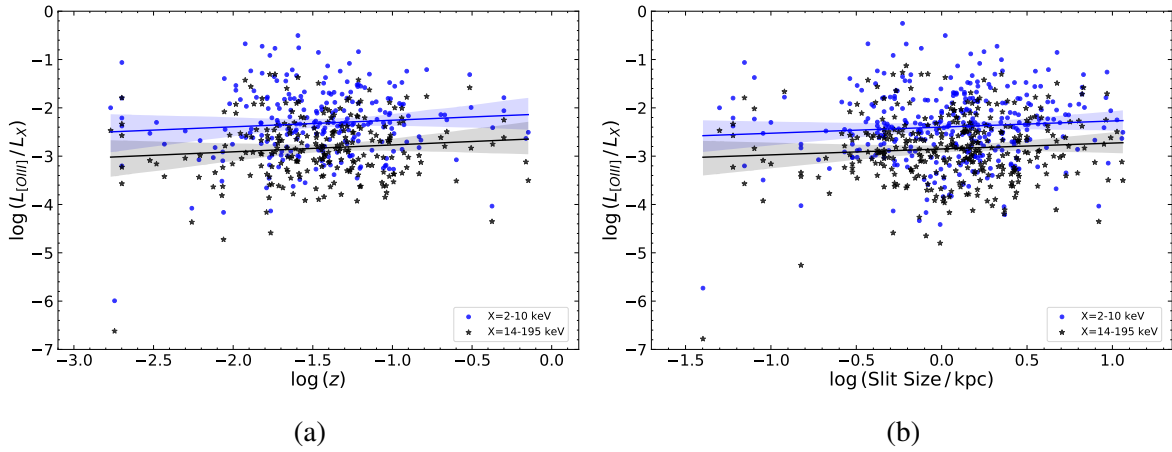


Figure 2.9: (a) The ratio of observed [O III] $\lambda 5007$ luminosity to intrinsic X-ray luminosity vs redshift. (b) The ratio of observed [O III] $\lambda 5007$ luminosity to intrinsic X-ray luminosity vs physical slit size (kpc) used for [O III] $\lambda 5007$ measurements. The blue and black lines show the linear regression fit to our data for intrinsic X-ray luminosity in the 2–10 keV and 14–195 keV energy bands, respectively. The shaded regions show uncertainty in the regression lines. The lack of correlation in both cases (r -value = 0.087 and 0.077, respectively) suggests that the [O III] $\lambda 5007$ measurements are not significantly affected by the aperture size of the sources.

Chapter 3

Optical-to-X-ray SEDs of Unobscured AGN

3.1 Introduction

While most of the light coming from a galaxy can be attributed to its stellar population that emits radiations primarily in the ultraviolet (UV) band and extends up to the optical and near-infrared energies, AGN are characterized by their multi-wavelength emission spanning the entire electromagnetic spectrum. This multi-wavelength emission is generated in different regions of the AGN via various physical processes (e.g., [Netzer 2013](#)). A detailed analysis of the broadband spectral energy distribution (SED; [Figure 3.1](#)) of a representative sample of AGN can therefore provide useful insights into the different physical processes at play. It can further be used to investigate relations between emissions at different wavelengths originating in different regions of the SMBH. Additionally, a complete and consistent study of broadband AGN SEDs can be used to constrain different AGN accretion models and compute various important quantities such as luminosities in different energy bands (L_λ), optical-to-X-ray spectral index (α_{OX}), bolometric luminosity (L_{bol}), mass accretion rate (\dot{M}_{acc}), Eddington ratio (λ_{Edd}), etc (e.g., [Vasudevan & Fabian 2009](#); [Vasudevan et al. 2010](#); [Lusso et al. 2012](#); [Marshall et al. 2022](#)). Moreover, one can also estimate what fraction of the total luminosity of the AGN is emitted at different wavelengths, in terms of bolometric corrections (κ_{bol} ; e.g., [Marconi et al. 2004](#); [Lusso et al. 2010](#); [Duras et al. 2020](#); [Saccheo et al. 2023](#)). However, the construction and

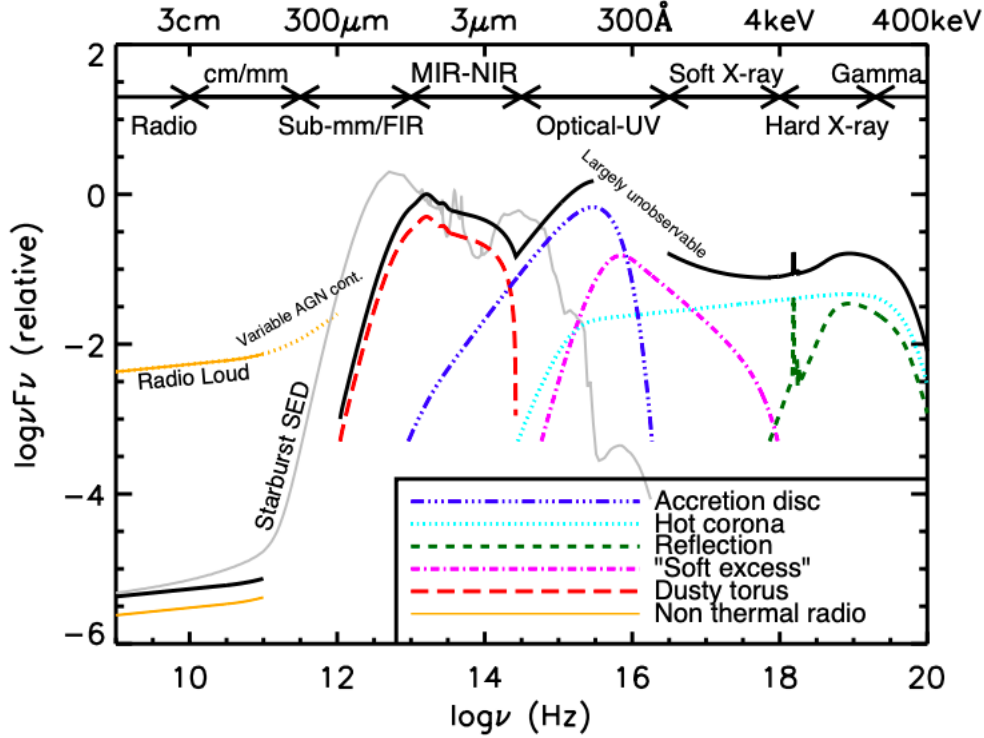


Figure 3.1: A schematic representation of the spectral energy distribution (SED) of an unobscured AGN. The colored curves depict the main physical components of AGN emission, while the SED of a star-forming galaxy is shown in grey. Figure from [Harrison \(2014\)](#).

fitting of AGN SEDs is not trivial and there are several key points that need to be considered, including:

- **Effects of obscuration:** AGN are majorly classified into two types: (a) type I and (b) type II, based on the presence and absence of broad emission lines in their optical spectra. According to the unified AGN model, these two classes of AGN are fundamentally similar and their observed optical properties simply reflect their different viewing angles (e.g., [Urry & Padovani 1995](#)). Type I AGN are viewed face-on and hence, are less affected by obscuration in the line of sight of the observer, whereas the type II AGN are viewed edge-on, through the dusty toroidal structure, due to which the optical emission lines are missing in their spectra. Therefore, we can evidently conclude from observations that type II AGN are more affected by obscuration by the circumnuclear material as compared to the type Is. This is also confirmed by the detection of strong absorption

in the X-ray band in type II AGN (e.g., [Awaki et al. 1991](#)). Consequently, the SEDs of these two classes of AGN have different shapes, with the type IIs showing higher levels of absorption, which needs to be considered when doing a comprehensive study of AGN SEDs (e.g., [Lusso et al. 2012](#); [Duras et al. 2020](#)).

- **Host galaxy contamination:** While analyzing multiband AGN SEDs, one needs to take into account the contribution from the host galaxy, especially in the optical and UV energy bands (see Figure 3.1). Almost always, we can expect mild to severe contamination from the host galaxy light, specifically in the case of low luminosity sources. Therefore, to obtain reliable measurements of the total AGN luminosity, one must separate the AGN light from the galaxy light. Over the years, different works have employed different techniques to handle host galaxy contamination in their SED fitting, based on their specific science goals. Some tend to get rid of the host galaxy light before the SED fitting, either by using an image decomposition software like GALFIT (e.g., [Vasudevan & Fabian 2009](#); [Shang et al. 2011](#)), or by using empirical correction factors based on quantities like the 4000 Å break (e.g., [Marchese et al. 2012](#)) or the 5100 Å luminosity (e.g., [Saccheo et al. 2023](#)). While others follow a different approach of fitting the entire SED with galaxy + AGN templates to also extract host galaxy properties (e.g., [Lusso et al. 2012](#); [Duras et al. 2020](#); [Marshall et al. 2022](#)).
- **Galactic dust extinction:** While studying the SEDs of distant objects, one also needs to account for Galactic extinction. This is usually handled by including different dust extinction curves during the fitting process like the [Cardelli et al. \(1989\)](#) extinction curve (e.g., [Shang et al. 2011](#)), the [Calzetti et al. \(2000\)](#) reddening curve (e.g., [Duras et al. 2020](#)), etc. Additionally, intrinsic extinction at the redshift of the source due to the host galaxy can also affect the final estimates of the AGN luminosity and must be included accordingly (e.g., [Temple et al. 2021](#)).
- **Variability:** Considering that the multi-wavelength emission in AGN originates in different regions of the AGN located at different physical scales (the optical/UV arising from the sub-parsec accretion disk and the X-rays originating much closer to the central SMBH), their variability timescales can range from hours to days to years. These flux variations can have large amplitude and be associated with strong spectral variability (e.g., [Ricci et al. 2021](#) and references therein). Hence, to obtain a consistent picture of the total emission from the AGN at a certain time, simultaneous observations in different bands are required to construct simultaneous broadband SEDs

of AGN. However, due to the difficulties associated with obtaining simultaneous observations, previous works have often either included an error term to account for the effects of variability in the SED (e.g., [Marchese et al. 2012](#)) or used quasi-simultaneous observations (e.g., [Shang et al. 2011](#); [Runnoe et al. 2012a](#)).

The need to study the SED of AGN to better understand the details of the physical mechanisms powering these objects has long been accepted. However, the lack of simultaneous, high-resolution, multi-wavelength data constrained much advancement in this area in the early 20th century. Several pioneering works on AGN SEDs were done in the 1980s (e.g., [Edelson & Malkan 1986](#); [Ward et al. 1987](#); [Sanders et al. 1989](#); [Sun & Malkan 1989](#)), but all of them relied on narrow-band AGN detections, and concentrated on limited regions of the energy spectrum for their analysis of the observed emission. The first large, high-quality atlas of quasar (high-luminosity AGN) SEDs over the whole accessible range of the electromagnetic spectrum, from radio to X-rays, was reported by [Elvis et al. \(1994\)](#). In this paper, they presented multi-wavelength SEDs of 47 quasars, including corrections due to dust extinction and contamination to the quasar SEDs due to the starburst emission from the host galaxy. From the SEDs, they calculated the bolometric luminosity for their sample by integrating over the full SED, considering the contribution from the IR emission as well. They also derived mean bolometric corrections in different bands, and mean energy distributions (MED) for their sample. They concluded that while their MED is a good description of a typical quasar, the full range of SEDs contains considerable variety.

Following this milestone work, many significant contributions were made to the investigation of multi-wavelength SEDs of AGN. It was also realized that some wavebands provide a better representative sample of the AGN population compared to others (e.g., hard X-rays are unbiased by the effects of obscuration and reprocessing along the line of sight, far-IR is independent of orientation). In this context, [Kuraszkiewicz et al. \(2003\)](#) presented the far-IR SEDs of 21 X-ray-selected AGN and discovered that type I and type II AGN, although differentiated by near-IR colors, have similar mid-IR flux ratios. They also concluded that an AGN-heated, dusty disk, extending up to a few hundred parsecs is capable of generating the observed wide range in their AGN SEDs. [Risaliti & Elvis \(2004\)](#) and [Marconi et al. \(2004\)](#), improved on the work of [Elvis et al. \(1994\)](#) by treating their selection effects in the X-rays and removing

the contribution of the reprocessed IR emission in the total accretion luminosity of AGN, respectively. They presented an updated quasar SED and derived bolometric corrections in the optical, IR, and soft-to-hard X-ray bands. Moving forward in this direction, [Richards et al. \(2006\)](#) covered the entire electromagnetic spectrum to construct the SEDs for 259 type I AGN. They found that the wide range of SED shapes influences the determination of bolometric luminosities and that assuming a mean SED can lead to errors as high as 50% when inferring the bolometric luminosity.

[Vasudevan & Fabian \(2009\)](#) and [Vasudevan et al. \(2009\)](#) used simultaneous optical, UV, and X-ray data, to present optical to X-ray SEDs of nearby hard-X-ray-selected low-absorption AGN. They successfully estimated the 2 – 10 keV bolometric corrections (κ_{2-10}) for their sample and found a strong dependence of κ_{2-10} on the Eddington ratio. [Lusso et al. \(2010\)](#) presented the X-ray to optical SEDs of a significantly large sample of 545 X-ray-selected type I AGN from the *XMM-COSMOS* survey, over a wide range of redshifts ($0.04 < z < 4.25$) and X-ray luminosities, and calculated the X-ray bolometric corrections for the whole sample and the Eddington ratios for a sub-sample of 150 objects for which black hole mass estimates were available. They obtained a tight correlation between the optical to X-ray spectral index (α_{ox}) and κ_{2-10} , which can be employed to estimate bolometric corrections using just optical and X-ray data. [Shang et al. \(2011\)](#) contributed to this field by using data from various space- and ground-based telescopes with improved spectral resolutions and constructed composite SEDs for quasars. Although the overall shape of these SEDs was similar to that obtained by [Elvis et al. \(1994\)](#), they revealed more detailed structures owing to better-quality data. However, even after all these efforts, the main parameter controlling the SED shapes and the bolometric corrections could not be determined.

About two decades after the first multi-wavelength SED study, [Elvis et al. \(2012\)](#) presented another SED catalog of 413 X-ray-selected type I AGN. The mean SED for the entire sample, as well as the dispersion SEDs, were presented, and it was concluded that reddening and host galaxy contamination were responsible for a large fraction of the observed SED variety. [Lusso et al. \(2012\)](#) analyzed an even larger sample of 929 AGN (including both type I and type II) from the *XMM-Newton* survey, complemented with IR to optical/UV data, and derived their bolometric luminosities and corrections, confirming the dependence of κ_{bol} on λ_{Edd} for both

classes of AGN. [Marchese et al. \(2012\)](#) also presented X-ray to optical SEDs of a sample of 195 X-ray-selected type I AGN belonging to the *XMM-Newton* bright serendipitous survey and found a tight correlation between α_{ox} and κ_{2-10} , concluding that both the X-ray spectral index (Γ_{2-10}) and α_{ox} can be used as a proxy for κ_{2-10} . A noteworthy contribution in the calculation of bolometric corrections was made by [Runnoe et al. \(2012a\)](#) and [Runnoe et al. \(2012b\)](#), who provided a new set of optical and IR bolometric corrections respectively, derived from the SEDs of [Shang et al. \(2011\)](#). On a similar footing, [Krawczyk et al. \(2013\)](#) constructed mid-IR to the far-UV SEDs of AGN in a wide range of redshift ($0.064 < z < 5.46$), and computed their bolometric corrections relative to 2500 Å using different models. However, all these studies majorly focused on calculating bolometric corrections for type I AGN. For the first time, [Brightman et al. \(2017\)](#) presented X-ray bolometric corrections for Compton-thick AGN ($N_{\text{H}} > 10^{24} \text{ cm}^{-2}$). They employed four different torus models to fit the SEDs and obtained consistent results, and hence, calculated the κ_{2-10} for their sample, which could prove useful to compute the bolometric luminosity of extremely obscured AGN, which is otherwise difficult to estimate.

A very different approach was taken by [Netzer \(2019\)](#), who focused on estimating optical, UV, and X-ray bolometric correction factors from theoretical calculations of geometrically thin, optically thick accretion disks and the observed X-ray properties of AGN. More recently, [Duras et al. \(2020\)](#) analyzed ~ 1000 AGN SEDs, including both type Is and type IIs and provided optical and X-ray bolometric corrections for their sample. They found that while the X-ray bolometric correction is correlated with L_{bol} , λ_{Edd} and M_{BH} , the optical bolometric correction tends to remain constant with all these parameters (see Figure 3.2). [Azadi et al. \(2022\)](#) presented accretion disk SEDs for a sample of type I AGN (both radio-quiet and radio-loud) and inferred strong dependence of the corresponding bolometric corrections on the spin, M_{BH} , and λ_{Edd} . [Marshall et al. \(2022\)](#) performed SED fitting of 711 luminous X-ray AGN at $0.7 < z < 4.5$ using [Temple et al. \(2021\)](#) AGN SED templates and reconfirmed the tight correlation between the X-ray luminosity and the optical 3000 Å luminosity. And finally, [Kumar et al. \(2023\)](#) studied the accretion disk emission in the FUV from eight type I AGN and emphasized the need for joint spectral modeling of simultaneously acquired UV/X-ray data to further investigate the nature of accretion disks in AGN.

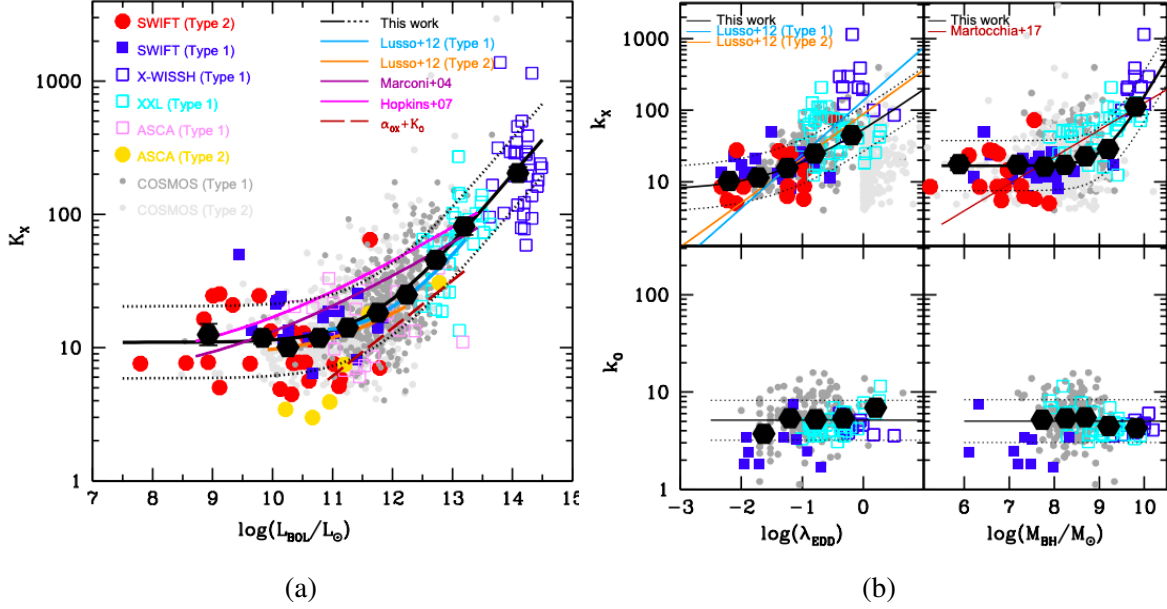


Figure 3.2: Several multi-wavelength SED studies of AGN have shown that the X-ray bolometric corrections correlate strongly with the bolometric luminosity and the Eddington ratio. Whereas, optical bolometric correction remains constant with these properties. Here we show results from some of these studies. Figure from [Duras et al. \(2020\)](#).

Following all the research that has been done so far to construct and fit AGN SEDs and calculate quantities like α_{ox} , L_{bol} , and κ_{bol} , significant advancements have been made in our understanding of AGN accretion. However, some questions still remain regarding the variety of AGN SEDs observed and the large scatter present in bolometric corrections. Opinions of AGN experts still do not converge on the primary parameter that regulates AGN accretion and influences the observed physical properties. With this work, we aim to contribute to this field a large and comprehensive multi-wavelength study of an almost complete sample of unobscured, hard-X-ray-selected type I AGN in the local universe ($z < 0.1$). We also want to provide the astronomy community with bolometric corrections at multiple energies, which are extremely important to estimate the bolometric luminosity of AGN when the entire broadband SED is unavailable. Through this study, we expect to get useful insights into AGN accretion occurring in the innermost regions which are difficult to probe and resolve. To do so, we have created and modeled optical-to-X-ray SEDs of a sample of ~ 250 nearby, unobscured AGN using simultaneous optical, UV, and X-ray data. A similar effort in this direction was made

by Vasudevan et al. (2009), who fitted the optical-to-X-ray SEDs of 26 hard-X-ray-selected AGN and reported their X-ray bolometric corrections. More than 10 years later, we have successfully improved the sample size by one dex. To date, this is one of the largest samples of hard-X-ray-selected AGN for which such an analysis has been carried out in a consistent way. Our analysis includes all the necessary corrections for host galaxy contamination, Galactic absorption, and intrinsic extinction. Based on our analysis, we present multi-wavelength fluxes and luminosities, along with estimates of the total accretion luminosity, Eddington ratio, α_{ox} , and bolometric corrections at multiple energies for our final sample of 236 unobscured, nearby AGN. We also discuss some important correlations between these quantities that help us better understand the accretion physics of unobscured AGN in the local universe (Chapters 4 and 5).

The structure of this chapter is as follows: in Section 3.2 we describe the sample used in this work, while Section 3.3 provides the data reduction process for the optical/UV (3.3.1) and X-ray data (3.3.2). In Sections 3.4 and 3.5 we explain the fitting analysis of the X-ray spectra and the image decomposition of the optical/UV images to correct for host galaxy contamination, respectively. And finally, Section 3.6 describes in detail the broadband SED fitting procedure. Throughout this work, we assume a cosmological model with $H_0 = 70 \text{ km s}^{-1} \text{ Mpc}^{-1}$, $\Omega_{\text{M}} = 0.3$, and $\Omega_{\Lambda} = 0.7$.

3.2 Sample

Unlike the optical/UV and soft X-ray radiation ($E < 10 \text{ keV}$), which is highly sensitive to extinction by the circumnuclear and interstellar dust, the hard X-rays ($E > 10 \text{ keV}$) are much less affected by obscuration (up to $N_{\text{H}} \sim 10^{24} \text{ cm}^{-2}$; see Figure 1 of Ricci et al. 2015) due to their high penetration power. They are also less contaminated by stellar emission from the host galaxy and can, therefore, be used to create a complete, unbiased sample of AGN including the most obscured sources which could be missed by optical/UV surveys. In this work, we use a sample of hard-X-ray-selected AGN detected by the Burst Alert Telescope (BAT: Barthelmy et al. 2005; Krimm et al. 2013) on board the NASA mission, *Neil Gehrels Swift Observatory* (Gehrels et al. 2004). The 14 – 195 keV hard-X-ray detector of *Swift*/BAT is highly sensitive to the most obscured sources and provides an almost complete sample of AGN in the local

Universe. *Swift* is a multi-wavelength space observatory with two additional instruments: the X-ray Telescope (XRT; Burrows et al. 2005) that operates in the 0.3 – 10 keV energy range, and the UV/Optical Telescope (UVOT; Poole et al. 2008; Breeveld et al. 2010) observing the sky in 6 filters ranging from 170 to 650 nm. Most of the sources detected by BAT in the hard X-rays are simultaneously observed in the soft X-rays by *Swift*/XRT and in the optical/UV band by *Swift*/UVOT.

A systematic multi-wavelength study of all the *Swift*/BAT sources has been carried out by the BAT AGN Spectroscopic Survey (BASS¹). BASS recently published their data release 2 (DR2; Koss et al. 2022a) with a complete, optical spectroscopic analysis of all the *Swift*/BAT AGN in the 70-month catalog (Koss et al. 2022b), thanks to their dedicated optical campaign for these sources. BASS also provides a comprehensive spectroscopic study of the *Swift*/BAT AGN in the X-rays (Ricci et al. 2017a), near-IR (Lamperti et al. 2017), mid-IR (Ichikawa et al. 2019a) and radio (Baek et al. 2019). Other data products from this release include measurements of the broad emission lines (Mejía-Restrepo et al. 2022), narrow emission line (Oh et al. 2022), velocity dispersions (Koss et al. 2022c), and the NIR spectroscopy (Ricci et al. 2022; den Brok et al. 2022).

For this study, we use the 70-month *Swift*/BAT catalog (Baumgartner et al. 2013) consisting of 838 hard-X-ray-selected AGN residing in the local universe (median redshift = 0.037). We focus on type I AGN to avoid the effects of obscuration, specifically on the optical and UV emission from the central AGN, and to have a sample of sources with optical/UV emission dominated by the AGN and not from the host galaxy. We start with an X-ray-selected sample of type I AGN, to have minimum obscuration due to the material in the line of sight. To do so, we use the X-ray column densities (N_{H}) to create a sample of unobscured AGN. As part of the first data release (DR1) of BASS, Ricci et al. (2017a; hereafter R17) performed detailed X-ray spectral analysis of all BAT AGN and reported the N_{H} values for 836/838 sources. For our primary sample, we shortlist all AGN with $N_{\text{H}} < 10^{22} \text{ cm}^{-2}$, which gives us a set of 367 unobscured AGN. This sample excludes all the sources that are flagged as blazars following the spectroscopic classification of the Roma Blazar Catalog (BZCAT; Massaro et al. 2009). We also have black hole mass estimates for most of these sources from the BASS DR2 (Mejía-

¹www.bass-survey.com

Table 3.1: Characteristics of *Swift*/UVOT Filters. The central wavelength corresponds to the mid-point between the wavelengths at the FWHM. The zeropoint magnitude indicates the magnitude of a source producing one count per second. The counts to flux conversion factor, when multiplied with the count rate, gives the flux (F_λ) in $\text{erg s}^{-1} \text{cm}^{-2} \text{\AA}^{-1}$.

Filter	Central Wavelength (\AA)	FWHM (\AA)	AB Zeropoint (mag)	Counts to Flux (F_λ) Ratio ($10^{-16} \text{ erg count}^{-1} \text{cm}^{-2} \text{\AA}^{-1}$)
UVW2	1928	657	19.11 ± 0.03	6.225 ± 0.1300
UVM2	2246	498	18.54 ± 0.03	8.489 ± 0.0530
UVW1	2600	693	18.95 ± 0.03	4.623 ± 0.1400
U	3465	785	19.36 ± 0.02	1.663 ± 0.0250
B	4392	975	18.98 ± 0.02	1.480 ± 0.0056
V	5468	769	17.88 ± 0.01	2.611 ± 0.0087

[Restrepo et al. 2022](#)), useful to calculate the Eddington ratios for all the AGN in our sample.

We use the HEASARC archive² to check for available *Swift* observations for our AGN sample. For best possible estimates of the optical/UV fluxes, we use the observation with the maximum exposure and coverage in all the six *Swift*/UVOT filters (V, B, U, UVW1, UVM2, UVW2; see Table 3.1). 226/367 ($\sim 62\%$) sources have *Swift* observations in all UVOT filters plus simultaneous X-ray observations using *Swift*/XRT. For the remaining 141 ($\sim 38\%$) sources, we check for *Swift* observations with the best possible wavelength coverage. 67/141 ($\sim 47\%$) sources have *Swift* observations with at least one optical and one UV filter in addition to simultaneous X-ray observations. So we have a total of 293/367 ($\sim 80\%$) sources (see Table 3.2 for the source list) with simultaneous optical/UV and X-ray observations (see Table 3.3) that can be used to extract their multi-wavelength fluxes, with $\sim 76\%$ sources having observations in all *Swift*/UVOT filters. And we perform the broadband SED fitting for a final sample of 236/293 ($\sim 80\%$) sources. We show the range of redshift, black hole mass, and X-ray luminosity covered by our final sample, as well as by the total unobscured, *Swift*/BAT AGN sample

²<https://heasarc.gsfc.nasa.gov/cgi-bin/W3Browse/w3browse.pl>

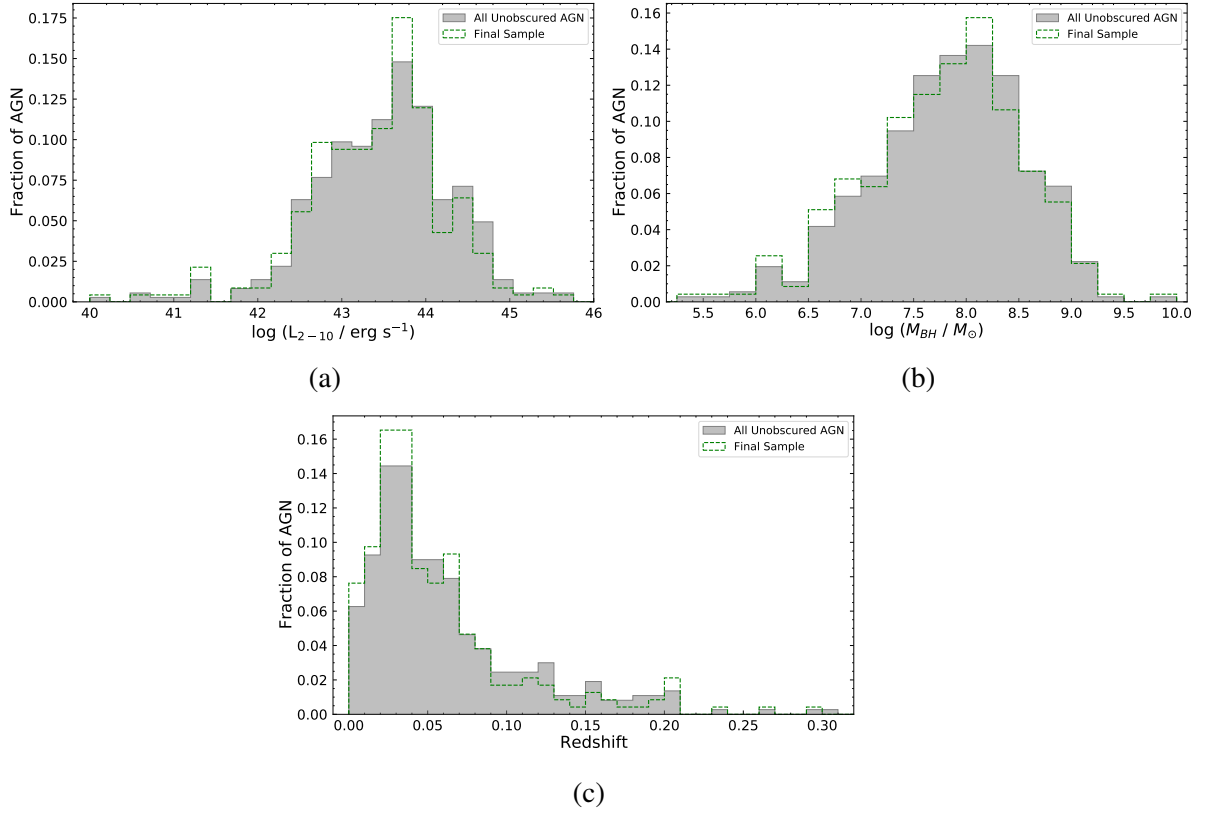


Figure 3.3: Distribution plots of the (a) black hole mass, (b) 2 – 10 keV intrinsic, X-ray luminosity, and (c) redshift of the total sample of unobscured *Swift*/BAT AGN (in grey) and our final sample of 236 unobscured AGN (dashed green histogram). The figures show that our sample covers the parameter space probed by the complete sample of unobscured *Swift*/BAT AGN, in terms of redshift, black hole mass, and luminosity.

in Figure 3.3. It is evident that our sample successfully spans the range explored by the original *Swift*/BAT sample in terms of black hole mass, luminosity, and redshift.

Table 3.2: The list of sources in our sample, along with their BAT and Swift IDs, counterpart names, coordinates (in degrees, J2000), redshifts, luminosity distances in Mpc (Koss et al. 2022b), and X-ray column density values from R17. The full version of this table is given in the appendix (Table 1).

BAT ID	Swift ID	Counterpart Name	R.A.	Dec.	Redshift	Distance (Mpc)	$\log(N_{\text{H}}/\text{cm}^{-2})$
2	SWIFTJ0001.6-7701	2MASXJ00014596-7657144	0.4420	-76.9540	0.0584	261.7	20.00
3	SWIFTJ0002.5+0323	NGC7811	0.6103	3.3519	0.0255	111.2	20.00
6	SWIFTJ0006.2+2012	Mrk335	1.5814	20.2030	0.0258	113.2	20.48
10	SWIFTJ0021.2-1909	LEDA1348	5.2814	-19.1682	0.0956	439.9	21.98
14	SWIFTJ0026.5-5308	LEDA433346	6.6695	-53.1633	0.0629	283.7	20.00
16	SWIFTJ0029.2+1319	PG0026+129	7.3071	13.2678	0.1420	671.7	20.00
19	SWIFTJ0034.5-7904	RHS3	8.5697	-79.0890	0.0740	335.9	20.00
34	SWIFTJ0051.6+2928	UGC524	12.8959	29.4013	0.0360	157.9	20.00
36	SWIFTJ0051.9+1724	Mrk1148	12.9782	17.4329	0.0640	287.5	20.30
39	SWIFTJ0054.9+2524	PG0052+251	13.7172	25.4275	0.1550	739.5	20.00

3.3 Data Reduction

3.3.1 *Swift*/UVOT

In order to take into account the changes in the data analysis due to the recent 2020 update in the *Swift* calibration database (CALDB), we carry out the UVOT data reduction for all our sources from scratch. We use the raw files in all available filters as the starting point and carry out the prescribed reduction techniques and procedures to create the final sky images that are later used to extract the preliminary flux and magnitudes of the sources. We only use image/event files in pointing mode. We follow the steps recommended by the *Swift*/UVOT Software Guide Version 2.2 (released in March 2008) to reduce the optical/UV data for our unobscured AGN. We start with the raw image HDUs in each filter provided in the HEASARC archive and create the corresponding bad pixel maps using the latest UVOT CALDB (`uvotbadpix`). Next, the flat field images are created for each filter using the attitude file and CALDB (`uvotflatfield`). The bad pixel maps and the flat field images are both used to create the sky images in each filter (`swiftxform`). One must note that some raw images might consist of multiple image HDUs corresponding to multiple exposures in the same filter that need to be summed to get the final, deeper image. In the case of single HDUs, the resultant sky image is used to extract the source and sky region with radii ~ 5 and ~ 20 arcsecs, respectively to calculate the source and background flux/magnitudes and errors (`uvotsource`). For source images with crowded fields, smaller background regions (~ 10 arcsecs) were selected accordingly. In the case of multiple image HDUs in the same filter, all the image HDUs are summed using the `uvotimsum` tool. This requires each of the image HDUs to be aspect corrected to be summed together (`uvotskycorr`). The final combined images were all visually inspected to make sure that the source of interest was perfectly aligned. The summed image was then used to extract the source and background regions as before to compute the source and background fluxes and magnitudes along with statistical errors. The `uvotsource` command includes corrections for coincidence loss, which becomes significant for sources with > 20 counts s^{-1} . All the source fluxes and magnitudes thus measured are listed in Tables 3.4 and 3.8 and their distributions are shown in Figures 3.4 and 3.5.

One source in our sample, SWIFTJ1940.4-3015 (BAT ID = 1045), has a very bright star

close to it, within the 5 arcsecs region. Due to strong contamination from the star to our source of interest, we are unable to extract reliable fluxes for this source in any of the *Swift*/UVOT filters. Hence, moving forward we remove this source from our sample, giving us a sample of 292 sources.

3.3.2 *Swift*/XRT

We downloaded the level 2 event files in photon counting mode from the HEASARC archive to extract the X-ray spectra for our sources. Following the procedure stated in the *Swift*/XRT Data Reduction Guide Version 1.2 (April 2005), we used the `xselect` package to select the source and background regions of radii ~ 50 and ~ 150 arcsecs, respectively from the event files. These regions were then used to extract the source and background spectra. The `xrtmkarf` tool was used to create the ARF (ancillary response file) and the RMF (response matrix file). The source spectra were linked with the background spectra, the ARF, and the RMF using `grppha` and binned with a minimum of one count/bin. All the source spectra were visually examined to check that the background counts were overall lower than the source counts.

One AGN in our sample, SWIFTJ1043.4+1105 (BAT ID = 512), shows two X-ray sources at the position of its optical counterpart. Since it is not possible to identify which of the two corresponds to our source of interest, we remove this source from our sample, giving us an updated sample size of 291 sources.

Table 3.3: The list of observation IDs of the observations used for each source, along with their exposure times with *Swift*/UVOT and *Swift*/XRT, and the available *Swift*/UVOT filters.

BAT ID	Swift ID	Obs. ID	UVOT Exposure (s)	XRT Exposure (s)	UVOT Filters
2	SWIFTJ0001.6-7701	00080854001	4419	4485	Only UV
3	SWIFTJ0002.5+0323	00047107014	1600	1625	All
6	SWIFTJ0006.2+2012	00090006004	7917	8136	All
10	SWIFTJ0021.2-1909	00040691001	6485	6493	U, UVW1
14	SWIFTJ0026.5-5308	00041141001	2669	2670	UVW1, UVM2
16	SWIFTJ0029.2+1319	00080859001	5976	6000	All
19	SWIFTJ0034.5-7904	00080861001	4782	4806	All
34	SWIFTJ0051.6+2928	00080867001	6222	6297	All
36	SWIFTJ0051.9+1724	00080868001	6696	6800	All
39	SWIFTJ0054.9+2524	00080869001	6117	6146	All

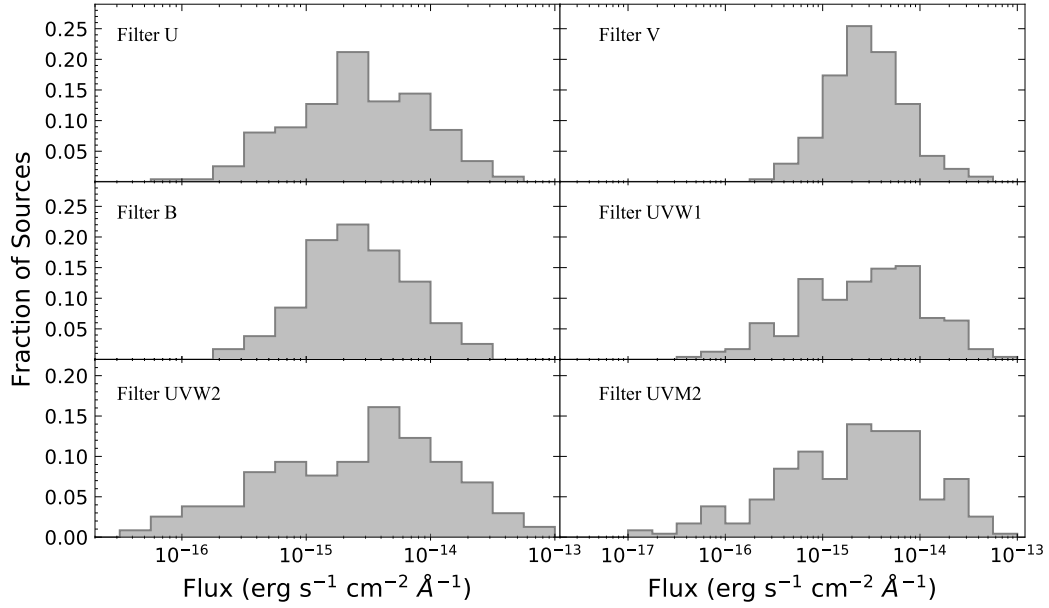


Figure 3.4: Pipeline estimated flux distribution for the 6 *Swift*/UVOT filters.

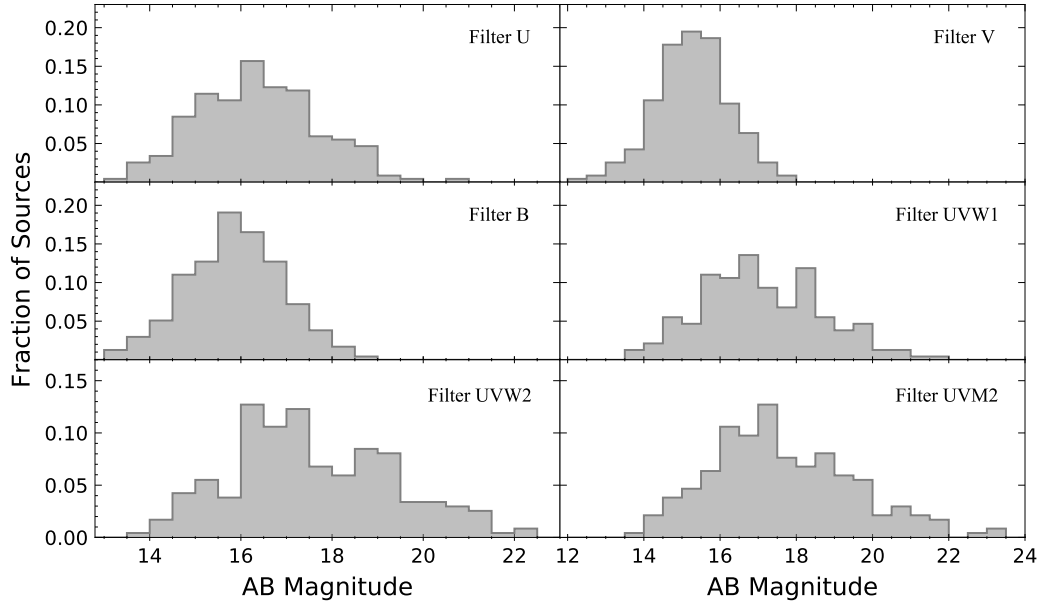


Figure 3.5: Pipeline estimated AB Magnitude distribution for the 6 *Swift*/UVOT filters.

Table 3.4: List of source fluxes as calculated by the *Swift*/UVOT command `uvotsource` via 5 arcsecs aperture photometry, along with statistical errors (Section 3.3.1). Flux units: $10^{-15} \text{ erg cm}^{-2} \text{ s}^{-1} \text{ \AA}^{-1}$.

BAT ID	Swift ID	F_U	F_V	F_B	F_{W1}	F_{W2}	F_{M2}
2	SWIFTJ0001.6-7701	—	—	—	2.40 ± 0.21	3.30 ± 0.2	2.49 ± 0.15
3	SWIFTJ0002.5+0323	3.18 ± 0.12	3.66 ± 0.15	3.29 ± 0.11	4.03 ± 0.13	4.73 ± 0.14	4.11 ± 0.12
6	SWIFTJ0006.2+2012	16.16 ± 0.36	7.43 ± 0.17	9.86 ± 0.19	22.65 ± 0.45	28.35 ± 0.56	23.56 ± 0.51
10	SWIFTJ0021.2-1909	0.19 ± 0.02	—	—	0.06 ± 0.01	—	—
14	SWIFTJ0026.5-5308	—	—	—	1.33 ± 0.17	—	1.06 ± 0.07
16	SWIFTJ0029.2+1319	4.93 ± 0.11	2.56 ± 0.10	3.26 ± 0.09	5.97 ± 0.16	8.16 ± 0.20	5.93 ± 0.18
19	SWIFTJ0034.5-7904	9.65 ± 0.25	4.64 ± 0.15	5.79 ± 0.15	12.81 ± 0.25	17.38 ± 0.38	13.74 ± 0.35
34	SWIFTJ0051.6+2928	1.74 ± 0.07	3.41 ± 0.12	2.75 ± 0.08	1.64 ± 0.07	1.61 ± 0.04	1.36 ± 0.07
36	SWIFTJ0051.9+1724	6.08 ± 0.13	2.46 ± 0.11	3.24 ± 0.11	7.83 ± 0.22	10.08 ± 0.21	7.39 ± 0.23
39	SWIFTJ0054.9+2524	5.25 ± 0.15	2.12 ± 0.09	3.05 ± 0.09	6.53 ± 0.18	10.49 ± 0.25	6.63 ± 0.14

3.4 X-Ray Spectral Fitting

In this section, we describe in detail the fitting procedure for the 0.3 – 10 keV X-ray spectra of the sources in our sample. A detailed broadband X-ray (0.3 – 150 keV) spectral analysis of all the 838 AGN in the 70-month *Swift*/BAT catalog was carried out using XSPEC (Arnaud 1996) as part of the BASS DR1 and is presented in R17). Following their analysis, we employed the models they used to fit the unobscured AGN in their catalog to fit the AGN in our sample. We used the models A1 and A2, which were used by R17 to fit a majority of the unobscured AGN in their sample. These two models are defined as follows:

- **Model A1** ($\text{TBABS}_{\text{Gal}} \times \text{ZPHABS} \times \text{CABS} \times \text{PEXRAV}$): This model has a component that accounts for the primary X-ray emission along with reflection by optically thick, neutral circumnuclear material (PEXRAV; Magdziarz & Zdziarski 1995). It also includes Galactic absorption ($\text{TBABS}_{\text{Gal}}$), and absorption by neutral material via photoelectric absorption (ZPHABS) and Compton scattering (CABS).
- **Model A2** [$\text{TBABS}_{\text{Gal}} \times \text{ZPHABS} \times \text{CABS} \times (\text{PEXRAV} + \text{BB})$]: This model is the same as model A1 with an additional blackbody component (BB) to account for the soft excess below 1 keV.

We begin the fitting for the 291 sources in our sample by using the best-fit values estimated by R17 as starting values for all the free parameters. These include N_{H} for ZPHABS and CABS, photon index (Γ), high-energy cutoff (E_{c}), and reflection parameter (R) for PEXRAV, and the temperature (kT_{bb}) for the BB component. In the cases where values for R , E_{c} or kT_{bb} were not reported by R17, either because they were not constrained or a different model was used to fit the source, we used as starting values $R = 0.0$, $E_{\text{c}} = 200$ keV, and $kT_{\text{bb}} = 0.1$ keV, respectively. The redshift parameter for both ZPHABS and PEXRAV was fixed at the respective redshift of the source. The inclination was fixed to 30° , the metallicity (Z) was fixed to solar, and the iron abundance was fixed at its default value, as done in R17. Parameters E_{c} and R were also frozen to the values reported by R17. Hence, only the column densities (which was tied to have the same value for ZPHABS and CABS), the photon index, and the normalization (K_{x} : for PEXRAV) were the free parameters in the fitting process. The N_{H} for Galactic absorption was also fixed at the value obtained for each source based on their sky coordinates from the HI 4-PI Survey (HI4PI; HI4PI Collaboration et al. 2016), which is a 21-cm all-sky survey of neutral atomic Hydrogen. In the case of model A2, both the additional parameters, temperature (kT_{bb}) and normalization (K_{bb}) of the blackbody component, were allowed to vary during the fitting.

The spectra were fitted using Cash statistics (C-stat; [Cash 1979](#)). The best-fit values of all free parameters were checked using the `steppar` command in XSPEC. Additionally, the 90% confidence intervals for all parameters were estimated using the `error` command in XSPEC. All the fit residuals were visually inspected and for $\sim 90\%$ of the sources we obtained good fits using either model A1 or A2. For the remaining 10% of the sources, we investigated the best-fit model and the fits individually. A component to account for absorption by ionized gas, ZXIPCF ([Reeves et al. 2008](#)), was added to the model to improve the fits. This component assumes a partial covering geometry of a partially ionized warm absorber. In the first step of the fitting, all the parameters except for the photon index and normalization of the power law were fixed to their best-fit values estimated by R17. After obtaining a decent fit with these conditions, the three parameters [column density (N_{H}^{W}), ionization parameter (ξ), and the covering factor ($f_{\text{cov}}^{\text{W}}$) of the warm absorber] corresponding to the ZXIPCF component were allowed to vary to improve the fit. After the fitting, the best-fit values of all the free parameters were checked using the `steppar` command to avoid local minima in the fitting. One of the sources, SWIFTJ1844.5-6221 (BAT ID = 995; commonly known as Fiarall 51), is known to show spectral variability on small timescales, due to the presence of a variable absorber, probably located in the BLR (see [Svoboda et al. 2015](#) and the references within). We found features of a possible changing-look AGN in its spectrum with a very low photon index ($\Gamma \sim 0.4$). Detailed analysis of the X-ray spectrum is beyond the scope of this work, hence, we decided to remove it from the final sample. One source, SWIFTJ0335.4+1907 (BAT ID = 187), was fitted using just a power law due to a low number of counts. Four sources (SWIFTJ0021.2-1909, SWIFTJ0945.6-1420, SWIFTJ1334.8-2328D2, and SWIFTJ1345.5+4139) showed signatures of strong obscuration in their spectra, corresponding to them being at the high end of the column density distribution of our sample. Hence, for these sources, we used model B1 from R17, which was specifically used to fit obscured sources. This model consists of additional components to account for the reprocessed primary X-ray emission and Thomson-scattered X-ray radiation ([Gupta et al. 2021](#)).

Finally, we obtained the best-fit values for parameters including, photon index (Figure 3.6a) and normalization of the primary power-law, line-of-sight column density of the neutral material responsible for absorption, and temperature, and normalization of the blackbody component (see Table 3.5), from the X-ray spectral fits. We calculated the observed and intrinsic 2 – 10 keV and 14 – 195 keV fluxes (Figure 3.6b) and luminosities for all our sources. All luminosities were estimated using redshift-independent distances listed in Table 3.2. The upper and lower uncertainties in the flux were estimated using the `cflux` command in XSPEC and these were then used to calculate the fractional errors in all the future calculations of X-ray fluxes and luminosities. In Figure 3.7, we show a comparison between

the 2 – 10 keV fluxes from this work and those estimated by R17 to confirm that we obtain similar values. The total X-ray luminosity was estimated from the 0.1 to 500 keV energy bin. The lower bound of this energy bin was determined based on the X-ray spectrum generated by the thermal model `NTHCOMP` (Zdziarski et al. 1996; Życki et al. 1999), which describes the X-ray corona. We assumed a photon index of 1.8 (Ricci et al. 2018), coronal or electron temperature (kT_e) of 100 keV (Ricci et al. 2018), and seed photon temperature (kT_{bb}) of 0.032 keV based on the median black hole mass ($\log [M_{BH}/M_\odot] = 7.9$) of our sample. The X-ray spectrum thus created, showed a sharp drop at 0.1 keV, indicating the lack of significant X-ray emission beyond those energies.

Table 3.5: Results of the X-ray spectral fitting (Section 3.4), with best-fit values of the photon index, the 2 – 10 keV intrinsic fluxes with errors, and the model used to attain the best fit (described in detail in R17). Flux units: $10^{-12} \text{ erg cm}^{-2} \text{ s}^{-1}$.

BAT ID	Swift ID	Γ	F_{2-10}	Model
2	SWIFTJ0001.6-7701	1.55	$2.90^{+0.48}_{-0.44}$	A1 + ZXIPCF
3	SWIFTJ0002.5+0323	1.97	$3.19^{+0.37}_{-0.34}$	A2
6	SWIFTJ0006.2+2012	2.34	$10.8^{+0.21}_{-0.21}$	A1
10	SWIFTJ0021.2-1909	1.60	$9.03^{+0.50}_{-0.48}$	B1
14	SWIFTJ0026.5-5308	1.70	$1.97^{+0.25}_{-0.23}$	A1
16	SWIFTJ0029.2+1319	2.20	$5.44^{+0.22}_{-0.21}$	A2
19	SWIFTJ0034.5-7904	2.36	$6.14^{+0.22}_{-0.21}$	A2
34	SWIFTJ0051.6+2928	1.99	$1.71^{+0.13}_{-0.13}$	A2
36	SWIFTJ0051.9+1724	1.91	$16.6^{+0.40}_{-0.40}$	A2
39	SWIFTJ0054.9+2524	1.97	$5.58^{+0.24}_{-0.23}$	A2

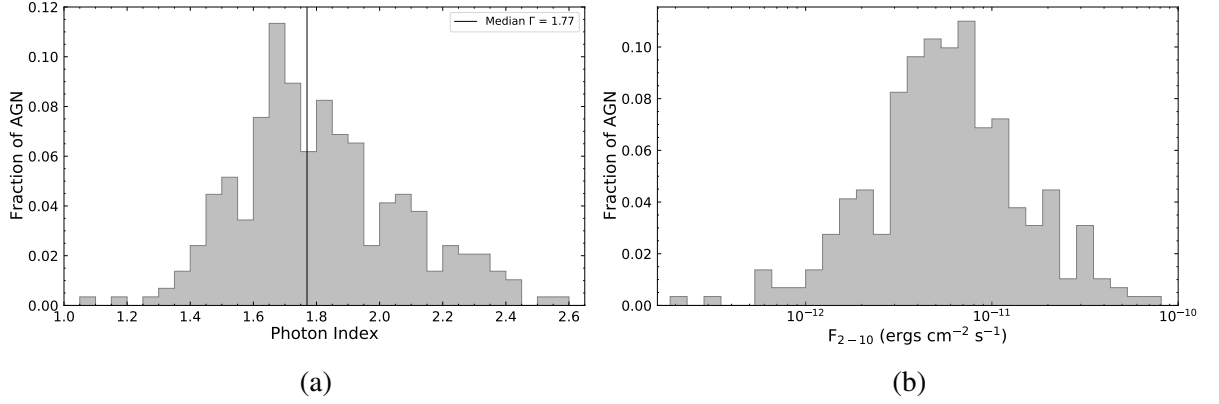


Figure 3.6: (a) Distribution of the best-fit values of photon index (Γ) obtained after the 0.3 – 10 keV X-ray spectral fitting (Section 3.4). The vertical line marks the median value of $\Gamma = 1.77$. (b) Histogram of the intrinsic 2 – 10 keV flux for our AGN sample.

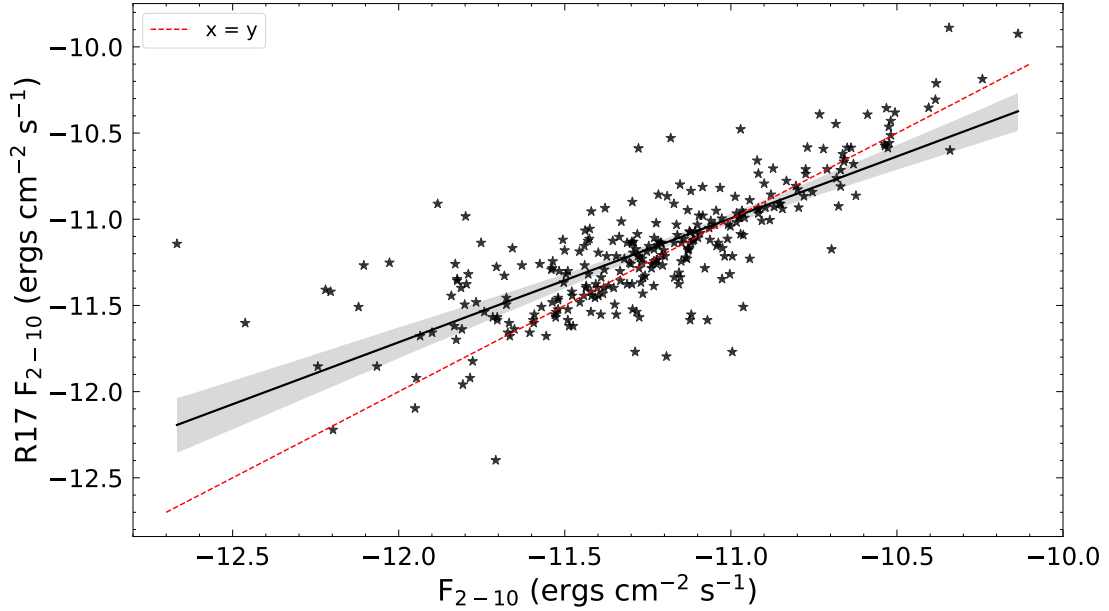


Figure 3.7: A comparison between the 2 – 10 keV intrinsic fluxes calculated from this work and those obtained by R17 following a detailed broadband X-ray spectral analysis. The black line shows the linear regression fit, while the red dashed line is $x = y$.

3.5 GALFIT Analysis

When estimating the optical/UV fluxes and magnitudes for AGN, one needs to correct for contamination due to the host galaxy light. Even though our sample consists of nearby unobscured AGN, where most of the time the central AGN is much brighter than the host galaxy in the optical/UV wavelengths, the magnitudes calculated by selecting 5 arcsecs regions around the AGN can have a significant contribution from the host galaxy starlight. To accurately measure the AGN flux devoid of any host galaxy light, we employ GALFIT³ (Peng et al. 2002; Peng et al. 2010) to fit the 2D surface brightness of the sources and decompose it into AGN and galaxy light. GALFIT is an image analysis tool that can be used to model light profiles of galaxies by separating them into different parts such as disk, bulge, point source, etc., and using different functions like point spread function (PSF), Sérsic profile, Gaussian function, etc. to fit them. For our analysis, we use a PSF profile to fit the AGN at the center of our sources and a Sérsic profile to fit the host galaxy, if and when needed, along with fitting the sky background. The size of the *Swift*/UVOT PSF ranges within 2–3 arcsecs, which translates to physical scales of ~ 40 pcs – 4 kpcs for the redshift range of the sources in our sample. This is comparable to the typical sizes of the bulge of a galaxy and the majority of the optical/UV emission from this region can be attributed to the central AGN. For some of the nearby sources with extended galaxy features, we used two Sérsic profiles to better estimate the AGN flux, while in most of the faintest sources, GALFIT was not able to fit a Sérsic profile to the images, and hence, we only used the PSF profile to estimate their AGN flux. Due to the flux-limited nature of the *Swift*/BAT AGN sample, the sources with the lowest fluxes are also the farthest with high redshift and are point-like in the images, suitable to be fitted with a PSF profile.

GALFIT purely consists of a function-fitting algorithm and gives the best-fit results based on least-squares statistics. Therefore, the user has to provide all the inputs needed to do the fitting. GALFIT requires a template file that consists of all the details about the input image including, name, location, size of the image region to fit, bad-pixel mask, zero-point magnitude, plate scale, etc. GALFIT needs some specific information for the input source image and looks for these in the image header corresponding to keywords EXPTIME (the exposure time), GAIN (electrons/counts), and NCOMBINE (number of images combined to create the source image). Therefore, the input image file has to be edited to include these keywords and their values in the image header. There is also the option to add a bad-pixel mask which is useful to discard very nearby sources like bright stars, stray objects, etc. contaminating the source of interest or its immediate surroundings.

³<https://users.obs.carnegiescience.edu/peng/work/galfit/galfit.html>

In case the user wishes to fit a PSF to the image, they have to provide the PSF image as well as the PSF fine sampling factor relative to the data in this template file. Additionally, all the functions/profiles corresponding to different parts of the galaxy that the user wants to fit along with the initial values of their fitting parameters are also defined in this template file. The user can also specify if a particular parameter is fixed or free to vary during the fitting. In the next section (Section 3.5.1), we describe in detail the different components we used for the image decomposition.

3.5.1 Light Profiles used in GALFIT

In our work, we use three different profiles/components to fit the source images. For most of the sources, this three-component fit works and we obtain good fit residuals. Using more than three components results in overfitting of the images and over-subtracted residuals. The three components used for the fitting are described as follows:

1. **Background Sky:** The background in the *Swift*/UVOT images is quite uniform for all the filters. Hence, we use a constant sky value to fit it. For the starting value, we use the background value as estimated by the Astropy (Astropy Collaboration et al. 2022) package `photutils`⁴ (used for photometry; Bradley et al. 2021), using the sigma-clipping method. By using a source detection threshold specified by the user, the median background value is calculated by removing the sources with source counts above the threshold and recalculating the background. Since this is just an input estimation for the background to be better fit by GALFIT, we use a value of 2 sigma (instead of the more widely used value of 3 sigma) above the median for source clipping. As input, GALFIT requires the user to provide an image region of the background without any sources to fit the sky. Wherever possible, we use background regions in close proximity to the source of interest to reduce small deviations across the area of the detector. For most of the sources, a region of 100×100 pixels was selected, which was otherwise modified according to the availability of larger regions in the image without any detections. Additionally, if the sky is not uniform, one can specify values for the sky gradient in the x and y directions, which we fix at zero.
2. **PSF Profile for the AGN:** To fit a PSF profile in GALFIT, one needs to provide as input a PSF image which is then convoluted to create the PSF function used to fit the point source in the image. For our analysis, we created the PSF images for each source in each filter using

⁴<https://photutils.readthedocs.io/en/stable/index.html>

the `EPSFBuilder` task in the `photutils` Astropy package, which uses bright, background stars in the source image to create an effective PSF. This method involves a series of steps, starting from finding the appropriate stars to create the PSF, extracting them, and finally iterating over the selected stars to build the PSF. Firstly, a few stars within a certain range of the count rate of the source of interest are selected. We use the `find_peaks` function to do this by specifying a threshold count rate slightly below that of the source, such that we have at least 5–10 stars with count rates similar to that of the source to begin with. We then use the `extract_stars` function to extract 25×25 pixel cutouts of these stars that are visually inspected for distortions, fake detections, and bad quality and to ensure that they are sufficiently isolated. Finally, 3–6 stars are selected to create the PSF using the `epsf_builder` function with an oversampling factor of unity and 10 iterations. The PSF image thus created is used as input in GALFIT along with the input source image and the bad-pixel mask. One needs to specify the region of the source image to be fitted in the GALFIT template file. For the majority of sources, we used a 100×100 pixel image region around the source, which is almost 25 times the size of the PSF and is sufficient to include the extended wings of the PSF. In the case of more extended sources, we used image regions large enough to include the source as well as some background. The PSF profile has only three free parameters in the GALFIT template file: the x and y coordinates and the total PSF magnitude. We specify the x and y coordinates based on the location of the center of the source and the input magnitude value as the one calculated for each source within the 5 arcsecs aperture using the `uvotsource` command of the *Swift*/UVOT data reduction pipeline.

3. **Sérsic Profile for the Host Galaxy:** The host galaxy light in our sources, if and when needed, is fitted using a Sérsic profile. The free parameters for this profile include the x and y coordinates of the source, the integrated magnitude, the Sérsic index, the effective radius, the axis ratio, and the position angle. In most cases, we leave all the parameters free to vary, unless the fit does not converge due to one specific parameter going out of bounds, then we fix that parameter to an appropriate value. For most of the sources, a single Sérsic profile along with a PSF was sufficient to account for all the light coming from the galaxy. However, for some extended sources, we employed two Sérsic profiles, one for the bulge and one for the disk, to fit the overall host galaxy light. On the contrary, for most of the distant sources ($z > 0.05$), the PSF was almost as large as the host galaxy, and hence, we only used a PSF profile to fit the source.

3.5.2 GALFIT Fitting Procedure

For our sample of 290 unobscured AGN across the six *Swift*/UVOT filters, we perform their image decomposition into the galaxy and AGN light profiles using GALFIT, following the procedure stated below:

1. We first fit a 100×100 pixel region of the blank sky in the source image with a constant sky background.
2. Next, we select a 100×100 pixel (or larger if needed) region around the source of interest to fit the central AGN and the background together using a sky + PSF profile. The input value for the sky is kept the same as the one obtained from the previous step and is allowed to vary within the error bars. If after the fit the sky is significantly different from the value obtained in the last step, then it is kept fixed and we run the fit again for the sky + PSF profile. For the PSF profile, all the parameters are kept free during the fit.
3. Finally, we fit the same source region as the previous step with a sky + PSF + Sérsic profile. The best-fit values estimated in the second step are used as input values for the sky and PSF parameters in this step, and they are allowed to vary. This is mainly done because in almost all the cases the residuals from the second step showed over-fitting, especially in the central pixels. Hence, in this step we allow the PSF and the Sérsic profiles to adjust to each other and simultaneously fit the source light profile. For the Sérsic profile, the starting values for the x and y coordinates and the integrated magnitude are kept the same as those of the PSF profile. The input value for the Sérsic index (n) is kept at 2.5, the axis ratio (b/a) at 1.0, the effective radius (half-light radius; R_e) at 5.0 pix, and the position angle (PA) at 0.0 deg. On most occasions, if the fit does not converge, it is either due to the Sérsic index or the effective radius reaching its upper or lower limits. In the case when it was the Sérsic index reaching its limit, we repeated the fit with different values, going in the following order: $n = 2.0, 1.5, 1.0, 0.5, 3.0, 3.5, 4.0$. In the case of the effective radius going out of bounds, we repeated the fit with values depending on the size of the source but also noticed that the input value of R_e does not affect the PSF (AGN) magnitude. And since this work aims to construct and fit AGN SEDs to measure quantities describing AGN physics, we focus on extracting reliable measurements of the AGN magnitudes through this image decomposition process. Hence, during the fitting, the Sérsic profile is primarily used to apply constraints on the PSF profile, instead of exactly describing the host galaxy light profile. So the input values

used for parameters like R_e , b/a , and PA are always kept the same as they do not affect the final estimates of the PSF magnitude. In this respect, in cases when the fit with sky + PSF + Sérsic profile does not converge due to one of the Sérsic profile parameters going out of bounds, we still obtain reliable estimates for the PSF magnitude that we can use for constructing the SEDs (see Figure 3.14 in Appendix 3.7). We have flagged such cases while reporting the best-fit values from the fitting.

We visually inspected all the residuals from the sky + PSF fit and the sky + PSF + Sérsic profile fit. We show a few examples of the fits with GALFIT and the obtained residuals in Figures 3.8 and 3.9. As expected from any fitting software, considering the wide variety of light profiles in our source sample in terms of spatial extension, brightness, etc., there were sources for which the fit residuals were not good or some parameters like the Sérsic index or the effective radius were not constrained. There were cases when either the residuals still contained some source emission which GALFIT was not able to model or the three component fit resulted in over-fitting of the source. For example, in the case of the farthest sources ($z > 0.01$) with very faint host galaxy profiles as compared to the central AGN, the fit residuals with GALFIT were negative at the central pixels, showing over-subtraction from the fitting. In such cases, we just used the magnitudes estimated using the `uvotsource` command of the *Swift*/UVOT data reduction pipeline for an aperture of 5 arcsecs around the source, since within the defined region the flux was dominated by the central AGN. To be consistent with our image decomposition, and to quantify GALFIT's response to *Swift*/UVOT images, we carried out numerous simulations to check the reliability of PSF magnitudes estimated by GALFIT. As described in detail in Appendix 3.7, we simulated a fake population of type I AGN by placing a star with varying magnitudes at the center of a type II AGN. We then fitted these fake type Is with GALFIT and compared the PSF magnitudes computed by GALFIT with the initial magnitude of the star. We did this for a total of 10 sources spanning the redshift range of our sample and also including different galaxy morphologies, and with 10 different star magnitudes to achieve 10 different AGN light-to-host light ratios (5% to 95%). Based on these simulations, we concluded that for sources at redshifts > 0.05 and with fluxes $< 10^{-15} \text{ erg cm}^{-2} \text{ s}^{-1} \text{ \AA}^{-1}$, the AGN magnitudes reported by GALFIT were lower (hence larger fluxes) than the actual values (see Figures 3.15, 3.17 and 3.16). This was primarily attributed to the fact that GALFIT was not able to fit a Sérsic profile for these sources and as a result, the PSF magnitudes and fluxes estimated by GALFIT also included contributions from the host galaxy. From these simulations, we calculated the necessary corrections needed to obtain improved estimates of PSF magnitudes for these sources (Figure 3.10). In section 3.5.3, we describe in detail how we estimated and employed these corrections in this work.

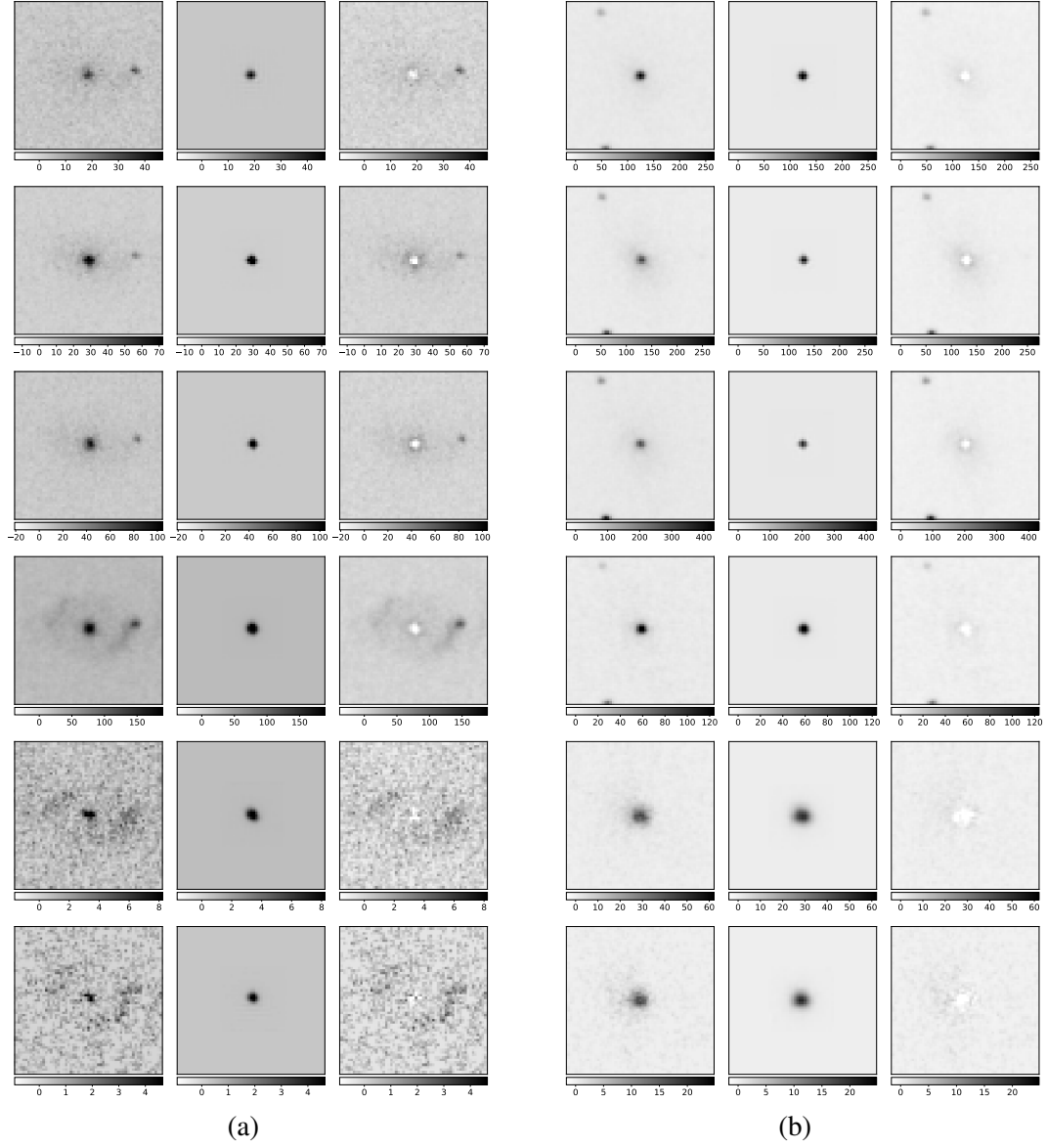


Figure 3.8: A few examples of source image fitting with GALFIT using a sky + PSF + Sérsic profile (Section 3.5): (a) SWIFTJ2226.8+3628 and (b) SWIFTJ0640.4-2554. In each panel, the left image is the source image, the middle one is the model, and the right one is the fit-residual. We show the fit in all six *Swift*/UVOT filters from top to bottom in order (U, V, B, UVW1, UVW2, and UVM2).

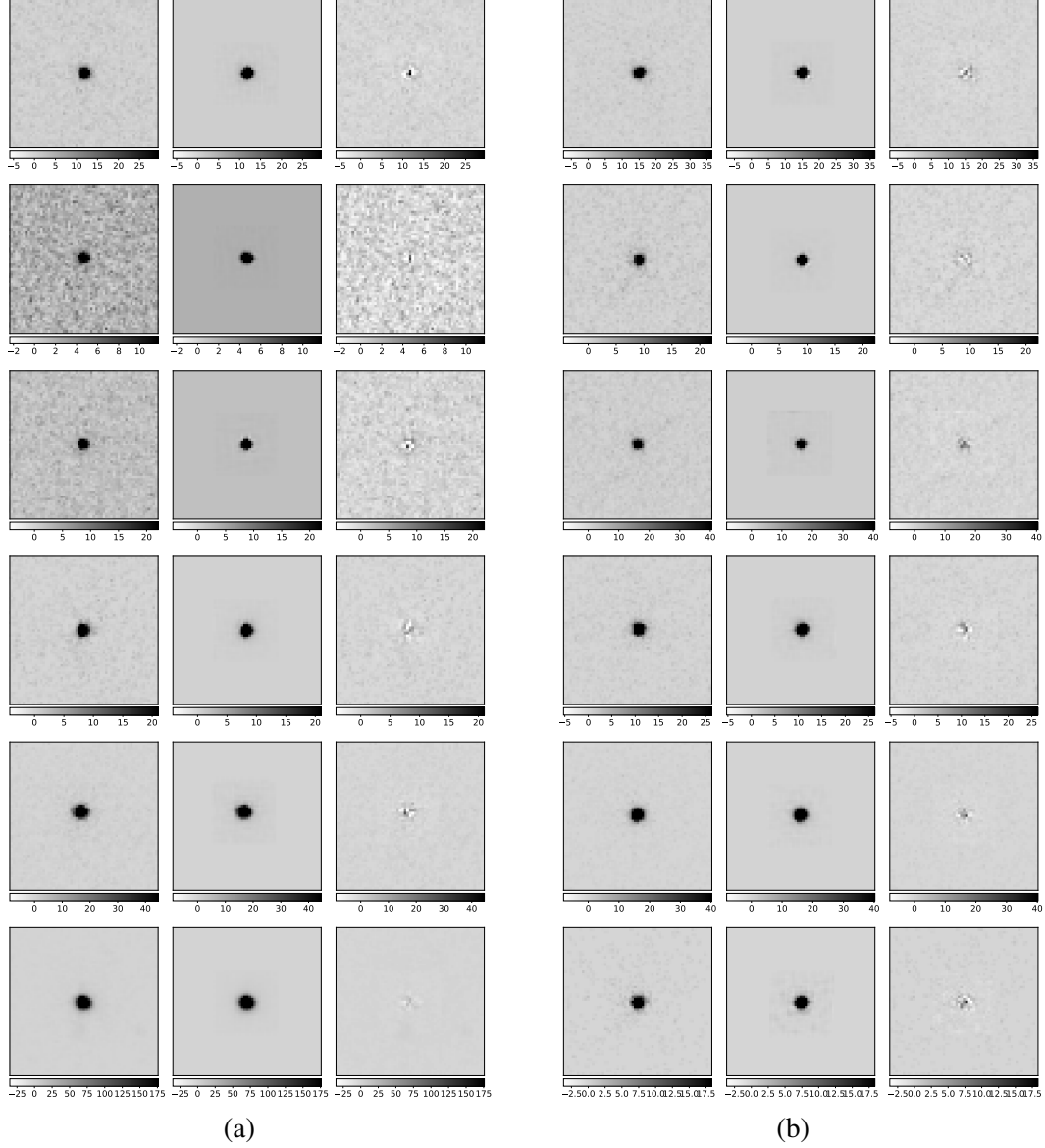


Figure 3.9: A few examples of source image fitting with GALFIT using a sky + PSF profile for high redshift sources: (a) SWIFTJ1723.2+3418 and (b) SWIFTJ1421.4+4747. We corrected the GALFIT-estimated fluxes for such sources (Section 3.5.3) as GALFIT was unable to fit a Sérsic profile to these sources and hence, missed some AGN flux. In each panel, the left image is the source image, the middle one is the model, and the right one is the fit-residual. We show the fit in all six *Swift*/UVOT filters from top to bottom in order (U, V, B, UVW1, UVW2, and UVM2).

We also did some tests to check how the GALFIT-estimated AGN magnitudes for our *Swift*/UVOT images compare with those obtained by fitting the Hubble Space Telescope (HST) images for the same sources. In Appendix 3.7, we describe these tests in detail. Our main conclusion from these tests was that, even if the HST images show detailed and extended host galaxy profiles, if we just fit a small region around the PSF with GALFIT, the estimated magnitudes are within 0.1 mags of those calculated using the lower resolution *Swift*/UVOT images. This is acceptable considering the difference in the central wavelengths of the overlapping HST and UVOT filters.

3.5.3 Corrections to GALFIT-estimated PSF Magnitudes

Based on the simulations (described in Appendix 3.7) performed to understand how GALFIT decomposes the *Swift*/UVOT images and how reliable the estimated fluxes are, we reached some important conclusions. Firstly, for sources with very high counts (> 1000 counts/pixel), GALFIT was unable to account for all the flux in the central pixels. However, the fit residuals in these cases were mostly $< 20\%$ of the source image, and therefore, the estimated PSF magnitudes were consistent with the expected AGN magnitudes within their error range. Secondly, in the case of higher redshift sources (> 0.05) with lower fluxes ($< 10^{-15}$ erg cm $^{-2}$ s $^{-1}$ Å $^{-1}$), most of the time GALFIT was unable to converge while fitting a sky + PSF + Sérsic profile to the source image. As a result, the estimated PSF fluxes were higher than usual. Even in cases when GALFIT successfully fitted a Sérsic profile to the source, the estimated PSF fluxes were higher than the expected values. We flagged such high redshift sources from our sample, to eventually be corrected before the final broadband SED fitting.

To calculate the appropriate corrections for different sources in different optical and UV filters, we first plotted the difference in the PSF magnitudes estimated by GALFIT and the actual magnitude of the star used to replicate the AGN at the center of the simulated type I AGN population (ΔM_{filter}) with respect to the AGN light ratio [$R_{\text{light}}^{\text{filter}} = \text{AGN Light}_{\text{filter}} / (\text{AGN Light}_{\text{filter}} + \text{Host Light}_{\text{filter}})$]. As shown in Figure 3.10, it is evident that the cases in which GALFIT was able to fit a Sérsic profile, occupy a different parameter space compared to those where a Sérsic profile fit was not achieved. Therefore, we used two separate functions to fit these two trends for all six filters. Compared to a second-degree polynomial, a cubic polynomial provided a better fit as it was able to better cover the sources at the higher end of $R_{\text{light}}^{\text{filter}}$. Based on these fits, we derived equations to calculate the value of ΔM for every filter corresponding to the two scenarios, whether a Sérsic fit was available or not. In the case of optical filters U, V, and B, the corrections from these equations were employed only for AGN light ratios of

25% to 75%, $< 75\%$, and $< 95\%$, respectively.

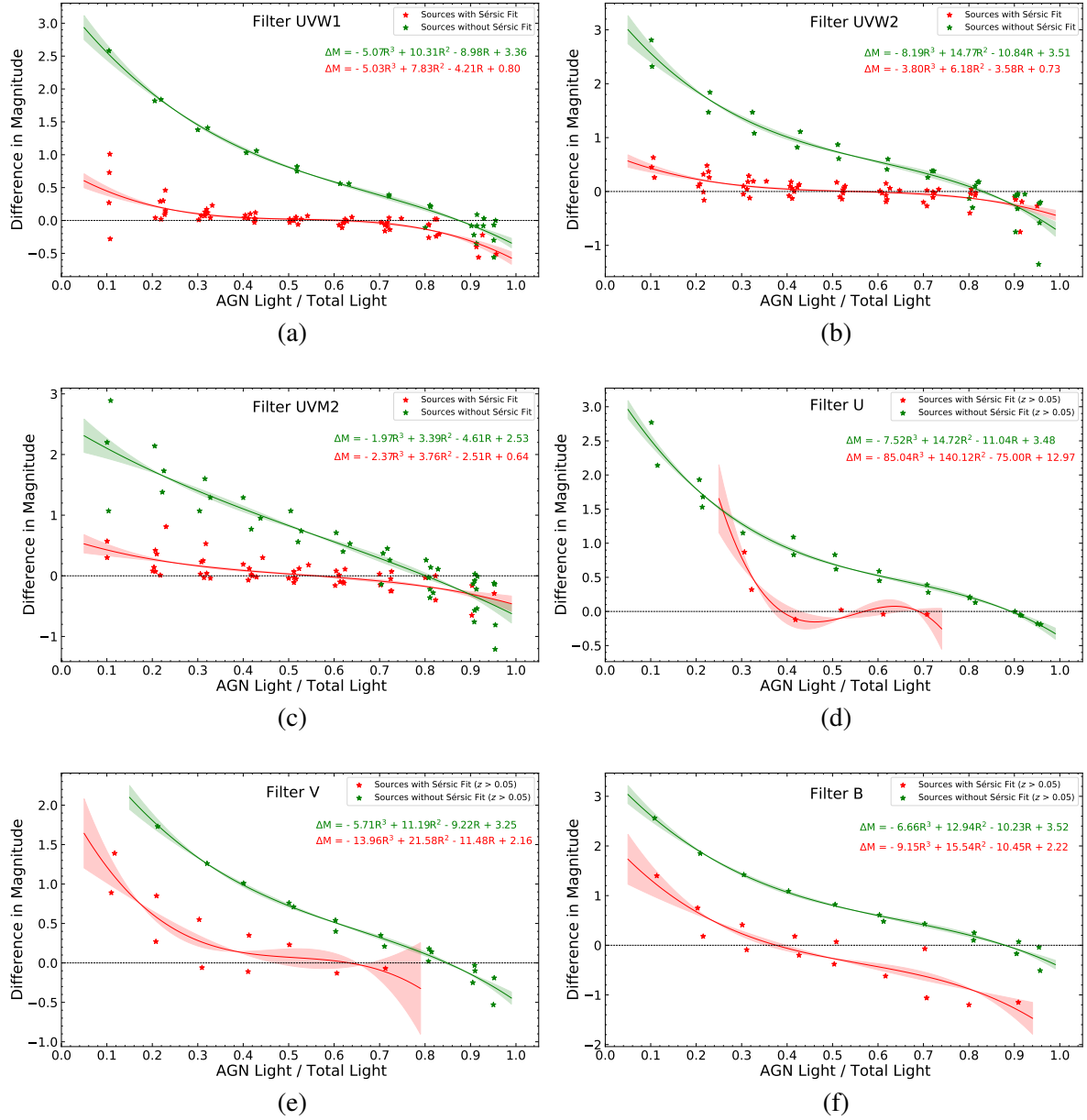


Figure 3.10: Plots showing the difference in the PSF magnitudes estimated by GALFIT and the actual magnitude of the star used to replicate the AGN at the center of the simulated type I AGN population (ΔM_{filter}) vs the AGN light ratio ($R_{\text{light}}^{\text{filter}}$) for all six *Swift*/UVOT filters, (a) UVW1, (b) UVW2, (c) UVM2, (d) U, (e) V, and (f) B, based on simulations (described in Appendix 3.7). The plots also show the best-fit function and their equations for both cases: when a Sérsic profile fit was obtained (in red) and when a fit with a Sérsic profile fit was not possible (in green). The equations mentioned in each figure were then used to calculate the corresponding corrections to improve the PSF magnitudes estimated by GALFIT during the source image decomposition to compute the AGN light devoid of host galaxy contamination.

Table 3.6: List of AGN fluxes (corrected) as estimated by GALFIT image decomposition (Section 3.5). The last column shows, in the form of flags, if the GALFIT-estimated flux was corrected (c) and if the UVOT pipeline estimated flux was used (for any of the filters) to create the final SEDs (p). Flux units: $10^{-15} \text{ erg cm}^{-2} \text{ s}^{-1} \text{ \AA}^{-1}$.

BAT ID	Swift ID	F_U	F_V	F_B	F_{W1}	F_{W2}	F_{M2}	Flag
3	SWIFTJ0002.5+0323	1.59 ± 0.10	0.75 ± 0.07	0.82 ± 0.06	1.59 ± 0.14	2.24 ± 0.15	2.17 ± 0.11	-
6	SWIFTJ0006.2+2012	10.89 ± 0.46	5.82 ± 0.13	6.70 ± 0.15	19.63 ± 1.14	24.60 ± 1.19	22.33 ± 0.76	-
16	SWIFTJ0029.2+1319	3.77 ± 0.16	3.17 ± 0.15	3.07 ± 0.08	4.90 ± 0.35	5.96 ± 0.52	6.50 ± 0.25	c
19	SWIFTJ0034.5-7904	2.53 ± 0.21	0.89 ± 0.07	1.09 ± 0.05	10.28 ± 0.75	12.30 ± 1.09	13.99 ± 0.60	c
34	SWIFTJ0051.6+2928	1.16 ± 0.07	1.17 ± 0.06	1.11 ± 0.05	1.14 ± 0.10	1.23 ± 0.07	1.00 ± 0.06	-
36	SWIFTJ0051.9+1724	4.55 ± 0.20	3.45 ± 0.24	3.01 ± 0.07	6.91 ± 0.44	6.26 ± 0.58	7.60 ± 0.31	c
39	SWIFTJ0054.9+2524	4.76 ± 0.21	1.68 ± 0.05	2.80 ± 0.06	5.40 ± 0.38	7.60 ± 0.66	7.24 ± 0.38	c
43	SWIFTJ0059.4+3150	0.97 ± 0.14	1.17 ± 0.07	0.46 ± 0.90	4.00 ± 0.30	3.55 ± 0.17	3.64 ± 0.16	p
45	SWIFTJ0101.5-0308	0.39 ± 0.02	0.36 ± 0.02	0.08 ± 0.01	0.45 ± 0.07	0.35 ± 0.02	0.36 ± 0.02	-
51	SWIFTJ0105.7-1414	3.57 ± 0.12	1.93 ± 0.14	2.50 ± 0.21	6.08 ± 0.43	8.87 ± 0.54	11.56 ± 2.29	c

In our final sample, for 46 sources ($\sim 20\%$) we used the corrections defined above to improve the PSF magnitudes estimated by GALFIT image decomposition. For 33 sources ($\sim 14\%$), we used the magnitudes estimated during the data reduction process instead of the GALFIT estimated PSF magnitudes due to over-subtracted residuals in at least one of the optical/UV filters. The final AGN magnitudes, fluxes, and errors are listed in Tables 3.6 and 3.9. The sources for which GALFIT magnitudes were corrected and the sources for which we used the UVOT pipeline magnitudes are flagged accordingly in the tables. As mentioned in Section 3.5.2, we do not report the values for the Sérsic profile (host galaxy) parameters, as the focus of this work is to solely constrain the AGN light to construct the corresponding AGN SEDs.

3.6 Broadband SED Fitting

In this final part of the analysis, we use the optical and UV magnitudes calculated for each source to create their optical/UV part of the SED. We start by using the PSF magnitudes estimated by GALFIT after the source image decomposition. We do not include the corrections computed on these magnitudes for the high redshift sources ($z > 0.05$) just yet, to understand how the results change before and after applying the corrections. As mentioned in the previous section, for 33 sources ($\sim 14\%$), we use the UVOT pipeline estimated magnitudes due to minimum contribution from the host galaxy. The original source PHA files for each source in each filter were edited to include the AGN magnitudes instead of the total source magnitudes estimated during the data reduction. The background PHA files were edited to have a value = 0.0 since the final magnitudes estimated by GALFIT are already corrected for the background in the first step of the decomposition (see Section 3.5). The response files from *Swift*/UVOT were edited to include the appropriate energy ranges (see Table 3.1) for respective filters.

The optical/UV part of the SED is fitted in XSPEC (Arnaud 1996) using the DISKPN model, which is a thermal accretion disk model comprising multiple blackbody components (e.g., Mitsuda et al. 1984; Makishima et al. 1986). We would like to mention here some caveats of the accretion disk model that could affect our analysis. Although it successfully describes the optical/UV disk emission in many AGN sources (e.g., Malkan & Sargent 1982; Malkan 1983), the multi-temperature accretion disk model, that is otherwise assumed to be in a quasi-steady state equilibrium (e.g., Shakura & Sunyaev 1973; Thorne 1974), is inadequate to explain the observed variability timescales in the UV (e.g., Alloin et al. 1985; Collier & Peterson 2001; Lawrence 2012). We also acknowledge that by using a common disk model for all sources, we are making an assumption regarding the type of accretion flow in these sources.

Numerous studies have shown that accretion in an AGN changes with its accretion rate, from possible ADAFs to standard thin disks to slim disks, as the accretion rate increases (see [Beloborodov 1999](#) for a review). However, at this point, we cannot assume or define specifically how the surrounding material is accreted onto the central SMBH. Hence, it is reasonable to fit all the SEDs with the widely acceptable thermal disk model, so that we can later evaluate our results in a consistent way. In addition to the disk model, we include two components of the ZDUST model to account for extinction due to dust grains ([Pei 1992](#)) in the optical and UV bands, due to the Milky Way (ZDUST_{MW}) and the host galaxy of the AGN (ZDUST_{HG}), respectively. We use the convolution model ZASHIFT to shift the disk spectrum to the redshift of the respective source. Hence, the final model used to fit the optical/UV SED is:

$$\text{ZDUST}_{\text{MW}} \times \text{ZDUST}_{\text{HG}} \times \text{ZASHIFT} \times \text{DISKPN}$$

For the two reddening components, we adopt a Milky Way (MW) extinction curve (method = 1) and $R_v = 3.08$. In the case of dust extinction due to our galaxy, we fix the $E(B - V)$ value to those estimated by [Schlegel et al. \(1998\)](#), who combined the results of IRAS and COBE/DIRBE to create a 100-micron intensity map of the sky. The $E(B - V)$ for the AGN host galaxy is allowed to vary during the fitting. The redshifts for the two components are fixed to 0.0 and the redshift of the source, respectively. For the DISKPN, the free parameters include the normalization (K_{uvo}) and the maximum temperature of the disk (kT_{max} ; in units of keV). Here, the normalization is defined as:

$$M^2 \cos(i) / (D^2 \times \beta^4) \quad (3.1)$$

where M is the mass of the central body (the SMBH in our case) in solar masses, i is the inclination angle of the disk, D is the distance to the source in kpc, and β is the color to effective temperature ratio. The inner radius of the disk (R_{in} ; in units of $R_g = GM/c^2$) is fixed to 6.0 gravitational radii.

After compiling and preparing all the source PHA files, and defining the model to be used, we begin by fitting 223/290 ($\sim 77\%$) sources that have observations in all the six *Swift*/UVOT filters. The best fit is obtained based on the reduced chi-square and visually inspecting the fit residuals. In cases when the host galaxy $E(B - V)$ was of the order 10^{-4} or less or when it was not constrained, we repeated the fit by fixing it to 0.0. The best-fit values of all free parameters were checked using the `steppar` command. The errors in all the free parameters ($E[B - V]_{\text{HG}}$, kT_{max} , and K_{uvo}) were calculated using the `error` command. For one source, SWIFTJ0753.1+4559 (BAT ID = 395), the error on the flux in the B band was large, in turn affecting the goodness of the overall fit. Hence, we removed the B filter for this specific source and redid the fit. Next, we fitted the sources with observations in at least four of the

Swift/UVOT filters (13/290 \sim 4.5% sources) following the same procedure as before. For the remaining 54/290 (\sim 18.5%) sources, we had observations in less than four filters. Considering the three free parameters in the model used for fitting, it was not possible to fit these sources (with three or fewer data points), and to accurately estimate all the fit parameters. Therefore, we did not fit the optical/UV SEDs for these sources due to missing observations in more than two *Swift*/UVOT filters. We show a few examples of our SED fits, along with the best-fit model and residuals, in Figures 3.12 and 3.13

Out of the 236 sources for which we performed the optical/UV SED fits, the parameter corresponding to the maximum temperature of the accretion disk (kT_{max}) was not constrained for 27 (\sim 11%) sources. To solve this issue, we fixed kT_{max} to its median value (2.7 eV) obtained from the sources that were successfully fitted while constraining the disk temperature. In Figure 3.11, we show the distribution in kT_{max} for all the sources in our sample. The final best fits were used to calculate the observed and intrinsic fluxes and luminosities in all the six *Swift*/UVOT filters. The total intrinsic optical + UV flux and luminosity were estimated in the energy range from 10^{-7} to 100 keV, since the standard [Shakura & Sunyaev](#) disk typically has very little to no emission above a few keV. The luminosity thus computed will later be used to estimate the total accretion luminosities (L_{bol}) of the AGN in our sample. The upper and lower limits of these fluxes were calculated using the 90% confidence intervals of K_{uvo} and $E(B - V)_{\text{HG}}$. The lower limit in the flux of each source corresponds to the best-fit model of that source with the highest $E(B - V)_{\text{HG}}$ (most dust-extinct) and lowest K_{uvo} as estimated during the fitting, and vice-versa. All the errors in subsequent flux calculations were mainly extensions of the fractional errors computed in this way (see Table 3.7).

We repeat the optical/UV SED fitting, as stated above, for the high redshift ($z > 0.05$) sources after applying the corrections to their GALFIT-estimated PSF magnitudes (described in Section 3.5.3). For a total of 46 (\sim 20%) sources, we redo the SED fitting after editing their source PHA files to include the corrected GALFIT PSF magnitudes. We report the best-fit values of kT_{max} and $E(B - V)_{\text{HG}}$ along with the various flags regarding the SED fitting in Table 3.7. We show all the broadband SED fits along with their best-fit SED models and residuals in Appendix 6.2. In the next two chapters, we discuss in detail the results we found for all three samples: (a) the total sample of 236 sources without applying corrections to the magnitudes necessary for high redshift sources, (b) a sub-sample of 190 sources, removing the sources that need to be corrected, and (c) the total sample of 236 sources including corrections to the magnitudes estimated by GALFIT for the high redshift sources.

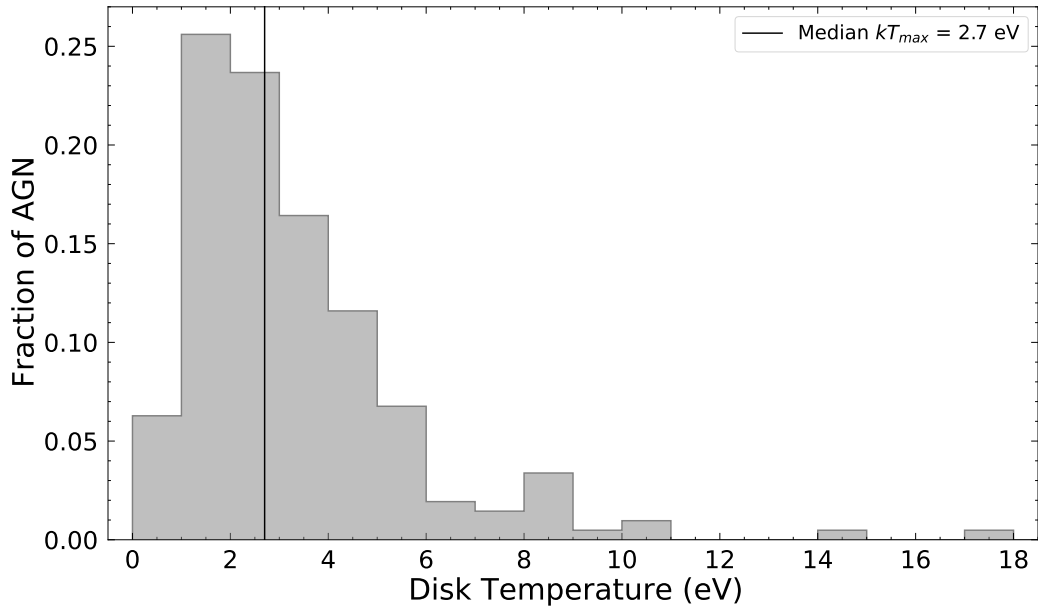


Figure 3.11: A distribution in the value of the maximum disk temperature as obtained after fitting the optical/UV SEDs of our source sample with a dust-extinction corrected thermal disk model (described in Section 3.6). The median value of kT_{max} from this distribution is 2.7 eV. This value was used to improve the optical/UV SED fits for sources whose disk temperatures could not be constrained.

Table 3.7: Results of the optical/UV SED fitting (Section 3.6), with the best-fit values of the disk temperature (kT_{max} in eV), the extinction due to the host galaxy $E(B - V)_{\text{HG}}$, and the total, intrinsic optical/UV flux (from $10^{-7} - 100$ keV) with errors. The last column shows, in the form of flags, if the disk temperature was fixed to its median value of 2.7 eV (t) and if the host galaxy extinction was fixed to 0.0 or was constrained as an upper limit during the fitting (e). Flux units: $10^{-11} \text{ erg cm}^{-2} \text{ s}^{-1}$.

BAT ID	Swift ID	kT_{max}	$E(B - V)_{\text{HG}}$	F_{uvo}	Flag
3	SWIFTJ0002.5+0323	2.8	0.058	$1.85^{+0.97}_{-0.65}$	-
6	SWIFTJ0006.2+2012	3.9	0.014	$17.6^{+5.05}_{-10.6}$	e
16	SWIFTJ0029.2+1319	6.1	0.117	$24.0^{+5.24}_{-3.37}$	-
19	SWIFTJ0034.5-7904	2.7	0.001	$3.05^{+0.13}_{-0.15}$	et
34	SWIFTJ0051.6+2928	3.7	0.298	$8.28^{+2.06}_{-1.55}$	-
36	SWIFTJ0051.9+1724	2.9	0.012	$6.13^{+0.28}_{-0.47}$	e
39	SWIFTJ0054.9+2524	6.4	0.058	$15.7^{+3.81}_{-1.67}$	-
43	SWIFTJ0059.4+3150	5.5	0.007	$3.89^{+4.64}_{-0.92}$	e
45	SWIFTJ0101.5-0308	2.8	0.268	$1.45^{+1.82}_{-0.70}$	-
51	SWIFTJ0105.7-1414	4.0	0.000	$5.50^{+0.13}_{-0.13}$	e

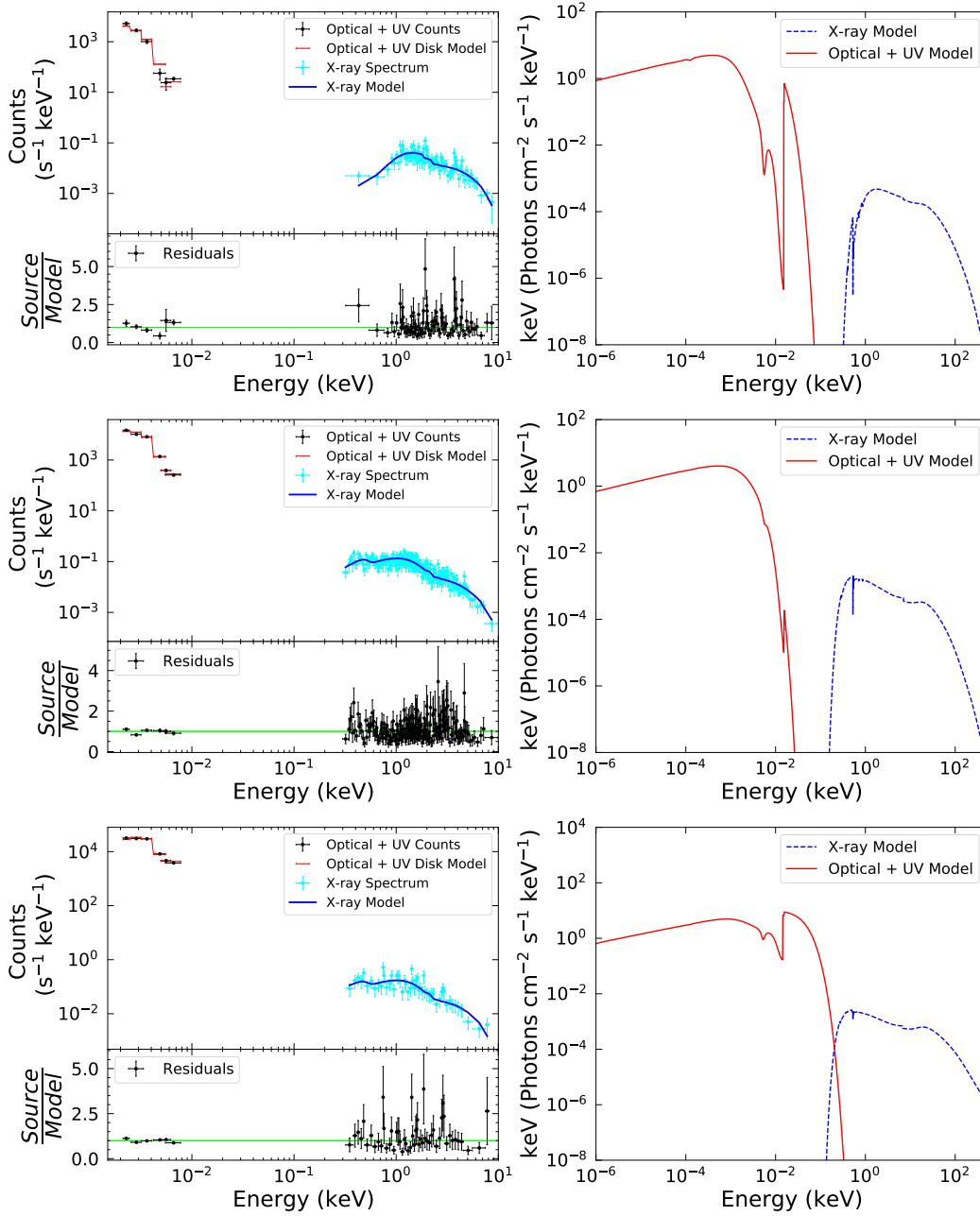


Figure 3.12: A few examples of the optical-to-X-ray SED fits. From top to bottom, the fits are for sources: SWIFTJ0208.2+4452, SWIFTJ0630.7+6342, and SWIFTJ1421.4+4747. The left panel shows the counts in the optical/UV filters (black points) and the 0.3 – 10 keV X-ray spectrum (cyan points). It also shows the fit obtained using the optical/UV disk model including dust extinction (in red) and the X-ray model (in blue), along with the fit residuals. The right panel shows the best-fit SED model for each source.

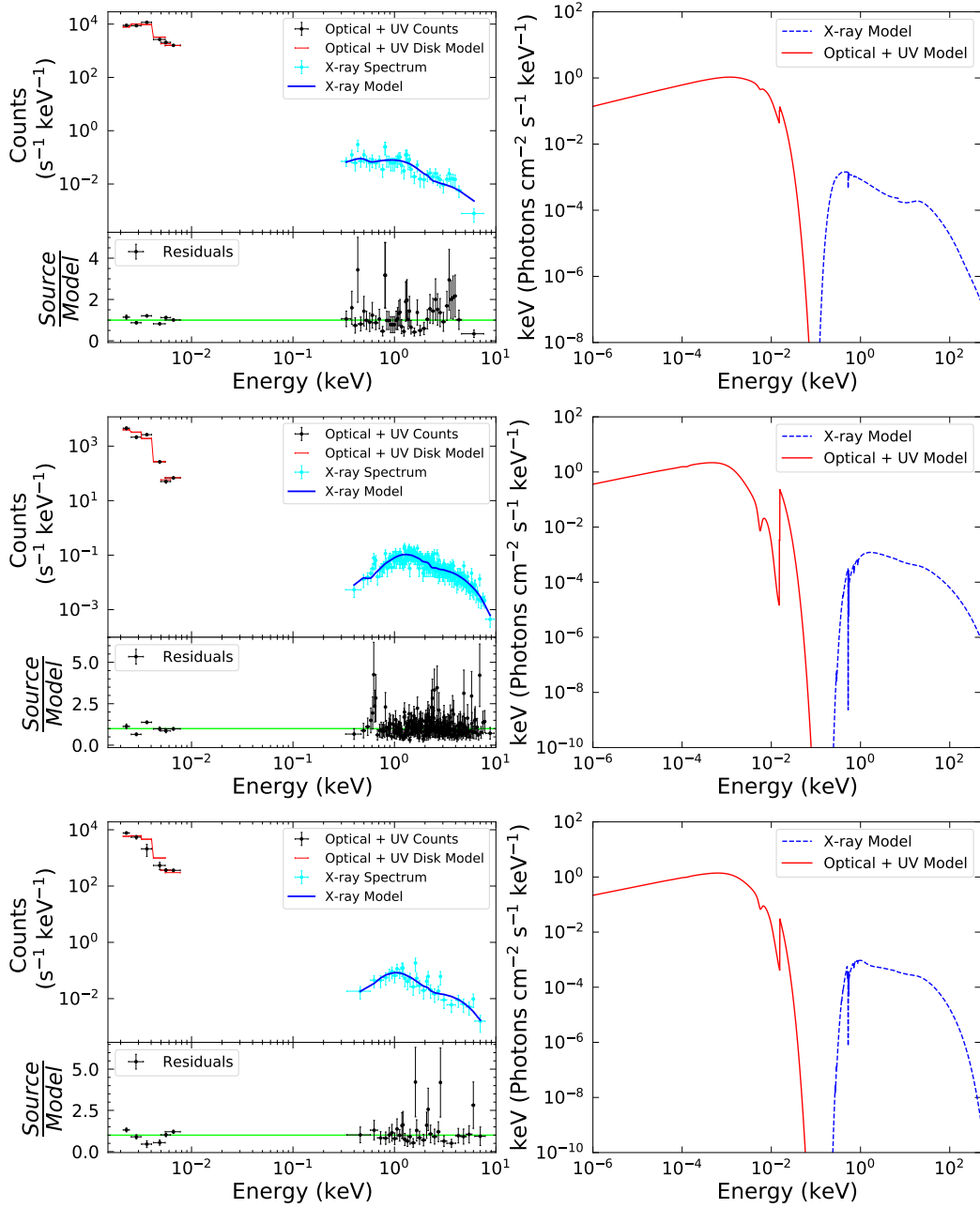


Figure 3.13: A few examples of the optical-to-X-ray SED fits. From top to bottom, the fits are for sources: SWIFTJ0002.5+0323, SWIFTJ0654.6+0700, and SWIFTJ1316.9-7155. The left panel shows the counts in the optical/UV filters (black points) and the 0.3 – 10 keV X-ray spectrum (cyan points). It also shows the fit obtained using the optical/UV disk model including dust extinction (in red) and the X-ray model (in blue), along with the fit residuals. The right panel shows the best-fit SED model for each source.

3.7 Summary

In this chapter, we have presented one of the largest studies, to date, of the broadband AGN SEDs from optical to X-ray wavelengths, for a sample of 236 unobscured, hard-X-ray-selected, nearby AGN from the 70-month *Swift*/BAT catalog. We compiled simultaneous, optical, UV, and X-ray observations for our sources to avoid any issues arising due to differences in the variability timescales at different wavelengths. We extracted the 0.3 – 10 keV X-ray spectra and magnitudes and fluxes in the six *Swift*/UVOT filters: U, V, B, UVW1, UVW2, and UVM2 for all our sources. We corrected the optical/UV fluxes for galactic dust extinction as well as host galaxy contamination. The latter was done by fitting the 2D surface brightness of the source images using a PSF and a Sérsic profile with GALFIT to fit the AGN and the host galaxy, respectively. We also performed numerous simulations by creating fake populations of type I AGN and fitting them using GALFIT, to quantitatively inspect the reliability of the AGN magnitudes calculated by GALFIT. As a result of these simulations, we were able to calculate correction factors in each of the six *Swift*/UVOT filters, that can be used to correct the GALFIT-estimated PSF fluxes. We constructed and fit the multi-wavelength AGN SEDs (10^{-7} to 500 keV) using a dust-reddened multi-temperature blackbody to model the optical/UV accretion disk and a variety of X-ray models consisting of multiple components to account for the primary X-ray emission and the reprocessed secondary emission. The main outcomes and findings of this analysis are discussed in detail in the next part of this thesis (Chapters 4 and 5).

Acknowledgements

This work made use of data from the NASA/IPAC Infrared Science Archive (IRSA) and NASA/IPAC Extragalactic Database (NED), which are operated by the Jet Propulsion Laboratory, California Institute of Technology, under contract with the National Aeronautics and Space Administration. This research has made use of data and/or software provided by the High Energy Astrophysics Science Archive Research Center (HEASARC), which is a service of the Astrophysics Science Division at NASA/GSFC and the High Energy Astrophysics Division of the Smithsonian Astrophysical Observatory. This research also made use of *photutils*, an Astropy package for the detection and photometry of astronomical sources (Bradley et al. 2021).

Appendix

A: GALFIT Simulations

AGN flux can be contaminated by the host galaxy’s light. To extract reliable AGN flux measurements, we used GALFIT to fit the two-dimensional surface brightness of our sources. However, considering the wide variety of sources in our sample, varying over redshift, morphology, total magnitude, etc., we carried out some simulations to check the reliability of the flux values estimated by GALFIT. We simulated a population of fake type I AGN covering the same redshift range as our original sample ($0.001 < z < 0.3$). We used 10 Seyfert 2 galaxies, classified so by the optical classification provided by [Koss et al. \(2017\)](#), with X-ray column densities above 10^{23} cm^{-2} to eliminate the possibility of any significant optical/UV radiation coming from the SMBH at the center. We pre-processed, aspect corrected, and reduced the raw *Swift*/UVOT images of these 10 sources in the three UV filters (UVW1, UVM2, UVM2). The final sky images were then used to extract the total galaxy magnitudes of these sources to be used in GALFIT later. We then randomly selected a field star from our images and placed it at the center of the galaxy to replicate an unobscured type I AGN. The magnitude of the star was varied by changing its normalization to reciprocate different AGN light ratios (AGN magnitude to total magnitude), ranging from 10% to 95%. We calculated the star’s magnitude using GALFIT before placing it on the galaxy to estimate the star flux that would later be compared to the PSF flux estimated by GALFIT. We also included different possible morphologies in this sample of 10 galaxies: edge-on galaxies, face-on galaxies, and indeterminate. We did not go with the traditional galaxy morphology classification of elliptical and spiral galaxies because on scales as small as the ones in our UVOT images, GALFIT cannot distinguish between bulge-dominated and disk-dominated morphologies. Also, we are not interested in fitting the extended features, like spiral arms, starburst regions, clumps, etc. of the host galaxy. Instead, we included Seyfert 2s with different orientations to understand GALFIT’s response to circular (face-on) vs elliptical (edge-on) galaxy shapes in two-dimension. In total, we simulated 270 type I AGN across the three *Swift*/UVOT UV filters with 10 different AGN light ratios.

The GALFIT analysis of these 270 simulated AGN was done following the same procedure as the one followed for our original sample (described in Section 3.5):

1. A relatively empty region was selected from the image to fit the background using the sky component in GALFIT. In the case of crowded fields, a bad pixel mask was incorporated into the GALFIT parameter file to mask the background sources.

2. A region around the source with the same dimension as the one used in the previous step was selected and fitted using the sky and PSF component in GALFIT. Like before, a bad pixel mask was used to mask the light from all the extra sources around our galaxy of interest. The sky estimated in the previous step was used as the input sky value in this step. However, we left the sky value to vary in general and fixed it only in cases when it was significantly different from the one estimated in the previous step. To fit the PSF component, GALFIT requires a PSF image that it, in turn, fits to the image. The PSF image was created using the `photutils` package in Python. This package uses a defined set of stars from the field of the source and reiterates over these star profiles to produce a PSF image. We used 3-6 bright background stars to create a PSF image for each of our 10 sources in each UV filter. The input value used for the PSF magnitude was the one calculated by GALFIT previously for the star in the absence of any host galaxy. All the residuals were visually examined for any flux remaining from the source.
3. Finally, the same source region as before was fitted using the sky, PSF, and Sérsic profile component in GALFIT. The sky and PSF input parameters used were the ones we obtained from the previous step. The input Sérsic magnitude was defined as the galaxy magnitude obtained from the UVOT pipeline. The input value for effective Sérsic radius was visually determined from the source images. The input values for the coordinates of the Sérsic profile were put as the ones for the PSF profile from the results of the previous step. We started with an input Sérsic index value of 2.5 and moved to 2.0, 1.5, 1.0, 0.5, 3.0, 3.5, and 4.0 in cases when GALFIT was not able to converge. All the other parameters of the Sérsic profile were left to their default values. In multiple cases, when GALFIT was unable to converge with these input parameters, we fixed the controversial parameters (generally, axis ratio or effective radius, sometimes the coordinates of the Sérsic profile) to specific acceptable values so as to allow GALFIT to converge and produce reliable fits, estimates, and residuals. All the residuals were visually inspected to confirm the reliability of the fits. In some cases, even after multiple repetitions, when GALFIT was not able to fit all the three components to the source, we quote results from step two, i.e., just the sky + PSF fits.

In Figures 3.15, 3.16, and 3.17, we plot our results from the GALFIT analysis of these 300 simulated type I AGN for the UVW1, UVW2, and UVM2 filters, respectively. In each case, the plot on the left shows the AGN (PSF) flux estimated by GALFIT with respect to the actual flux of the star used as an AGN replica in these fake type I galaxies, while the plot on the right shows the same information

but segregated into different redshift bins. The symbols are color-coded based on the AGN to total light ratio. In general, the figures show a pretty good agreement between the AGN fluxes estimated by GALFIT and the actual star flux. We start seeing some significant difference only as we move to lower fluxes ($< 10^{-15} \text{ erg cm}^{-2} \text{ s}^{-1} \text{ \AA}^{-1}$) and specifically in AGN light ratios below 80% in that flux regime. Some smaller deviations from the $x = y$ line are seen at the highest fluxes ($> 10^{-13} \text{ erg cm}^{-2} \text{ s}^{-1} \text{ \AA}^{-1}$) and AGN light ratios around and above 90%. The differences at higher fluxes are more prominent for filters UVW2 and UVM2 as compared to the UVW1 filter. However, looking at the redshift-specific plots, it is evident that the large differences in the GALFIT estimates when compared to the star flux are restricted to the highest redshift range ($0.05 < z < 0.3$). On further inspection, we found that these are, without exception, the sources for which GALFIT was not able to fit a Sérsic profile to the source, and the flux estimates are thereby from the sky + PSF fit only. This could be because of very faint detections of the host galaxy at such large distances, a consequence of the flux-limited nature of the *Swift*/BAT AGN sample. The significant difference in the fluxes is, therefore, quite understandable, considering the fact that GALFIT tried to fit the host as well the AGN light at the center with only the PSF component and hence gives much larger flux values for the AGN as compared to the expected star's flux at the center. In the case of small deviations seen at the highest flux and AGN light ratios above 90%, in filters UVW2 and UVM2 for redshift range $0.01 < z < 0.05$, these cases again correspond to scenarios where GALFIT was not able to attain reliable Sérsic fits for the source images. This could be because the AGN, in these cases, is responsible for most of the light coming from the galaxy, and hence, the AGN flux is extremely high when compared to the host galaxy flux. As a result, GALFIT is not able to fit the host galaxy in the background of such a strong central AGN light source that dominates the entire galaxy. Therefore, we obtain GALFIT flux estimates that are lower than the actual AGN flux.

In Figure 3.18, we have plotted the star flux vs the GALFIT estimated PSF flux for the three UV filters in different morphology classes. We have also included redshift information in these plots in the form of different symbols. At first look, based on these plots, it might seem like GALFIT works much better for edge-on galaxies as compared to the indeterminates and face-on galaxies in filters UVW1 and UVM2, and for filter UVW2, it works quite nicely for both edge-ons and face-ons. However, if we take a look at the redshift distribution in all these plots, it is abundantly clear that the differences in the flux estimates are strongly dependent on the redshift. The simulated edge-on galaxies of our test sample are all lying in the lower redshift bins and hence give good fit results. Whereas, the indeterminates belong to the highest redshift range. The few sources that show significant deviations from the $x = y$ line with face-on orientation are also part of the highest redshift bin.

Based on the results we obtained from these simulations in the UV filters, we repeat a similar analysis for the three *Swift*/UVOT optical filters but only in the highest redshift bin. This is a reasonable approach, considering that the sources in our sample are brighter in the optical compared to the UV (see in Figure 3.19). And as the UV simulations show that it is only the faintest sources that the GALFIT-estimated magnitudes are not reliable, we calculate the optical corrections for the same set of sources ($z > 0.05$).

B: Comparison with the HST

Thanks to the follow-up observations of *Swift*/BAT AGN by HST (as part of the optical campaign of BASS), we have high-quality HST images in filter F225W (similar to UVM2) for several sources in our sample. We use simultaneous HST observations in the F225W filter for two AGN in our sample (SWIFTJ1708.6+2155 and SWIFTJ1925.0+5041). We fit these images with GALFIT following the procedure mentioned in Section 3.5.2 and extract their AGN flux to compare with those obtained from the *Swift*/UVOT images in the UV filter M2. Considering the high resolution of HST images with detailed and extended galaxy profiles, we focus on fitting just a small region around the PSF to estimate the AGN flux. For both sources, the magnitudes estimated from the HST images are within 0.1 mags of the ones from the UVOT images. This is acceptable, since the central wavelengths of the two filters are slightly different (F225W: 2371 Å and UVM2: 2246 Å). Therefore, we can conclude that the GALFIT-estimated AGN magnitudes for our *Swift*/UVOT images are consistent with those from the HST images.

Table 3.8: List of source magnitudes as calculated by the *Swift*/UVOT command `uvotsource` via 5 arcsecs aperture photometry, along with statistical errors (Section 3.3.1).

BAT ID	Swift ID	M_U	M_V	M_B	M_{W1}	M_{W2}	M_{M2}
2	SWIFTJ0001.6-7701	—	—	—	17.16 ± 0.03	17.30 ± 0.03	17.37 ± 0.03
3	SWIFTJ0002.5+0323	16.16 ± 0.04	15.01 ± 0.05	15.61 ± 0.04	16.60 ± 0.03	16.91 ± 0.03	16.83 ± 0.03
6	SWIFTJ0006.2+2012	14.39 ± 0.02	14.24 ± 0.02	14.42 ± 0.02	14.72 ± 0.02	14.96 ± 0.02	14.93 ± 0.02
10	SWIFTJ0021.2-1909	19.21 ± 0.06	—	—	21.20 ± 0.08	—	—
14	SWIFTJ0026.5-5308	—	—	—	17.80 ± 0.08	—	18.30 ± 0.03
16	SWIFTJ0029.2+1319	15.68 ± 0.02	15.40 ± 0.04	15.62 ± 0.03	16.17 ± 0.03	16.32 ± 0.03	16.43 ± 0.03
19	SWIFTJ0034.5-7904	14.95 ± 0.03	14.76 ± 0.04	15.00 ± 0.03	15.34 ± 0.02	15.50 ± 0.02	15.52 ± 0.03
34	SWIFTJ0051.6+2928	16.81 ± 0.04	15.09 ± 0.04	15.81 ± 0.03	17.57 ± 0.05	18.08 ± 0.02	18.03 ± 0.05
36	SWIFTJ0051.9+1724	15.45 ± 0.02	15.44 ± 0.05	15.63 ± 0.04	15.88 ± 0.03	16.09 ± 0.02	16.19 ± 0.03
39	SWIFTJ0054.9+2524	15.61 ± 0.03	15.61 ± 0.05	15.69 ± 0.03	16.07 ± 0.03	16.04 ± 0.03	16.31 ± 0.02

Table 3.9: List of AGN magnitudes (corrected) as estimated by GALFIT image decomposition (Section 3.5). The last column shows in the form of flags if the GALFIT-estimated magnitude was corrected (c) and if the UVOT pipeline estimated magnitude was used (for any of the filters) to create the final SEDs (p).

BAT ID	Swift ID	M_U	M_V	M_B	M_{W1}	M_{W2}	M_{M2}	Flag
3	SWIFTJ0002.5+0323	16.91 ± 0.03	16.74 ± 0.09	17.12 ± 0.05	17.61 ± 0.03	17.72 ± 0.02	17.52 ± 0.02	-
6	SWIFTJ0006.2+2012	14.82 ± 0.01	14.51 ± 0.01	14.84 ± 0.00	14.88 ± 0.00	15.12 ± 0.00	14.99 ± 0.00	-
16	SWIFTJ0029.2+1319	15.97 ± 0.01	15.17 ± 0.04	15.69 ± 0.00	16.39 ± 0.01	16.66 ± 0.04	16.33 ± 0.00	c
19	SWIFTJ0034.5-7904	16.40 ± 0.05	16.54 ± 0.08	16.81 ± 0.03	15.58 ± 0.02	15.87 ± 0.04	15.50 ± 0.01	c
34	SWIFTJ0051.6+2928	17.25 ± 0.03	16.25 ± 0.04	16.79 ± 0.03	17.97 ± 0.03	18.37 ± 0.01	18.36 ± 0.03	-
36	SWIFTJ0051.9+1724	15.77 ± 0.01	15.08 ± 0.06	15.71 ± 0.00	16.01 ± 0.01	16.60 ± 0.05	16.16 ± 0.01	c
39	SWIFTJ0054.9+2524	15.72 ± 0.01	15.86 ± 0.02	15.79 ± 0.00	16.28 ± 0.01	16.39 ± 0.04	16.21 ± 0.00	c
43	SWIFTJ0059.4+3150	17.45 ± 0.12	16.25 ± 0.05	17.75 ± 0.18	16.61 ± 0.02	17.22 ± 0.00	16.96 ± 0.01	p
45	SWIFTJ0101.5-0308	18.44 ± 0.02	17.54 ± 0.04	19.64 ± 0.04	18.99 ± 0.10	19.73 ± 0.02	19.47 ± 0.03	-
51	SWIFTJ0105.7-1414	16.03 ± 0.00	15.71 ± 0.07	15.91 ± 0.07	16.15 ± 0.01	16.23 ± 0.01	15.70 ± 0.18	c

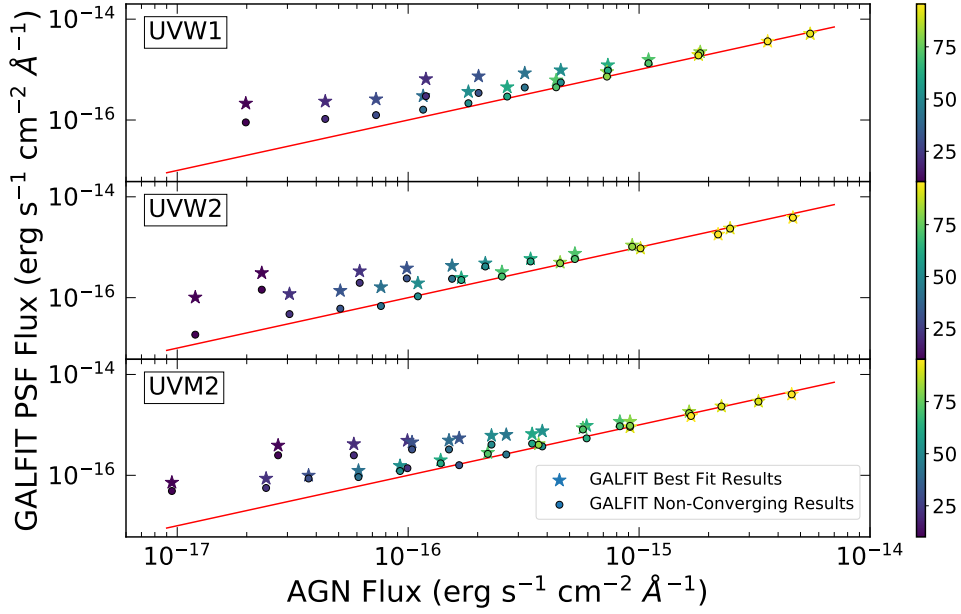


Figure 3.14: Comparing the expected AGN (star) flux to the PSF flux estimated by GALFIT for the three UV filters. The star symbols show the best-fit results without a Sérsic profile, while the circle symbols show the results when the fitting with a Sérsic profile does not converge but we still obtain better constraints on the PSF profile compared to the fit without a Sérsic profile. The $x = y$ line is shown in red. The color bar indicates the AGN light ratio.

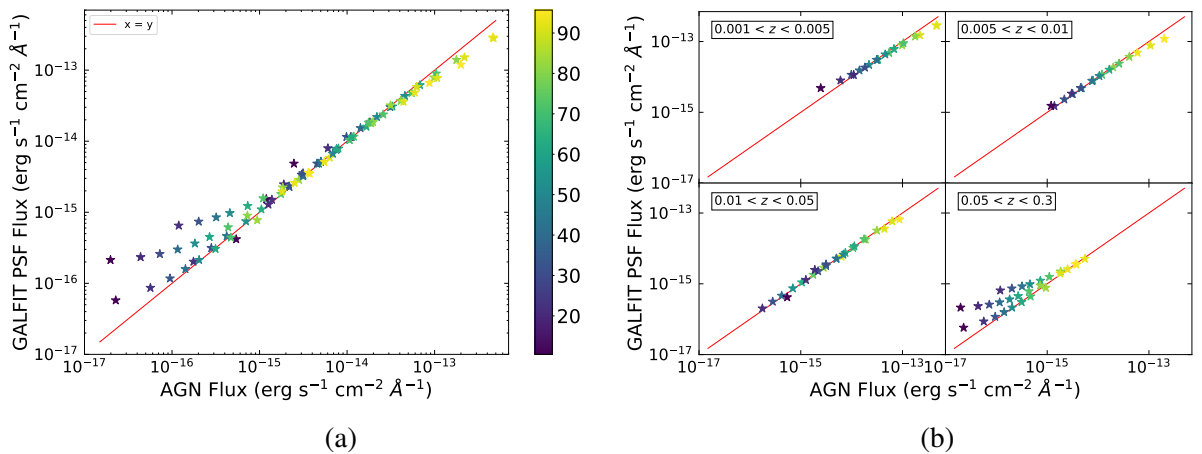


Figure 3.15: (a) Comparing the expected AGN (star) flux to the PSF flux estimated by GALFIT for UVOT filter UVW1. (b) The same plot as (a) but in different redshift bins. The $x = y$ line is shown in red. The color bar indicates the AGN light ratio.

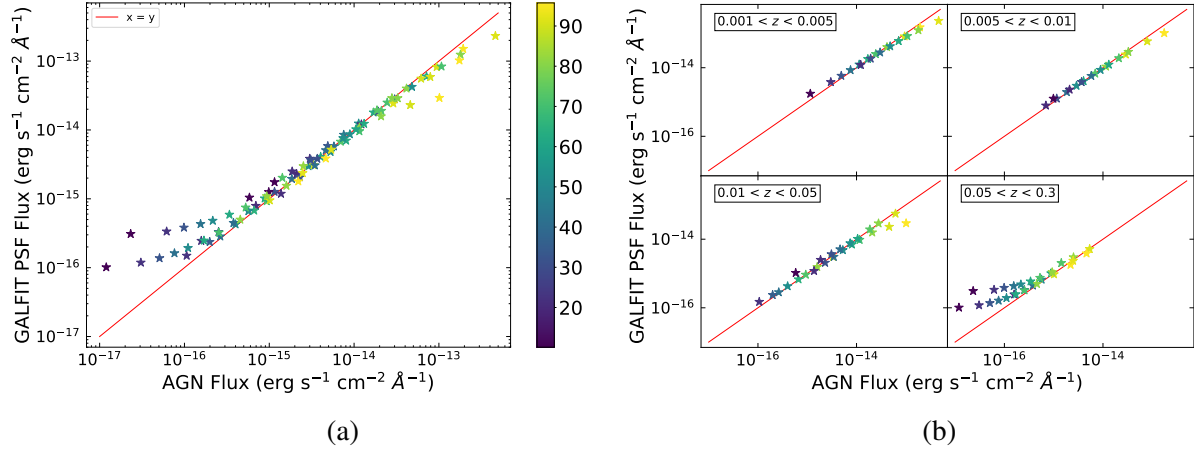


Figure 3.16: (a) Comparing the expected AGN (star) flux to the PSF flux estimated by GALFIT for UVOT filter UVW2. (b) The same plot as (a) but in different redshift bins. The $x = y$ line is shown in red. The color bar indicates the AGN light ratio.

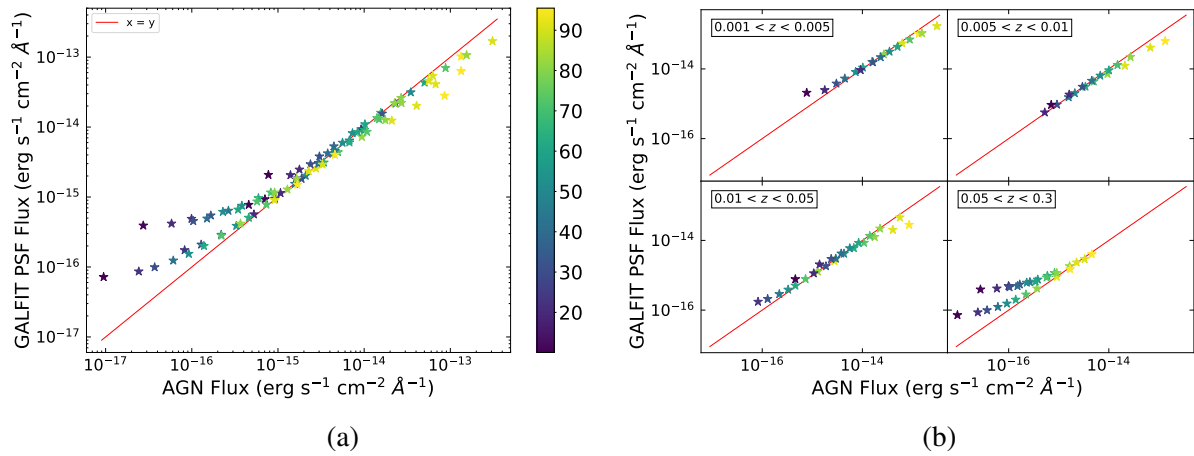


Figure 3.17: (a) Comparing the expected AGN (star) flux to the PSF flux estimated by GALFIT for UVOT filter UVM2. (b) The same plot as (a) but in different redshift bins. The $x = y$ line is shown in red. The color bar indicates the AGN light ratio.

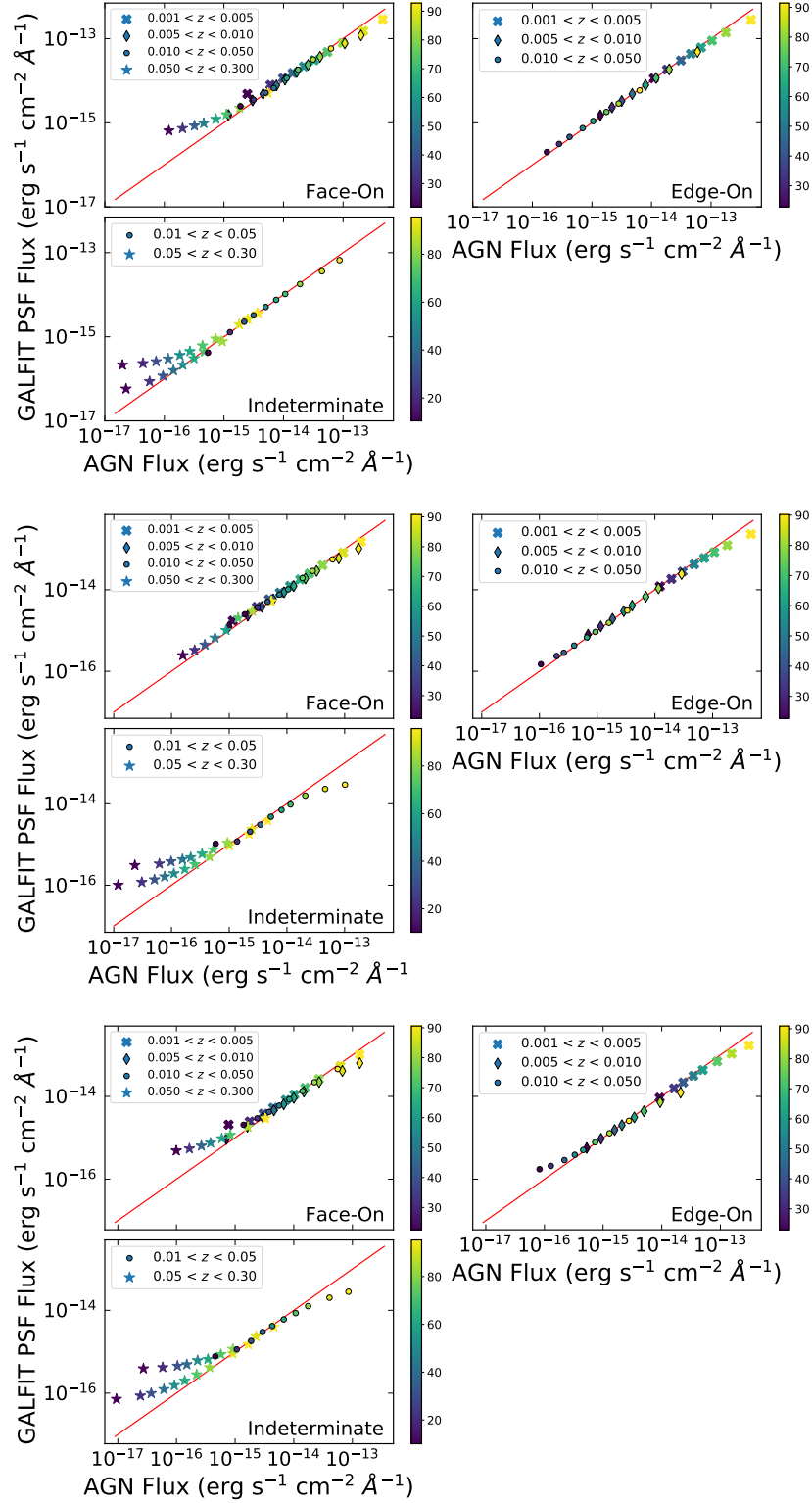


Figure 3.18: Comparing the expected AGN (star) flux to the PSF flux estimated by GALFIT for filters (top to bottom) UVW1, UVW2, and UVM2. The three subplots in each figure show the three different morphologies considered and the different symbols correspond to the redshift range. The $x = y$ line is shown in red. The color bar indicates the AGN light ratio.

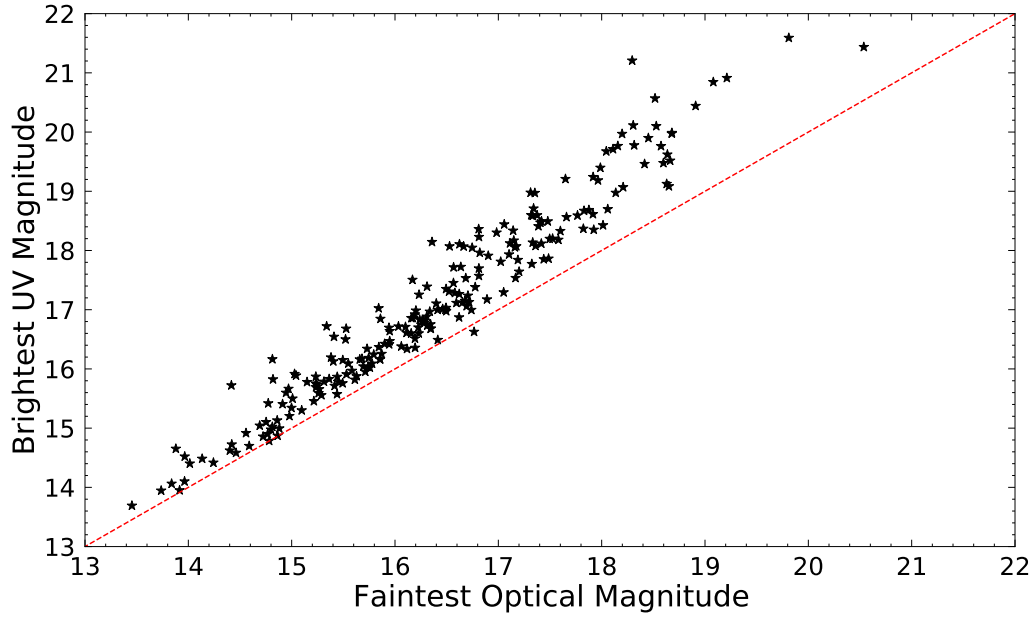


Figure 3.19: Plot showing the source magnitudes in the faintest optical band against the brightest UV band. It is evident from this figure that the AGN in our sample are brighter in the optical when compared to the UV and even the faintest optical band is brighter than the brightest UV band. Therefore, based on the GALFIT simulations carried out in the UV band to calculate the correction factors for GALFIT-estimated PSF magnitudes and fluxes, only the faintest and farthest sources need to be corrected in the optical as well. The $x = y$ line is shown in red.

Chapter 4

Optical, UV and X-ray Emission Properties of Unobscured AGN

In the previous chapter, we explained in detail the various steps we followed to systematically construct and fit the optical-to-X-ray SEDs of a sample of ~ 240 unobscured AGN. In this chapter, we focus on the outputs of our SED fitting and explore some important correlations between them. We also report the main correlations we found for these quantities with various physical properties of AGN, such as their black hole mass, bolometric luminosity, Eddington ratio, etc. All the results reported in this and the following chapter are for the final sample of 236 unobscured AGN with GALFIT fluxes corrected as explained in Section 3.5.3 for the high redshift sources. However, we did check all our results for the sample without employing these corrections and did not find any significant differences. We also confirmed all our results to hold for a cleaner sample of 190 AGN excluding the high redshift sources that need to be corrected. In Section 4.1, we present the median SED model for our sample, along with a couple of examples of typical SEDs with and without dust extinction. In section 4.2, we look at some of the parameters useful to describe the optical/UV disk emission of AGN. And finally, in sections 4.3, 4.4, and 4.5, we present the optical-to-X-ray spectral index (α_{ox}), the X-ray and the optical/UV bolometric corrections (κ_{bol}), respectively, and explore their dependence on different physical properties of AGN, like the black hole mass, bolometric luminosity, Eddington ratio, etc.

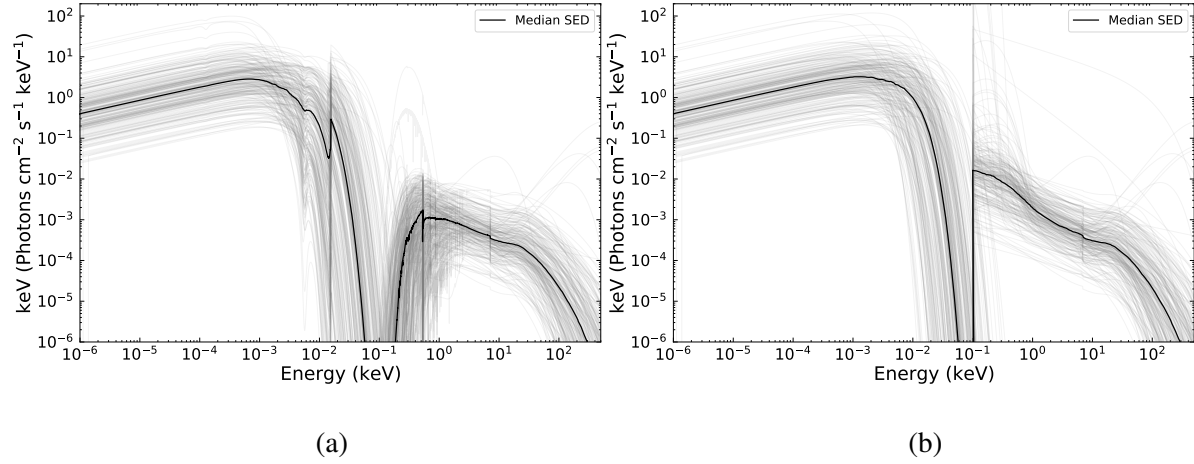


Figure 4.1: Rest frame optical-to-X-ray best-fit SED models (a) with absorption and (b) without absorption, for the 236 unobscured, nearby AGN in our sample (in grey). The median SED model is shown as the black solid line.

4.1 Median SED Models

In Figure 4.1a, we show all the optical-to-X-ray SED models for our sample, as well as the median SED (MSED) model, in the rest frame (in solid black). Next to it (Figure 4.1b), we show the intrinsic, absorption-corrected SED models for our sample along with the median, absorption-corrected SED (in solid black). Between the two figures, we can clearly see the absorption features due to the host galaxy and the Milky Way in the optical/UV and soft X-rays. A reflection feature around 7 keV is visible in both cases. As mentioned in many previous works on broadband SED fitting (e.g., Elvis et al. 1994; Richards et al. 2006; Vasudevan et al. 2009), and also visible in Figure 4.1, the median SED does not necessarily represent the full range of properties exhibited by the AGN population and there exists a large variety in the shapes of AGN SEDs.

Next, we plotted the median SEDs in bins of X-ray luminosity, bolometric luminosity, black hole mass, and Eddington ratio (Figure 4.2). We use the median value of each parameter in our sample to divide the sample into two bins and visualize the differences, if any, in the SED shapes. We have normalized all the MSEDs at 1eV to compare them. The variation in the MSED shape for different luminosity bins is prominent in the top two panels of Figure 4.2. For larger bolometric luminosities, the MSED in the optical/UV extends to higher energies and represents higher disk temperatures (also discussed in Section 4.2.1 and 4.5). The lack of any change in the X-ray part of the MSED suggests

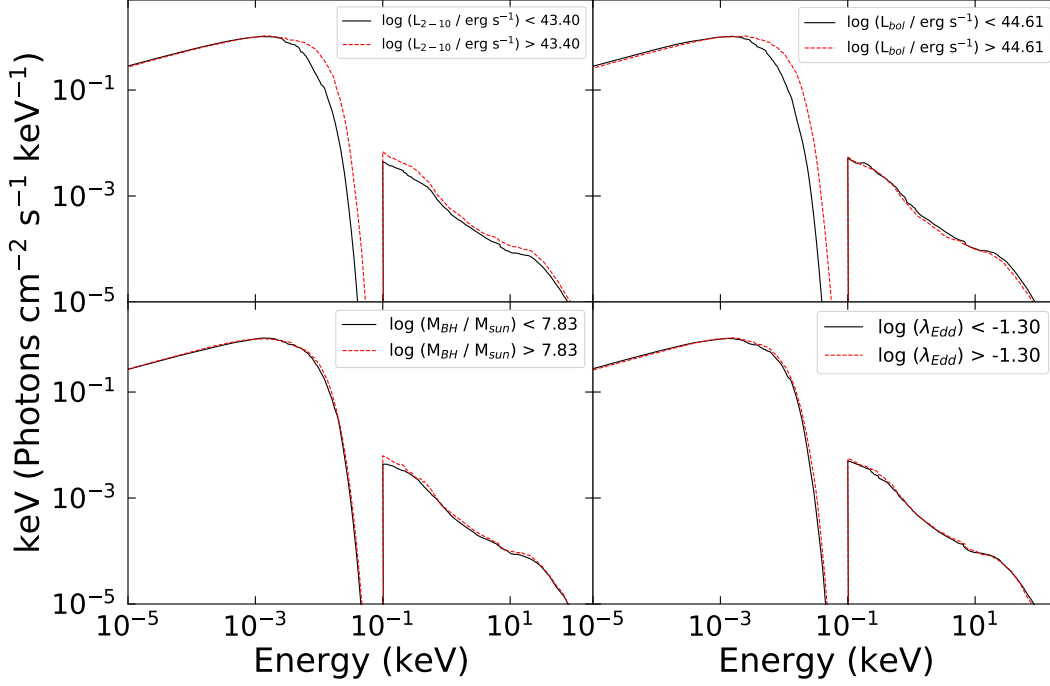


Figure 4.2: The absorption corrected, median SED (normalized at 1 eV) in bins of (a) 2 – 10 keV X-ray luminosity, (b) bolometric luminosity, (c) black hole mass, and (d) Eddington ratio. The black solid curve shows the lower value bin and the red dashed curve is the higher value bin, for each panel.

that an increase in the bolometric luminosity does not necessarily imply a direct increase in the X-ray fraction of the AGN luminosity. Furthermore, we see an overall change in the MSED shape between the two X-ray luminosity bins. Increasing the X-ray luminosity affects not only the X-ray flux but also the optical/UV part of the SED. This can be explained as a consequence of the X-ray luminosity scaling the bolometric luminosity. Implications of this will be discussed in more detail later in Section 5.1.

In terms of black hole mass and Eddington ratio (bottom two panels of Figure 4.2), we do not see any significant changes in the MSED shapes for the two bins. The absence of any differences in SED shapes for lower and higher black hole masses indicates that it is not a dominating factor influencing the total AGN emission or the fractions of emission at different energies contributing to the total emission. In the case of the Eddington ratio, although we do not see any considerable variation in the MSED shapes when we divide the sample into two bins, we will revisit this point and discuss it further in Section 5.2.1.

4.2 Optical/UV Disk Emission

The optical/UV part of the multi-wavelength AGN SED corresponds to the emission that is believed to be originating in the disk at different radii, as material spirals into the central SMBH. This emission is the largest contributor to the total accretion luminosity of the AGN. In the following two sections, we look in detail at the three parameters obtained from the optical/UV SED fitting.

4.2.1 Disk Temperature and Normalization

If we consider the standard accretion disk model suggested by [Shakura & Sunyaev \(1973\)](#), it assumes a geometrically thin and optically thick structure for the disk with a temperature gradient, such that higher temperatures are expected at closer proximities to the SMBH, until the innermost stable circular orbit. Based on our SED fitting analysis, we obtained a distribution of the maximum temperatures of the disk for our sample of unobscured AGN with a median $kT_{\text{max}} = 2.70 \pm 0.01$ eV. We show kT_{max} as a function of redshift in Figure 4.3a. The positive correlation between kT_{max} and z does not necessarily imply that higher redshift sources have higher disk temperatures. Since our SED models already included a term to account for the redshift of the source, this dependence should come from something intrinsic to the fitting procedure. To investigate this further, we inspected the other parameter that plays an important role in the fitting, i.e. the normalization of the disk component (K_{uvo}). We plot kT_{max} as a function of K_{uvo} in Figure 4.3b and obtain a strong anti-correlation between the two parameters (also see Table 4.1). A possible explanation for this could be that standard disks with higher values of kT_{max} would tend to have bluer spectra, which could, in turn, force the normalization to go down so as to fit the defined energy range in our SEDs. This is also visible in Figure 4.1, where the SED models with higher disk normalization are redder compared to the ones with lower disk normalization. As stated in Eq. 3.1, K_{uvo} is a function of the black hole mass and the distance to the source, and therefore, we expect it to anti-correlate with redshift (see Table 4.1). As a result, this positive trend between kT_{max} and redshift, could just be a consequence of the inverse correlations of K_{uvo} with both redshift and kT_{max} .

One might also argue that the positive trend between kT_{max} and redshift could just be a reflection of the luminosity distribution of our sample with respect to redshift, where we have the largest luminosity sources at the highest redshifts. To check this scenario, we repeated the SED fitting for our entire sample following the procedure stated by [Vasudevan et al. \(2009\)](#), where they fixed the disk normalization using their black hole mass estimates. As part of the BASS DR2, [Mejía-Restrepo et al. \(2022\)](#) presented virial black hole mass estimates for almost all *Swift*/BAT type I AGN in the 70-month catalog using broad-

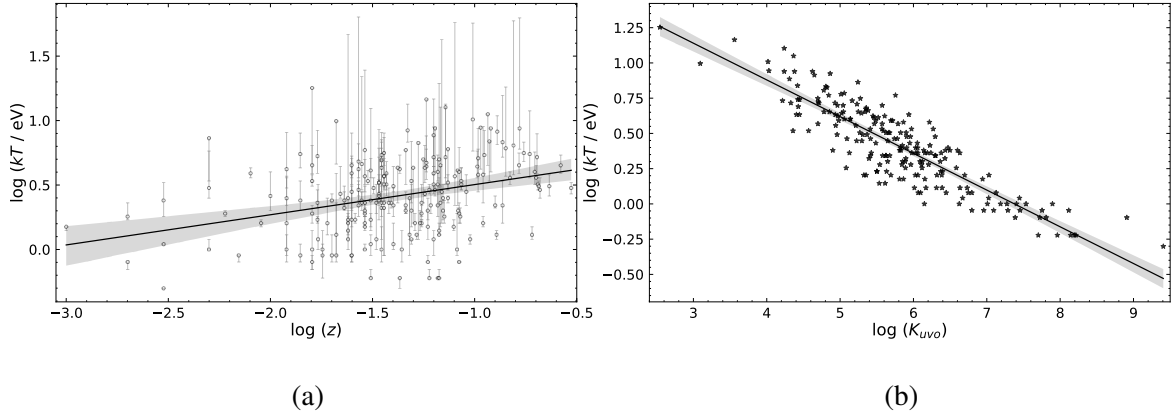


Figure 4.3: The maximum disk temperature (kT_{max}) as a function of (a) the redshift of the source, and (b) the disk normalization (K_{UVO}). The black solid line shows the best-fit relation.

emission line measurements. Assuming the virialized motion of the gas in the broad line region (BLR) and employing the empirical relations between the continuum luminosity and the size of the BLR (from reverberation mapping), the mass of the black hole can be calculated using the width of certain broad emission lines. They specifically used the $\text{H}\alpha$, $\text{H}\beta$, $\text{Mg II } \lambda 2798$ and/or $\text{C IV } \lambda 1549$ broad emission lines and followed the respective prescriptions described by [Greene & Ho \(2005\)](#), [Trakhtenbrot & Netzer \(2012\)](#), and [Mejía-Restrepo et al. \(2016\)](#). We use these black hole mass estimates provided by [Mejía-Restrepo et al. \(2022\)](#) throughout this work. Similar to the approach taken by [Vasudevan et al. \(2009\)](#), we calculated the disk normalizations from Eq. 3.1, using $M = M_{\text{BH}}$, our redshift-independent distances for D , inclination angle ($i = 0$) corresponding to face-on disks for our unobscured AGN sample, and a color-to-temperature ratio (β) of unity. We fixed K_{UVO} to this value and redid the SED fitting. We then checked how the new kT_{max} evolved with redshift and obtained an inverse correlation. The fact that the original relation not only disappeared but also inverted suggests that it is not related to the redshift-luminosity distribution of our sources. We then checked if the dependence of the normalization on redshift changed and in fact, found an inversion relative to the original trend and a positive correlation between the two. This was mainly due to the black hole mass of our sample increasing with redshift. Finally, only the anti-correlation between kT_{max} and K_{UVO} was retained, which further confirmed that the disk normalization was indeed the deciding factor here.

Aside from the dependence of kT_{max} on redshift, which, as we discussed, was not linked to AGN physics but instead was an outcome of the SED fitting technique, we also found strong positive correla-

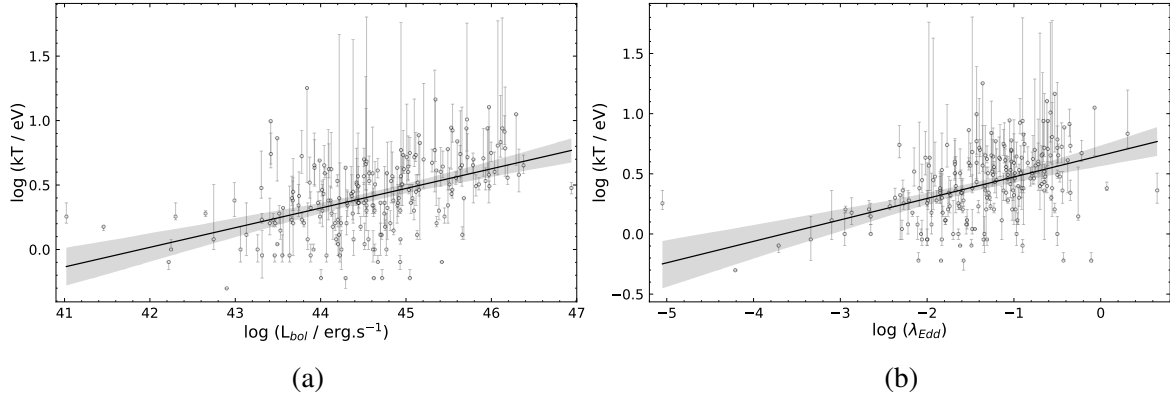


Figure 4.4: The maximum disk temperature (kT_{\max}) as a function of (a) the bolometric luminosity, and (b) the Eddington ratio. The black solid line shows the best-fit relation.

tions of the disk temperature with both L_{bol} and λ_{Edd} (Figure 4.4), defined below:

$$\log(kT_{\max}) = (0.152 \pm 0.020) \times \log(L_{\text{bol}}) + (-6.379 \pm 0.881) \quad (4.1)$$

$$\log(kT_{\max}) = (0.178 \pm 0.025) \times \log(\lambda_{\text{Edd}}) + (0.652 \pm 0.038) \quad (4.2)$$

This is not surprising, as we would expect sources with larger luminosities and accretion rates to have hotter disks, under the assumption of the standard disk model (e.g., Shakura & Sunyaev 1973; Novikov & Thorne 1973). Since our sample does not probe higher Eddington ratios ($\lambda_{\text{Edd}} < 1$), this is a reasonable assumption. We also checked if kT_{\max} relates with M_{BH} , but did not find any correlation.

4.2.2 Host Galaxy Dust Extinction

One of the components (ZDUST) in our optical/UV SED model accounts for the intrinsic dust extinction of the source emission due to its host galaxy. This is quantified by the parameter $E(B - V)_{\text{HG}}$. In Figure 4.5, we show the distribution of $E(B - V)_{\text{HG}}$ and also how it evolves with redshift. We do not find any dependence of the intrinsic dust extinction observed by the disk emission on the redshift. We also checked if $E(B - V)_{\text{HG}}$ correlates with any other physical properties of the AGN, such as L_{bol} , M_{BH} , and λ_{Edd} but did not find any significant trends.

The analog of $E(B - V)_{\text{HG}}$ in the X-rays could be the line-of-sight column density (N_{H}) causing obscuration of the X-ray emission from the AGN. We plot the two quantities against each other in Figure 4.6 and obtain a weak positive correlation between them (see Table 4.1). Even if both parameters quantify the level of obscuration of the emission at respective energies, considering that this emission

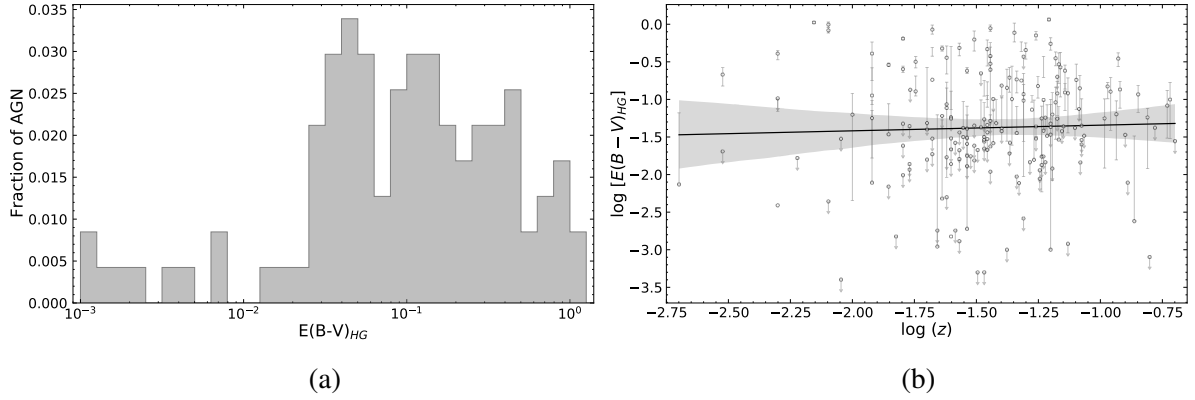


Figure 4.5: (a) Distribution of $E(B-V)_{\text{HG}}$, that quantifies the intrinsic dust extinction of the AGN emission in the optical/UV due to the host galaxy. (b) $E(B-V)_{\text{HG}}$ as a function of the redshift. The black solid line shows the best-fit relation.

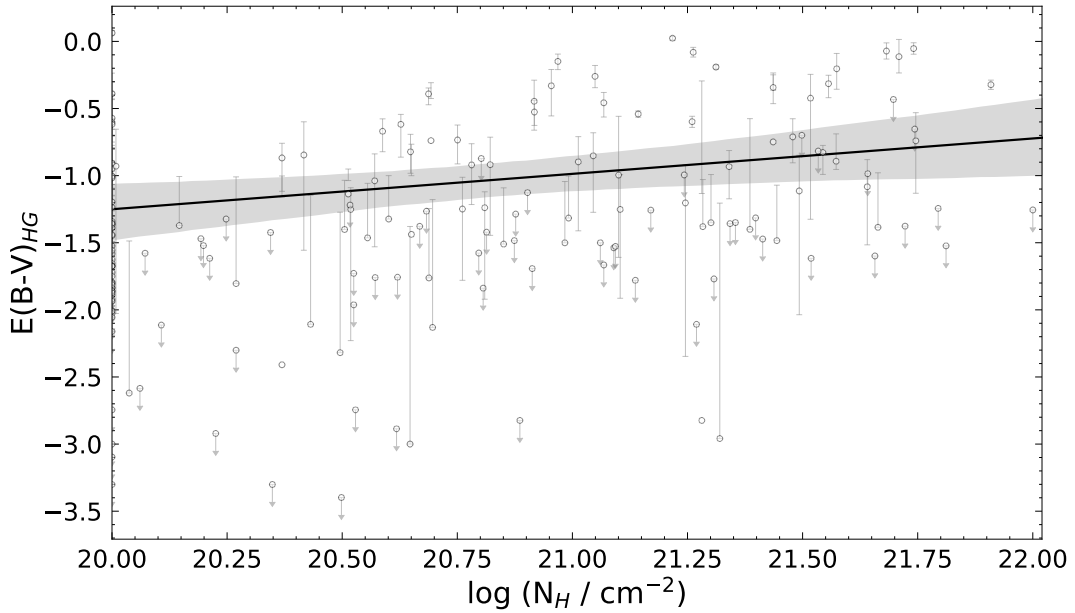


Figure 4.6: The host galaxy dust extinction in the optical/UV $[E(B-V)_{\text{HG}}]$ as a function of the X-ray column density (N_{H}). The black line shows the weak correlation between the two quantities.

Table 4.1: Correlation results for Figures 4.3, 4.4, 4.5, and 4.6, described in Section 4.2.

Correlation	R-Value ^a	P-Value ^b
$kT_{\text{max}} - z$	0.32	2.31×10^{-6}
$kT_{\text{max}} - K_{\text{uvo}}$	-0.88	4.05×10^{-68}
$K_{\text{uvo}} - z$	-0.38	6.20×10^{-9}
$kT_{\text{max}} - L_{\text{bol}}$	0.47	5.18×10^{-13}
$kT_{\text{max}} - \lambda_{\text{Edd}}$	0.45	1.47×10^{-11}
$E(B - V)_{\text{HG}} - z$	-0.14	0.05
$E(B - V)_{\text{HG}} - N_{\text{H}}$	0.25	0.02

^a The Pearson's correlation coefficient.

^b The probability of the data set appearing if the null hypothesis is correct.

originates in different regions of the AGN (at different physical scales), the material responsible for the extinction or obscuration is different. Since the X-rays are produced much closer to the central SMBH, they are also obscured by the gas and dust surrounding the AGN, apart from just the host galaxy. Hence, we do not expect the two quantities to be very strongly correlated.

Table 4.2: List of outputs from the broadband SED fitting, including the 2500 Å, 2 keV, and the bolometric luminosities in units of $\log(L/\text{erg s}^{-1})$. We also present the black hole masses (M_{BH}) of our sources as estimated by [Mejía-Restrepo et al. \(2022\)](#) in units of $\log(M_{\text{BH}}/M_{\odot})$. Finally, we list the estimated value of the optical-to-X-ray spectral indices (α_{ox} ; Section 4.3), the soft X-ray (κ_{2-10} ; Section 4.4) and 4400 Å optical bolometric corrections ($\kappa_{4400\text{Å}}$; Section 4.5), and the Eddington ratios (λ_{Edd} in log). The full version of this table is given in the appendix (Table 2).

BAT ID	Swift ID	$\log(L_{2500\text{Å}})$	$\log(L_{2\text{keV}})$	$\log(L_{\text{bol}})$	$\log(M_{\text{BH}}/M_{\odot})$	α_{ox}	$\kappa_{4400\text{Å}}$	κ_{2-10}	$\log(\lambda_{\text{Edd}})$
3	SWIFTJ0002.5+0323	43.07	42.35	43.68	6.70	-1.27	5.59	10.09	-1.20
6	SWIFTJ0006.2+2012	43.99	43.11	44.57	7.23	-1.34	5.86	22.26	-0.84
16	SWIFTJ0029.2+1319	45.49	44.32	46.16	8.49	-1.45	8.12	49.53	-0.50
19	SWIFTJ0034.5-7904	44.26	43.78	44.95	8.02	-1.19	6.56	10.70	-1.25
34	SWIFTJ0051.6+2928	43.96	42.49	44.44	7.62	-1.56	4.63	53.75	-1.36
36	SWIFTJ0051.9+1724	44.43	43.91	45.15	7.75	-1.20	7.38	8.66	-0.77
39	SWIFTJ0054.9+2524	45.36	44.28	46.08	8.46	-1.41	9.13	32.70	-0.56
43	SWIFTJ0059.4+3150	42.69	41.96	43.42	7.56	-1.28	8.96	14.26	-2.32
45	SWIFTJ0101.5-0308	43.90	42.75	44.38	8.13	-1.44	4.19	23.78	-1.93
51	SWIFTJ0105.7-1414	44.30	43.48	45.03	7.88	-1.32	8.37	16.79	-1.03

4.3 Optical-to-X-ray Spectral Index (α_{ox})

The relation between the optical/UV and X-ray emission of AGN has long been an area of extensive investigation to better understand the energy generation mechanism in AGN (e.g., [Tananbaum et al. 1979](#)). In this context, the optical-to-X-ray spectral index or α_{ox} is widely used to explore how the optical/UV disk emission couples with the X-ray coronal emission of AGN. It is mainly used to quantify the shape of the AGN SED and also used as a proxy for bolometric corrections as it is relatively easier to calculate from limited data. α_{ox} is defined as:

$$-0.3838 \times \log [L_{\nu}(2500 \text{ \AA}) / L_{\nu}(2 \text{ keV})] \quad (4.3)$$

where L_{ν} is the luminosity at the specific wavelength or energy in units of $\text{erg s}^{-1} \text{ Hz}^{-1}$ (e.g., [Strateva et al. 2005](#), [Steffen et al. 2006](#)). Over the years, many studies have been carried out focusing on how α_{ox} evolves with redshift, and the AGN luminosity. Although no strong dependence has been reported with redshift, studies have shown that α_{ox} has a significant anti-correlation with luminosity (e.g., [Strateva et al. 2005](#), [Steffen et al. 2006](#), [Lusso et al. 2010](#)). In this section, we check if we get similar results for our sample of hard-X-ray-selected local, unobscured AGN.

To calculate α_{ox} using Eq. (4.3), we estimate the monochromatic fluxes and luminosities at 2500 Å and 2 keV using the best-fit models obtained from the broadband SED fitting. We first have a look at the well-known correlation between the two luminosities ($L_{2500 \text{ \AA}}$ and $L_{2 \text{ keV}}$). Most studies have defined the correlation between the UV and X-ray luminosity as $L_{2 \text{ keV}} \propto L_{2500 \text{ \AA}}^{\beta}$, where β ranges between 0.7 to 0.8. In Figure 4.7, we plot the rest-frame monochromatic luminosity at 2 keV as a function of the rest-frame monochromatic luminosity at 2500 Å along with the best-fit relation we found:

$$\log (L_{2 \text{ keV}}) = (0.726 \pm 0.029) \times \log (L_{2500 \text{ \AA}}) + (4.544 \pm 0.821) \quad (4.4)$$

For comparison, we show the correlation obtained by [Lusso et al. \(2010\)](#). We also show how our best-fit relation is consistent with the ones reported by works like [Steffen et al. \(2006\)](#) and [Lusso & Risaliti \(2016\)](#) that used optically-selected AGN for their analysis.

Next, we show the distribution of α_{ox} for our AGN sample in Figure 4.8a. Our α_{ox} values range from -2.0 to -0.7 with a median at -1.28 (also see Table 4.2). We do not see any significant trend of α_{ox} with redshift (Figure 4.8b, Table 4.3) as confirmed by previous works (but see [Yuan et al. 1998](#) and [Bechtold et al. 2003](#)). In Figure 4.9a, we show α_{ox} as a function of the monochromatic 2500 Å luminosity and the best-fit relation:

$$\alpha_{\text{ox}} = (-0.105 \pm 0.011) \times \log (L_{2500 \text{ \AA}}) + (1.745 \pm 0.315) \quad (4.5)$$

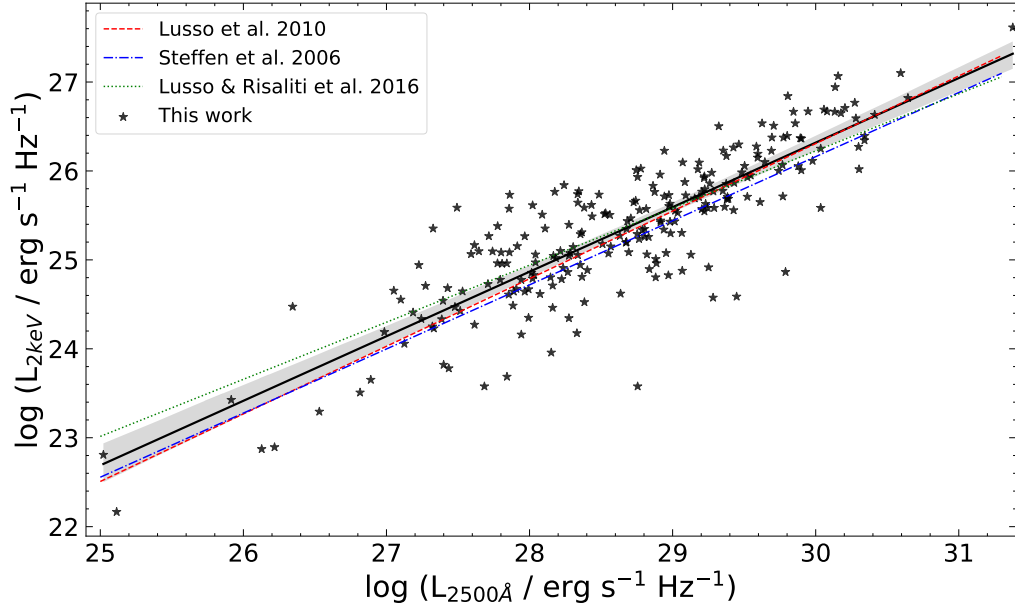


Figure 4.7: The monochromatic luminosity at 2500 Å vs the monochromatic luminosity at 2 keV. The best-fit relation from our work is shown as a black solid line, while the grey-shaded region shows the one-sigma confidence interval for the best fit. We also show the relation reported by [Steffen et al. \(2006\)](#), [Lusso et al. \(2010\)](#), and [Lusso & Risaliti \(2016\)](#) as a blue dash-dotted line, red dashed line, and green dotted line, respectively.

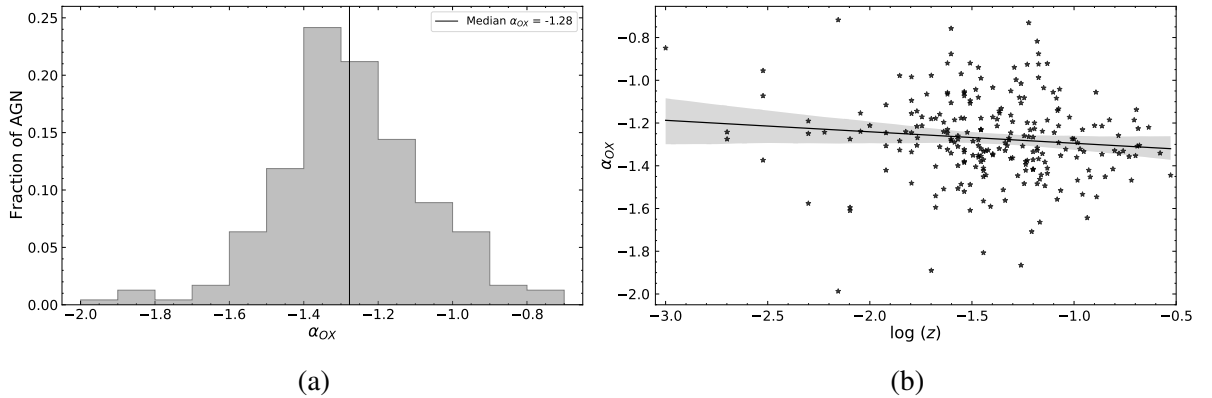


Figure 4.8: (a) A distribution plot of the optical-to-X-ray spectral index (α_{OX}) for our sample of hard-X-ray-selected nearby, unobscured AGN. (b) A plot showing α_{OX} as a function of redshift, but we do not find any significant correlation between the two parameters (black solid line shows the best-fit relation).

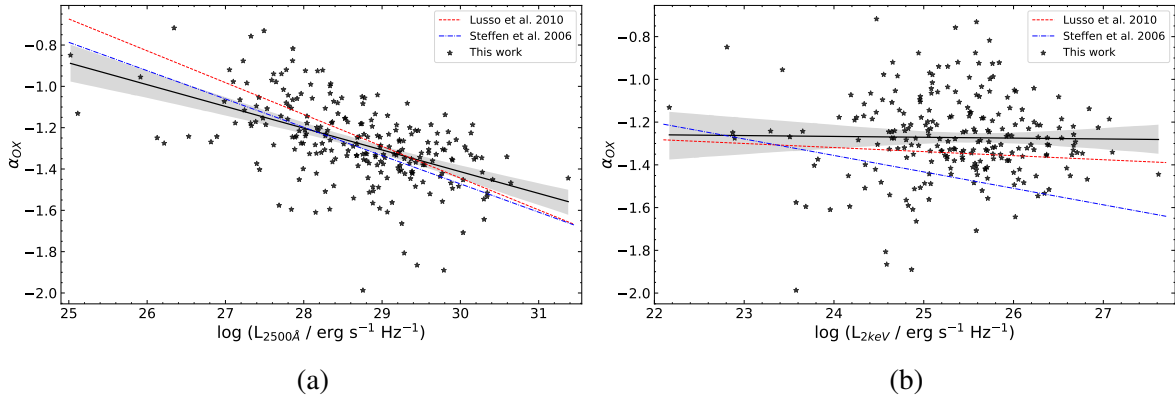


Figure 4.9: α_{ox} as a function of the rest-frame monochromatic luminosity at (a) 2500 Å (UV) and (b) 2 keV (X-ray). We find a tight anti-correlation between α_{ox} and $L_{2500\text{Å}}$ (shown as the black solid line in the left panel) but no significant relation with $L_{2\text{keV}}$ (shown as a black solid line in the right panel), as confirmed by previous works. For comparison, we also plot the best-fit relations from [Steffen et al. \(2006\)](#); blue dash-dotted line) and [Lusso et al. \(2010\)](#); red dashed line). The grey-shaded region shows the one-sigma confidence interval for our best-fit relation.

Compared to the slopes estimated by [Steffen et al. \(2006\)](#); -0.137) and [Lusso et al. \(2010\)](#); -0.154), we measure a shallower slope which could be attributed to the fact that we cover lower luminosity regimes. We have a few sources going down to $10^{25} \text{ erg s}^{-1} \text{ Hz}^{-1}$, which is 1 – 2 orders of magnitude below the luminosity range covered by the other two works. This effect is also prominent in Figure 4.9b, where we plot α_{ox} as a function of the 2 keV monochromatic luminosity. Although in agreement with other works, we also do not find any significant correlation between α_{ox} and $L_{2\text{keV}}$:

$$\alpha_{\text{ox}} = (-0.004 \pm 0.015) \times \log(L_{2\text{keV}}) + (-1.172 \pm 0.388) \quad (4.6)$$

However, even in this case, we go down to luminosity values of $10^{22} \text{ erg s}^{-1} \text{ Hz}^{-1}$, which is up to 2 orders magnitudes lower compared to [Steffen et al. \(2006\)](#) and [Lusso et al. \(2010\)](#). This could explain the higher value we obtain for the slope of our best-fit relation compared to those obtained by [Steffen et al. \(2006\)](#); -0.077) and [Lusso et al. \(2010\)](#); -0.019). It is also worth mentioning here that the optical/UV and X-ray observations used by [Steffen et al. \(2006\)](#) were not simultaneous, which could be a leading cause of the discrepancies between their results and ours.

Lastly, in this part, we specifically investigate some correlations presented by [Lusso et al. \(2010\)](#) for the first time. They found that for their sample α_{ox} showed a correlation with Eddington ratio (λ_{Edd}), unlike [Vasudevan et al. \(2009\)](#). Although they do comment that this could simply be due to better

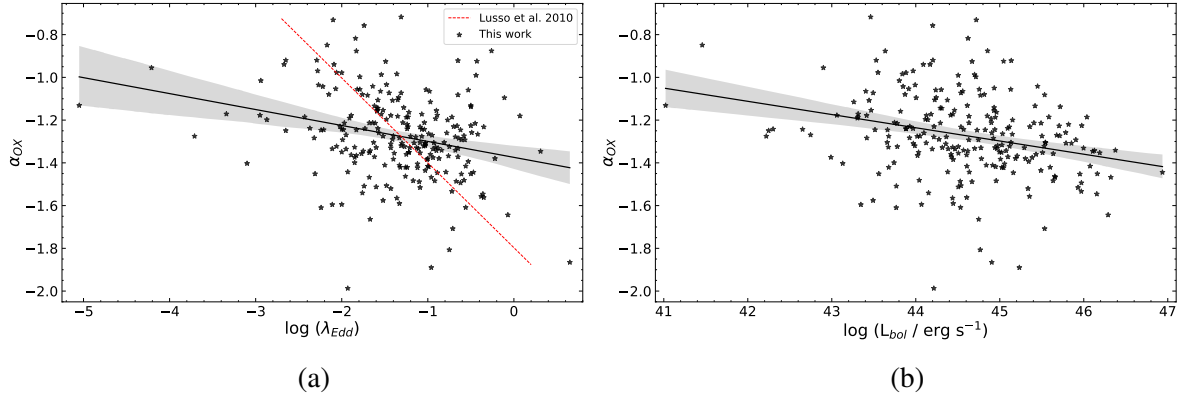


Figure 4.10: (a) α_{OX} as a function of Eddington ratio. We find a weak anti-correlation between the two parameters (black solid line), unlike the strong anti-correlation reported by Lusso et al. (2010; red dashed line). (b) α_{OX} as a function of bolometric luminosity. We find a significant anti-correlation between the two quantities (see Table 4.3). The black solid line shows the best-fit relation.

statistics since the dispersion was also very large. We show the plot of α_{OX} against λ_{Edd} for our sample in Figure 4.10a, where we find a weak negative correlation between the two quantities:

$$\alpha_{\text{OX}} = (-0.075 \pm 0.017) \times \log(\lambda_{\text{Edd}}) + (-1.374 \pm 0.026) \quad (4.7)$$

Unlike Lusso et al. (2010), the correlation we find is relatively weaker but significant (p -value = 2.42×10^{-5} ; see Table 4.3). However, compared to Vasudevan et al. (2009), we have much better statistics that allow us to constrain this possible anti-correlation better (but with a large scatter). Lusso et al. (2010) also reported a strong correlation between the 2 – 10 keV bolometric correction (κ_{2-10}) and α_{OX} , which in principle could be used to estimate bolometric corrections and in turn, bolometric luminosities from just α_{OX} values. In Figure 4.11, we show the same $\alpha_{\text{OX}} - \kappa_{2-10}$ relation obtained from our work, which agrees extremely well with the one that Lusso et al. (2010) found. The best-fit relation between α_{OX} and κ_{2-10} is represented by a second-degree polynomial as follows:

$$\log(\kappa_{2-10}) = (1.339 \pm 0.143) \times \alpha_{\text{OX}}^2 + (2.267 \pm 0.370) \times \alpha_{\text{OX}} + (1.911 \pm 0.239) \quad (4.8)$$

We also investigated if α_{OX} correlates with any other physical properties of AGN, like their black hole mass (M_{BH}) and bolometric luminosity (L_{bol}). We do not find any significant correlation of α_{OX} with M_{BH} . However, we do find an anti-correlation with L_{bol} (Figure 4.10b):

$$\alpha_{\text{OX}} = (-0.062 \pm 0.014) \times \log(L_{\text{bol}}) + (1.486 \pm 0.617) \quad (4.9)$$

Although the anti-correlation is significant (p -value = 4.253×10^{-3} ; see Table 4.3), the scatter is large.

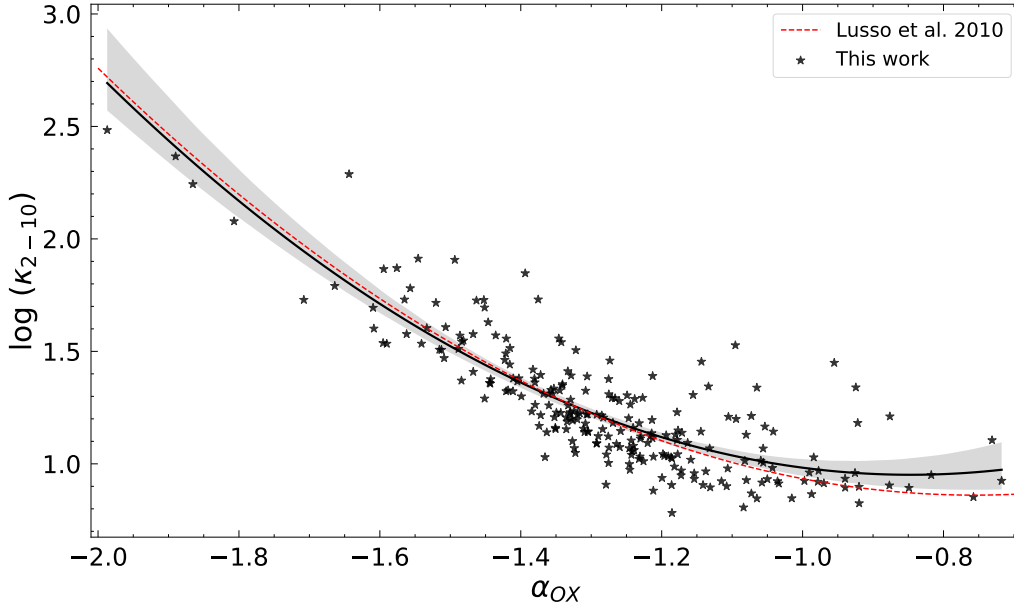


Figure 4.11: Plot of the 2 – 10 keV bolometric correction (κ_{2-10}) against α_{ox} . The black solid line shows the best-fit relation we obtained, which is in good agreement with the one estimated by Lusso et al. (2010; red dashed line).

Table 4.3: Correlation results for Figures 4.7, 4.8, 4.9, 4.10, and 4.11, described in Section 4.3.

Correlation	R-Value ^a	P-Value ^b
$L_{2\text{keV}} - L_{2500\text{\AA}}$	0.86	4.29×10^{-69}
$\alpha_{\text{ox}} - z$	-0.11	0.09
$\alpha_{\text{ox}} - L_{2500\text{\AA}}$	-0.53	1.46×10^{-18}
$\alpha_{\text{ox}} - L_{2\text{keV}}$	-0.02	0.80
$\alpha_{\text{ox}} - \lambda_{\text{Edd}}$	-0.27	2.42×10^{-5}
$\alpha_{\text{ox}} - L_{\text{bol}}$	-0.28	1.21×10^{-5}
$\alpha_{\text{ox}} - \kappa_{2-10}$	0.86	6.51×10^{-69}

^a The Pearson’s correlation coefficient.

^b The probability of the data set appearing if the null hypothesis is correct.

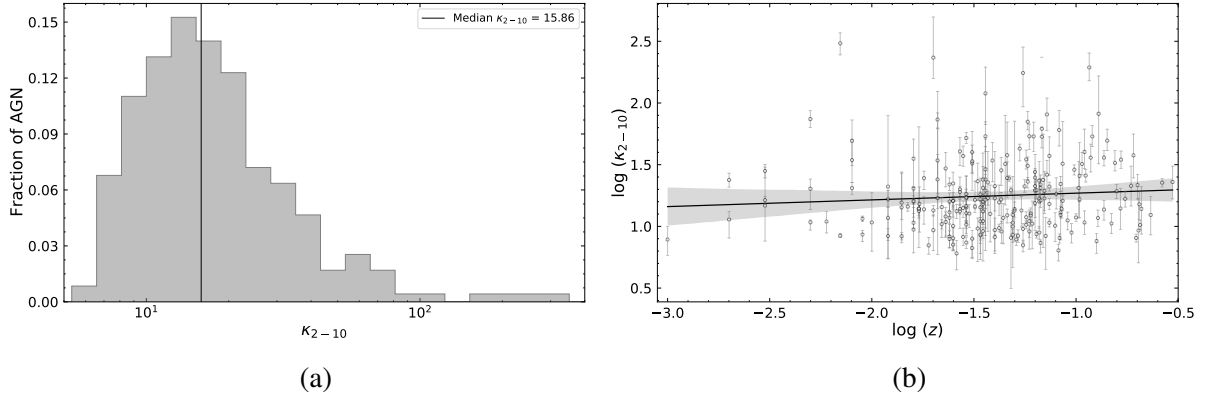


Figure 4.12: (a) A distribution plot of the soft X-ray bolometric correction (κ_{2-10}) for our sample of hard-X-ray-selected nearby, unobscured AGN. (b) A plot showing how κ_{2-10} evolves with redshift, and we do not find any significant dependence of κ_{2-10} on redshift (black solid line shows the best-fit relation).

4.4 X-Ray Bolometric Corrections

Following the broadband SED fitting, we use the X-ray flux from 0.1 to 500 keV and the optical/UV flux from 10^{-7} to 100 keV to estimate the total accretion luminosity or the bolometric luminosity for our unobscured AGN sample (see Table 4.2). All luminosities are calculated using redshift-independent distances listed in Table 3.2. We then calculate the bolometric corrections in different energy bands by taking a ratio of the bolometric luminosity and the luminosity in the specific energy range. For the X-rays, we report bolometric corrections in two energy bins, the 2 – 10 keV (soft X-rays; κ_{2-10}) and the 14 – 195 keV (hard X-rays; κ_{14-195}). In Figure 4.12a we show the distribution in the values of κ_{2-10} for our sample (also see Table 4.2). We do not find any dependence of κ_{2-10} on the redshift (Figure 4.12b). We report a median value of $\kappa_{2-10} = 15.9 \pm 0.2$, which can be used to roughly estimate the bolometric luminosity from the intrinsic 2 – 10 keV luminosity. However, this value changes with the bolometric luminosity and the Eddington ratio of the source, also confirmed by previous works (e.g., Vasudevan et al. 2009; Lusso et al. 2010; Duras et al. 2020). A detailed study of the main parameters regulating κ_{2-10} and how it correlates with various physical properties of AGN has been discussed in Chapter 5.

We report the values of the hard X-ray bolometric correction κ_{14-195} based on our analysis in Table 4.5. We obtain a median value of $\kappa_{14-195} = 6.0 \pm 0.1$, that can be used to convert the intrinsic 14 – 195 keV luminosity into bolometric luminosity. An anti-correlation is recovered between κ_{14-195} and L_{14-195} (Figure 4.13a), probably an obvious consequence of how we define bolometric corrections. We

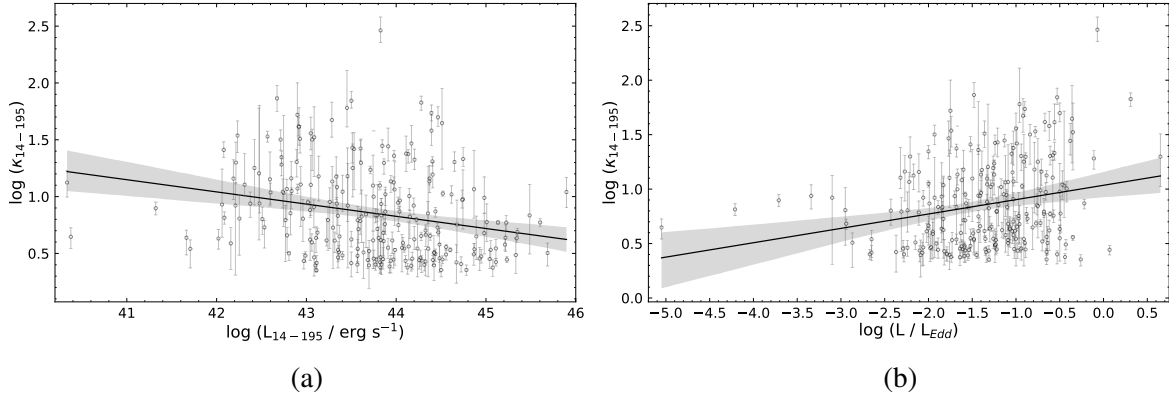


Figure 4.13: Plot of the 14 – 195 keV bolometric correction (κ_{14-195}) against (a) L_{14-195} and (b) λ_{Edd} . The black solid line shows the best-fit relation we obtained.

also checked if κ_{14-195} correlates with any other physical properties of AGN, such as L_{bol} , M_{BH} , and λ_{Edd} . κ_{14-195} shows a positive correlation with λ_{Edd} , as follows (see Figure 4.13b and Table 4.4):

$$\log(\kappa_{14-195}) = (0.132 \pm 0.035) \times \log(\lambda_{\text{Edd}}) + (1.035 \pm 0.053) \quad (4.10)$$

It also shows a weak correlation with L_{bol} . However, we did not find any significant dependence of κ_{14-195} on M_{BH} .

4.5 Optical/UV Bolometric Corrections

Based on the optical/UV wavelength regime of the broadband SED, we also calculated bolometric corrections in the optical and UV energy bands. In Table 4.5, we list the optical/UV bolometric corrections in the six *Swift*/UVOT filters (U, V, B, UVW1, UVW2, UVM2) and in the energy band 10^{-7} to 100 keV (κ_{uvo}). We also report the 4400 Å bolometric correction ($\kappa_{4400\text{\AA}}$; in the optical B-band) as done by many previous works (e.g., Hopkins et al. 2007; Lusso et al. 2012; Shen et al. 2020; Duras et al. 2020). First, we explore how these bolometric corrections evolve with redshift and if our analysis had any artifacts due to redshift. We do not find any relation with redshift for any of the optical/UV bolometric correction factors. The absence of any dependence on redshift confirms that our SED analysis is consistent throughout the redshift range of our sample. Even though the *Swift*/BAT AGN sample is flux-limited, due to which the farthest sources are typically very faint and we had to apply corrections to the GALFIT-estimated AGN fluxes (described in Section 3.5.3) for the high redshift sources, our results

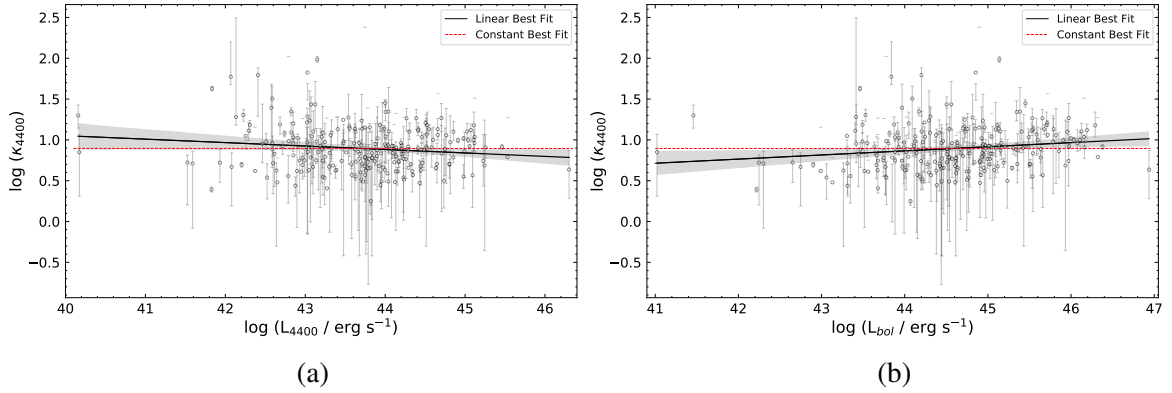


Figure 4.14: 4400 Å bolometric correction as a function of (a) the 4400 Å monochromatic luminosity and (b) the bolometric luminosity. We find a very weak correlation in both cases (Section 4.5, Table 4.4) shown as the black line. Hence, we show the best fit with a constant value as well (red dashed line). For both cases, we obtain a value of $\kappa_{4400\text{\AA}} = 7.9 \pm 0.3$.

are not influenced by it. This also verifies that the corrections that we calculated for GALFIT fluxes did not introduce any biases to our analysis.

Next, we check if any of the optical/UV bolometric correction factors show any dependence on L_λ , L_{bol} , M_{BH} or λ_{Edd} . Starting with $\kappa_{4400\text{\AA}}$, in Figure 4.14 we show it as a function of $L_{4400\text{\AA}}$ and L_{bol} . Similar to other studies (e.g., Lusso et al. 2012; Duras et al. 2020), we did not find any significant correlation of $\kappa_{4400\text{\AA}}$ with either the intrinsic monochromatic luminosity at 4400 Å or the bolometric luminosity (see Table 4.4). Hence, we recommend the constant value fit which gives a value of $\kappa_{4400\text{\AA}} = 7.9 \pm 0.3$. Additionally, $\kappa_{4400\text{\AA}}$ also does not show any dependence on M_{BH} or λ_{Edd} . We investigate the same trends for the bolometric corrections in the six *Swift*/UVOT filters (κ_{U} , κ_{V} , κ_{B} , κ_{W1} , κ_{W2} , and κ_{M2}) and in the energy bin 10^{-7} to 100 keV (κ_{uvo}). We summarize our results below:

- As expected, similar to $\kappa_{4400\text{\AA}}$, κ_{B} also does not show any correlation with L_{B} , L_{bol} , M_{BH} or λ_{Edd} .
- Bolometric corrections of the highest energy optical filter U and the lowest energy UV filter W1 show a strong negative correlation with the intrinsic luminosities in their respective bands. They do not show dependence on any other properties of the AGN.
- The V filter bolometric correction factor shows a weak positive correlation with the bolometric luminosity but with a large scatter. It does not relate to any other parameter.
- The bolometric corrections for the high energy UV filters: M2 and W2, and the one for the entire

Table 4.4: Correlation results for Figures 4.13a and 4.14, described in Sections 4.4 and 4.5.

Correlation	R-Value ^a	P-Value ^b
$\kappa_{14-195} - L_{14-195}$	-0.25	1.20×10^{-4}
$\kappa_{14-195} - L_{\text{bol}}$	0.19	3.79×10^{-3}
$\kappa_{14-195} - \lambda_{\text{edd}}$	0.24	1.91×10^{-4}
$\kappa_{4400 \text{ \AA}} - L_{4400 \text{ \AA}}$	-0.14	0.03
$\kappa_{4400 \text{ \AA}} - L_{\text{bol}}$	0.17	0.01

^a The Pearson’s correlation coefficient.

^b The probability of the data set appearing if the null hypothesis is correct.

optical/UV energy range show significant anti-correlations with the intrinsic luminosities in their respective energy bands, as well as with L_{bol} and λ_{Edd} . They do not show any dependence on M_{BH} .

Based on the individual trends mentioned above, we can draw some important conclusions. Firstly, we should pay attention to how the lowest energy bolometric corrections (κ_V and κ_B) do not correlate with any physical properties of the AGN. While the ones at the highest energies (κ_{M2} and κ_{W2}) show strong correlations with all our parameters of interest, except black hole mass. Studies have shown that compared to a disk model based on single-temperature blackbody emission, a multi-temperature accretion disk model better describes the optical/UV spectrum of AGN (e.g., Shields 1978; Malkan 1983). Assuming the disk to have a radial temperature profile [$T_{\text{eff}}(R) \propto R^{-p}$; $p = 0.75$ for the standard Shakura & Sunyaev disk], with smaller radii being at higher temperatures, we expect the highest energy photons to originate in the inner regions of the accretion disk, much closer to the central SMBH. Therefore, it is not surprising that the corresponding κ_{bol} correlate with quantities like λ_{Edd} (proxy of the accretion rate) and L_{bol} (total emission of the AGN). The observed negative correlations suggest that as the accretion luminosity of the AGN increases, so does the contribution from these high-energy disk photons. Hence, the decrease in the κ_{bol} for these energies is expected. Secondly, we consistently do not find a dependence on M_{BH} for any of the optical/UV (or X-ray) bolometric corrections. This indicates that the mass of the central SMBH does not control or influence the total radiation emitted by the accreting material at different wavelengths. The main driving factor here is in fact the Eddington ratio or the

Table 4.5: A list of the estimated values of the optical, UV, and hard X-ray bolometric corrections (described in Sections 4.4 and 4.5).

BAT ID	Swift ID	κ_U	κ_V	κ_B	κ_{W1}	κ_{W2}	κ_{M2}	κ_{uvo}	κ_{14-195}
3	SWIFTJ0002.5+0323	21.04	50.67	26.02	14.94	10.68	16.98	7.15	1.74
6	SWIFTJ0006.2+2012	21.09	54.23	27.10	14.00	8.98	15.22	31.73	1.37
16	SWIFTJ0029.2+1319	28.12	76.37	37.31	17.68	10.40	18.57	49.89	1.12
19	SWIFTJ0034.5-7904	24.84	59.30	30.56	17.82	12.93	20.36	17.20	2.16
34	SWIFTJ0051.6+2928	16.75	42.70	21.41	11.22	7.30	12.27	32.27	1.11
36	SWIFTJ0051.9+1724	27.61	67.06	34.31	19.44	13.70	21.96	4.84	2.34
39	SWIFTJ0054.9+2524	31.51	85.93	41.90	19.72	11.53	20.66	21.44	1.16
43	SWIFTJ0059.4+3150	31.22	83.93	41.17	19.83	11.85	20.95	12.71	1.39
45	SWIFTJ0101.5-0308	15.78	38.02	19.52	11.21	8.01	12.74	8.32	1.41
51	SWIFTJ0105.7-1414	30.01	77.48	38.66	19.85	12.65	21.52	5.03	1.79

accretion rate. This emphasizes the importance and requirement of detailed studies of AGN physics in different regimes of λ_{Edd} . We report the median values for all the optical/UV bolometric corrections, with uncertainties, in Table 4.6.

4.6 Summary and Conclusion

In this chapter, we have discussed some of the main findings of our large, multi-wavelength study of optical-to-X-ray SEDs of hard-X-ray-selected, unobscured, nearby AGN. Based on the broadband SED fitting, we calculated some important quantities used to describe AGN properties, such as the total accretion luminosity or bolometric luminosity of AGN, intrinsic optical, UV, and X-ray luminosities, optical-to-X-ray spectral indices, multi-wavelength bolometric corrections, and Eddington ratios. In the following, we summarize our main results:

1. The X-ray luminosity and the bolometric luminosity are the primary factors influencing the shape

Table 4.6: Median values of the optical/UV bolometric corrections with respective uncertainties (Section 4.5).

	Median Value	Errors
κ_U	29.3	0.2
κ_V	65.4	0.5
κ_B	35.5	0.2
κ_{W1}	21.4	0.3
κ_{W2}	15.0	0.9
κ_{M2}	24.0	0.6
κ_{uvo}	2.0	0.02

of AGN SEDs (Figure 4.2). Since the X-ray luminosity scales with the bolometric luminosity, it alters the optical/UV part of the SED as well. On the other hand, between higher and lower values of bolometric luminosity, we do not see any corresponding effect on the shape of the X-ray spectrum, suggesting that there is no direct correlation between the total AGN luminosity and the X-ray contribution to this luminosity.

2. We obtained a strong correlation of the maximum disk temperature with the bolometric luminosity and the Eddington ratio, which can be explained by the standard, multi-blackbody disk model (used to fit the optical/UV SED), as hotter disks are expected to emit more radiation at higher energies.
3. We confirmed previous results on the strong correlation between the monochromatic luminosity at 2 keV and 2500 Å, with $L_{2\text{keV}} \propto L_{2500\text{Å}}^\beta$, where $\beta = 0.073 \pm 0.03$ (Figure 4.7).
4. We calculated the optical-to-X-ray spectral index for our AGN sample and obtained a median $\alpha_{\text{ox}} = -1.28$. We did not find any dependence of α_{ox} on redshift or $L_{2\text{keV}}$ (Figures 4.8b and 4.9b), in agreement with previous works. We also reconfirmed the strong anti-correlation between α_{ox} and $L_{2500\text{Å}}$ (Figure 4.9a). We also investigated if α_{ox} correlates with L_{bol} , M_{BH} or λ_{Edd} , and found weak anti-correlations with both L_{bol} and λ_{Edd} (Figure 4.10).

5. We computed the 2 – 10 keV soft X-ray bolometric corrections for our unobscured AGN sample and found a median $\kappa_{2-10} = 15.9 \pm 0.2$. This value can be used to convert the 2 – 10 keV luminosity into bolometric luminosity. However, we would like to add that κ_{2-10} depends strongly on L_{bol} and λ_{Edd} . Therefore, one should be cautious when using the median value for a sample with a large range in luminosity. More findings related to κ_{2-10} have been presented in Chapter 5.
6. We presented κ_{2-10} as a second-order function of α_{ox} , a relation that can be used to calculate L_{bol} from just optical/UV data, in the absence of high-quality X-ray data (Eq. 4.8, Figure 4.11). This relation is in good agreement with those found in the literature.
7. We also calculated the 14 – 195 keV hard-X-ray bolometric corrections for our sample and reported a median $\kappa_{14-195} = 6.0 \pm 0.1$ for conversions from intrinsic L_{14-195} to L_{bol} . We found a strong correlation between κ_{14-195} and λ_{Edd} (Eq. 4.10, Figure 4.13b), which must be considered when using the median value to estimate L_{bol} .
8. With respect to the optical/UV energies, we listed eight different bolometric corrections: the 4400 Å optical bolometric correction, one for each of the six *Swift*/UVOT filters, and one in the 10^{-7} to 100 keV energy range. None of these κ_{bol} show any dependence on redshift, hence negating any biases due to redshift in our SED fitting analysis. We explored if and how these optical/UV bolometric corrections correlate with different physical properties of AGN. Our results showed that the highest energy bolometric corrections (κ_{M2} and κ_{W2}) showed significant negative correlations with both L_{bol} and λ_{Edd} , while the lowest energy ones (κ_V , κ_B , and $\kappa_{4400\text{\AA}}$) show no dependence on any of the AGN accretion properties. Assuming the standard disk model with a multi-temperature blackbody emission, such that the innermost regions are at the highest temperatures and consequently emit higher energy photons, we expect them to have stronger correlations with the accretion properties of the AGN and the disk. Furthermore, the lack of any kind of dependence of κ_{bol} on black hole mass implies that it is not, in any way, a controlling factor for the radiation emitted via accretion at different energies and wavelengths.

Chapter 5

2 – 10 keV X-Ray Bolometric Correction for Unobscured AGN

In this chapter, we present our main findings for the 2 – 10 keV bolometric correction (κ_{2-10}), following the broadband SED analysis of 236 hard-X-ray-selected, nearby, unobscured *Swift*/BAT AGN (discussed in Chapter 3). We have listed the values of κ_{2-10} for all the sources in our sample in Section 4.4, Table 4.2. We also showed the distribution we obtain in κ_{2-10} values for our sample with a median $\kappa_{2-10} \sim 16.0$ (Figure 4.12a). We did not see any dependence of κ_{2-10} on redshift (Figure 4.12b), confirming that our analysis does not include any caveats due to redshift, even if the *Swift*/BAT AGN sample is flux-limited in nature and we applied corrections to the AGN fluxes estimated by GALFIT for the highest redshift sources (details in Section 3.5.3). In the following sections, we investigate how κ_{2-10} correlates with the other physical properties of AGN. The structure of this chapter is as follows. In Section 5.1, we show κ_{2-10} as a function of the 2 – 10 keV X-ray luminosity (Section 5.1.1) and the total bolometric luminosity (Section 5.1.2) and state some key results of our analysis. In Section 5.2, we discuss the dependence of κ_{2-10} on the Eddington ratio (Section 5.2.1) and the black hole mass (Section 5.2.2). And finally, in Section 5.3, we summarize our main results and their implications.

5.1 The Correlation of κ_{2-10} with Luminosity

We calculated the 2 – 10 keV bolometric correction for our sample of unobscured AGN by dividing the total bolometric luminosity (L_{bol}) with the intrinsic X-ray luminosity in the 2 – 10 keV energy band (L_{2-10}). In this section, we explore how κ_{2-10} correlates with both L_{2-10} and L_{bol} .

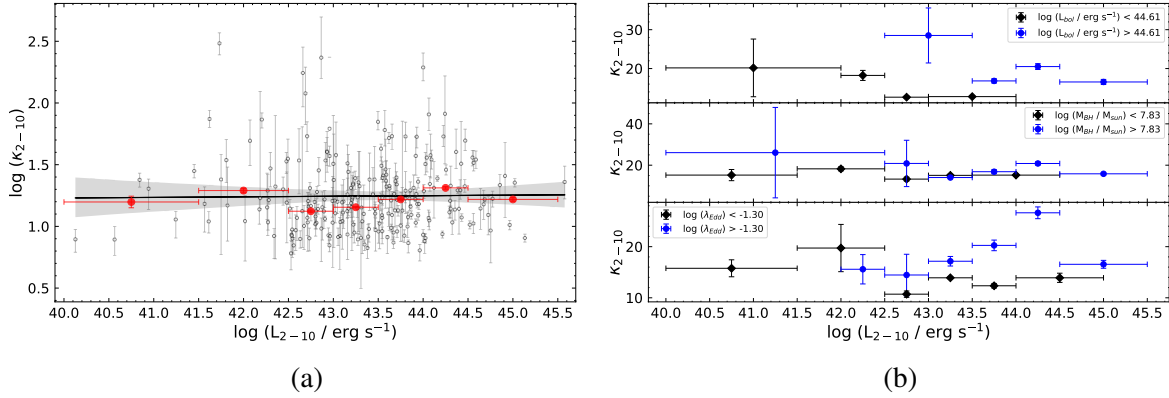


Figure 5.1: (a) κ_{2-10} as a function of L_{2-10} . The data points from this work are shown in the background as grey circles. The red points show the binned data and the black line is the best linear fit relation. (b) κ_{2-10} as a function of L_{2-10} in bins of (from top to bottom) L_{bol} , M_{BH} , and λ_{Edd} . The black points represent the lower-value bin and the blue points correspond to the higher-value bin in each panel.

5.1.1 κ_{2-10} vs L_{2-10}

We first plot κ_{2-10} as a function of the L_{2-10} (Figure 5.1a). The data points from this work are shown as grey circles with error bars in the background. The binned data in red shows the median value of κ_{2-10} in each luminosity bin (with a minimum of six sources) and the best-fit relation is shown in black. We do not find any dependence of κ_{2-10} on L_{2-10} (see Table 5.1), even though it is calculated from L_{2-10} and mathematically one would expect an inverse correlation between the two quantities. We also show κ_{2-10} against L_{2-10} in different bins of L_{bol} , M_{BH} , and λ_{Edd} in Figure 5.1b. These bins are created based on the median value of each parameter for our sample. Even after dividing the sample into these bins, we do not obtain any significant relation of κ_{2-10} with L_{2-10} . The lack of any correlation implies that an increase in the X-ray emission does not translate to a lower value of κ_{2-10} and vice-versa. This indicates that the bolometric luminosity scales with L_{2-10} and as L_{2-10} increases, so does the bolometric luminosity, in turn keeping κ_{2-10} constant. If we fit a constant to the data shown in Figure 5.1a, we obtain a value of $\kappa_{2-10} = 17.6 \pm 0.8$.

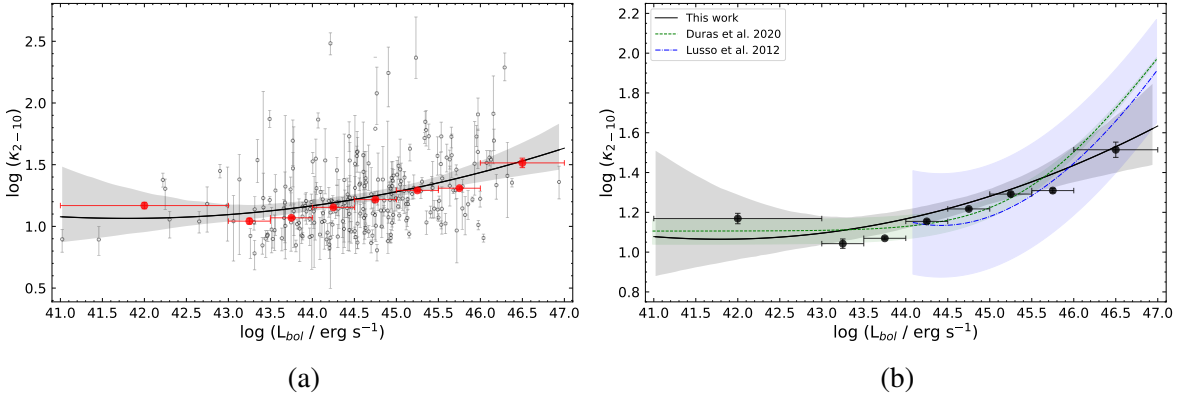


Figure 5.2: (a) κ_{2-10} as a function of L_{bol} . The data points from this work are shown in the background as grey circles. The red points show the binned data and the black line is the best-fit relation. (b) Comparison plot of the relation between κ_{2-10} and L_{bol} from various works. The black points show the binned data from this work along with the best-fit relation as the black solid line. The green dashed line is the best-fit relation from [Duras et al. \(2020\)](#) and the blue dash-dotted line shows the result of [Lusso et al. \(2012\)](#).

5.1.2 κ_{2-10} vs L_{bol}

Next, we study the dependence of κ_{2-10} on the bolometric luminosity. As shown in Figure 5.2a, κ_{2-10} increases with L_{bol} following a 2nd-order polynomial equation, given as:

$$\log(\kappa_{2-10}) = (0.021 \pm 0.013) \times (\log[L_{\text{bol}}])^2 + (-1.755 \pm 1.179) \times \log(L_{\text{bol}}) + (37.746 \pm 26.151) \quad (5.1)$$

The grey points in the background are the data set from this work. The red points show the median of κ_{2-10} in each of the bolometric luminosity bins, with a minimum of six sources per bin. We also show the best fit to the data as the black solid line. This strong correlation between κ_{2-10} and L_{bol} (see Table 5.1) and the absence of any relation between κ_{2-10} and L_{2-10} , further confirms that a higher bolometric luminosity does not necessarily imply more contribution from the X-rays. On the contrary, sources with large accretion luminosities could still have lower X-ray emission in the 2 – 10 keV energy band, resulting in an overall increase in κ_{2-10} . This also puts into perspective the anti-correlation between UV bolometric corrections and L_{bol} (discussed in Section 4.5). From both results combined, we can speculate that as the bolometric luminosity increase, the contribution from the UV to L_{bol} also increases, whereas the X-rays do not show similar behavior. Many previous works have reported the strong correlation between κ_{2-10} and L_{bol} (e.g. [Lusso et al. 2012](#); [Duras et al. 2020](#)) and we plot them,

for comparison, against the fit we obtained, in Figure 5.2b. The relation from Duras et al. (2020) is shown as the green dashed line and it agrees well with our best-fit relation up to $L_{\text{bol}} \sim 10^{46} \text{erg s}^{-1}$. The slight deviation above those values could be a consequence of the small number of sources in our sample in that last bin. We also over-plot the relation obtained by Lusso et al. (2012; as the blue dash-dotted line), and it is consistent (within the uncertainties shown as the blue shaded region) with our results within the luminosity window that contains most of the sources from our sample.

Thanks to the large sample size, we could also examine if the correlation between κ_{2-10} and L_{bol} sustains if we limit the sample based on other properties like X-ray luminosity, black hole mass, and Eddington ratio. In Figure 5.3a, we show κ_{2-10} against L_{bol} for sources with lower and higher values of L_{2-10} , M_{BH} , and λ_{Edd} , divided so based on their median values for the entire sample. We clearly recover the positive correlation when we divide the sample based on L_{2-10} and M_{BH} . However, a noteworthy observation here is that the strong dependence of κ_{2-10} on L_{bol} completely disappears for the $\log(\lambda_{\text{Edd}}) < -1.3$ bin, while it still exists for the higher value bin. To investigate this further, and determine the exact value of λ_{Edd} where the correlation ceases to exist, we divide the sample into three bins of Eddington ratio. As shown in Figure 5.3b, the black diamonds correspond to the $\lambda_{\text{Edd}} < 0.01$ bin, the blue circles represent the sources with $0.01 < \lambda_{\text{Edd}} < 0.1$, and the red squares are for the $\lambda_{\text{Edd}} > 0.1$ bin. For each L_{bol} bin, we make sure that it contains a minimum of six sources and then plot the median value of κ_{2-10} in that bin. The resultant figure clearly shows an increment in κ_{2-10} with L_{bol} for the largest as well as the intermediate value bin. We obtain an increase from almost 10 to 35 in κ_{2-10} for the largest λ_{Edd} bin. In the case of λ_{Edd} ranging between 0.01 and 0.1, κ_{2-10} changes from around 12 up to 22 for a four-order of magnitude increase in the bolometric luminosity. However, for the lowest Eddington ratio bin (below 0.01), the value of κ_{2-10} oscillates between 10 to 15, not showing any significant positive trend with L_{bol} .

Based on the above results, we can draw some important conclusions. Firstly, the lack of any correlation between κ_{2-10} and L_{bol} , specifically below $\lambda = 0.01$, suggests a prominent change in AGN accretion around this value. It is reasonable to claim that this change is not solely related to the X-ray emission of AGN since we do not see any change in the κ_{2-10} vs L_{2-10} plot for sources with low values of the Eddington ratio. Moreover, numerous studies on accretion disk models have argued that the standard disk model (e.g., Shakura & Sunyaev 1973; Novikov & Thorne 1973) seems to fail for sources with sub-Eddington accretion rates (e.g., Koratkar & Blaes 1999; Narayan 2005; Yuan & Narayan 2014). In such sources with very low accretion rates, radiatively inefficient, advection-dominated accretion flow (ADAF; Ichimaru 1977) models have been proposed to describe AGN accretion. Many authors have

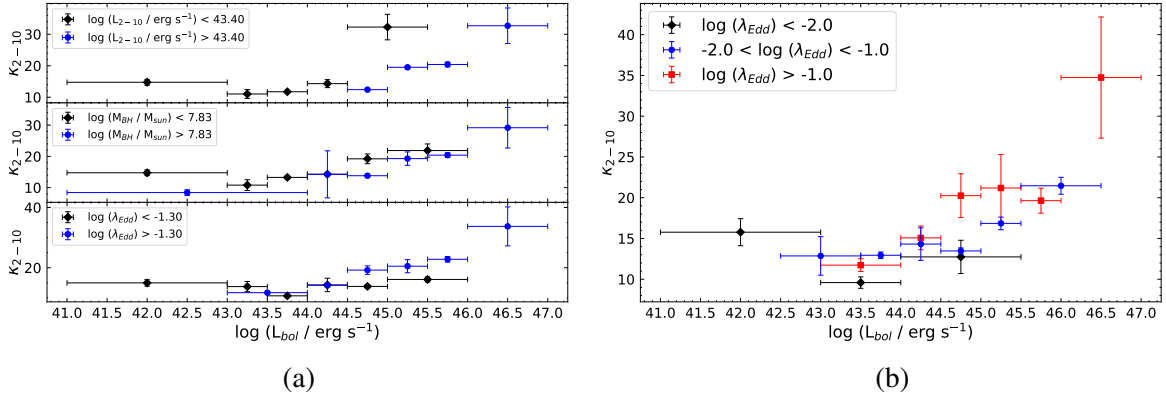


Figure 5.3: (a) κ_{2-10} as a function of L_{bol} in bins of (from top to bottom) L_{2-10} , M_{BH} , and λ_{Edd} . The black points represent the lower-value bin and the blue points correspond to the higher-value bin in each panel. (b) κ_{2-10} as a function of L_{bol} in 3 bins of λ_{Edd} . The lowest bin of $\lambda_{\text{Edd}} < 0.01$ is shown as black diamonds, the $0.01 < \lambda_{\text{Edd}} < 0.1$ bin is shown as blue circles, and the highest $\lambda_{\text{Edd}} > 0.1$ bin is shown by red squares.

employed ADAF models to explain the observed emission properties of X-ray binaries (e.g., [Esin et al. 1997](#)), low-luminosity AGN (e.g., [Fabian & Rees 1995](#)), quiescent black holes (e.g., [Reynolds et al. 1996](#) for the black hole in M87; [Di Matteo & Fabian 1997](#) for the black hole in M60 (NGC 4649); [Narayan & Yi 1995](#) for underfed black holes) and also Sagittarius A* (Sgr A*), the SMBH at our Galactic center (e.g., [Narayan et al. 1995](#)). However, on the contrary, studies have also shown that ADAFs alone cannot account for all the emission in these sources, such as their compact radio emission (e.g., [Herrnstein et al. 1998](#) for NGC 4258; [Bietenholz et al. 2000](#) for M81; [Falcke & Markoff 2000](#) for Sgr A*). Instead, for these sources dominated by jet emission, jet models are believed to be more suitable (e.g., [Falcke et al. 2000](#); [Markoff et al. 2001](#)). But at the same time, ADAFs are needed to explain the decrease in disk emission in these sources. To resolve this dilemma, some attempts have also been made to combine the ADAF and jet models to explain the emission in low-luminosity AGN (e.g., [Ulvestad & Ho 2001](#); [Yuan et al. 2002](#) for Sgr A*; [Anderson et al. 2004](#)). The primary difference between ADAFs and the standard thin disk arises due to the low density of electrons in ADAFs that causes the heat generated due to turbulence to be advected towards the central SMBH along with the accretion flow, instead of being radiated outwards. This causes the disk to have higher temperatures and also a geometrically thick structure compared to the standard geometrically thin accretion disk (see [Beloborodov 1999](#) for a review). The optical/UV spectrum of these sources is not expected to show the

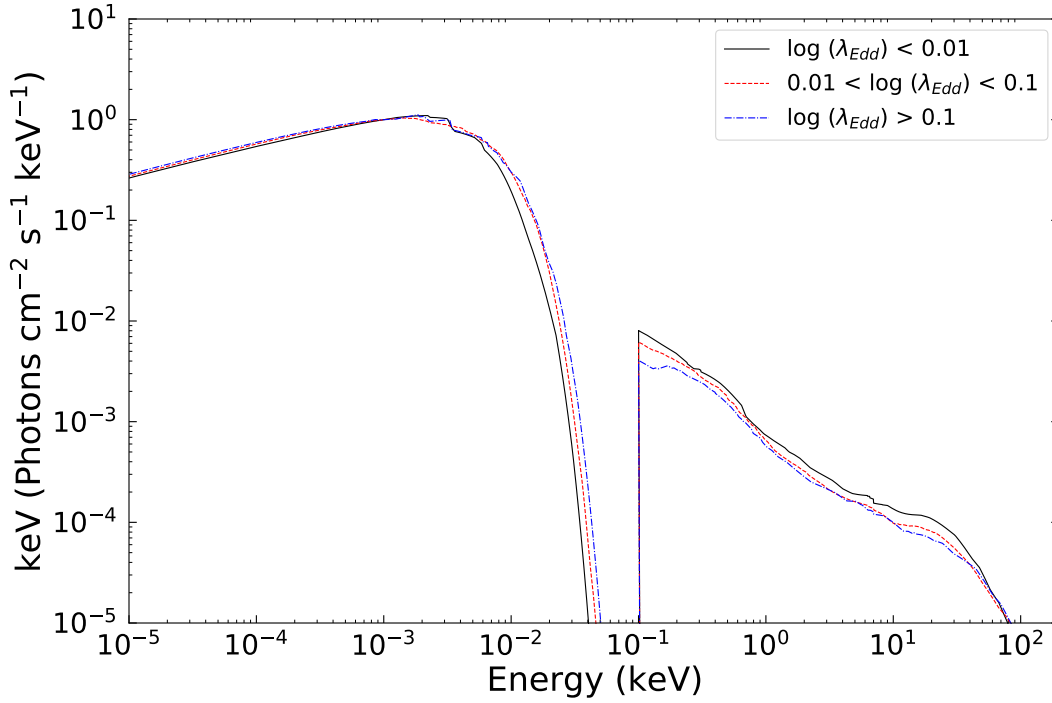


Figure 5.4: The absorption corrected median SED (normalized at 1 eV) in three bins of Eddington ratio. The black solid curve shows the lowest value bin, the red dashed curve is the intermediate value bin and the blue dash-dotted curve is the highest value bin.

obvious UV bump (BBB), which could be a possible explanation of why the correlation between κ_{2-10} and L_{bol} disappears for these sources. We individually inspected the optical spectra of the 36 sources in the $\lambda_{\text{Edd}} < 0.01$ bin and most of the sources did not show a blue continuum. In Figure 5.4, we show the median SEDs (normalized at 1 eV) for the three Eddington ratio bins, where the difference in the SED shape for the lowest bin is apparent. The black curve, representing the sources with $\lambda_{\text{Edd}} < 0.01$, has a relatively lower flux in the optical/UV, accompanied by a systematic increase in the X-ray emission, while the red ($0.01 < \lambda_{\text{Edd}} < 0.1$) and the blue ($\lambda_{\text{Edd}} > 0.1$) SEDs do not show significant variations with respect to each other.

Additionally, the sources with low accretion rates are also expected to have low luminosities due to inefficient accretion to radiation conversion. Therefore, it is evident that the lack of any trend between κ_{2-10} and L_{bol} for $\lambda_{\text{Edd}} < 0.01$, indicates a change in the accretion physics of these sources relative to those with higher Eddington ratios. We would also like to mention here that the reason no previous studies on AGN SEDs or bolometric corrections have been able to make such claims, is either due to

a lack of sources and poor statistics below $\lambda_{\text{Edd}} = 0.01$ or because of different science goals. Most of the research done in this field has not explicitly investigated the relationship between κ_{2-10} and L_{bol} for different values of the Eddington ratio. But our representative sample of hard-X-ray-selected unobscured nearby AGN, spanning over five dex in λ_{Edd} and six dex in L_{bol} , is ideal to do such a study.

The disappearance of the trend between κ_{2-10} and L_{bol} for lower values of λ_{Edd} also suggests that the Eddington ratio is the primary factor regulating the bolometric corrections, if not the only one, since the bolometric luminosity also plays a role, particularly for high Eddington ratio sources. Numerous studies have shown that the 2 – 10 keV X-ray bolometric correction correlates with both, the bolometric luminosity and the Eddington ratio (e.g., Vasudevan & Fabian 2007; Vasudevan & Fabian 2009; Vasudevan et al. 2009; Lusso et al. 2012; Duras et al. 2020). However, taking into consideration that these two quantities are interlinked ($\lambda_{\text{Edd}} = L_{\text{bol}}/L_{\text{Edd}}$), it has been almost impossible to disentangle their effects on the bolometric corrections. A possible way to do so is to study the two correlations separately by adjusting the third parameter. But one needs to have enough sources over the entire range covered by both quantities to carry out such an analysis. Our sample size of ~ 240 sources, spanning multiple decades in both L_{bol} and λ_{Edd} , allows us to perform a detailed study of the two trends. We discuss the dependence of κ_{2-10} on λ_{Edd} in detail in the next section (Section 5.2.1). However, based on the results so far, the direct effect of the Eddington ratio on κ_{2-10} is very prominent.

Table 5.1: Correlation results for Figures 5.1a, 5.2a, 5.5a, and 5.6a, described in Sections 5.1 and 5.2.

Correlation	R-Value ^a	P-Value ^b
$\kappa_{2-10} - L_{2-10}$	0.01	0.84
$\kappa_{2-10} - L_{\text{bol}}$	0.34	2.52×10^{-7}
$\kappa_{2-10} - \lambda_{\text{edd}}$	0.34	3.28×10^{-7}
$\kappa_{2-10} - M_{\text{BH}}$	0.11	0.07

^a The Pearson’s correlation coefficient.

^b The probability of the data set appearing if the null hypothesis is correct.

5.2 The Correlation of κ_{2-10} with Eddington Ratio and Black Hole Mass

In this section, we look at the possible impact of changing the Eddington ratio and the black hole mass on the 2 – 10 keV X-ray bolometric correction. We have virial black hole mass estimates for 235/236 sources in our sample, provided by [Mejía-Restrepo et al. \(2022\)](#). The Eddington ratios for these sources have been calculated by dividing the bolometric luminosity with the Eddington luminosity (L_{Edd}), calculated using the black hole masses as follows:

$$L_{\text{Edd}} = 1.5 \times 10^{38} \times \frac{M_{\text{BH}}}{M_{\odot}} \text{ erg s}^{-1} \quad (5.2)$$

5.2.1 κ_{2-10} vs λ_{Edd}

We show κ_{2-10} as a function of the Eddington ratio in Figure 5.5a and obtain a significant positive correlation (see Table 5.1). The data from this work is shown as grey points in the background, while the red points are the median values of κ_{2-10} in each of the λ_{Edd} bins. The bins are created such that we have a minimum of six sources per bin. The black line shows the best-fit relation to the data in the form of a second-degree polynomial equation, given by:

$$\log(\kappa_{2-10}) = (0.054 \pm 0.034) \times (\log[\lambda_{\text{Edd}}])^2 + (0.309 \pm 0.095) \times \log(\lambda_{\text{Edd}}) + (1.538 \pm 0.063) \quad (5.3)$$

The above relation is computed by fitting only the sources with $\lambda_{\text{Edd}} > 0.001$. For visual purposes, in Figure 5.5a, we show the fit obtained after fitting all the sources. But the visible increase in κ_{2-10} as λ_{Edd} decreases is merely an effect of the low statistics in the last bin spanning two dex of Eddington ratio. To exclude the influence of these five sources on the overall correlation, we report the above equation that describes the actual dependence of κ_{2-10} on λ_{Edd} without being affected by bins with low source count. For comparison, we show the best-fit relations obtained by [Lusso et al.\(2012\)](#); blue dash-dotted line) and [Duras et al.\(2020\)](#); green dashed line) along with our results (black solid line) in Figure 5.5b. Our correlation is relatively less steep compared to the one reported by [Duras et al. \(2020\)](#) due to the additional sources in the last 0.5 dex bin not covered by [Duras et al. \(2020\)](#). Otherwise, the two correlations are consistent for sources with λ_{Edd} between 0.01 and 1.

Similar to the procedure followed in Section 5.1, we study the dependence of κ_{2-10} on λ_{Edd} in different bins of L_{2-10} , L_{bol} , and M_{BH} . The bins are created to distinguish the sources with values greater than and less than the median value of each of the parameters. As shown in Figure 5.5c, dividing our

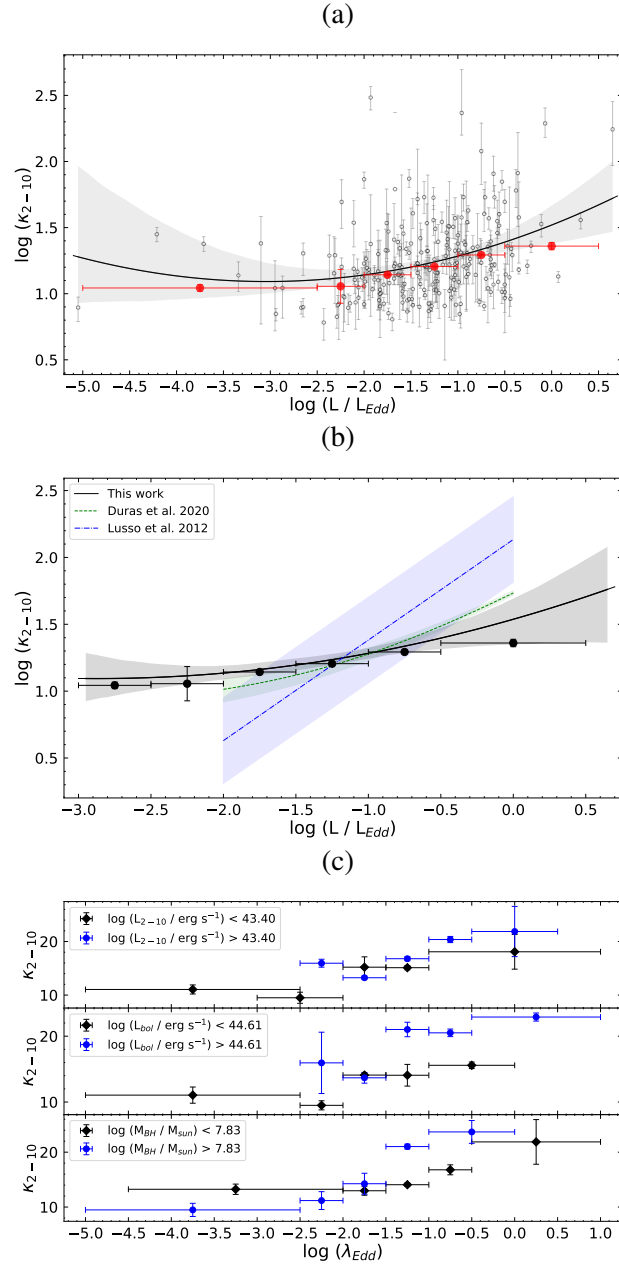


Figure 5.5: (a) κ_{2-10} as a function of the λ_{Edd} . The data points from this work are shown in the background as grey circles. The red points show the binned data and the black line is our best linear fit relation. (b) Comparison plot of the relation between κ_{2-10} and λ_{Edd} from various works. The black points show the binned data from this work along with the best-fit relation as the black solid line. The green dashed line is the best-fit relation from [Duras et al. \(2020\)](#) and the blue dash-dotted line shows the result of [Lusso et al. \(2012\)](#). (c) κ_{2-10} as a function of the λ_{Edd} in bins of (from top to bottom) L_{2-10} , L_{bol} , and M_{BH} . The black points represent the lower-value bin and the blue points correspond to the higher-value bin in each panel.

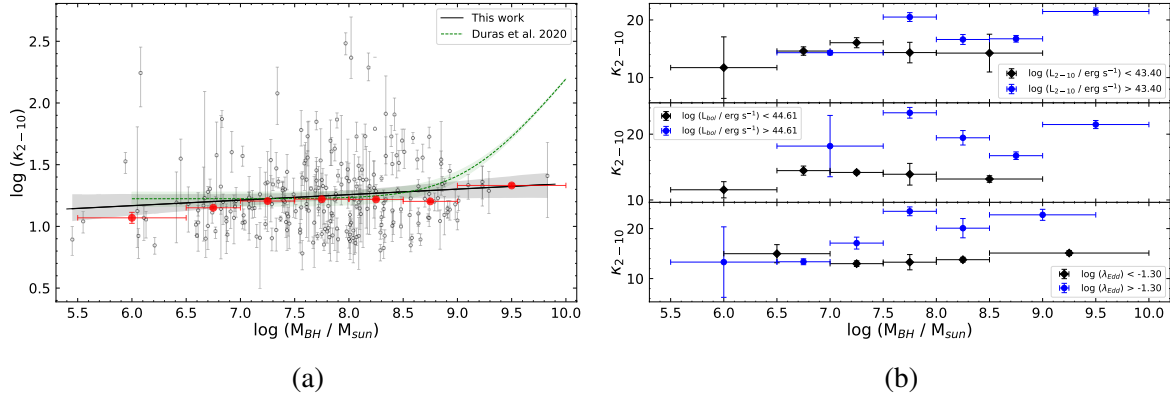


Figure 5.6: (a) κ_{2-10} as a function of the M_{BH} . The data points from this work are shown in the background as grey circles. The red points show the binned data and the black line is our best linear fit relation. For comparison, we also show the best-fit relation from [Duras et al. \(2020\)](#) as a green dashed line. (b) κ_{2-10} as a function of the M_{BH} in bins of (from top to bottom) L_{2-10} , L_{bol} , and λ_{Edd} . The black points represent the lower-value bin and the blue points correspond to the higher-value bin in each panel.

sample based on luminosity and black hole mass does not affect the positive trend between κ_{2-10} and λ_{Edd} . This further confirms our second conclusion drawn from the results presented in Section 5.1, that the Eddington ratio (or the accretion rate) of an AGN is indeed the key parameter regulating its X-ray bolometric correction. And hence, it is also the dominant property influencing the accretion physics and emission of AGN. Although it has already been claimed by many previous theoretical studies on AGN accretion models (e.g., [Koratkar & Blaes 1999](#); [Yuan & Narayan 2014](#)), we can empirically conclude based on our analysis that the Eddington ratio, and in turn the accretion rate determines how the surrounding material is accreted onto the central SMBH. It governs the type of accretion flow occurring in an AGN and dictates the resultant fraction of radiation emitted in the optical/UV and the X-rays.

5.2.2 κ_{2-10} vs M_{BH}

Lastly, we look at how κ_{2-10} changes with the mass of the SMBH located at the center of the AGN. Figure 5.6a shows κ_{2-10} against black hole mass for the 235/236 sources in our sample with black hole mass estimates ([Mejía-Restrepo et al. 2022](#)). We do not obtain any significant correlation between the two properties (see Table 5.1). [Duras et al. \(2020\)](#) reported an increase in κ_{2-10} with black hole mass, which we show for comparison in Figure 5.6a. However, it is apparent that the correlation they found is

mainly due to the last M_{BH} bin ($M_{\text{BH}} = 10^{9-10} M_{\odot}$). Since we only have a few sources in that bin, we cannot make any similar claims. Over the remaining parameter space, our results agree. Unlike [Duras et al. \(2020\)](#), [Vasudevan et al. \(2009\)](#) found an inverse dependence of κ_{2-10} on M_{BH} . But considering their small sample size of 26 sources, the anti-correlation could just be the result of low statistics. We further divide our sample into two bins each of L_{2-10} , L_{bol} , and λ_{Edd} and revisit the evolution of κ_{2-10} with M_{BH} . However, as visible in Figure 5.6b, we still do not see any significant trends between κ_{2-10} and M_{BH} . Therefore, we can conclusively state that the black hole mass does not play a very crucial role in governing the accretion and emission properties of AGN.

5.3 Summary and Conclusion

In this chapter, we have examined in detail how the 2 – 10 keV X-ray bolometric correction correlates with the physical properties of AGN. Our sample of 236 hard-X-ray-selected nearby unobscured AGN, spanning 5-6 decades in luminosity, Eddington ratio, and black hole mass, allows us to further evaluate how these correlations evolve with respect to modifications in other parameters used to describe AGN physics. We summarize some of the key findings of our study here:

1. We do not record any dependence of the X-ray bolometric correction on the intrinsic X-ray luminosity for our sample of unobscured AGN (Figure 5.1). Therefore, we can claim that the total accretion luminosity of an AGN scales with its X-ray luminosity, hence keeping κ_{2-10} constant. In fact, a constant value of κ_{2-10} over five dex of L_{2-10} (as well as M_{BH} and λ_{Edd}), is a very robust indicator of the linear relation between the X-ray emission and the total emission of an AGN. Based on a constant value fit of the κ_{2-10} vs L_{2-10} distribution, we obtain a value of $\kappa_{2-10} = 17.6 \pm 0.8$, independent of L_{2-10} .
2. κ_{2-10} shows a strong positive correlation with the bolometric AGN luminosity (Equation 5.1, Figure 5.2). This correlation persists for the entire range of black hole masses in our sample, extending from $\sim 10^5 - 10^{10} M_{\odot}$. The consistent increase in κ_{2-10} with L_{bol} suggests that larger bolometric luminosities do not necessarily translate into a higher fraction of X-ray emission. And hence, the optical/UV disk emission contributes a significant proportion to the total radiation emitted by an AGN. However, if we divide AGN based on their Eddington ratio or accretion rates, the above is applicable only for sources with $\lambda_{\text{Edd}} > 0.01$.

3. Our analysis shows that for sources with $\lambda_{\text{Edd}} < 0.01$, the correlation between κ_{2-10} and L_{bol} completely disappears (Figure 5.3b), suggesting a change in accretion physics of AGN around this value. Many theoretical studies on accretion disk models have argued that the accretion rate primarily determines the type of accretion flow in AGN. It has been proposed that for sources with low, sub-Eddington accretion rates, the standard geometrically thin optically thick disk model fails and instead a radiatively inefficient, advection-dominated accretion flow model is more suitable to describe their overall emission properties. Although providing an accurate description of the type of accretion flow in these low Eddington ratio sources is beyond the scope of this work, we can still draw some important conclusions regarding their observed emission properties from this empirical study. Firstly, the median SEDs clearly show a decrease in the optical/UV disk emission for these sources, accompanied by a systematic increase in their X-ray emission. Secondly, the optical spectrum of these sources does not show a blue continuum corresponding to the disk emission. And lastly, the lack of any correlation between κ_{2-10} and L_{bol} for these sources further implies a decrease in the otherwise dominant optical/UV emission. Collectively, all these observations point towards a prominent change in the accretion mechanism of AGN around $\lambda_{\text{Edd}} = 0.01$.
4. We found a significant dependence of κ_{2-10} on the Eddington ratio for our source sample (Equation 5.3, Figure 5.5). Also supported by literature, the 2 – 10 keV bolometric correction consistently increases with the Eddington ratio. This trend exists throughout the range of black hole masses and luminosities spanned by our sample.
5. Based on the above two findings, we infer that the Eddington ratio (or the accretion rate) is indeed the main regulator of the 2 – 10 keV bolometric correction. Consequentially, the accretion rate of an AGN is the principal parameter that governs its accretion and emission properties.
6. We do not obtain any correlation between κ_{2-10} and M_{BH} for our unobscured AGN sample. Further division of the sample on the basis of luminosity and Eddington ratio confirms the absence of any correlation between these two properties. As a result, we propose that the mass of the central black hole is not a primary factor controlling AGN emission and accretion mechanisms.

Chapter 6

Concluding Remarks

In this dissertation, we have explored the multi-wavelength emission properties of local AGN, with the aim to gain fundamental insights into their accretion physics and to develop a better understanding of their inner regions, which are otherwise difficult to probe. We exploited the hard X-ray emission of AGN to detect them in an unbiased way and to obtain an almost complete sample of nearby AGN. The high penetration power and low host galaxy contamination of the hard X-rays allow them to identify both unobscured as well as obscured AGN. In this respect, the *Swift*/BAT catalog of hard-X-ray-selected sources provides a representative sample of AGN suitable to investigate their accretion properties. Additionally, simultaneous follow-up observations of *Swift*/BAT AGN in the optical/UV (by *Swift*/UVOT) and the X-rays (by *Swift*/XRT) present the perfect opportunity to study AGN at multiple wavelengths, without encountering issues related to dissimilar variability timescales of the optical/UV and X-ray emission. We would also like to highlight here the important role played by the BAT AGN Spectroscopic Survey (BASS) in contributing to the plethora of data available for studying *Swift*/BAT AGN across the entire electromagnetic spectrum. Thanks to their dedicated optical campaign and additional observations of *Swift*/BAT AGN with various other instruments and missions (HST, *NuSTAR*, *XMM-Newton*, ESO-VLT, to name a few), we have reliable spectroscopic measurements of quantities like, emission line ratios, velocity dispersions, black hole masses, etc. for these sources. As a result, we were able to perform one of the largest multi-wavelength studies of AGN in the local Universe, which allowed us to make some important predictions about the structure of AGN and their accretion and emission processes. In Section 6.1, we summarize some of the main results of this thesis, and in Section 6.2, we discuss the future prospects of this work.

6.1 Key Findings

We carried out a comprehensive study of hard-X-ray-selected obscured and unobscured nearby AGN ($z < 0.1$) and performed an in-depth analysis of their radiation spanning five orders of magnitudes in energy (a few eVs to a few 100 keVs). Here, we list the key outcomes of our research:

1. Obscured AGN show signatures of Thomson-scattered X-ray radiation in their broadband X-ray spectrum. We used a sample of 386 obscured AGN to investigate how the scattered X-ray radiation correlates with other physical properties of AGN such as its column density, luminosity, black hole mass, etc (Chapter 2). We found a strong inverse correlation between the fraction of scattered radiation (f_{scatt}) and the line-of-sight column density (N_{H}). We confirmed that this correlation is not due to any degeneracy between the two parameters and exists over the entire range of luminosities and black hole masses covered by our sample. We proposed that this anti-correlation either could be a consequence of the inclination angle dependence of the Thomson cross-section or it indicates that more obscured sources host a torus with a higher covering factor, which in turn reduces the amount of scattered radiation that can escape out. We also obtained a positive correlation of the scattered fraction with the [O III] $\lambda 5007$ to X-ray luminosity ratio, which allowed us to predict the possible region of origin of the scattered radiation to be somewhere in the narrow-line region.
2. In the second part of the thesis (Chapters 3 to 5), we presented an optical-to-X-ray SED study of unobscured AGN. We compiled high-quality, simultaneous, photometric (in optical/UV) and spectroscopic (in X-rays) data of 236 AGN to construct and model their broadband SEDs after removing any contamination due to the host galaxy and including the effects of dust reddening. Based on this work, we reported AGN bolometric correction factors in the optical, UV, and X-ray bands (Tables 4.2 and 4.5). We have provided median values of κ_{bol} in all the six *Swift*/UVOT filters, at 4400 Å, in the 10^{-7} to 100 keV optical/UV energy band and the 2 – 10 keV and 14 – 195 keV X-ray energy bands. These values can be used by the AGN community to convert luminosities in various bands to bolometric luminosity when multi-wavelength data is unavailable. We have also calculated the optical-to-X-ray spectral index (α_{ox}) for our sources and reported a relation between α_{ox} and κ_{2-10} (Eq. 4.8), also useful to estimate the AGN bolometric luminosity.
3. We have presented an elaborate discussion on the 2 – 10 keV X-ray bolometric corrections in Chapter 5. We checked for possible correlations between κ_{2-10} and other properties useful to

quantify AGN accretion and emission, including their X-ray and bolometric luminosity, and Eddington ratio (a proxy for accretion rate), all computed from our SED fitting analysis. We found that κ_{2-10} remains constant with the intrinsic 2 – 10 keV X-ray luminosity. We also verified that other AGN properties like the mass of the central SMBH or the accretion rate do not change the constant behavior of κ_{2-10} with L_{2-10} . This could imply that the total bolometric luminosity of AGN scales with its X-ray luminosity and an increase in L_{2-10} directly translates into an increase in L_{bol} , thus keeping their ratio constant at $\kappa_{2-10} \sim 17.6$.

4. Next, we obtained a positive correlation between κ_{2-10} and L_{bol} , consistent with previous works. This correlation persists for all black hole masses spanned by our sample and suggests a dominant contribution from the optical/UV to the total accretion luminosity of AGN. However, the strong dependence of κ_{2-10} on L_{bol} vanishes for sources with low Eddington ratios ($\lambda_{\text{Edd}} < 0.01$), indicating an obvious change in the accretion mechanism of these sources, relative to higher accretion rate AGN. Studies on accretion disk models have long stated that accretion rate influences the type of accretion flow in AGN. Many attempts were made in the late 1990s and early 2000s to describe the accretion flow in AGN with low accretion rates (using ADAFs or jet models). However, for the first time, we have reached this conclusion empirically and can argue that a definite distinction exists in the accretion physics of AGN below and above Eddington ratios ~ 0.01 . The primary reason we could make such a claim was because our sample spans five decades of Eddington ratios, enabling us to compare the properties of low and high Eddington ratio sources.
5. As an extension of the previous result, we have also proposed that the Eddington ratio of an AGN is the property that mainly regulates its emission and accretion. Over the years, many researchers have shown the dependence of κ_{2-10} on both L_{bol} and λ_{Edd} . However, considering that the two quantities are interlinked, it was almost impossible to disentangle their effects on κ_{2-10} . Through the work presented in this thesis, we were able to separately examine the correlation of κ_{2-10} with both these parameters. And therefore, we could conclusively show that it is indeed the Eddington ratio, and in turn, the accretion rate of an AGN that determines its accretion process and emission properties.

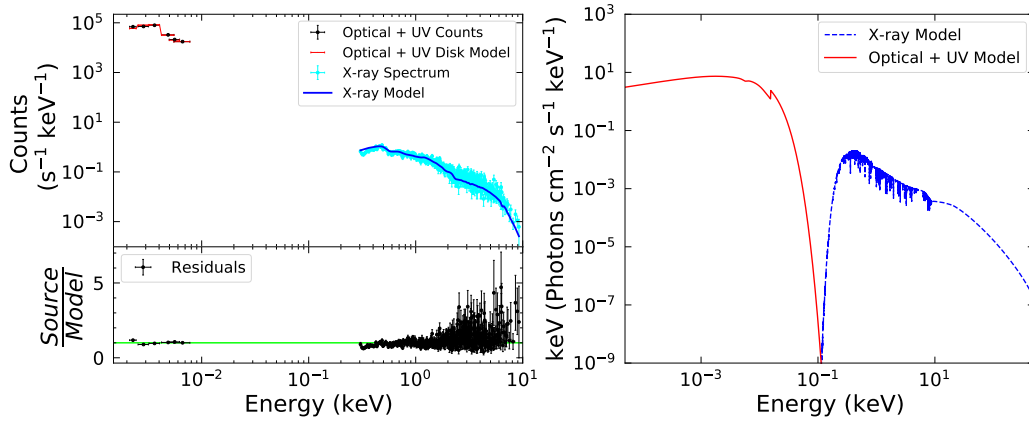
6.2 Future Prospects

With this work, we have made an attempt to contribute to the AGN community a preliminary study of AGN SEDs and their multi-wavelength emission, that allowed us to make some important predictions about AGN accretion. By utilizing, what we believe is, the best available sample of hard-X-ray-selected AGN in the local Universe, we were able to provide bolometric correction factors for unobscured AGN, that could be useful to fellow astronomers for their research. However, our analysis can still be improved in many ways. Firstly, we acknowledge that much better and more sophisticated AGN models exist, that can be used to fit our broadband SEDs, especially in the optical/UV. Considering that we used a multi-temperature blackbody model to fit all the sources in our sample, is in contradiction with our main result that clearly shows that low Eddington ratio AGN exhibit a different type of accretion flow compared to those with higher accretion rates. In the future, we hope a similar analysis can be done but with disk models that include ADAFs or slim disk assumptions based on the accretion rate of the source.

Secondly, as a direct outcome of our study, it would be interesting to individually analyze the 36 low Eddington ratio sources in our sample. Thanks to *Swift*, we have multiple observations of these sources over a span of at least 10 years, along with observations from other missions, such as *XMM-Newton*. A detailed analysis of the evolution of the SEDs of these sources could provide useful insights into their accretion properties and if and how they changed over time. Lastly, although in our study we made extra efforts to remove any contribution from the host galaxy to our AGN SEDs, it would be useful if one could focus on characterizing the host galaxy properties of these AGN by including its contribution to the SEDs and fitting them accordingly. It is well established that the growth of the SMBHs at the center of massive galaxies is connected to the evolution of the host galaxy. However, considering the small size of the AGN and its sphere of influence relative to the vast galaxies it resides in, this co-evolution is still not properly understood. Hence, an exhaustive study of AGN + galaxy SEDs would be extremely useful for the community to improve our knowledge about how the AGN affects its host galaxy and vice-versa.

Appendix A: Broadband SED Fits

SWIFTJ0006.2+2012



SWIFTJ0029.2+1319

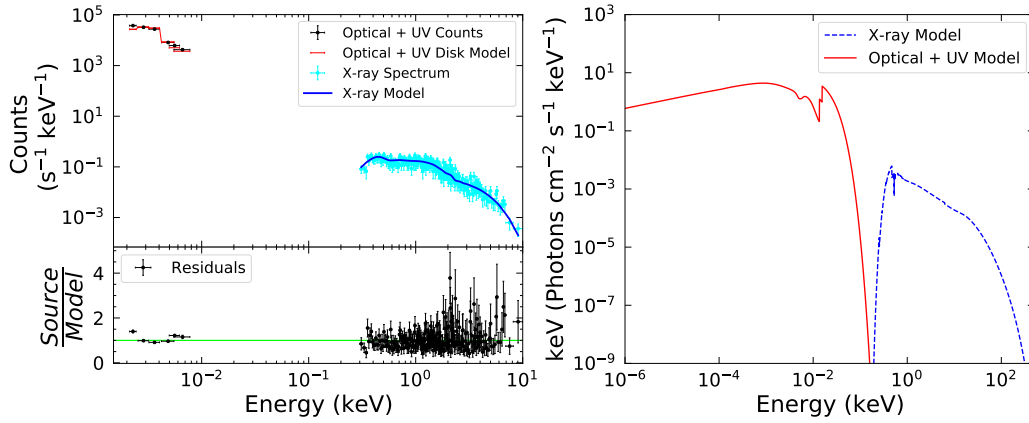
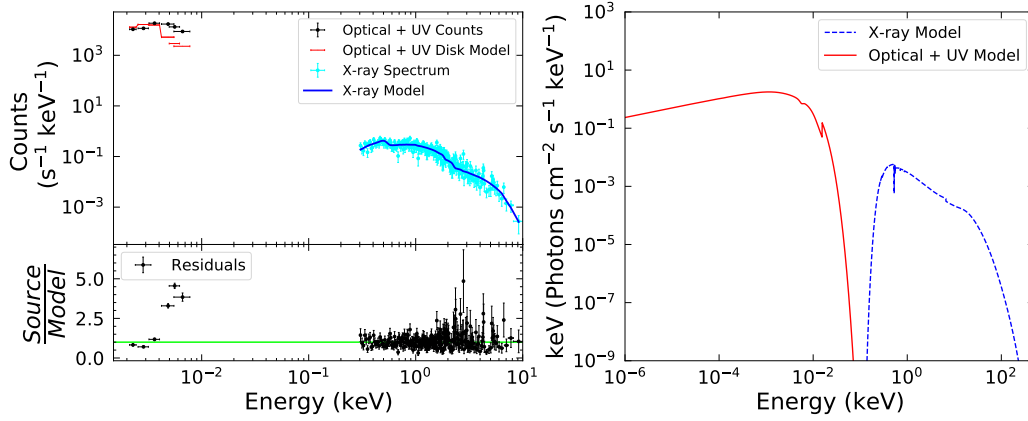
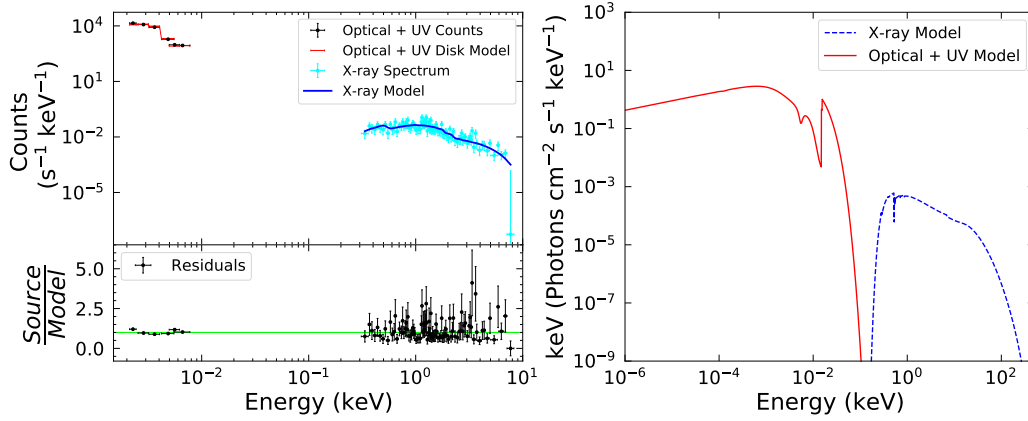


Figure 1: Continued from Figure 3.13, showing broadband SED fits, best-fit SED models, and fit residuals for all the sources in our sample.

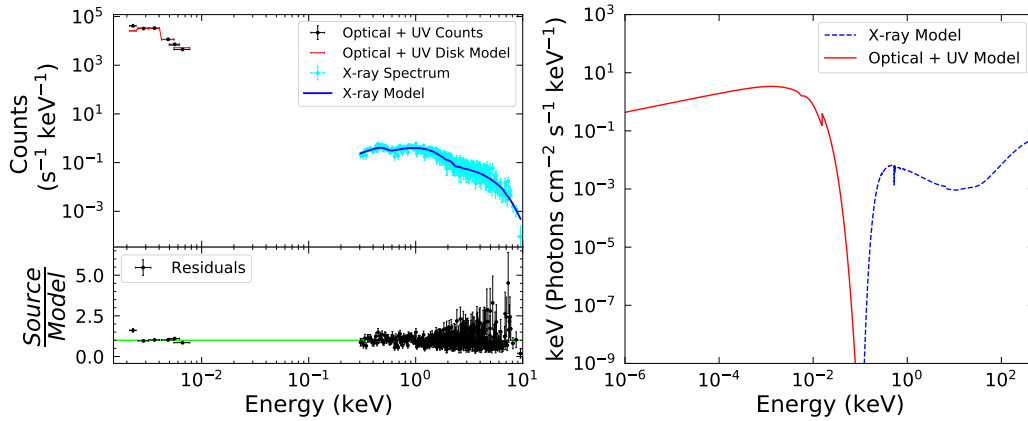
SWIFTJ0034.5-7904



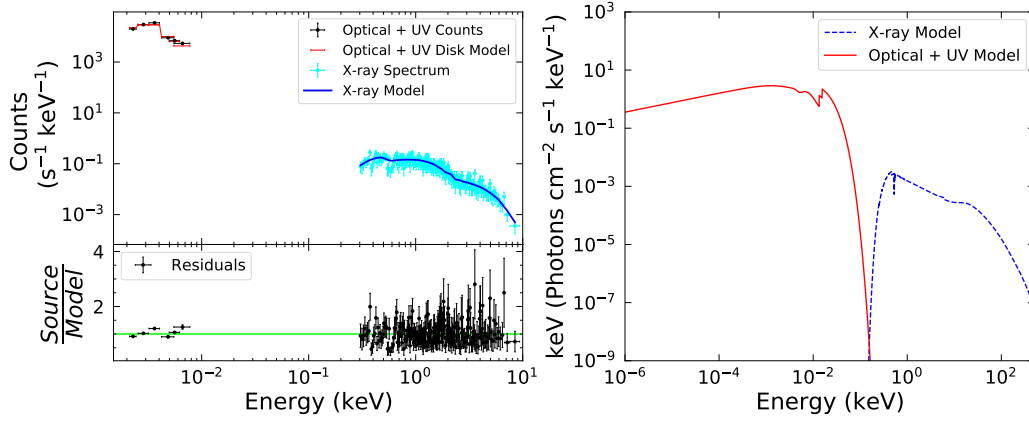
SWIFTJ0051.6+2928



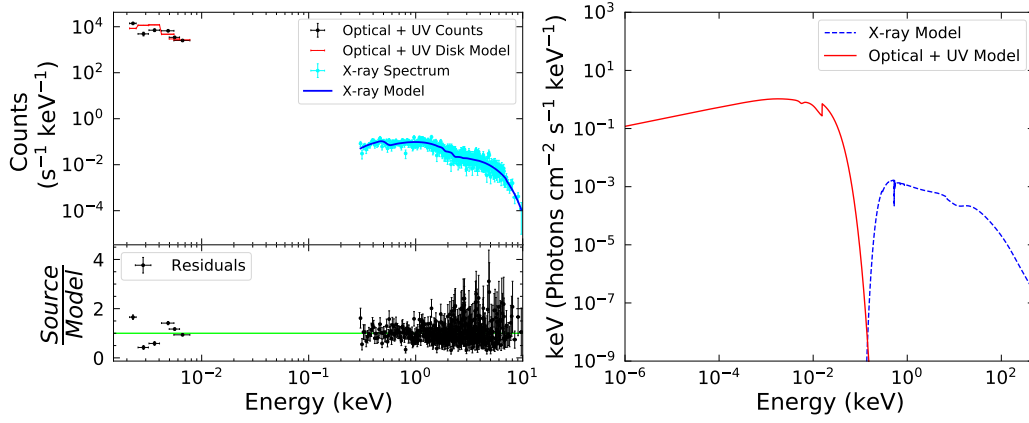
SWIFTJ0051.9+1724



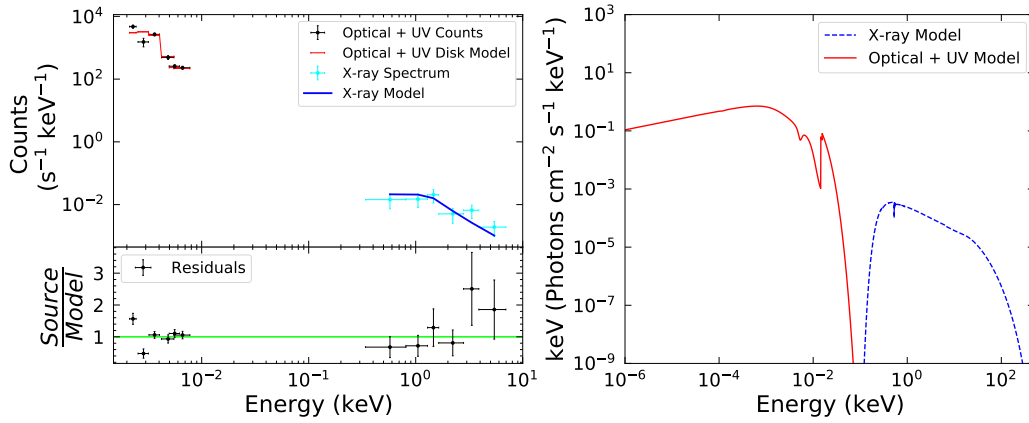
SWIFTJ0054.9+2524



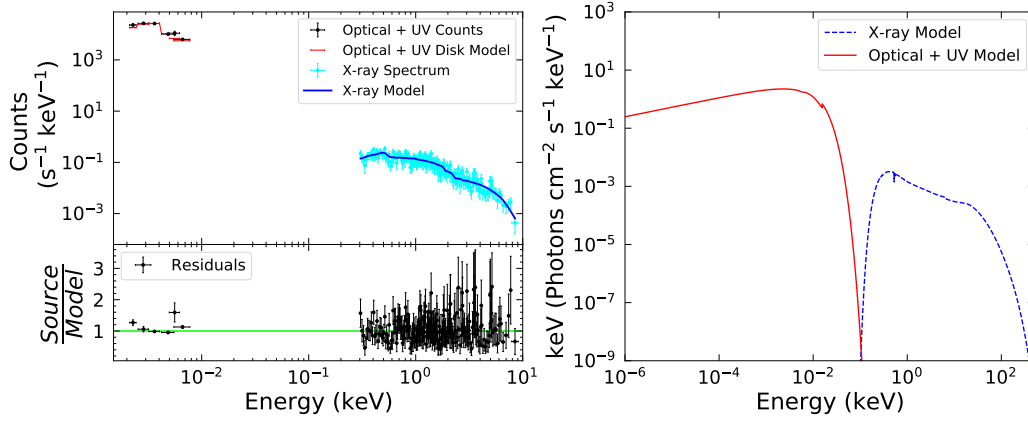
SWIFTJ0059.4+3150



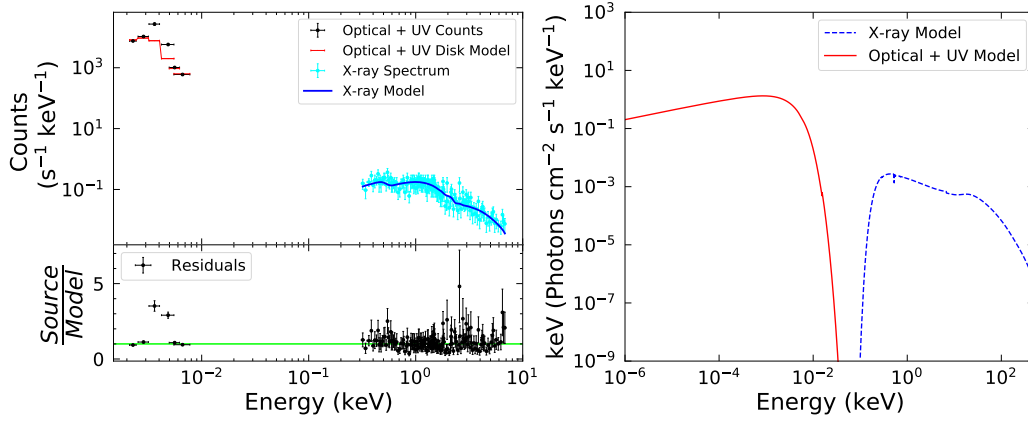
SWIFTJ0101.5-0308



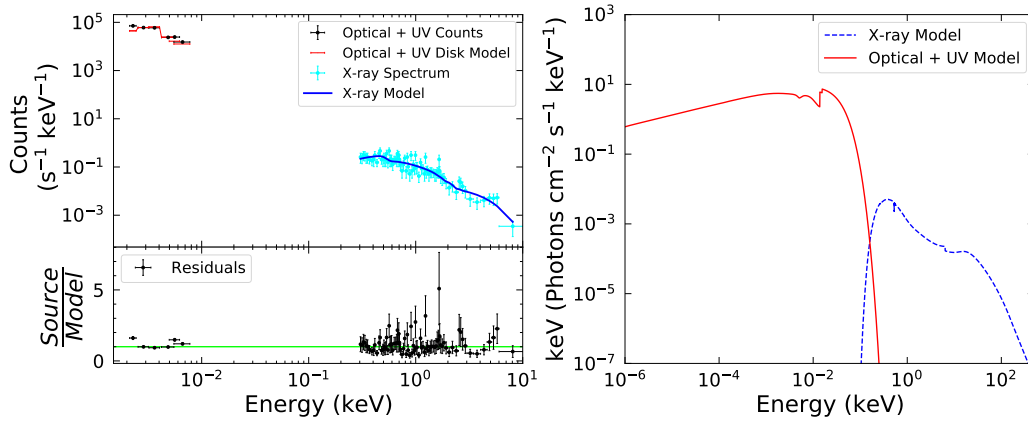
SWIFTJ0105.7-1414



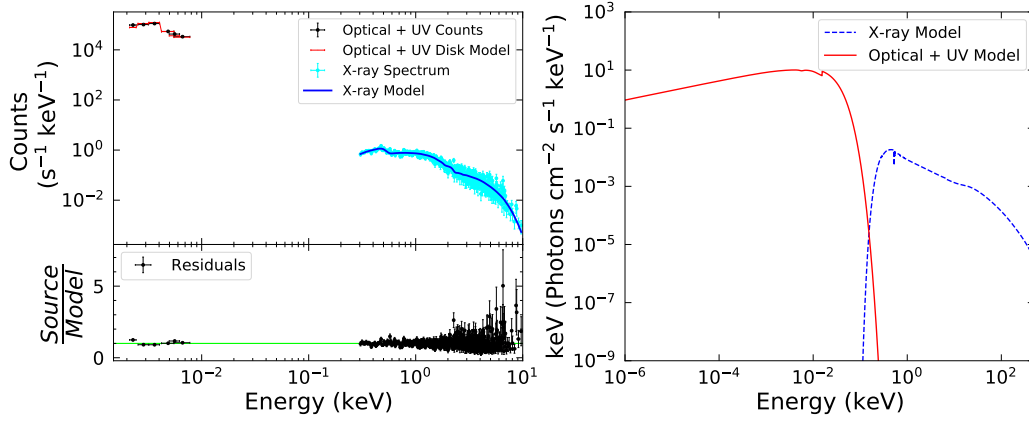
SWIFTJ0113.8-1450



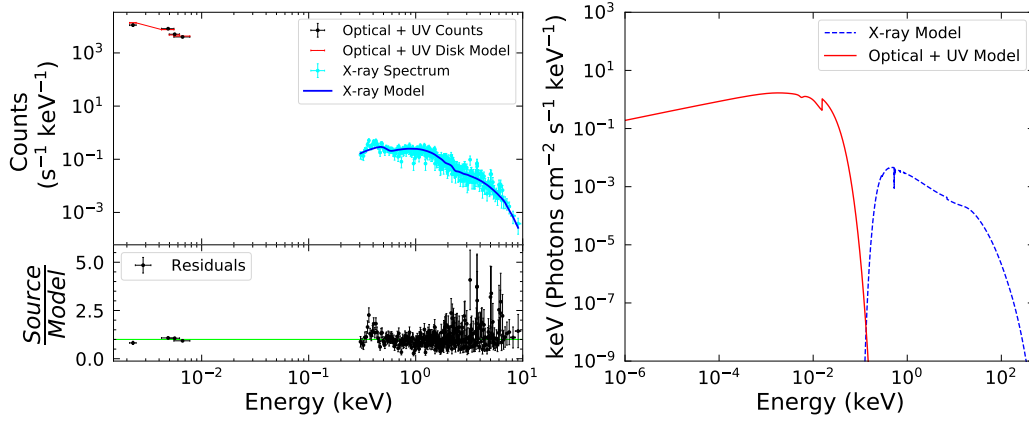
SWIFTJ0122.0-2818



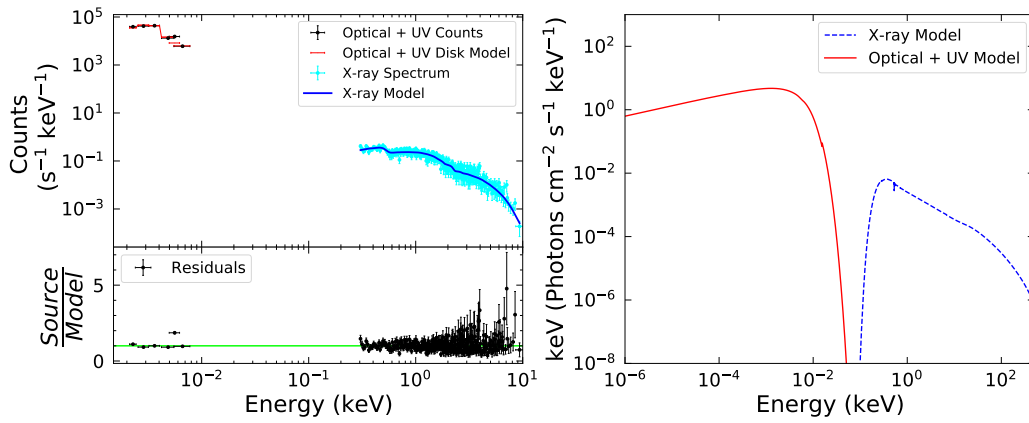
SWIFTJ0123.9-5846



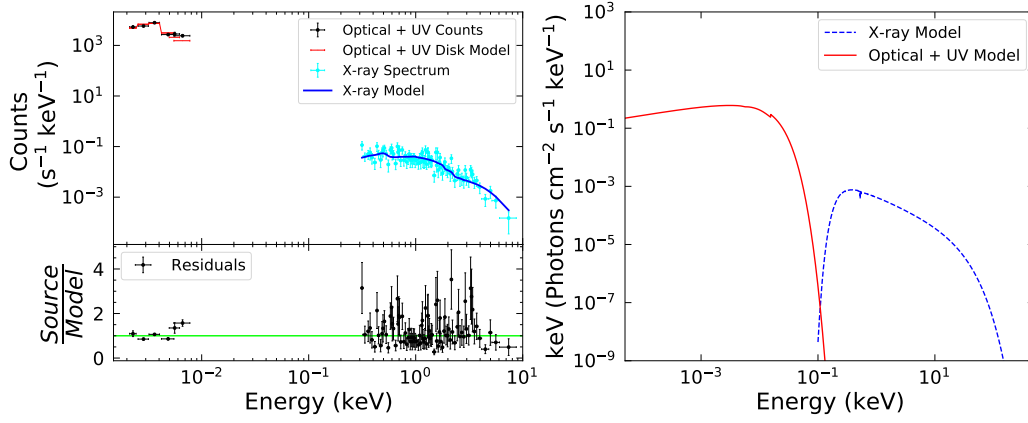
SWIFTJ0127.5+1910



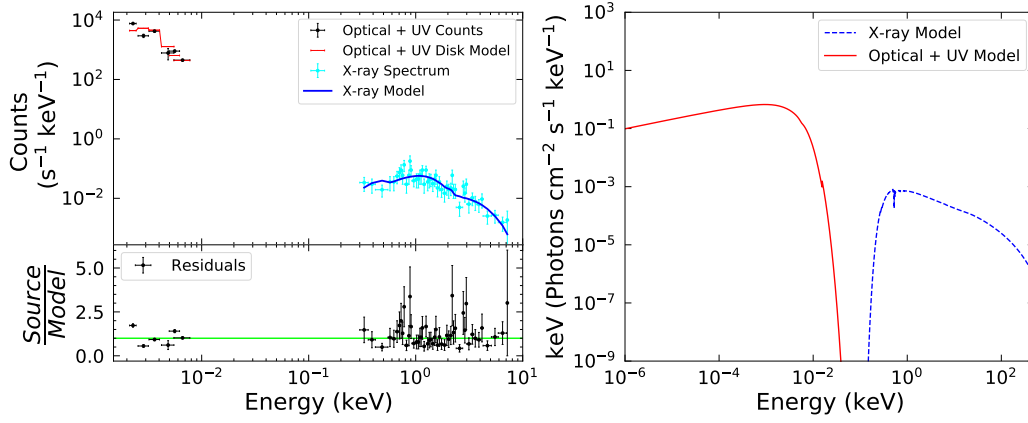
SWIFTJ0128.0-1850



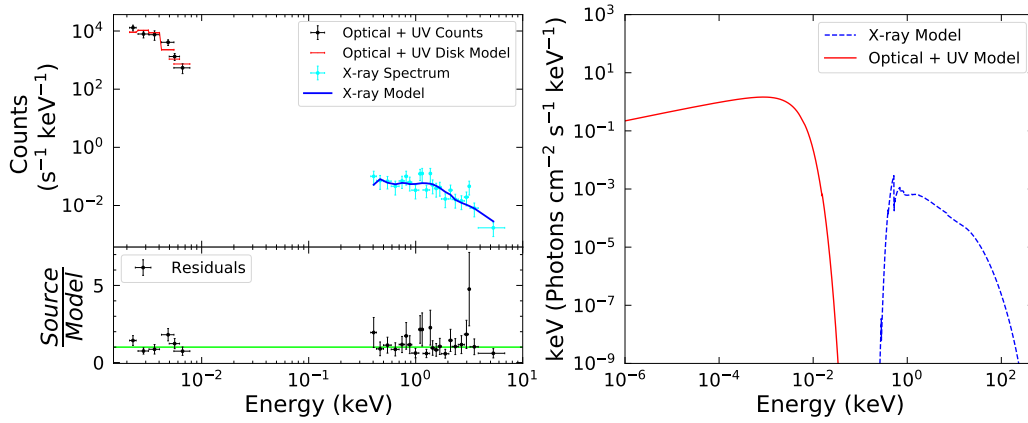
SWIFTJ0130.2-4552



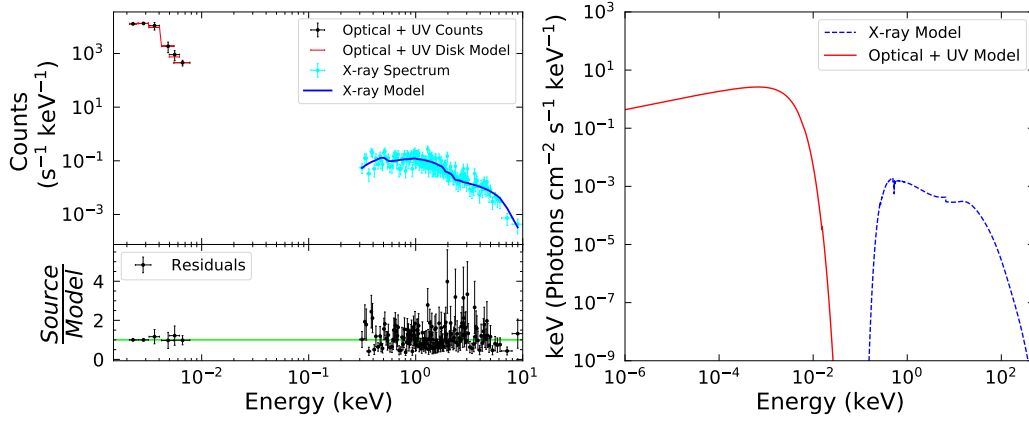
SWIFTJ0134.8-0430



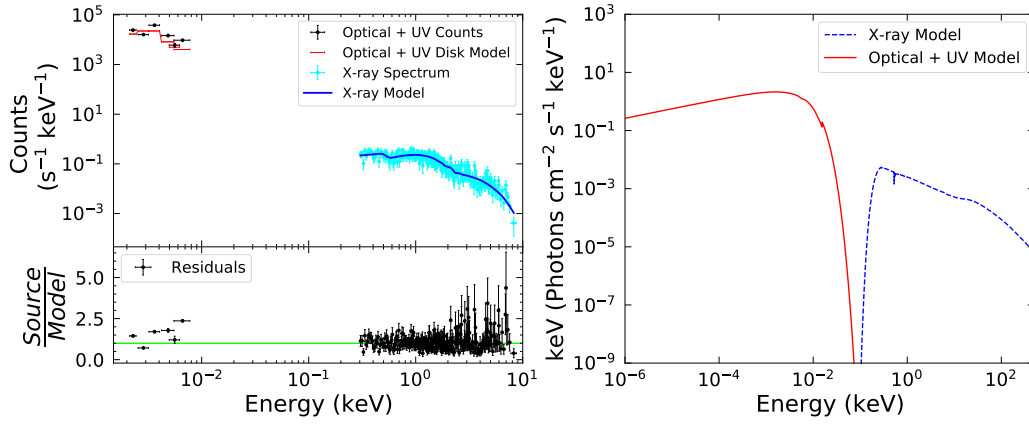
SWIFTJ0151.3-3610



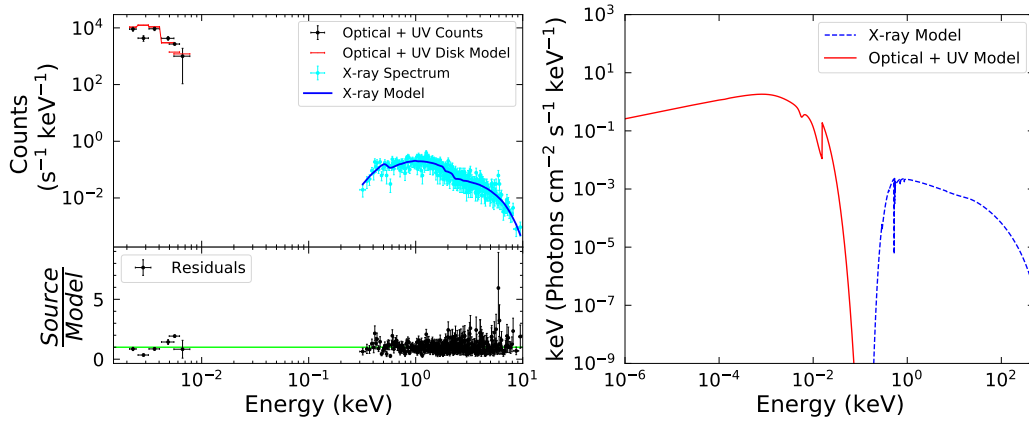
SWIFTJ0155.4+0228



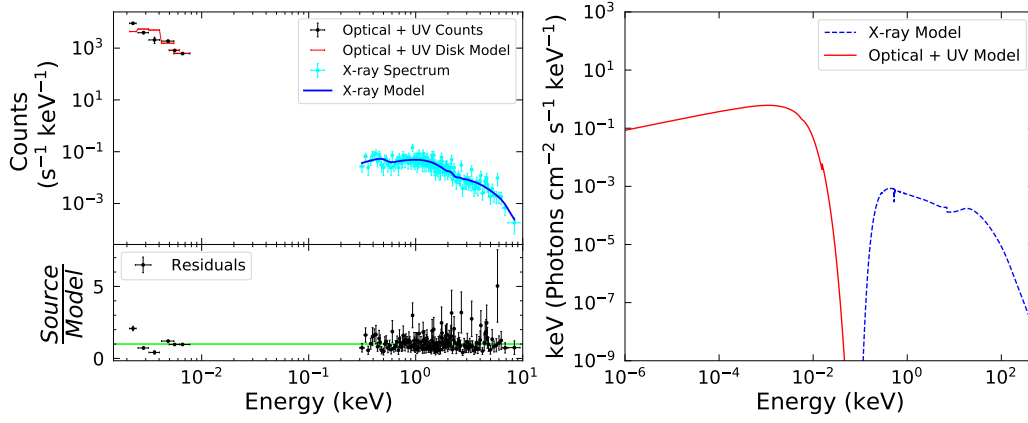
SWIFTJ0206.2-0019



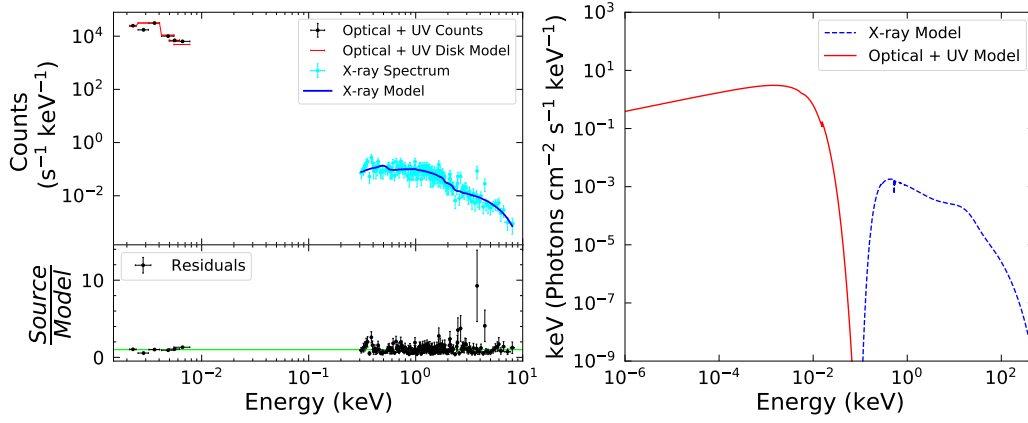
SWIFTJ0209.7+5226



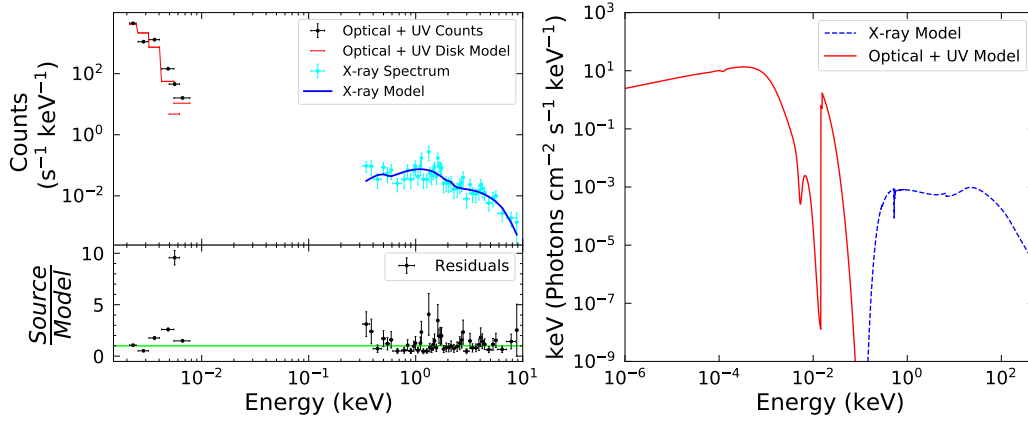
SWIFTJ0214.6-0049



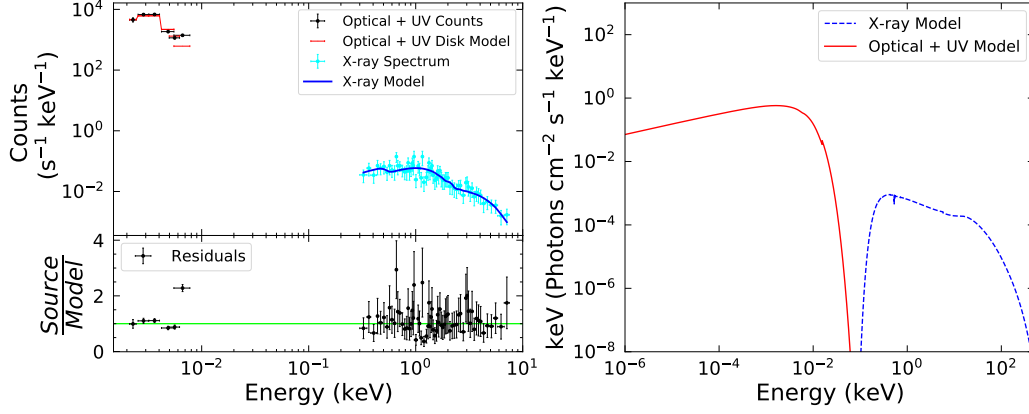
SWIFTJ0214.9-6432



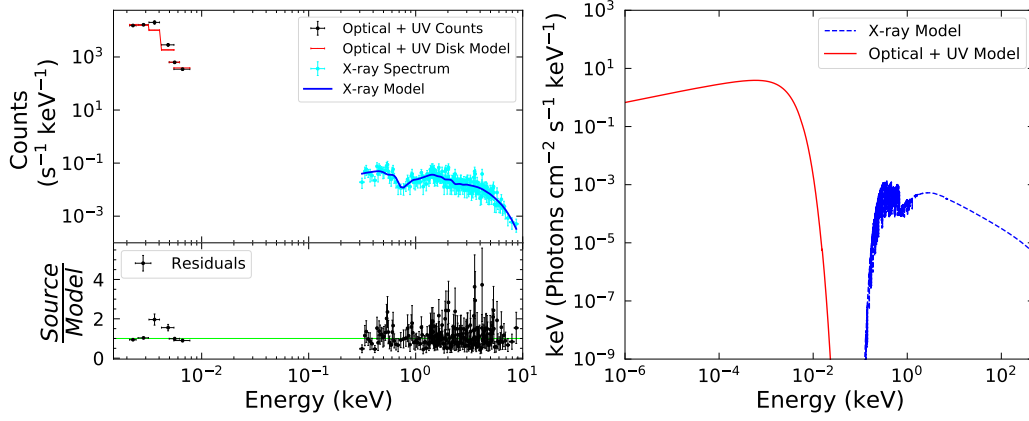
SWIFTJ0222.3+2509



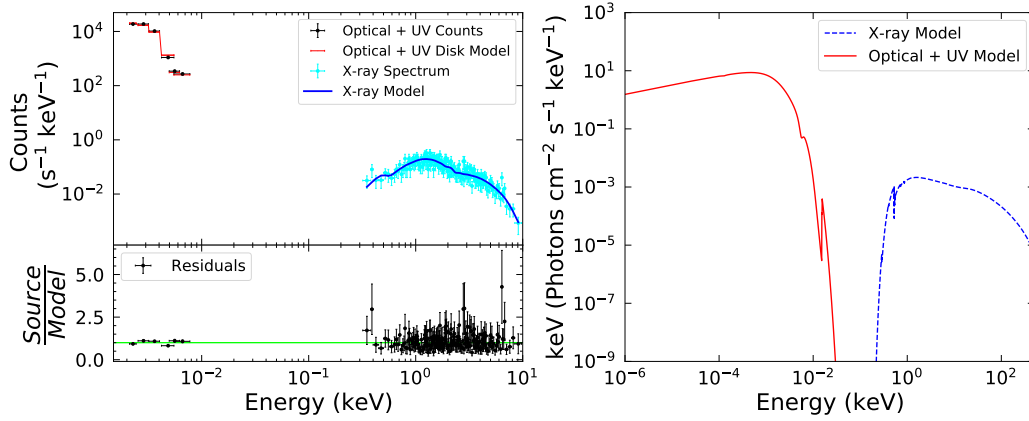
SWIFTJ0225.0-2312



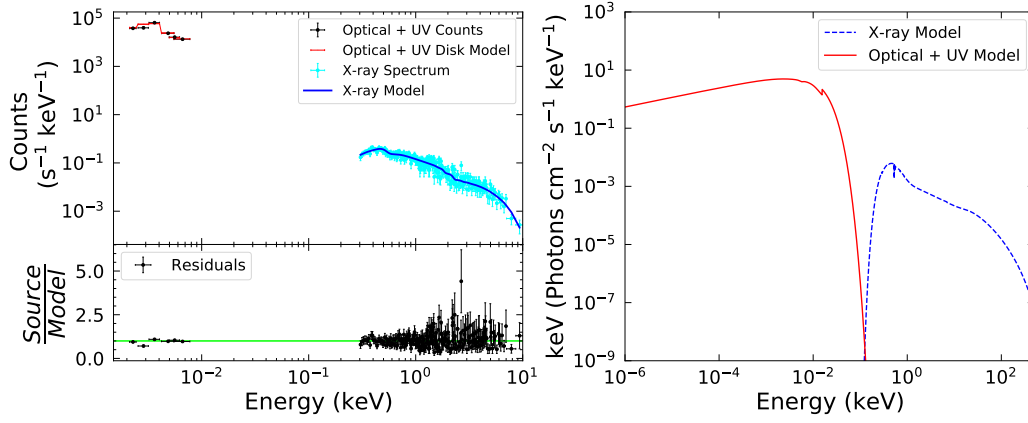
SWIFTJ0226.4-2821



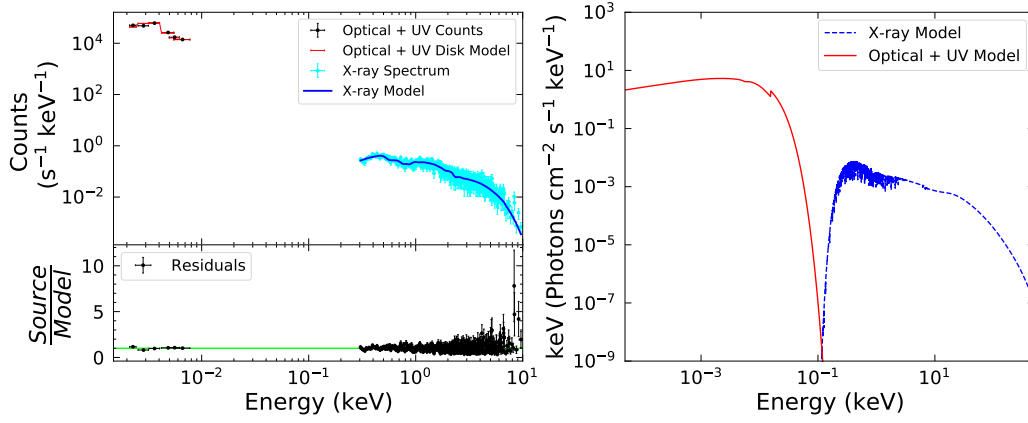
SWIFTJ0228.1+3118



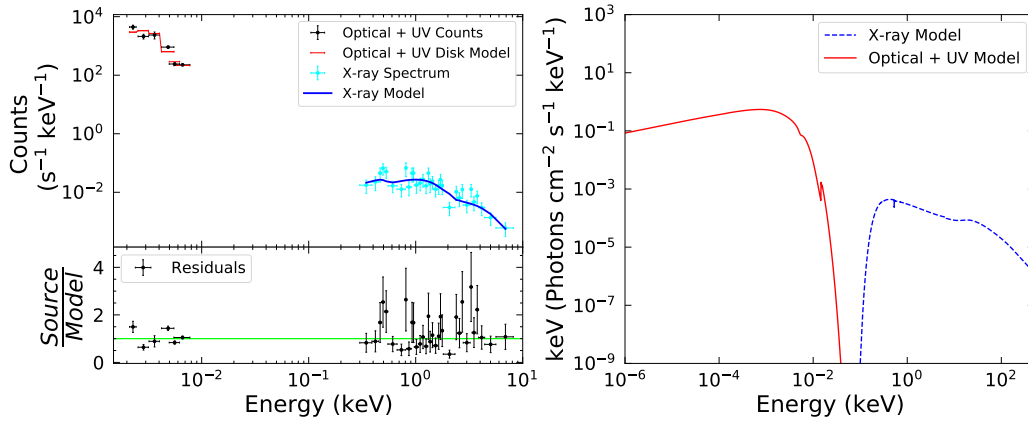
SWIFTJ0230.2-0900



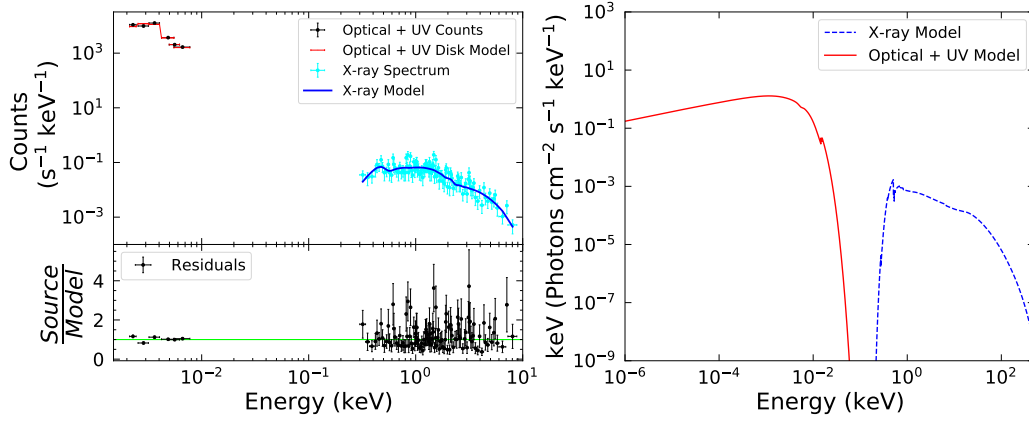
SWIFTJ0234.6-0848



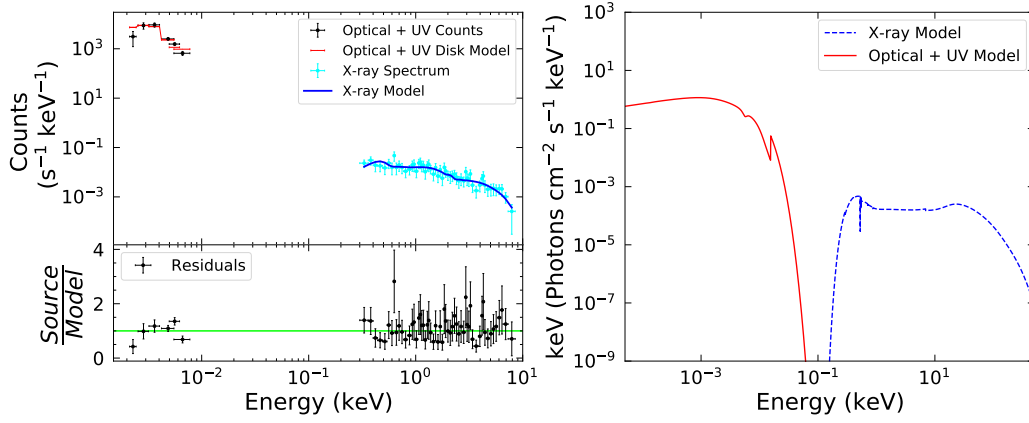
SWIFTJ0235.3-2934



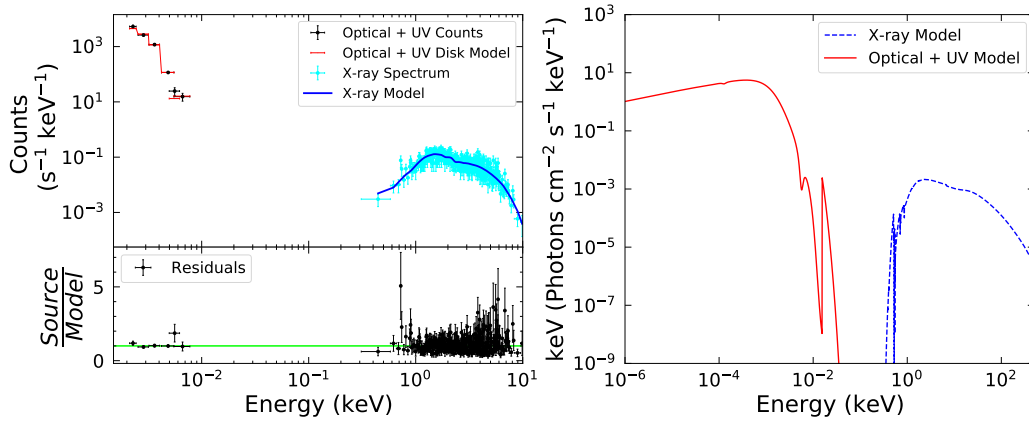
SWIFTJ0238.8-4039



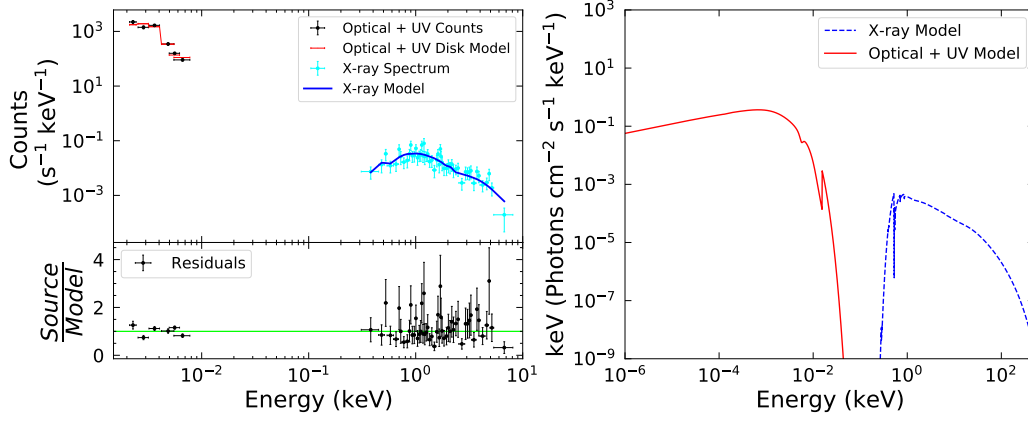
SWIFTJ0241.6+0711



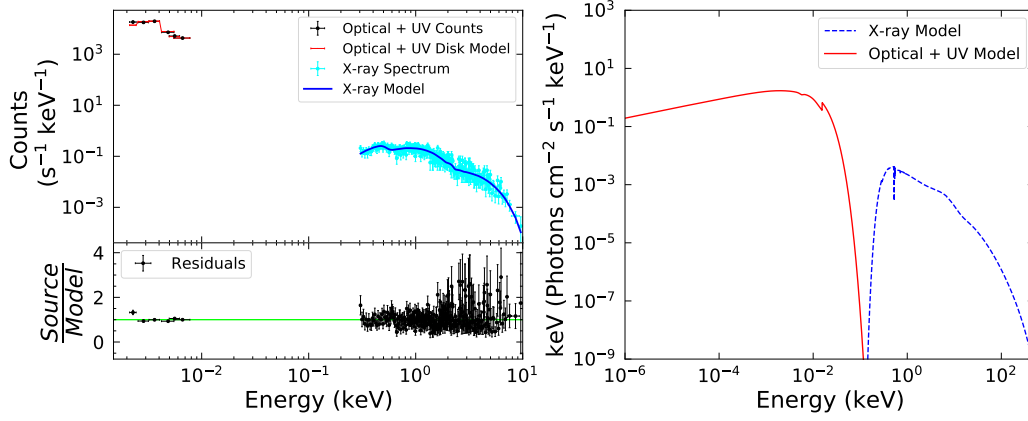
SWIFTJ0244.8+6227



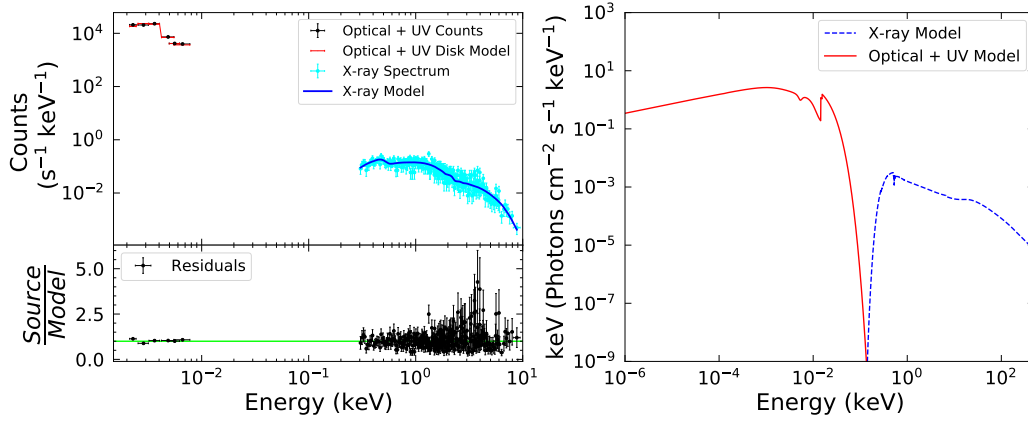
SWIFTJ0259.9+4419



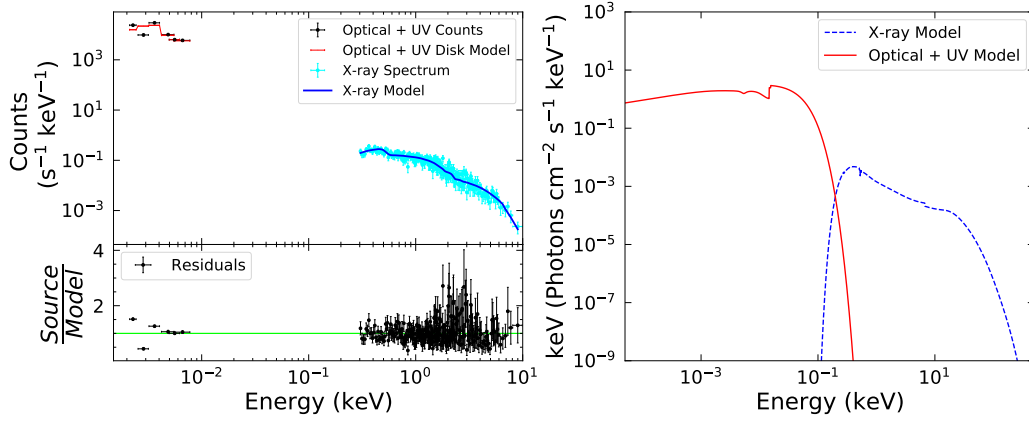
SWIFTJ0308.5-7251



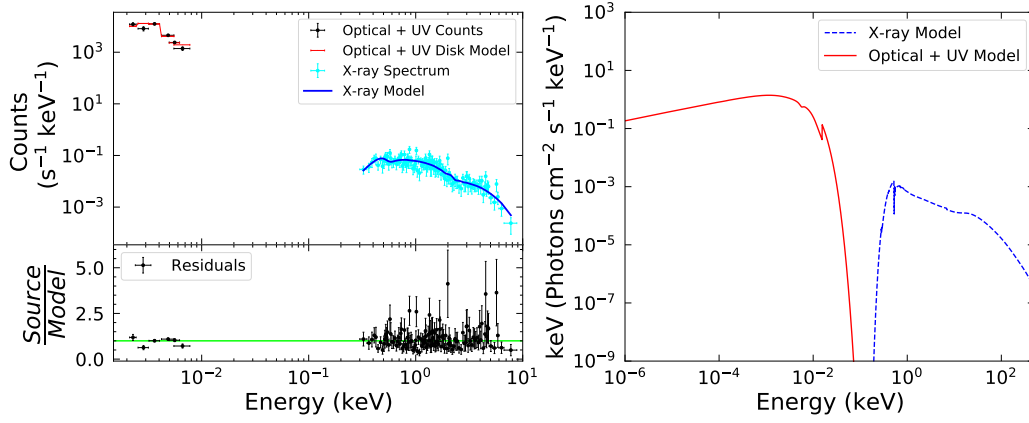
SWIFTJ0311.5-2045



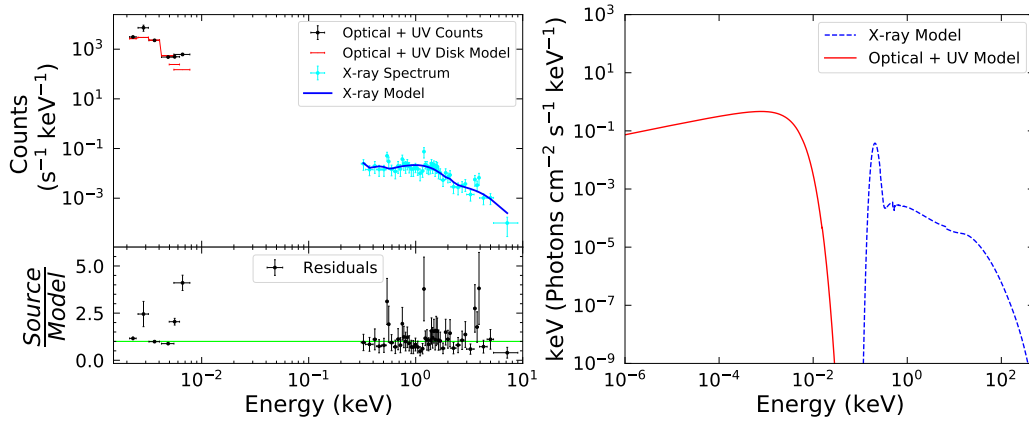
SWIFTJ0325.0-4154



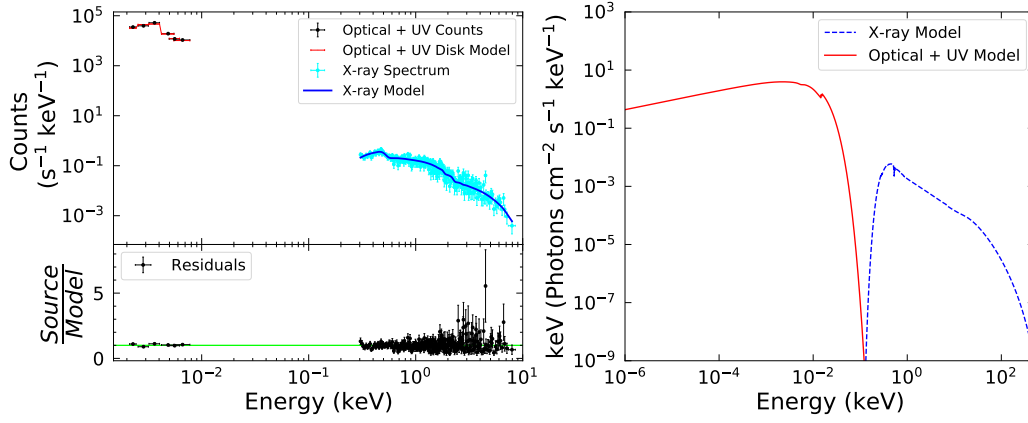
SWIFTJ0334.4-1515



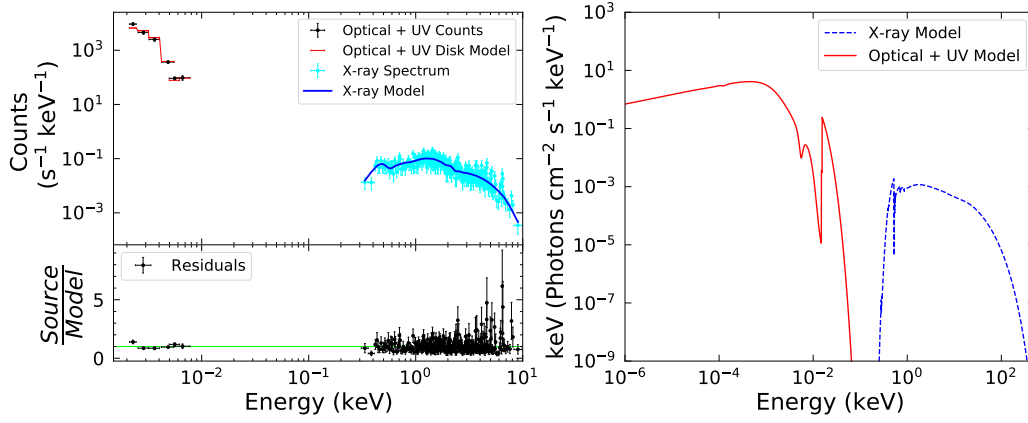
SWIFTJ0347.0-3027



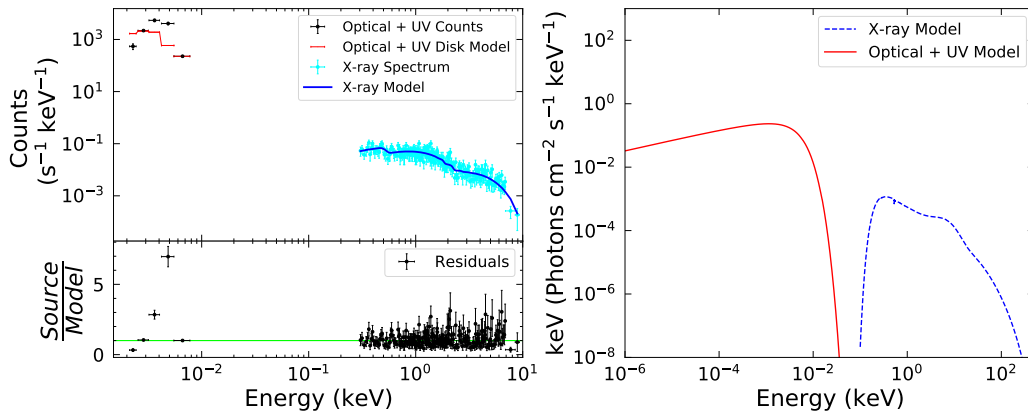
SWIFTJ0351.7-4030



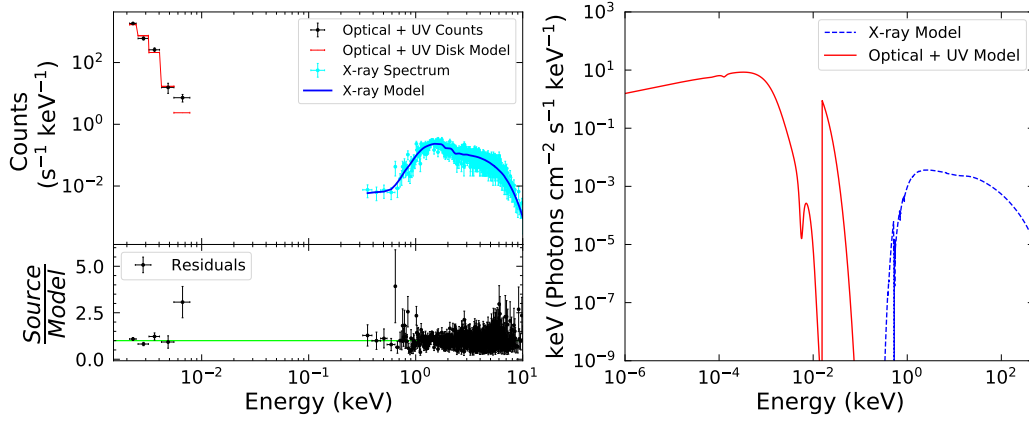
SWIFTJ0354.2+0250



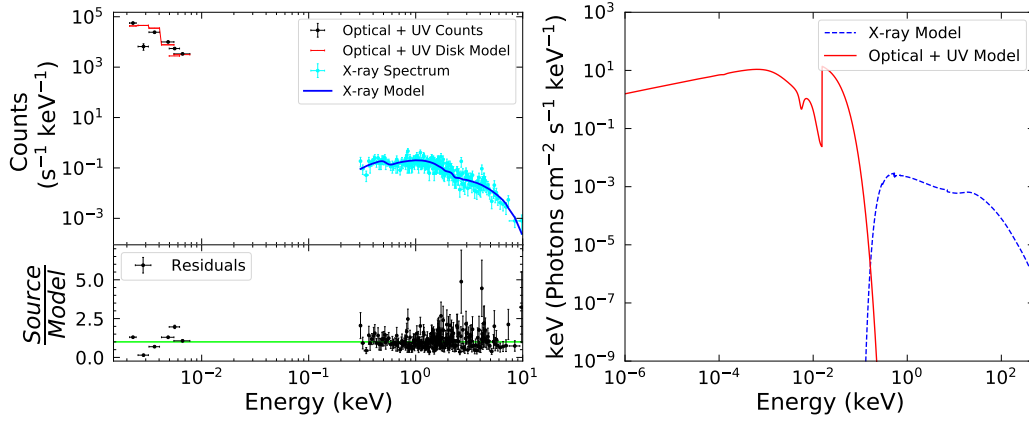
SWIFTJ0405.3-3707



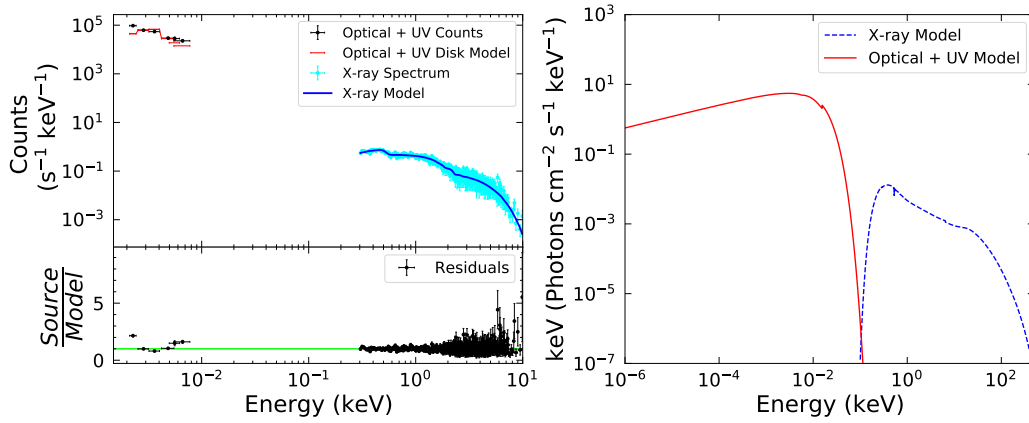
SWIFTJ0418.3+3800



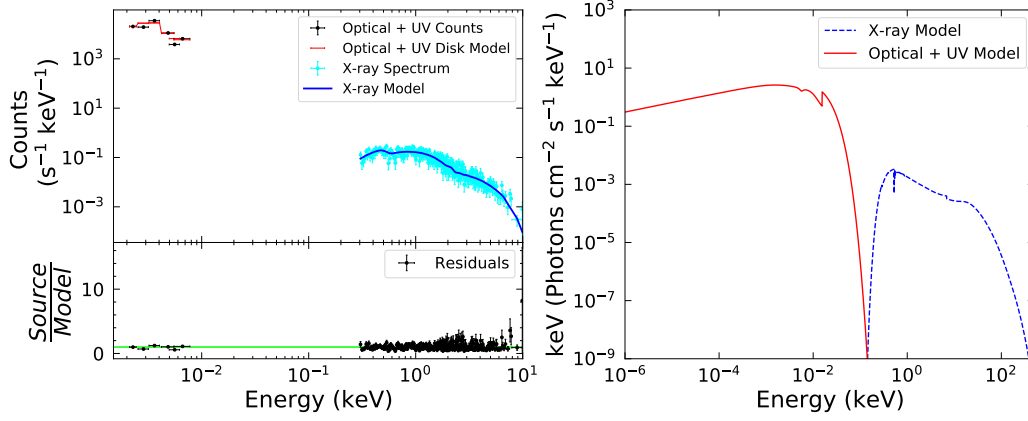
SWIFTJ0420.0-5457



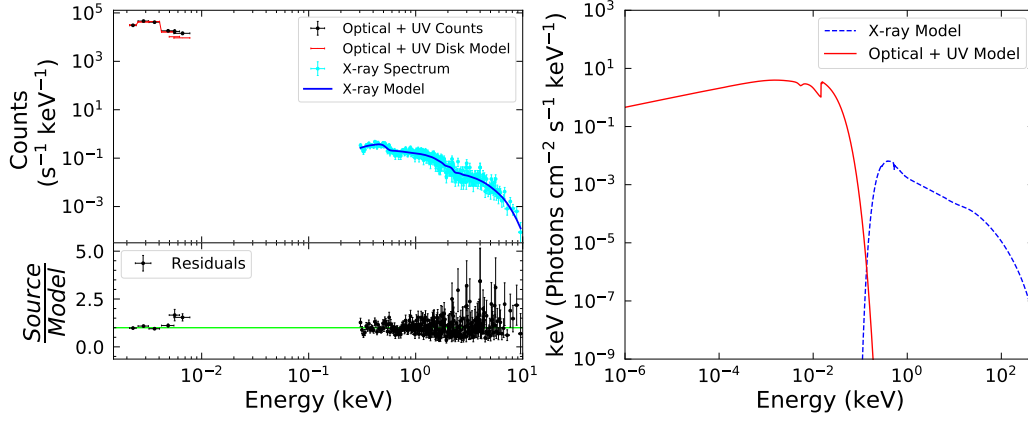
SWIFTJ0426.2-5711



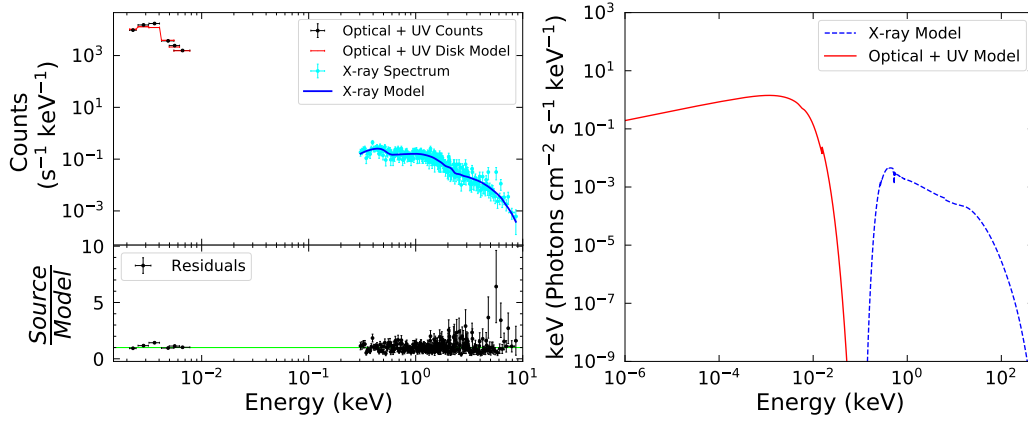
SWIFTJ0436.3-1022



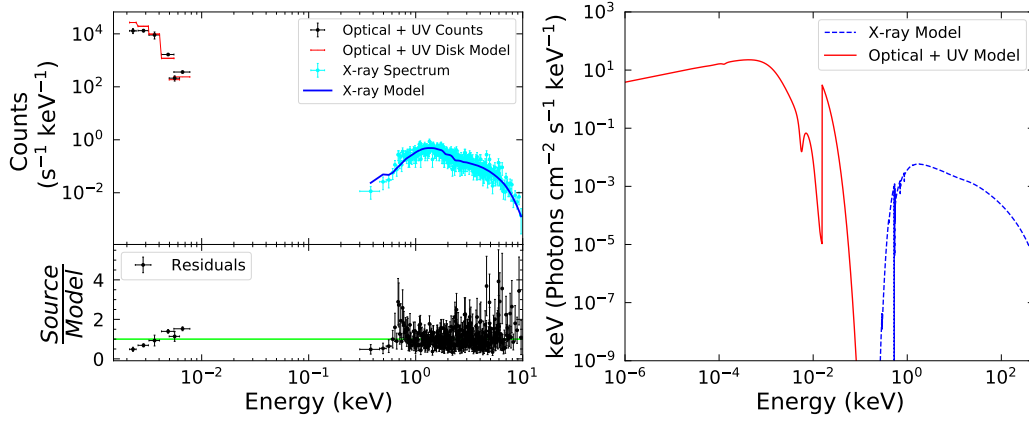
SWIFTJ0437.4-4713



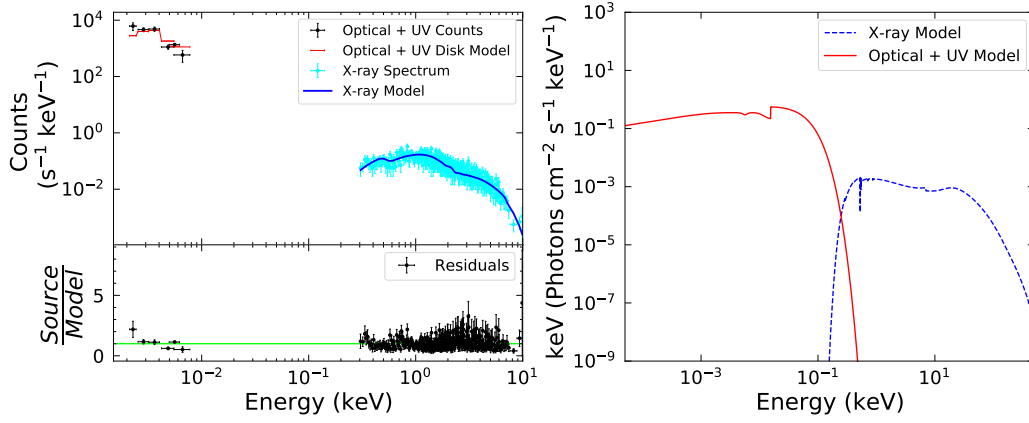
SWIFTJ0441.2-2704



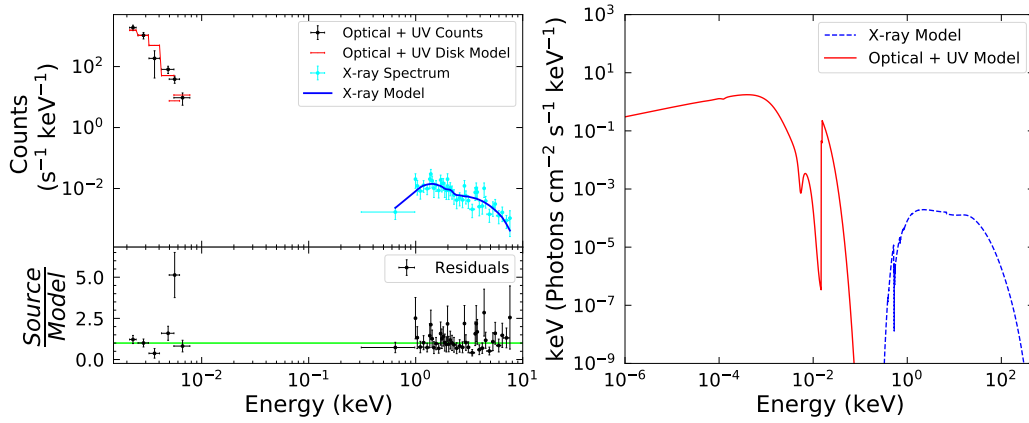
SWIFTJ0452.2+4933



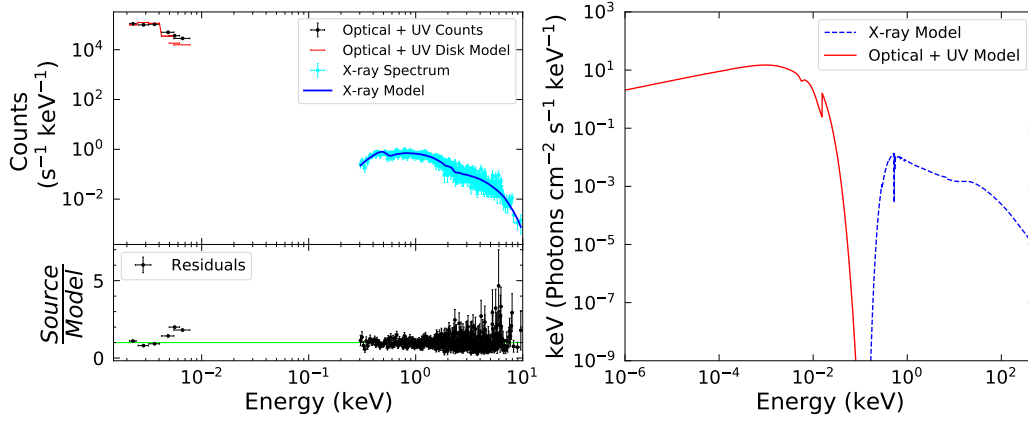
SWIFTJ0502.1+0332



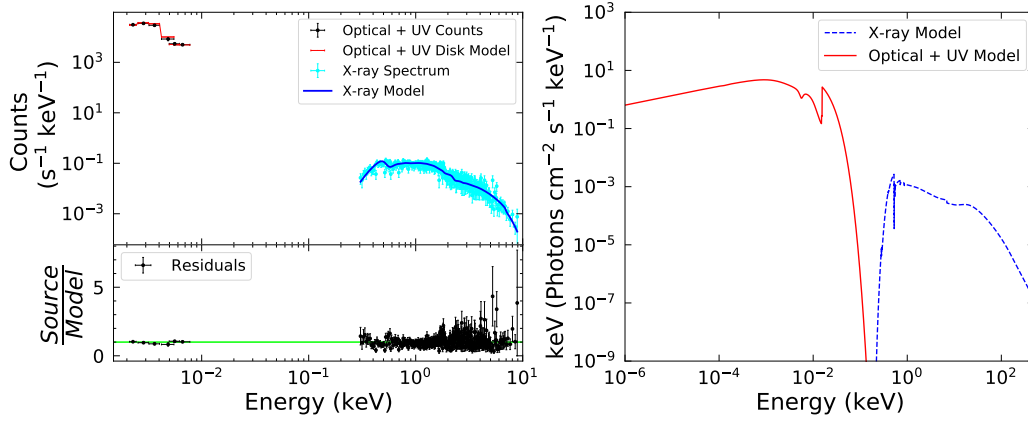
SWIFTJ0504.6-7345



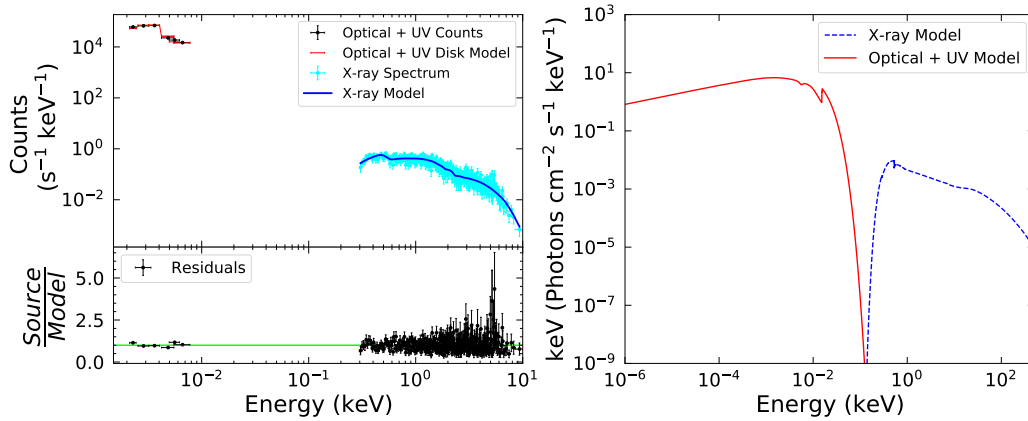
SWIFTJ0516.2-0009



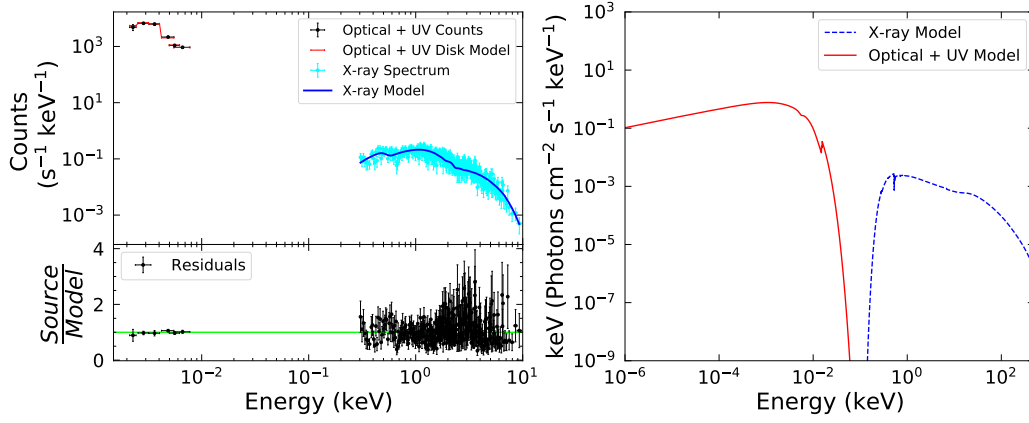
SWIFTJ0516.4-1034



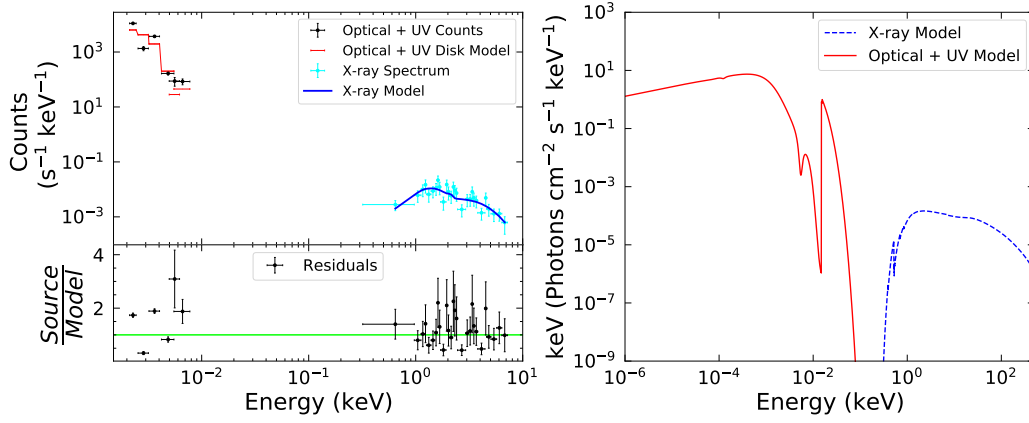
SWIFTJ0501.9-3239



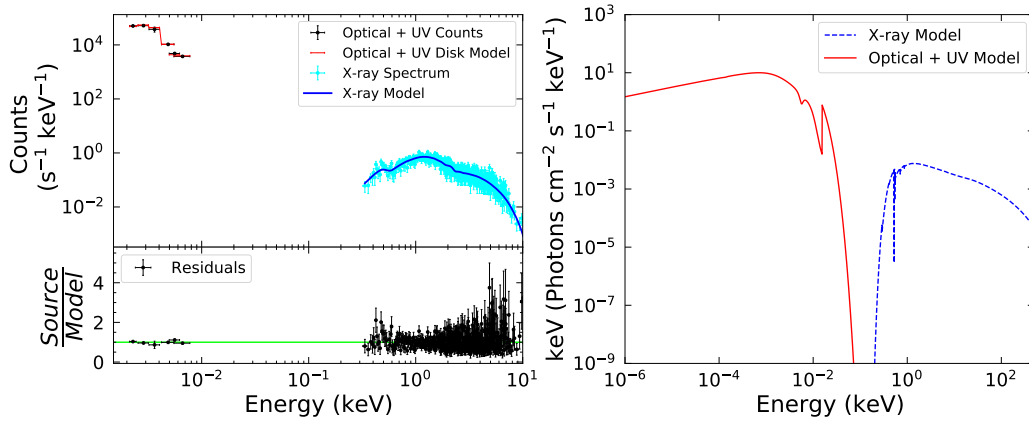
SWIFTJ0519.5-4545



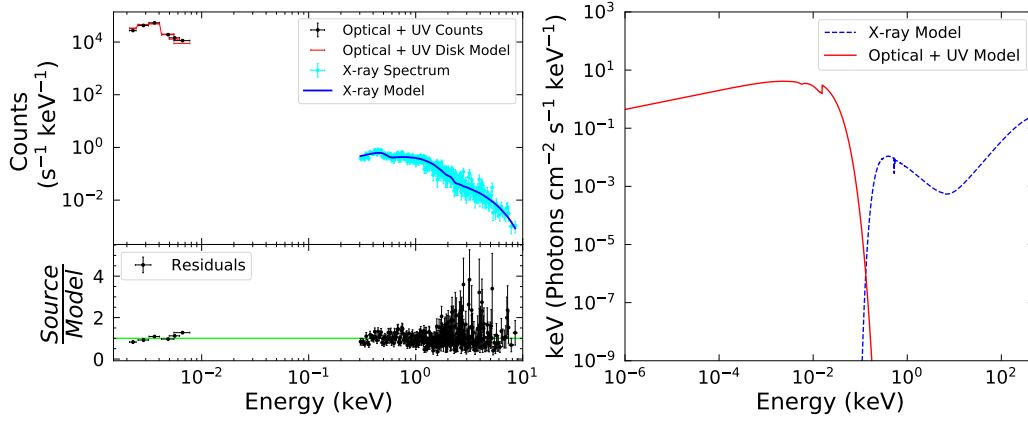
SWIFTJ0528.1-3933



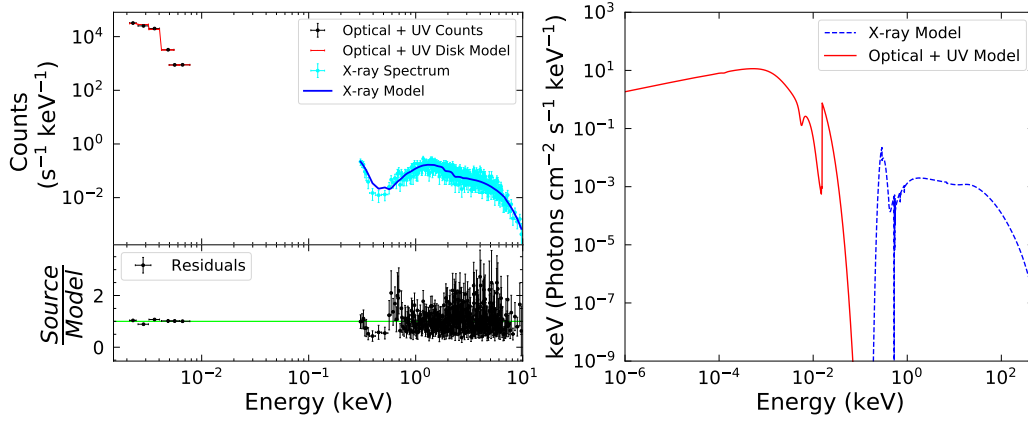
SWIFTJ0554.8+4625



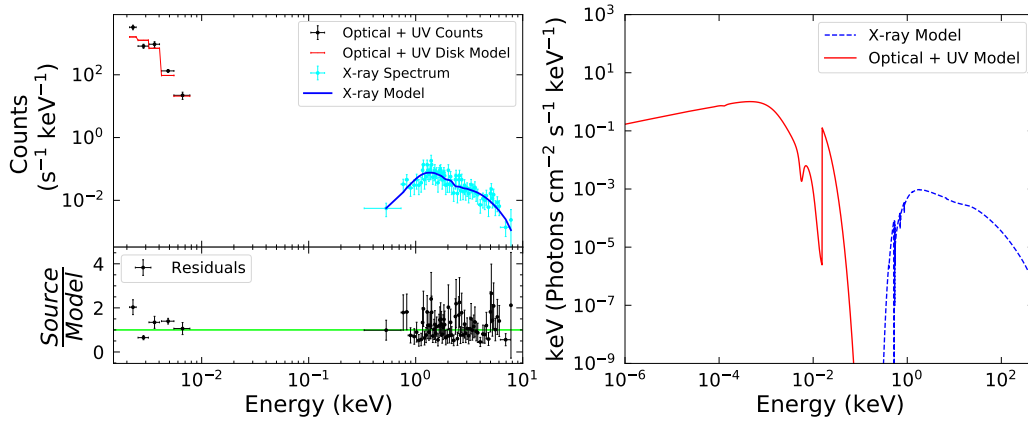
SWIFTJ0559.8-5028



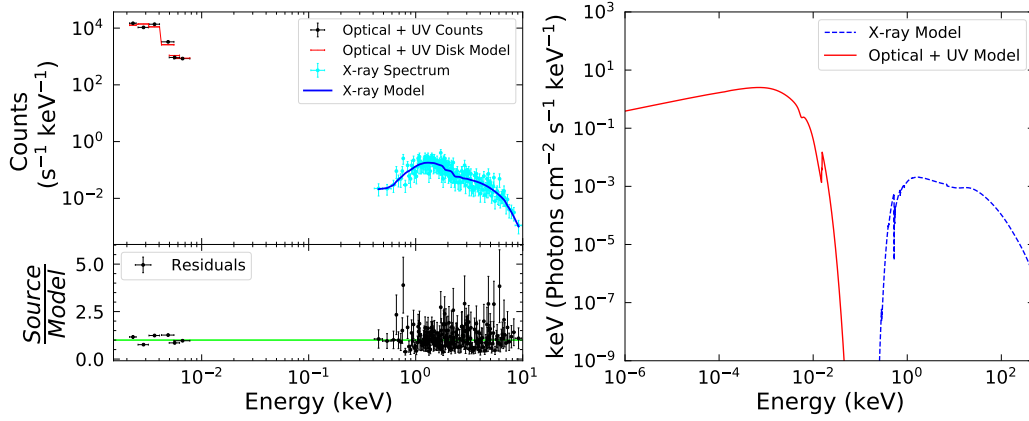
SWIFTJ0602.2+2829



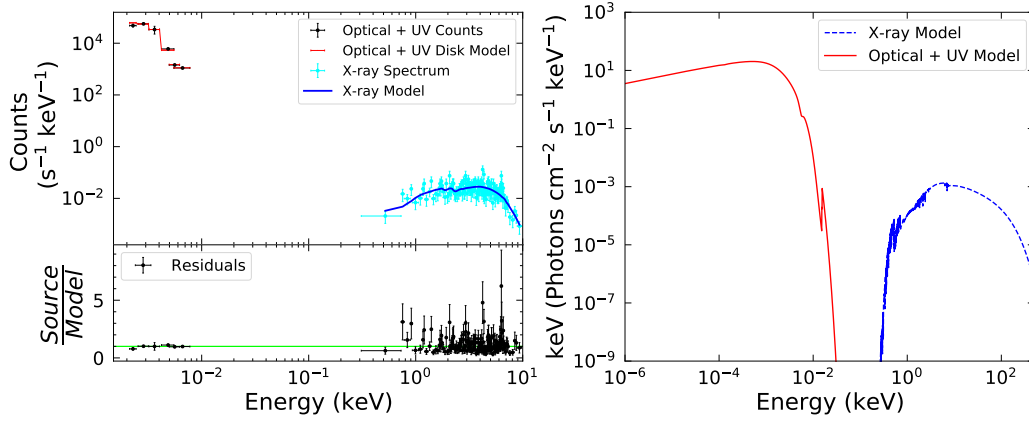
SWIFTJ0626.6+0729



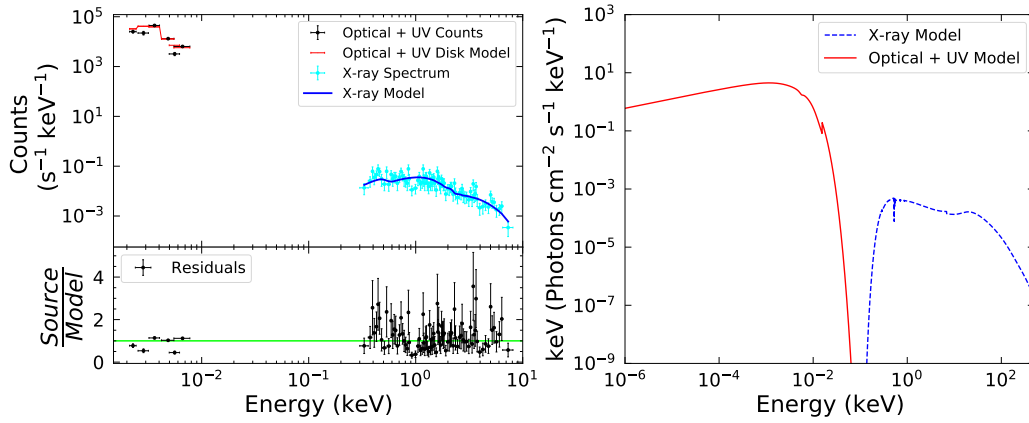
SWIFTJ0640.4-2554



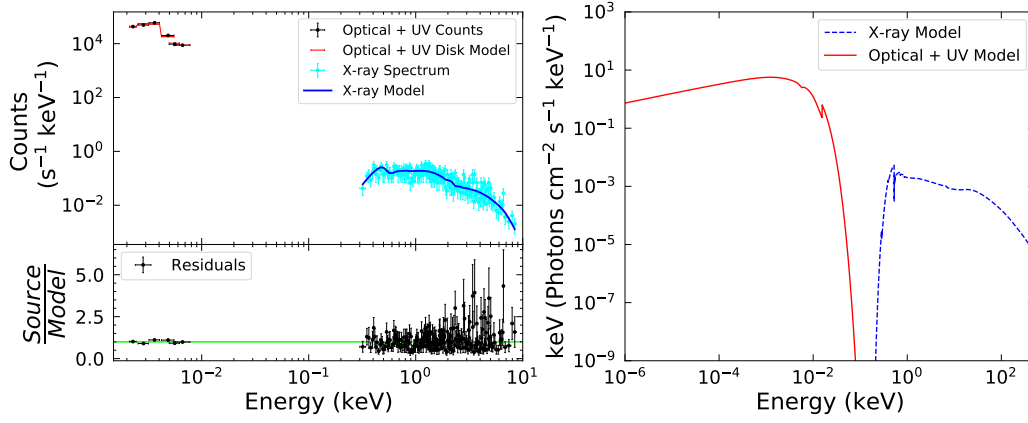
SWIFTJ0651.9+7426



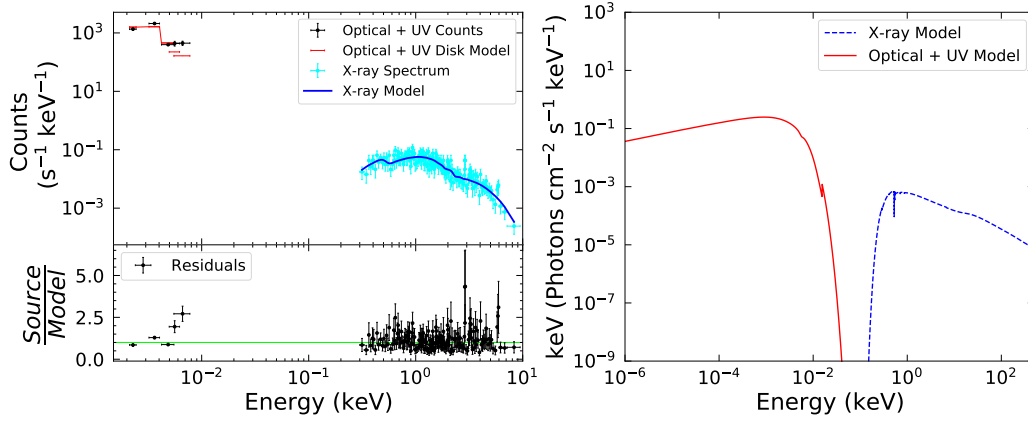
SWIFTJ0736.9+5846



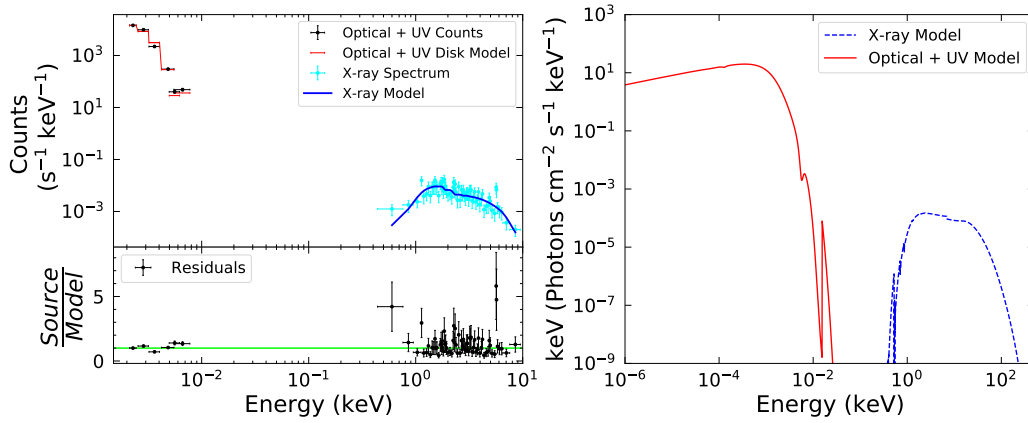
SWIFTJ0742.5+4948



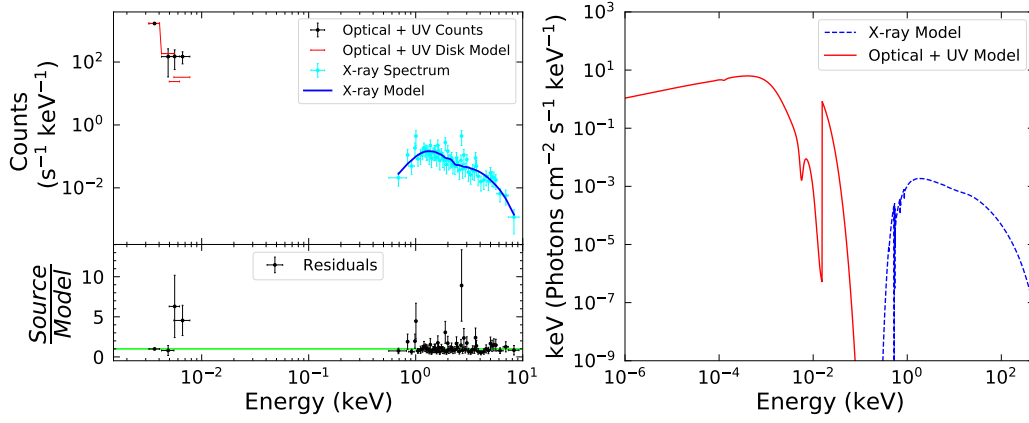
SWIFTJ0753.1+4559



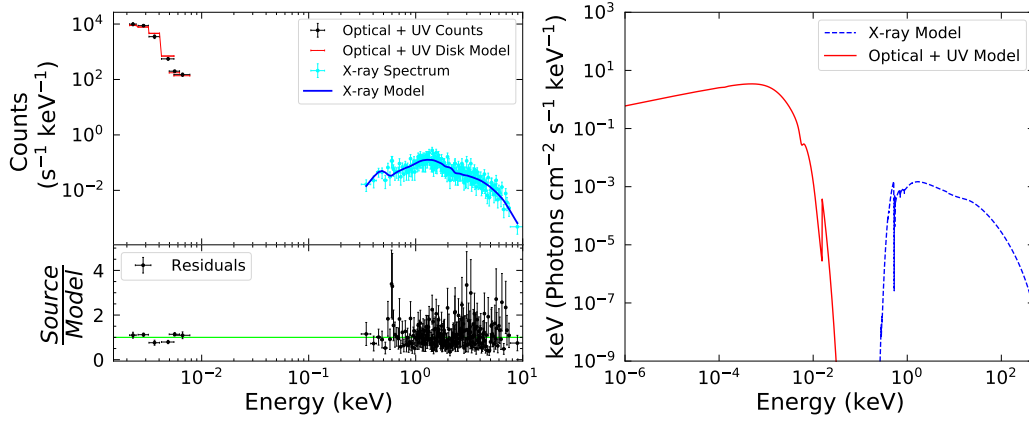
SWIFTJ0756.3-4137



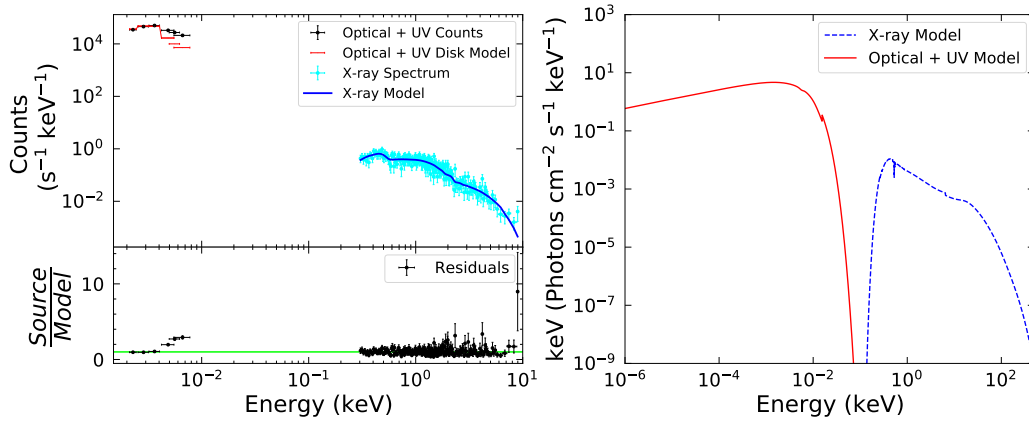
SWIFTJ0759.8-3844



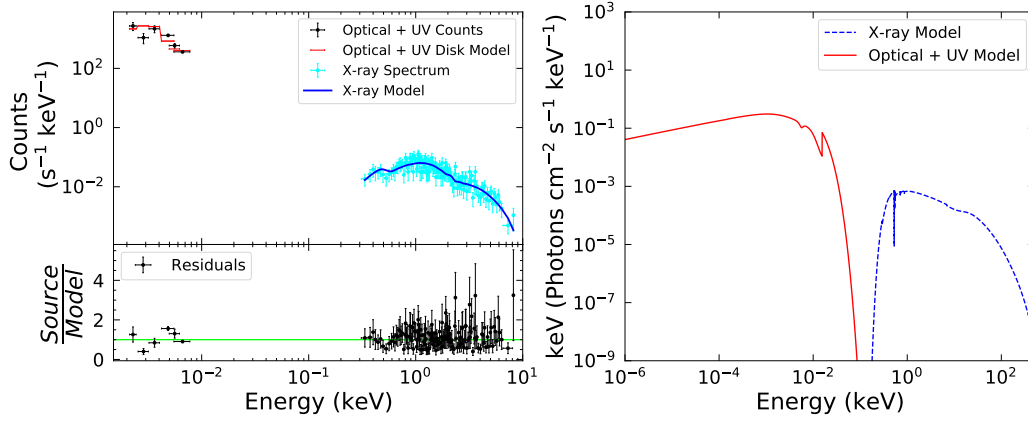
SWIFTJ0801.9-4946



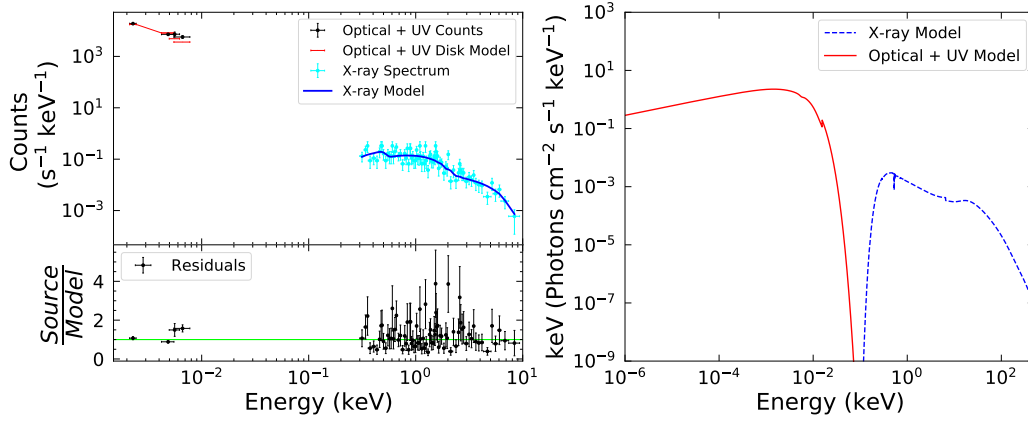
SWIFTJ0810.9+7602



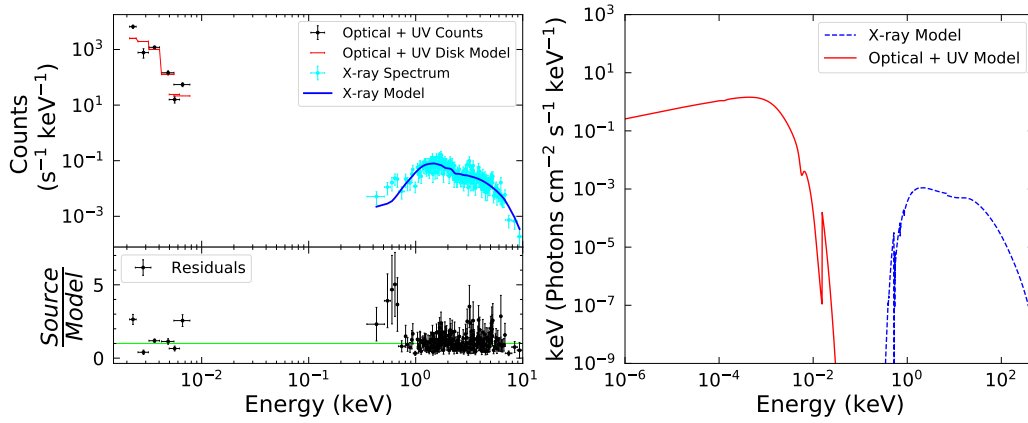
SWIFTJ0819.2-2259



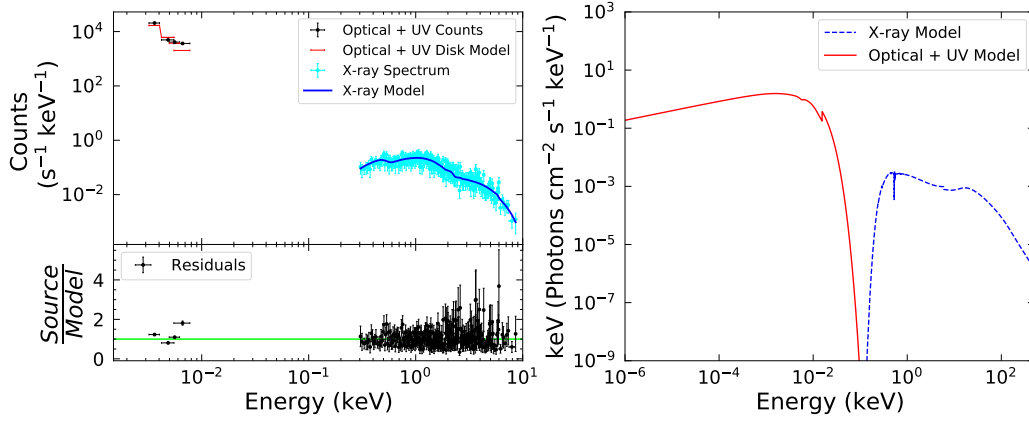
SWIFTJ0832.5+3703



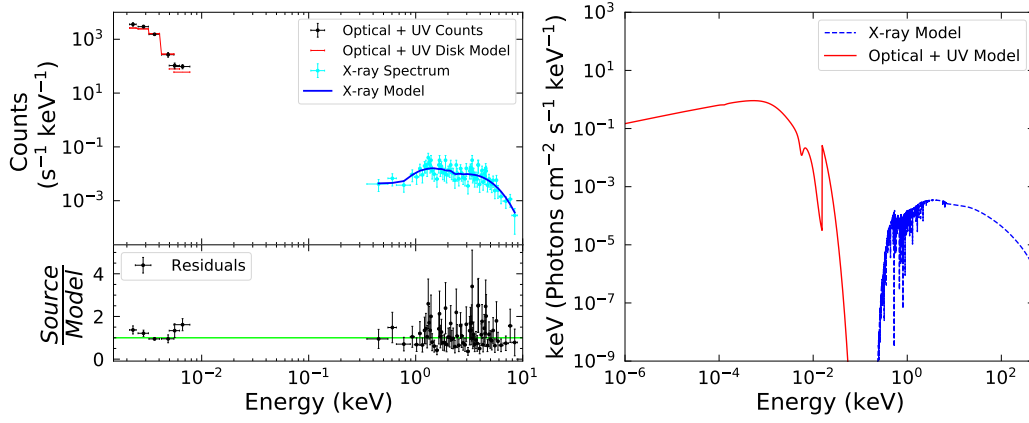
SWIFTJ0838.4-3557



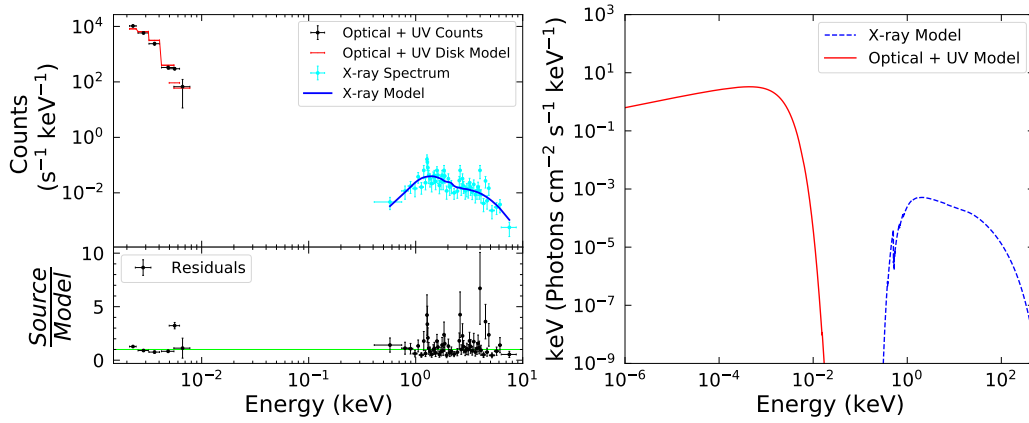
SWIFTJ0839.6-1213



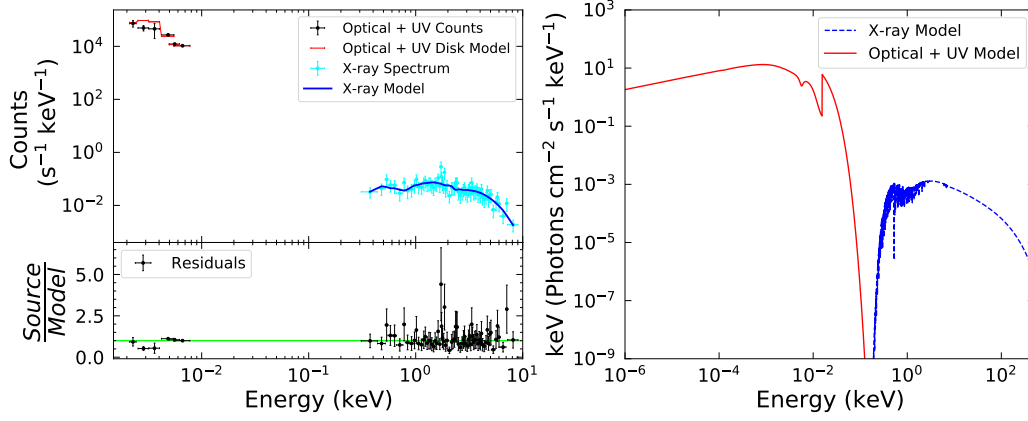
SWIFTJ0845.0-3531



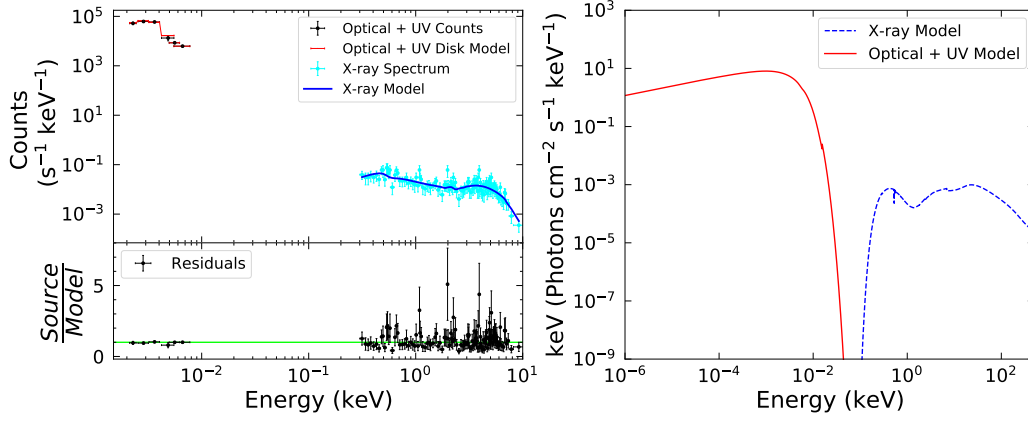
SWIFTJ0845.3+1420



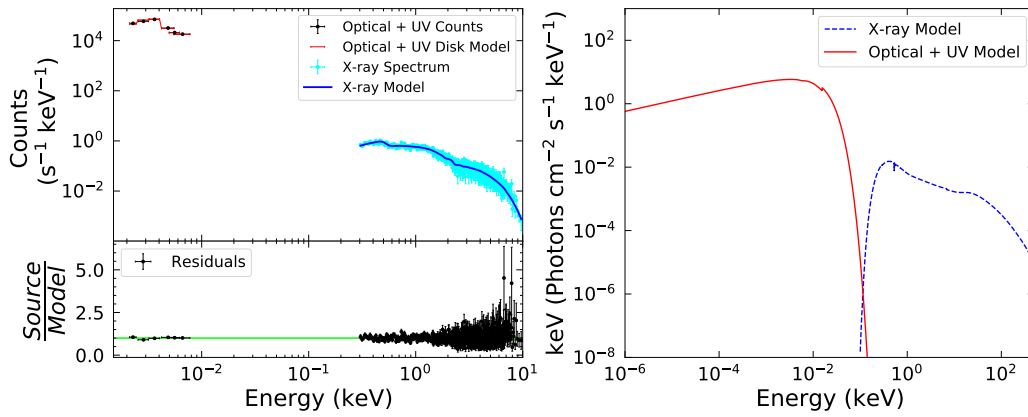
SWIFTJ0917.2-6221



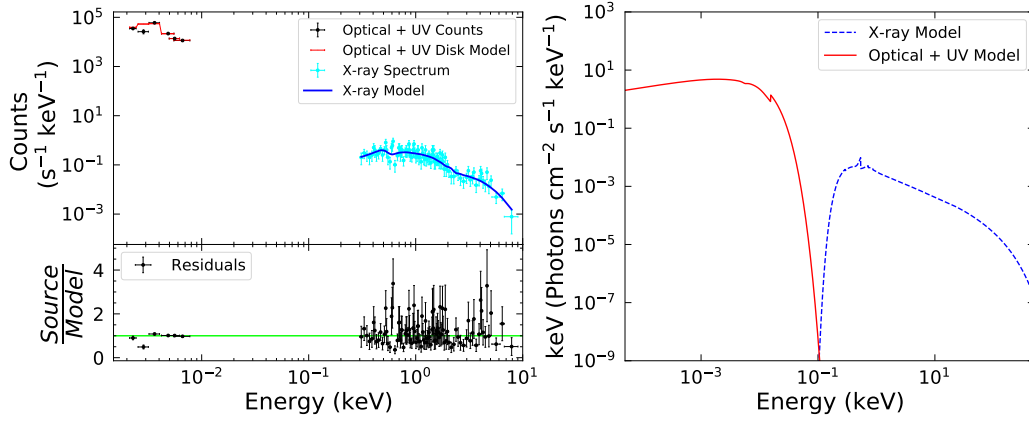
SWIFTJ0918.5+1618



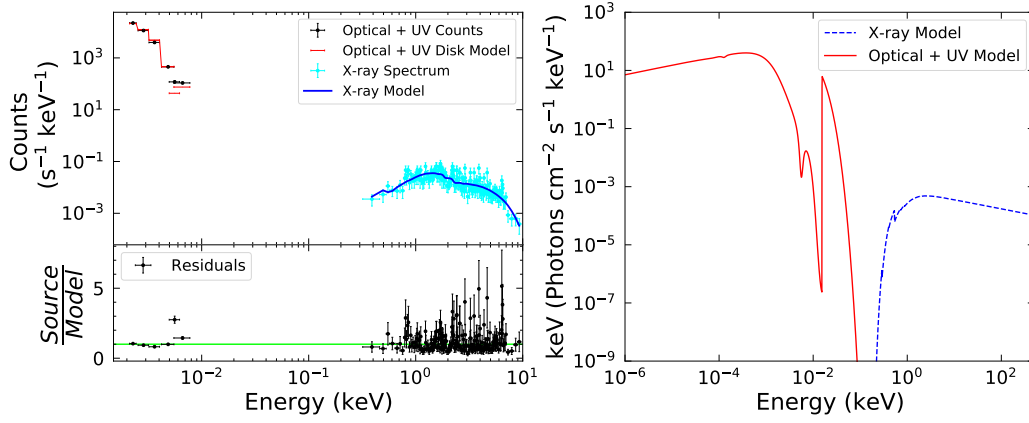
SWIFTJ0925.0+5218



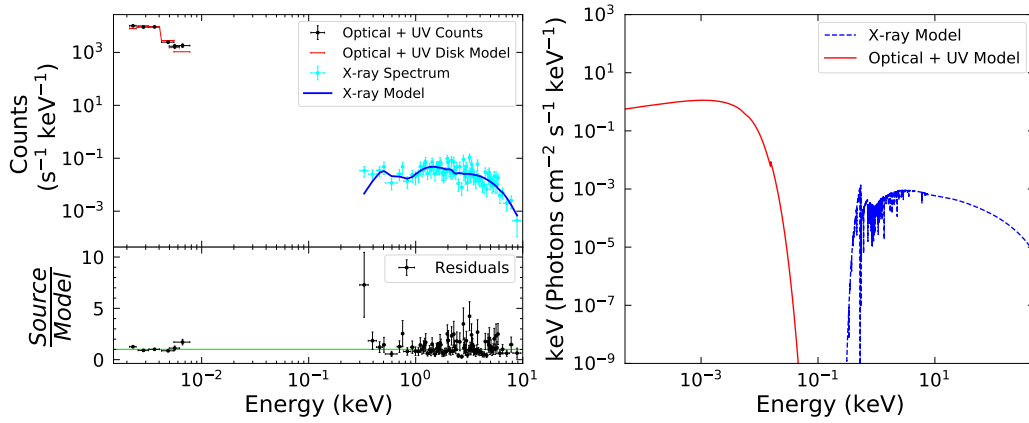
SWIFTJ0926.2+1244



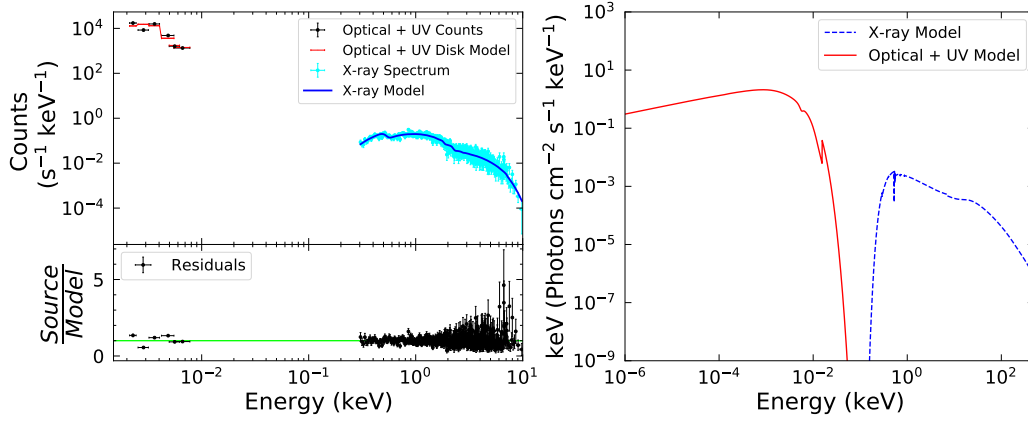
SWIFTJ0945.6-1420



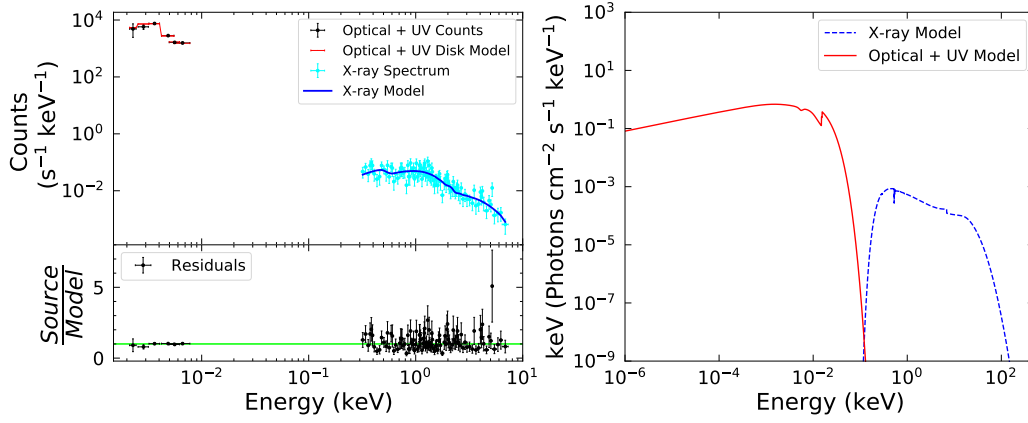
SWIFTJ0947.7+0726



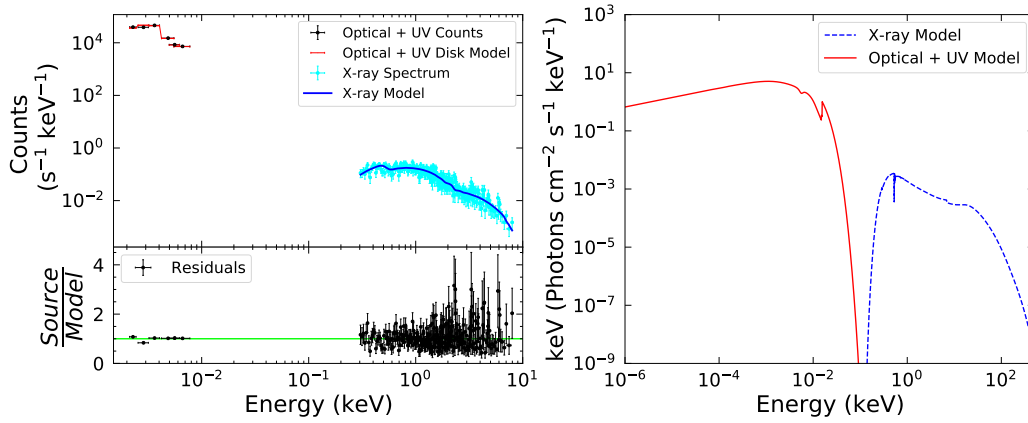
SWIFTJ0955.5+6907



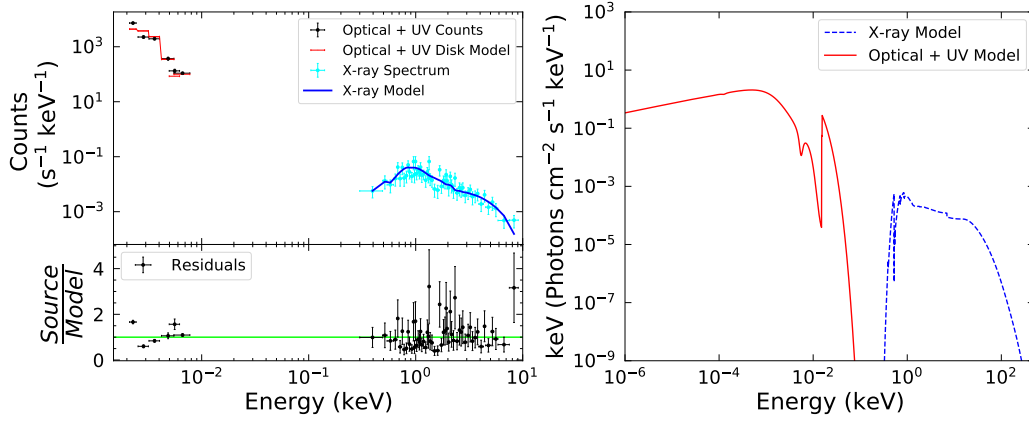
SWIFTJ0959.9+1303



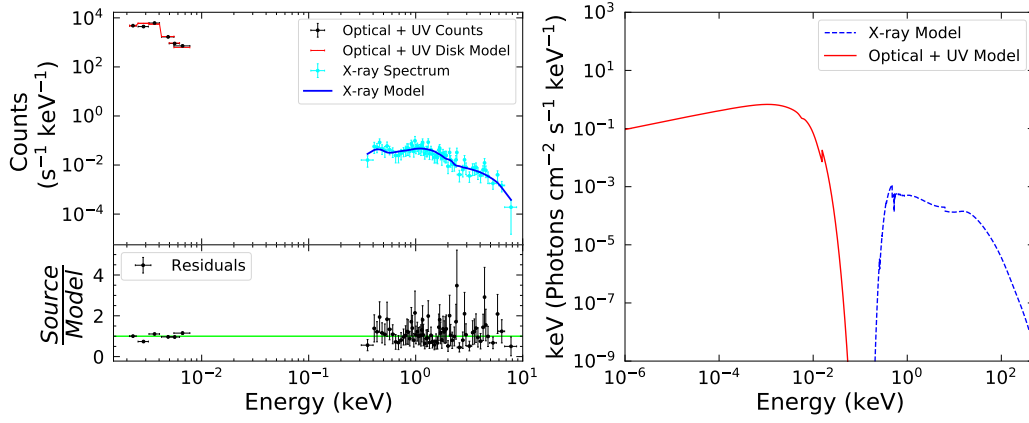
SWIFTJ0959.7-3112



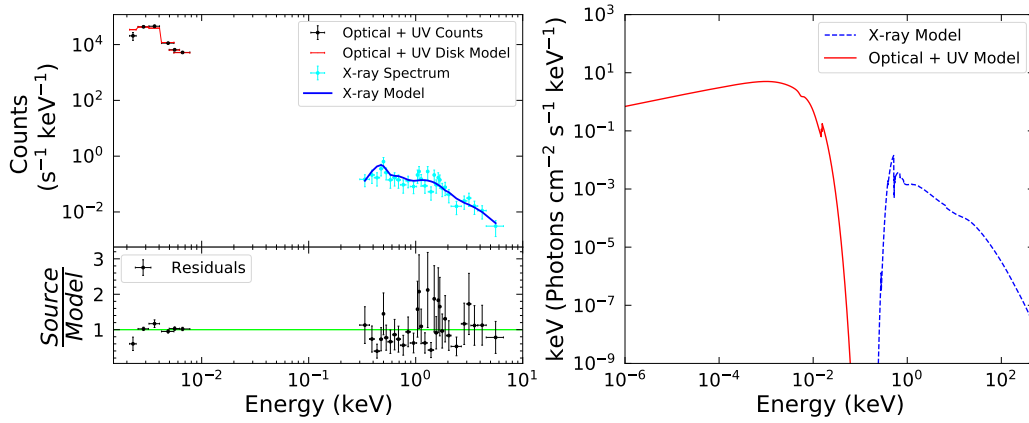
SWIFTJ1003.4-3726



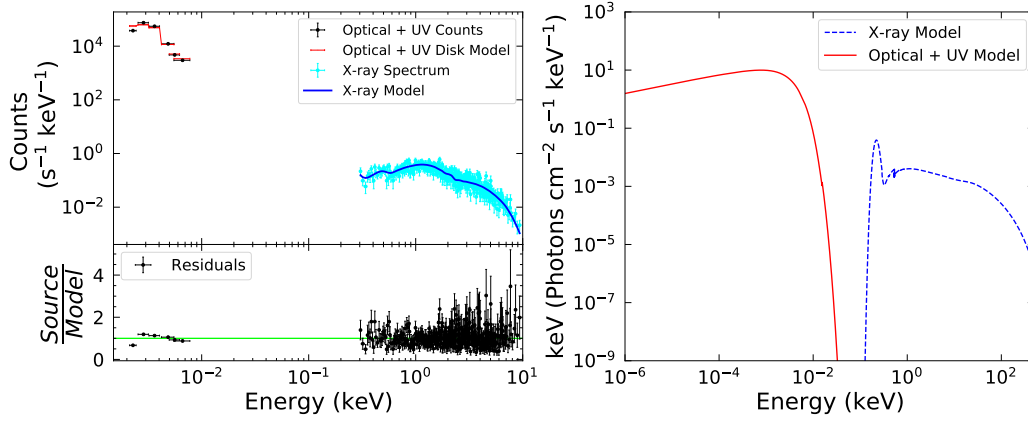
SWIFTJ1007.4+6534



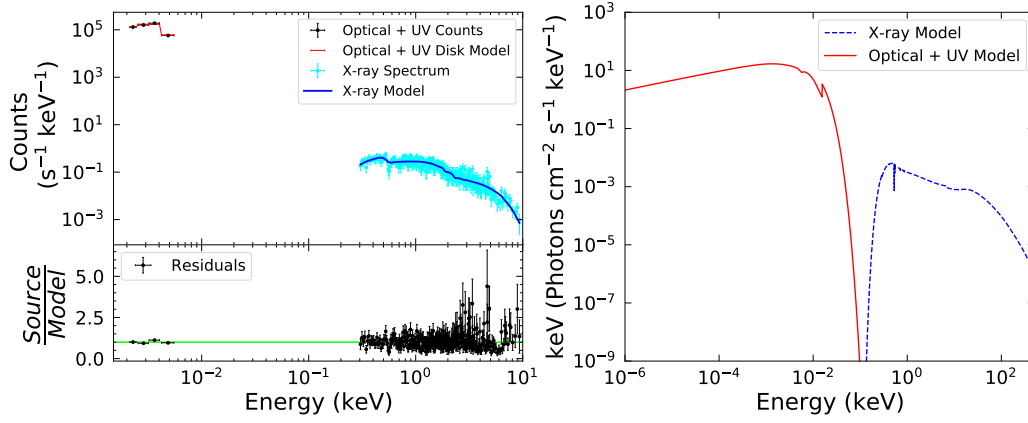
SWIFTJ1021.7-0327



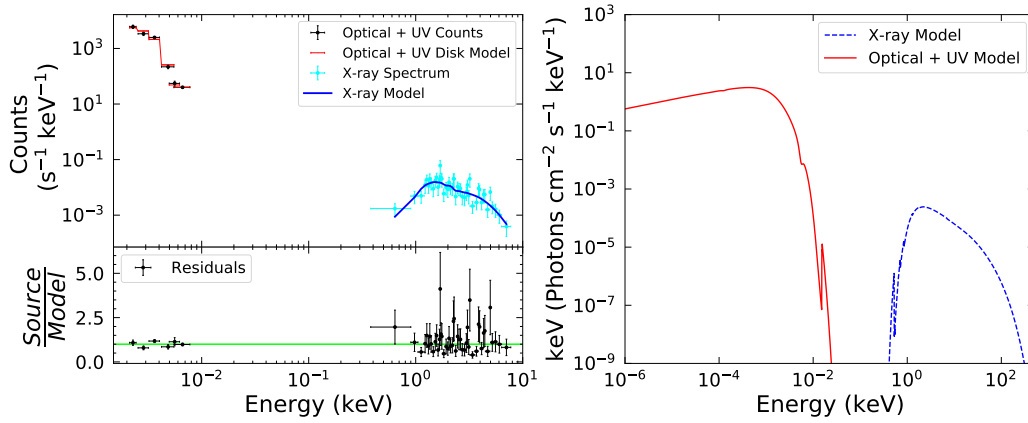
SWIFTJ1023.5+1952



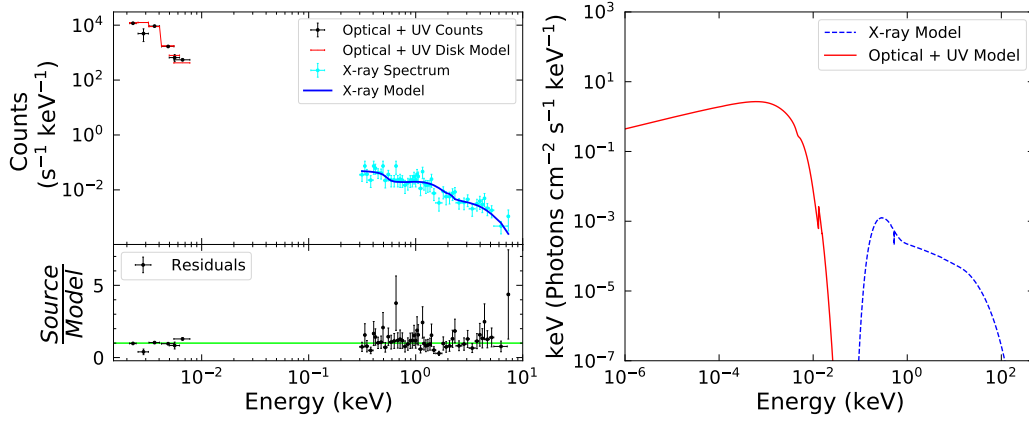
SWIFTJ1031.9-1418



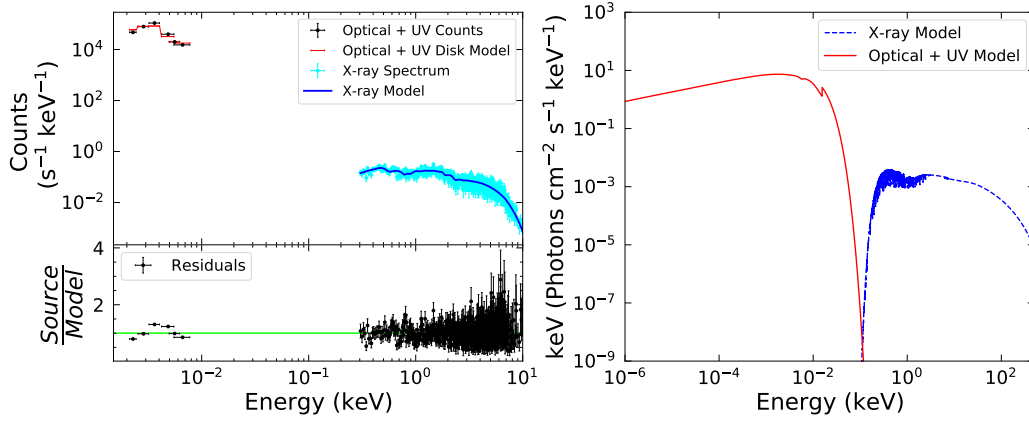
SWIFTJ1051.2-1704B



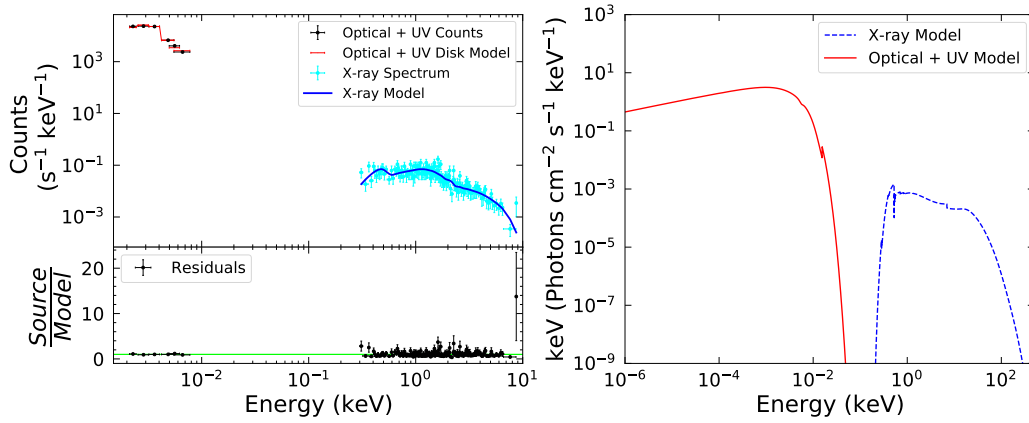
SWIFTJ1105.7+5854B



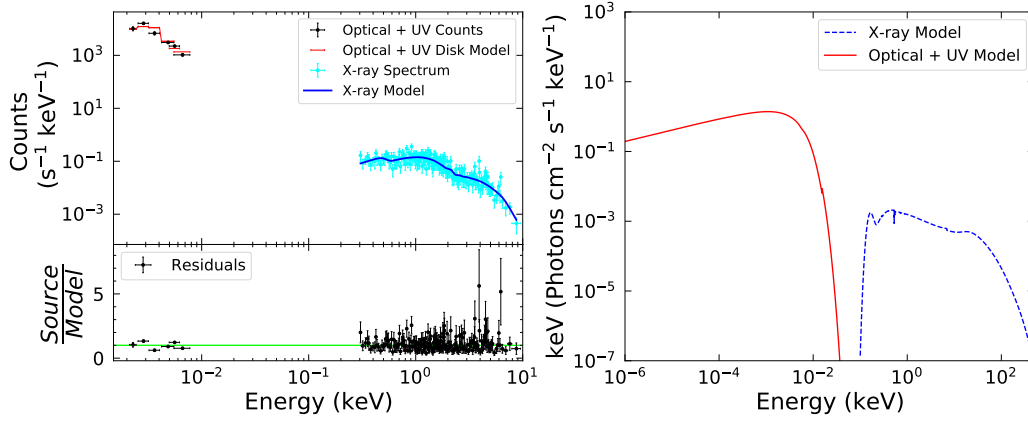
SWIFTJ1106.5+7234



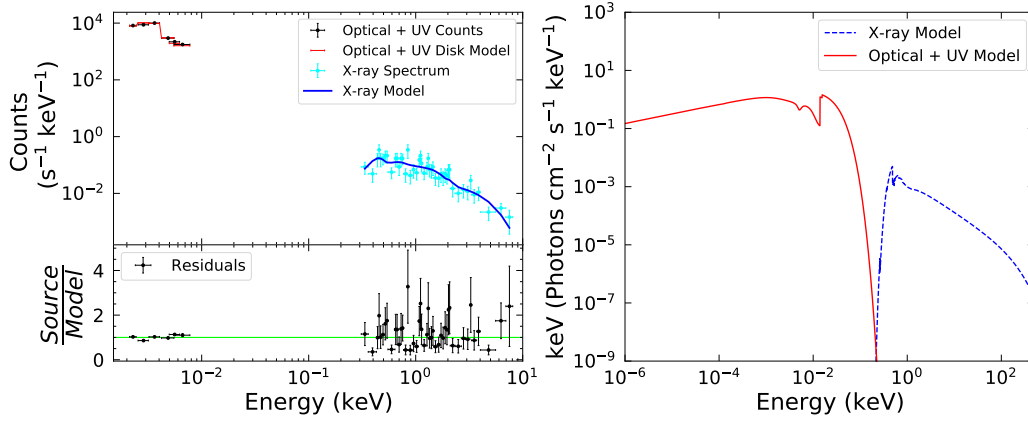
SWIFTJ1110.6-2832



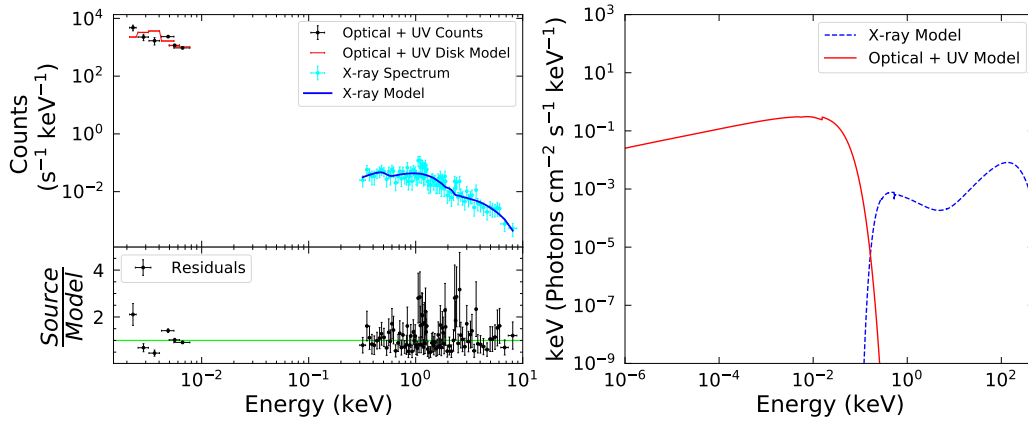
SWIFTJ1113.6+0936



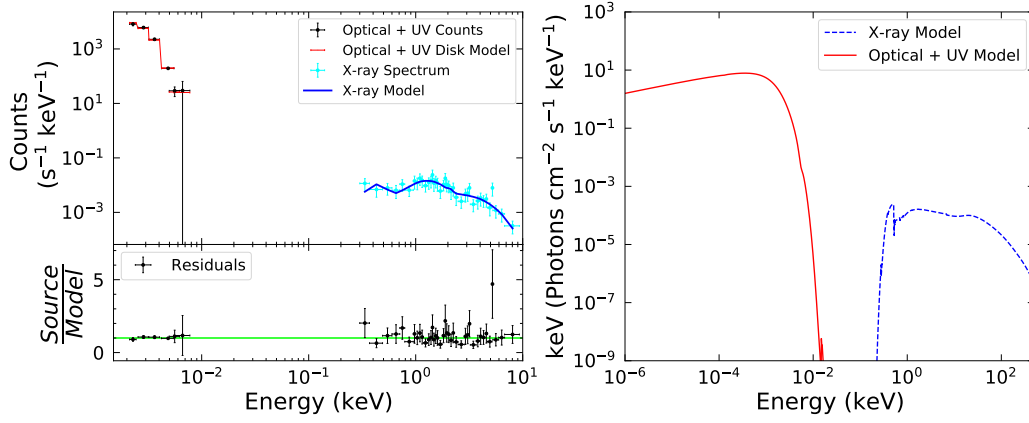
SWIFTJ1119.5+5132



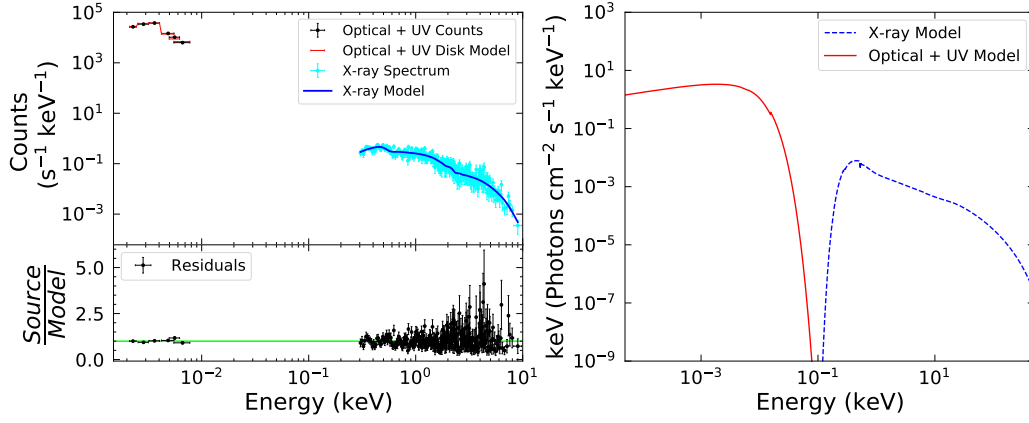
SWIFTJ1125.6+5423



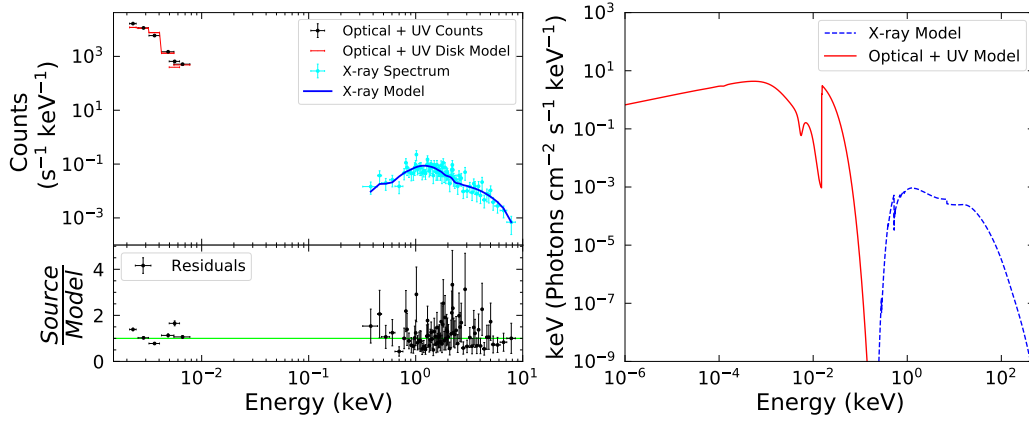
SWIFTJ1132.9+1019A



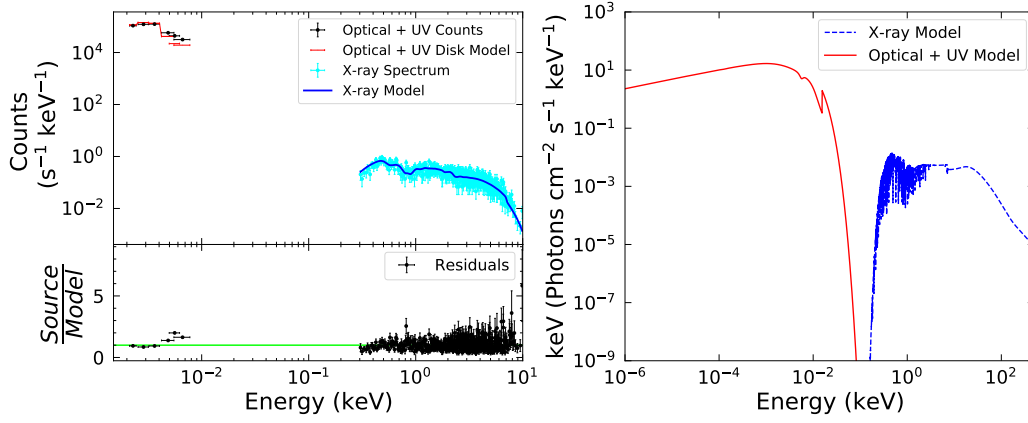
SWIFTJ1139.1+5913



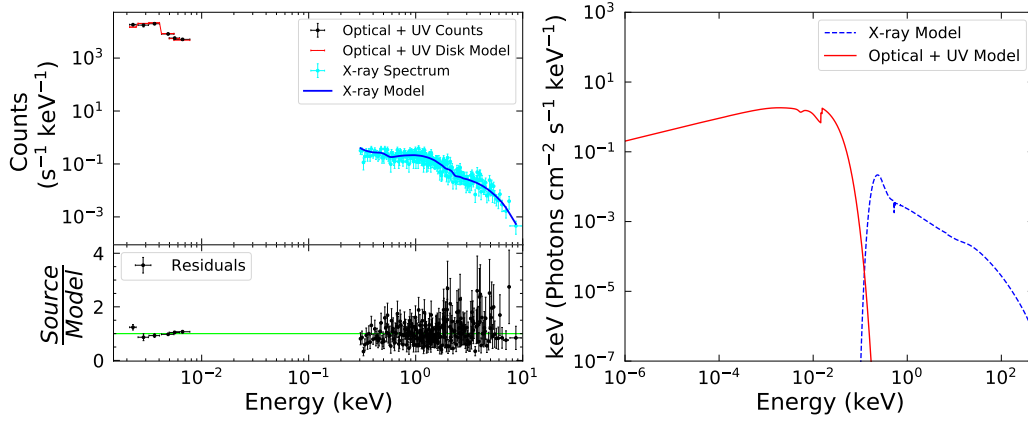
SWIFTJ1139.0-2323



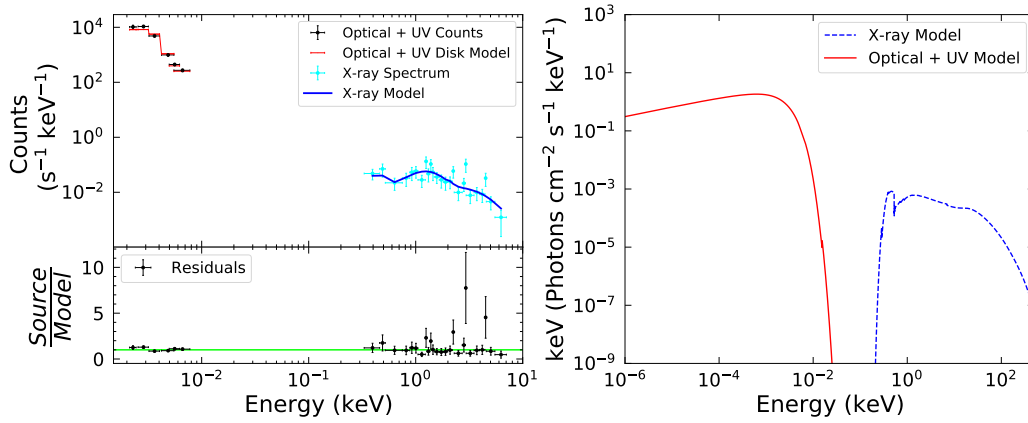
SWIFTJ1139.0-3743



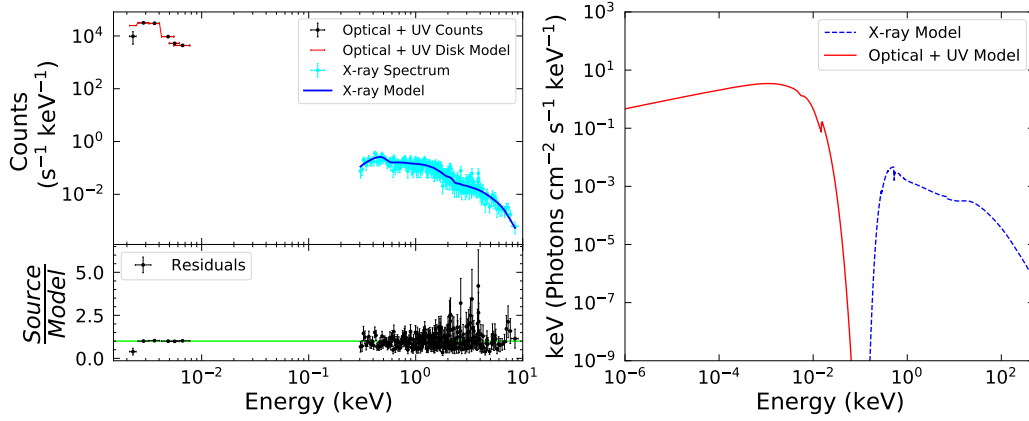
SWIFTJ1141.3+2156



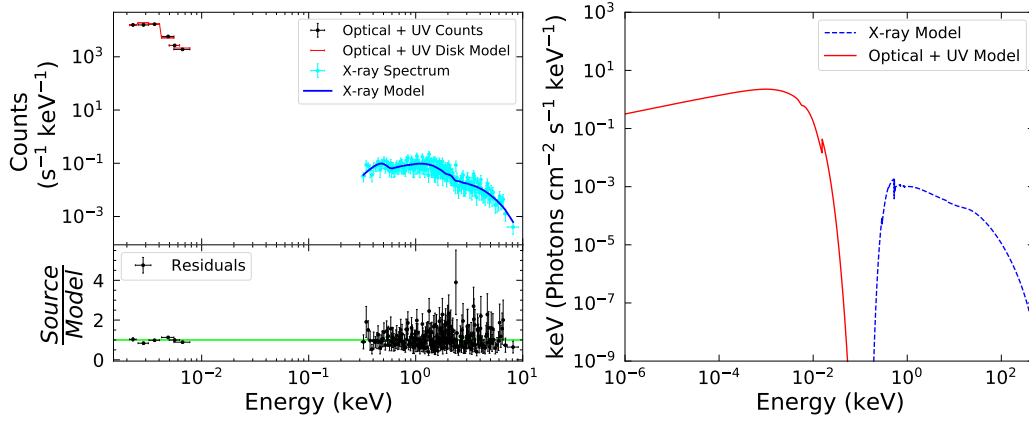
SWIFTJ1142.2+1021



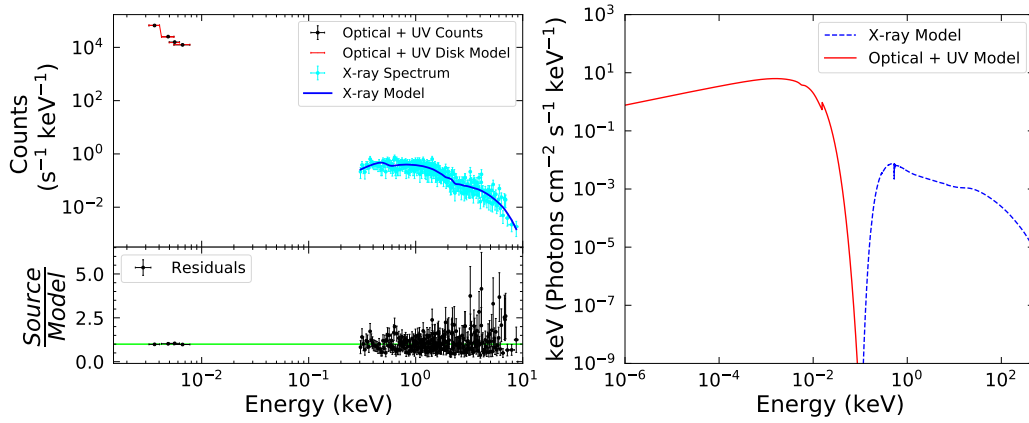
SWIFTJ1144.1+3652



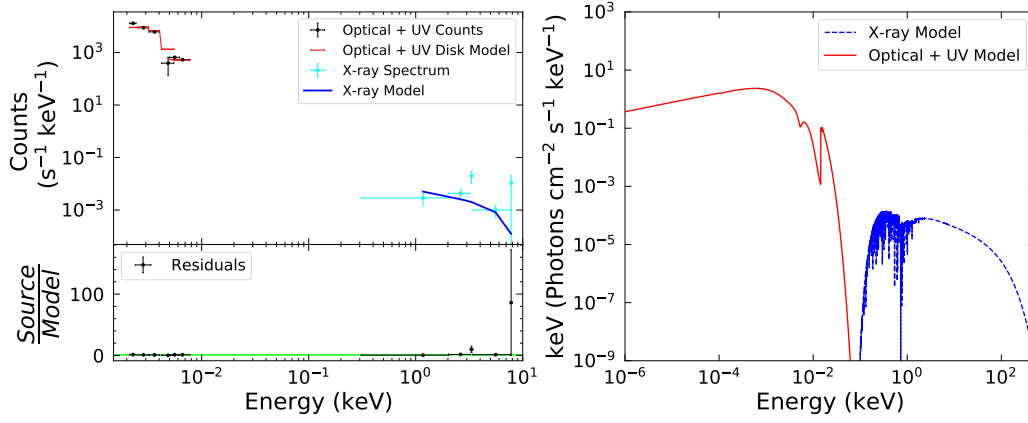
SWIFTJ1143.7+7942



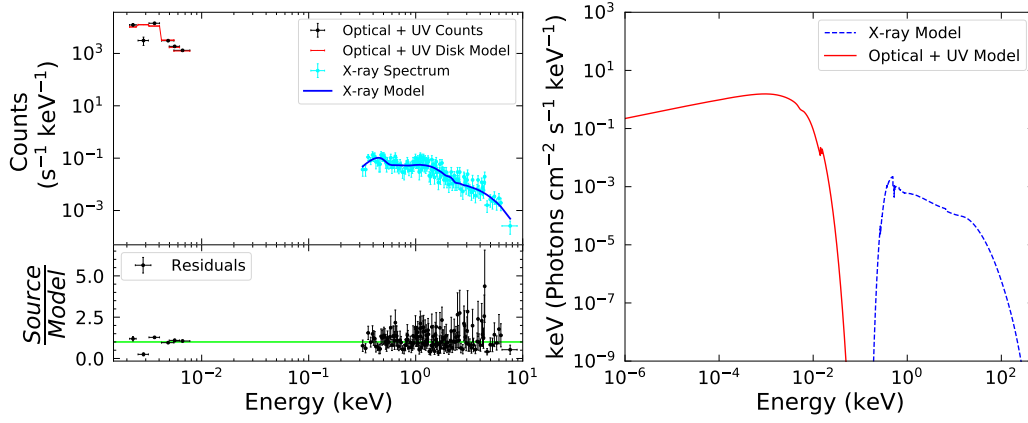
SWIFTJ1145.6-1819



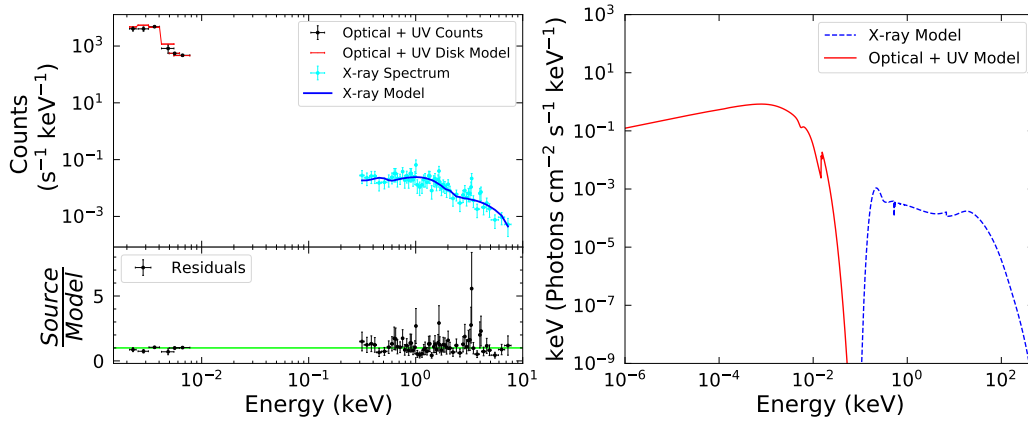
SWIFTJ1148.3+0901



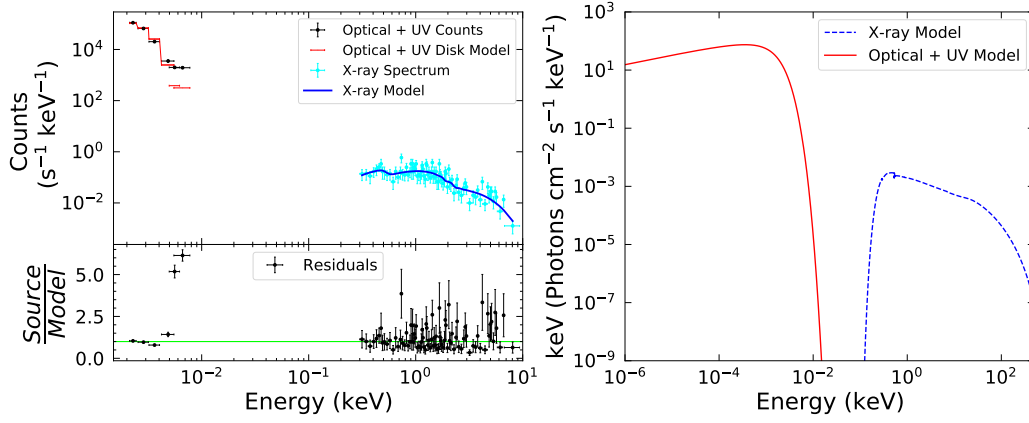
SWIFTJ1149.3-0414



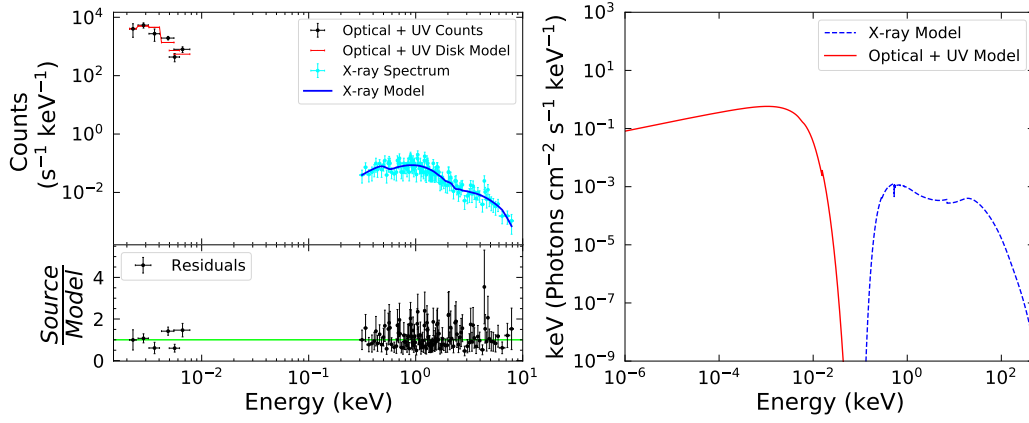
SWIFTJ1152.1-1122



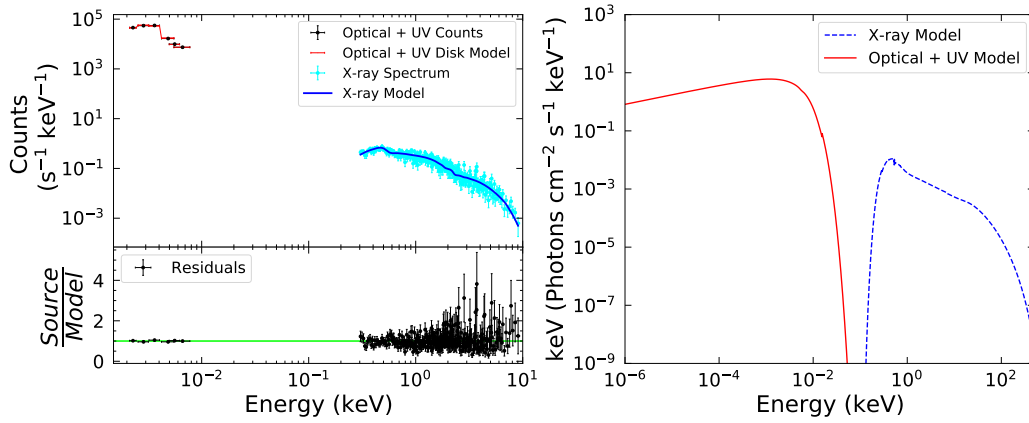
SWIFTJ1157.8+5529



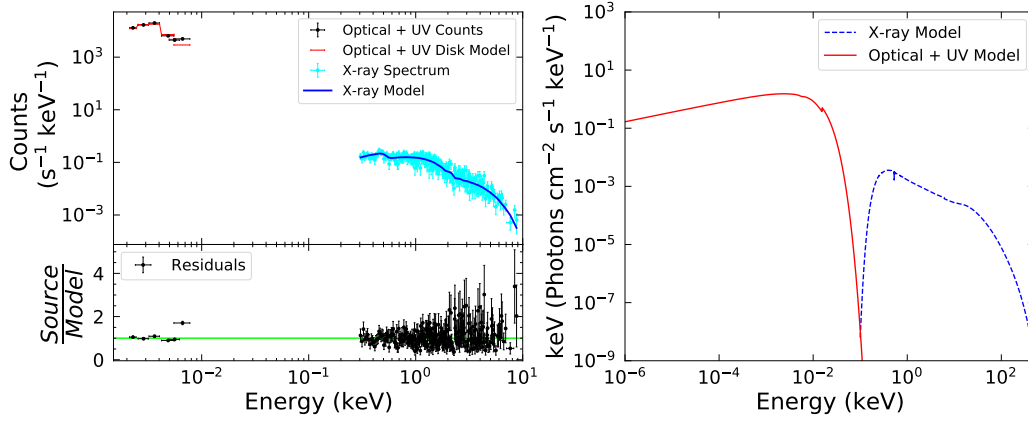
SWIFTJ1201.2-0341



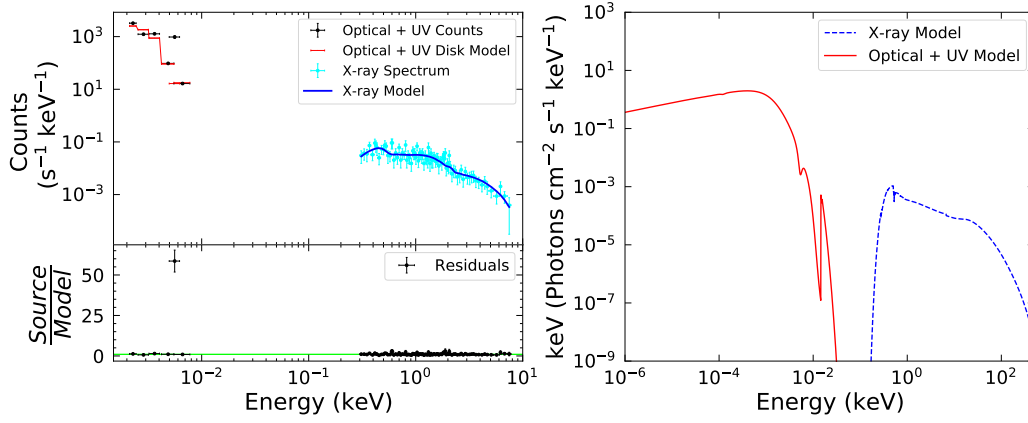
SWIFTJ1203.0+4433



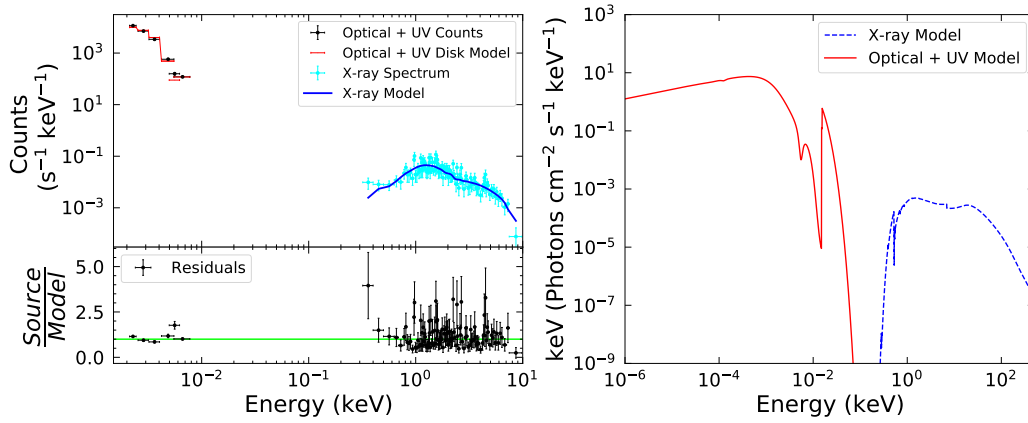
SWIFTJ1204.8+2758



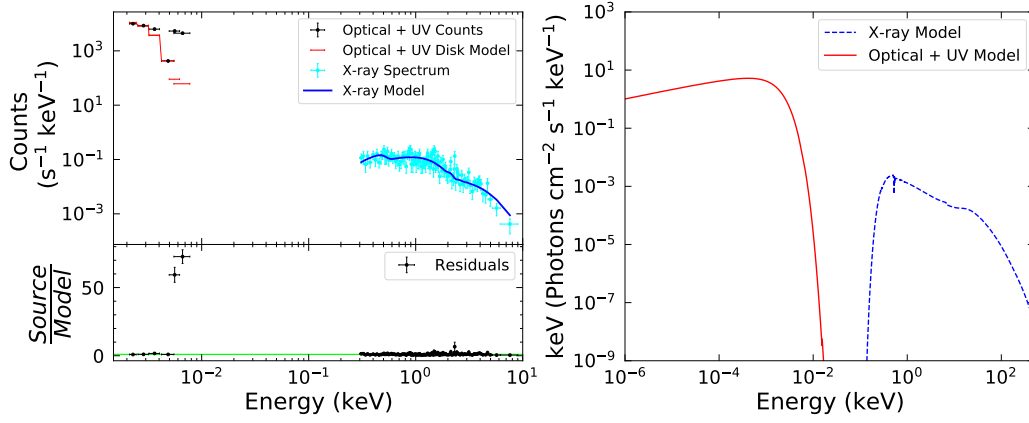
SWIFTJ1205.8+4959



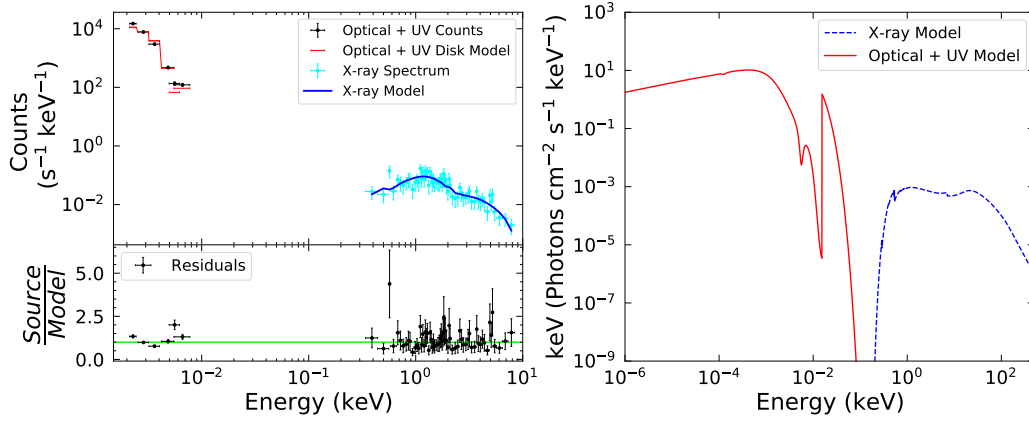
SWIFTJ1210.1-4637



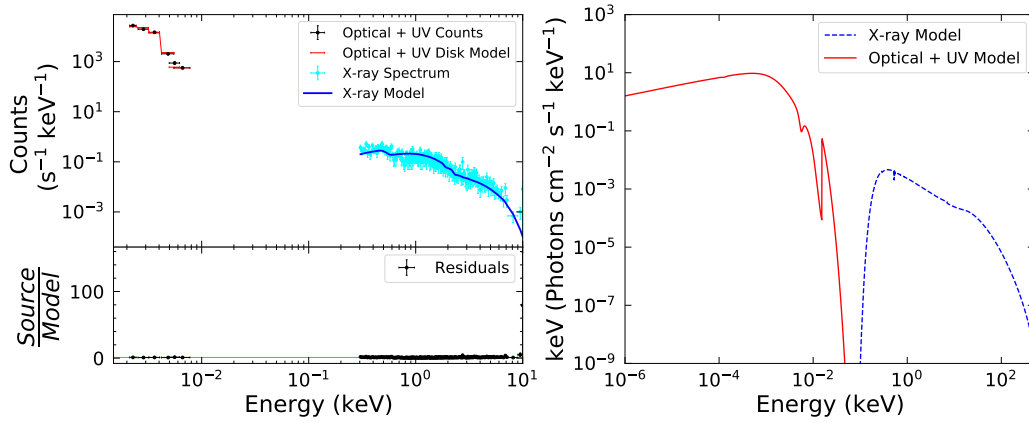
SWIFTJ1213.9-0531



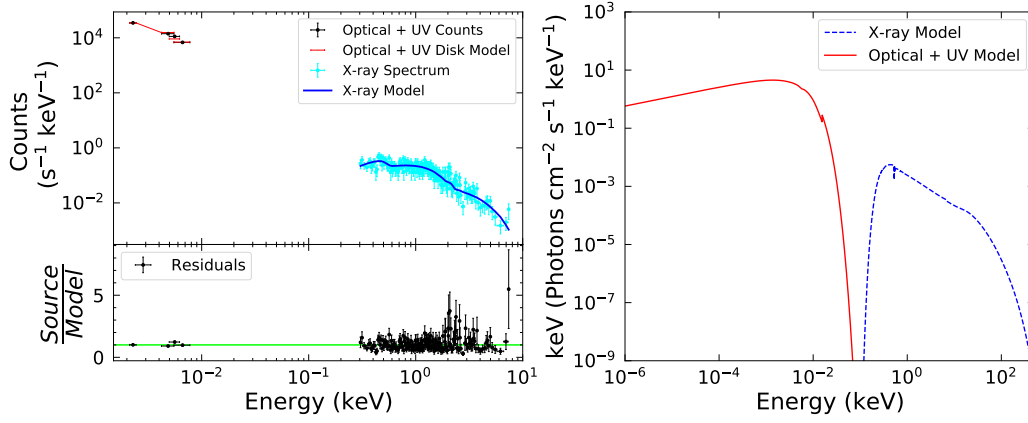
SWIFTJ1217.3+0714



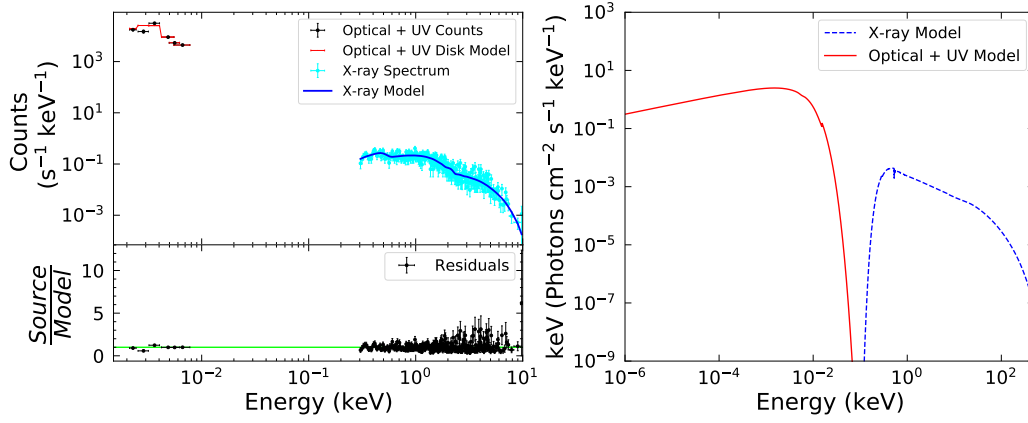
SWIFTJ1218.5+2952



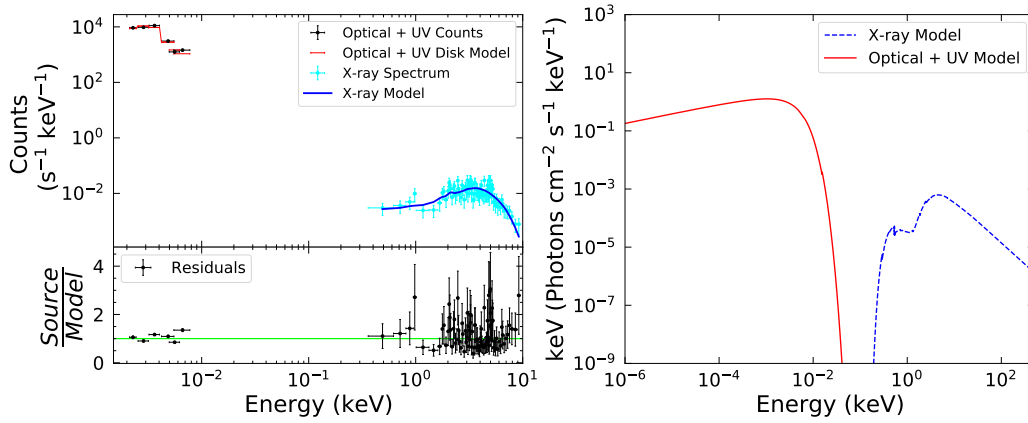
SWIFTJ1222.4+7520



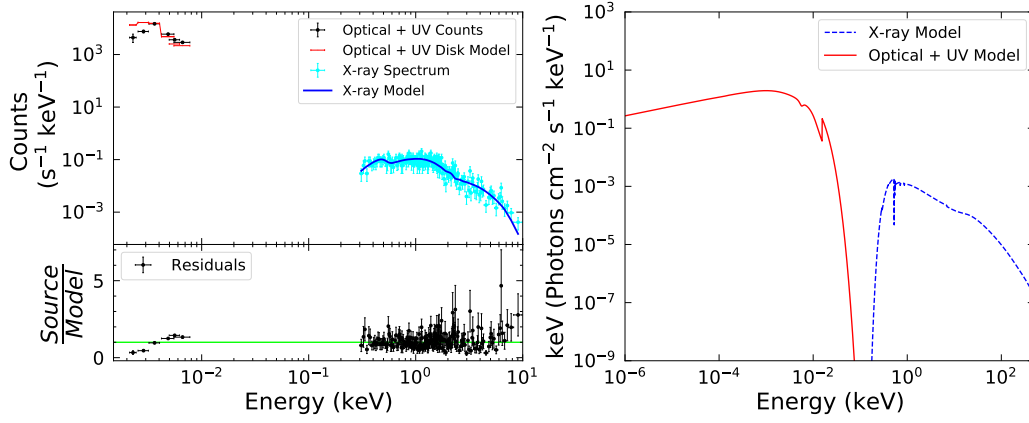
SWIFTJ1223.7+0238



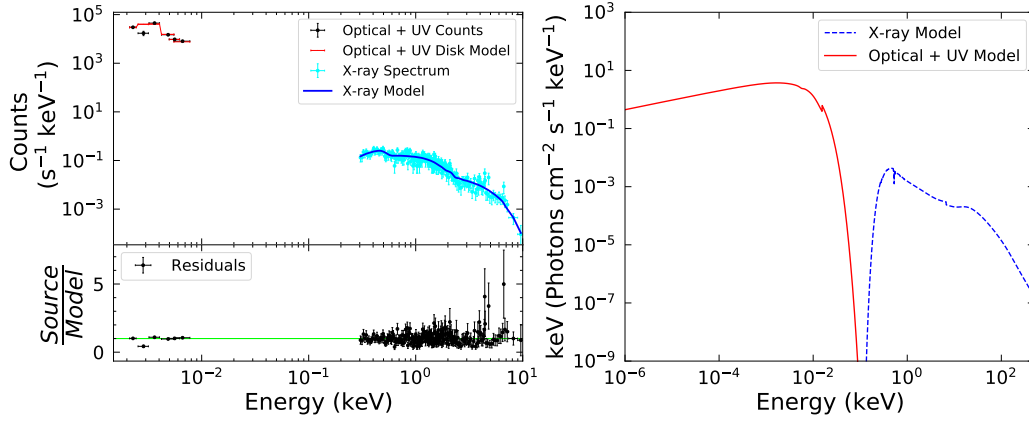
SWIFTJ1202.5+3332



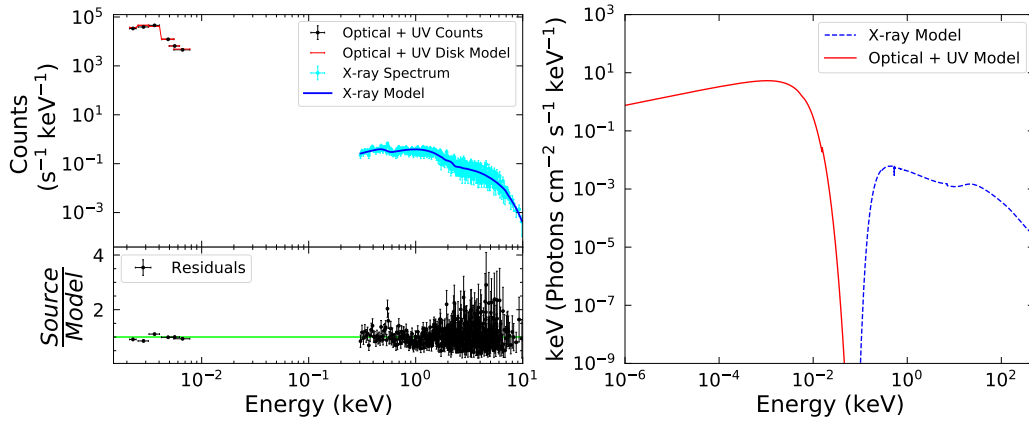
SWIFTJ1232.0-4802



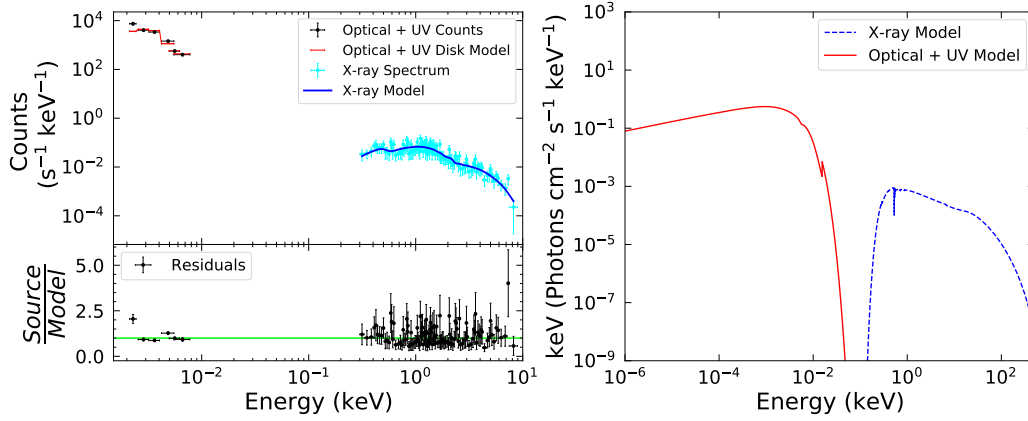
SWIFTJ1232.1+2009



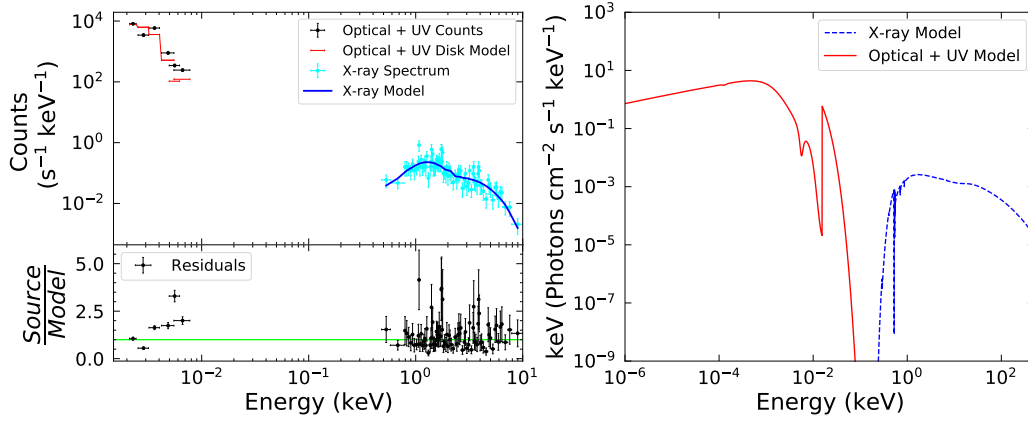
SWIFTJ1239.6-0519



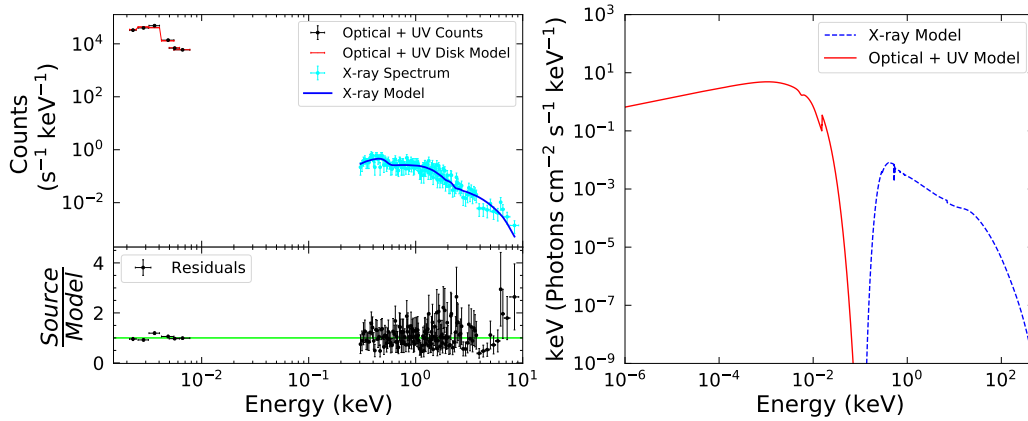
SWIFTJ1240.9-3331



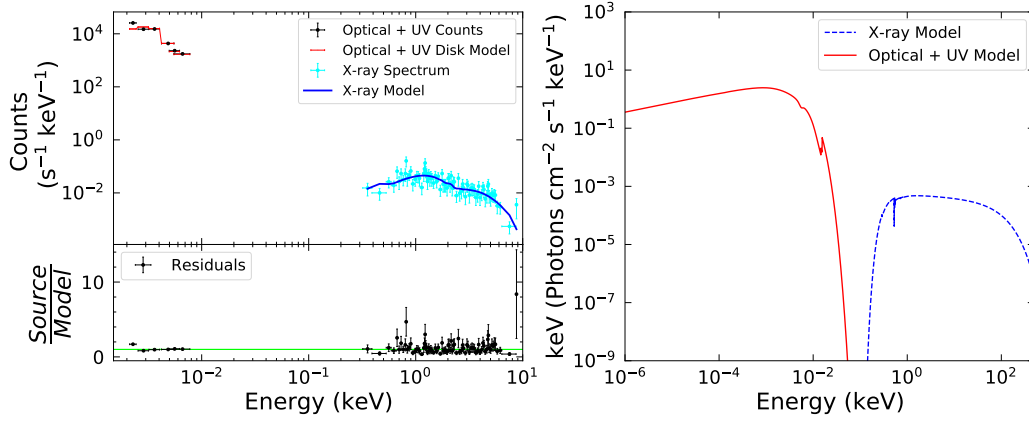
SWIFTJ1241.6-5748



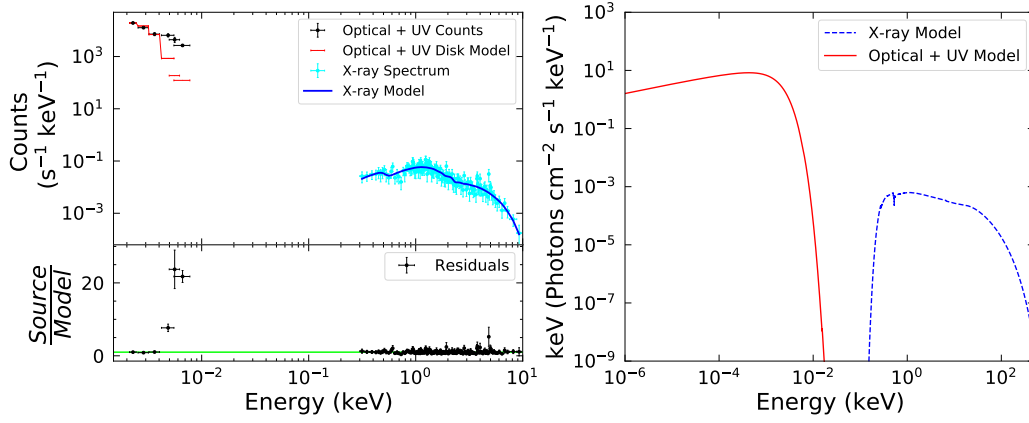
SWIFTJ1252.3-1323



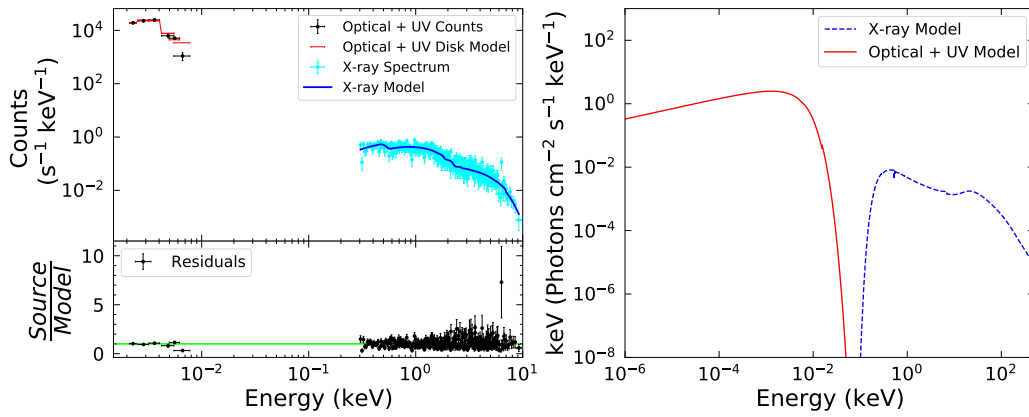
SWIFTJ1255.0-2657



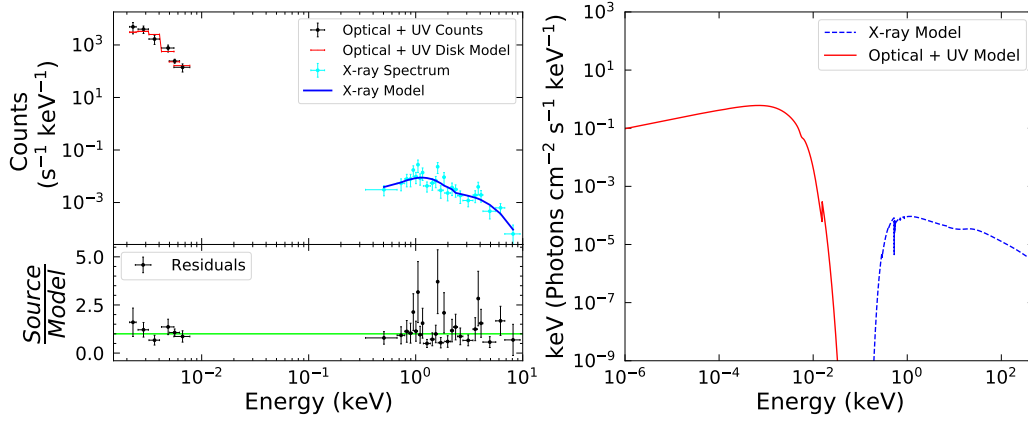
SWIFTJ1302.9+1620



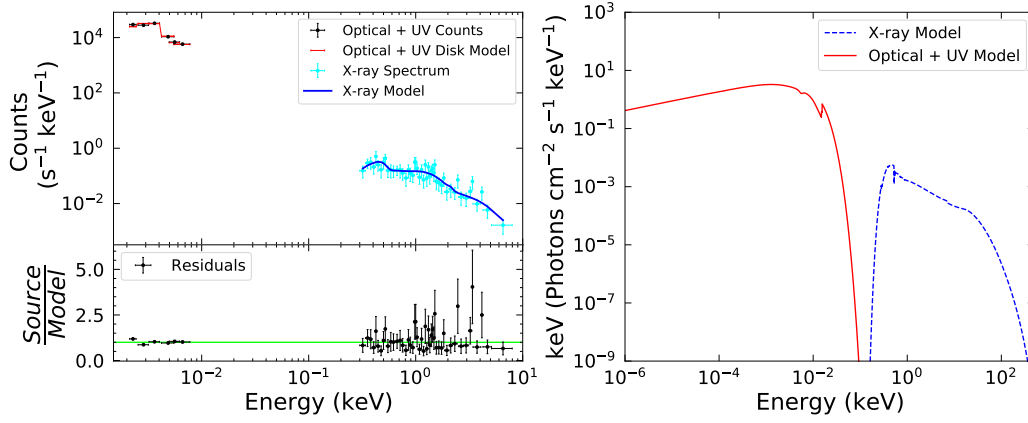
SWIFTJ1303.8+5345



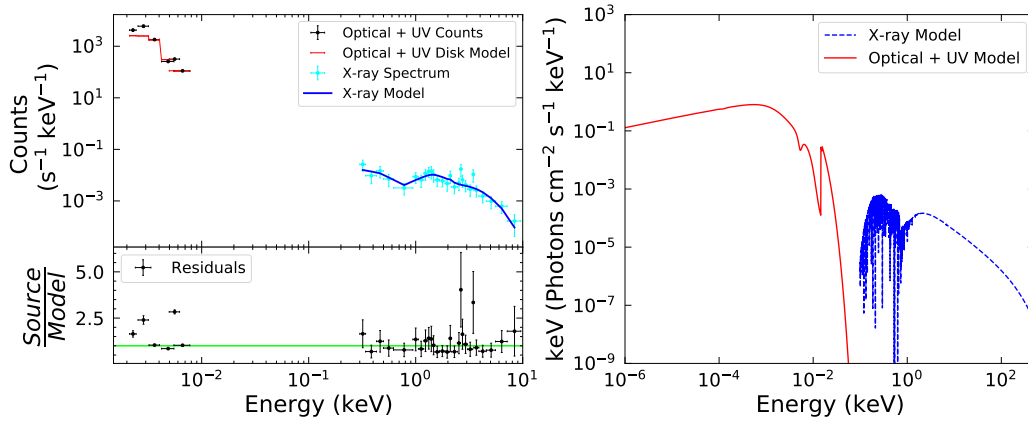
SWIFTJ1306.4-4025B



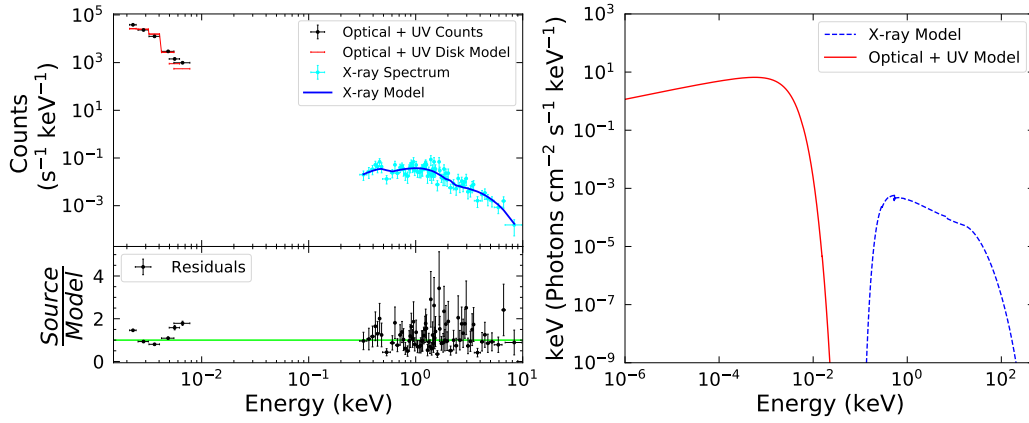
SWIFTJ1313.1-1108



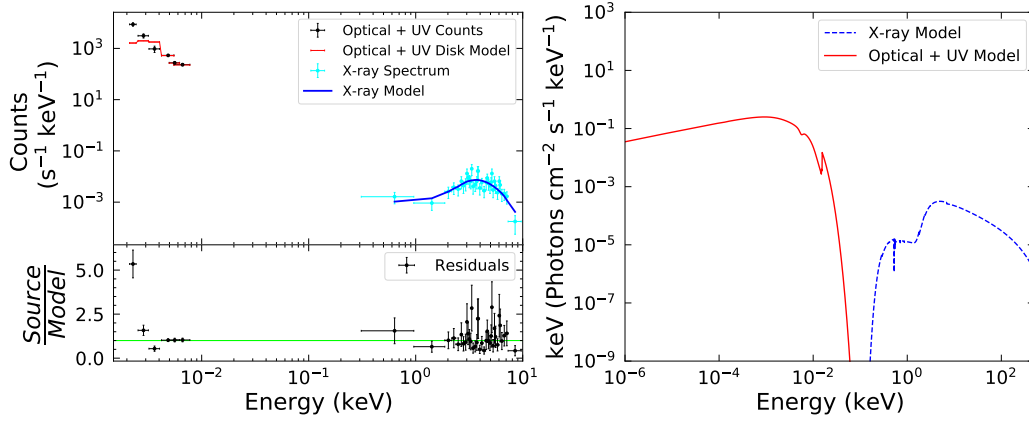
SWIFTJ1313.6+3650A



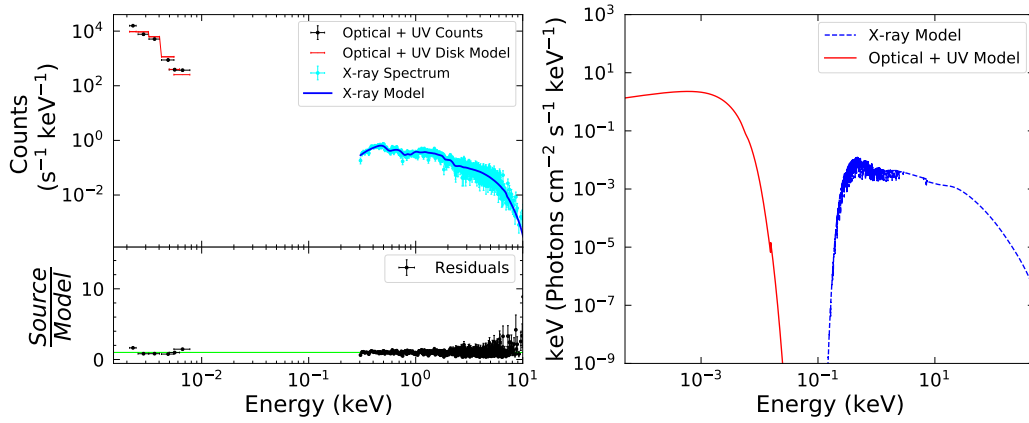
SWIFTJ1313.6+3650B



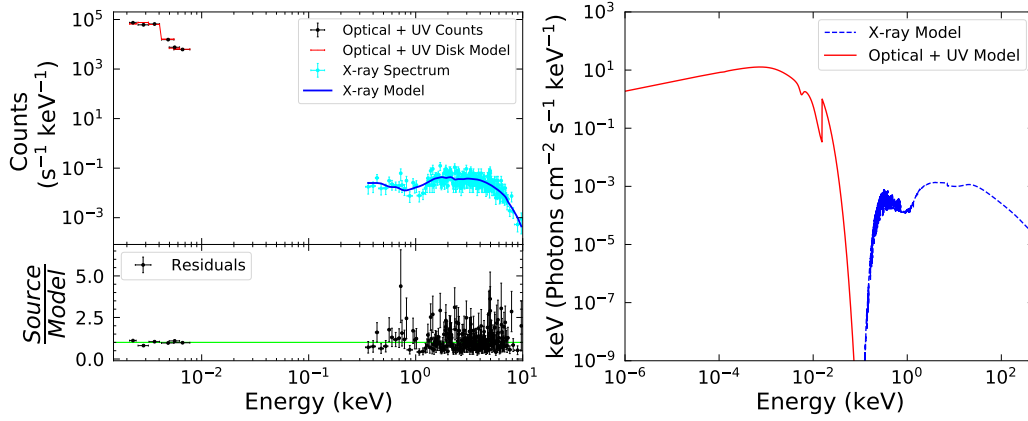
SWIFTJ1334.8-2328D2



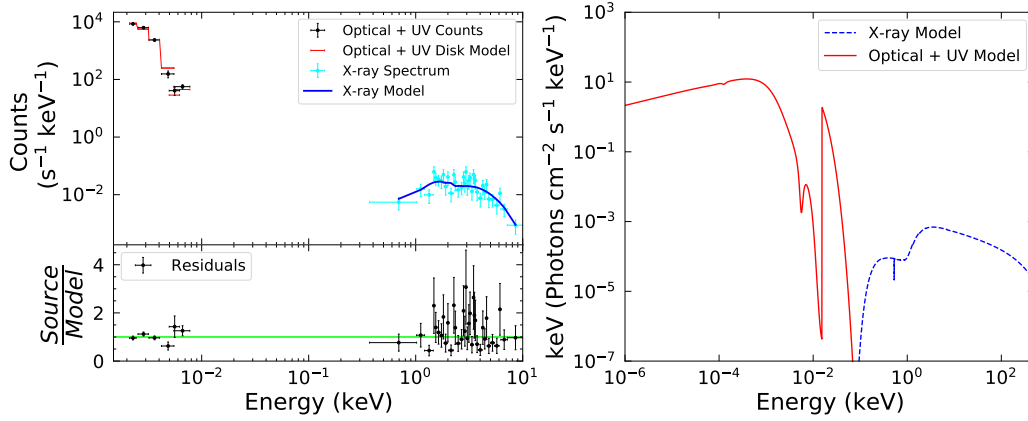
SWIFTJ1335.8-3416



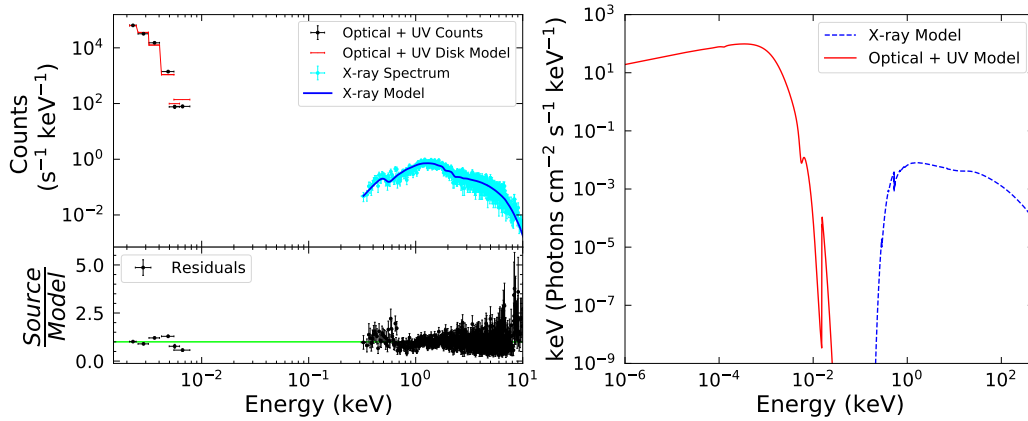
SWIFTJ1341.9+3537



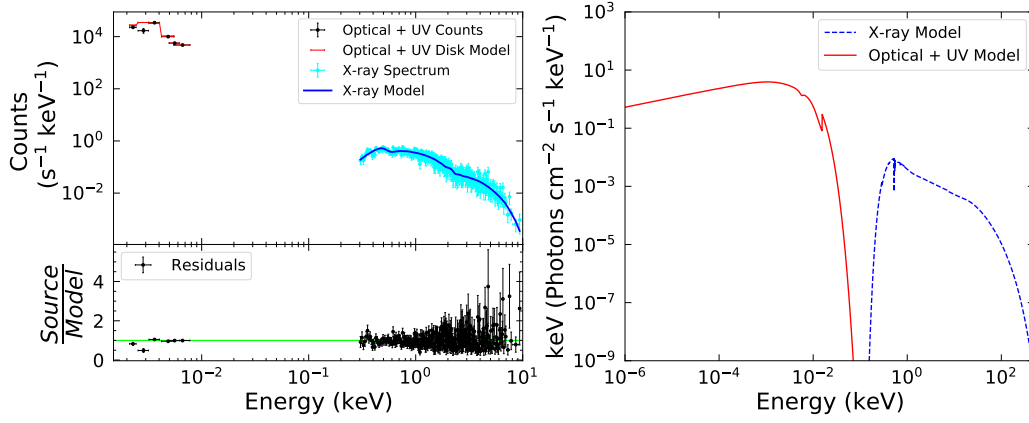
SWIFTJ1345.5+4139



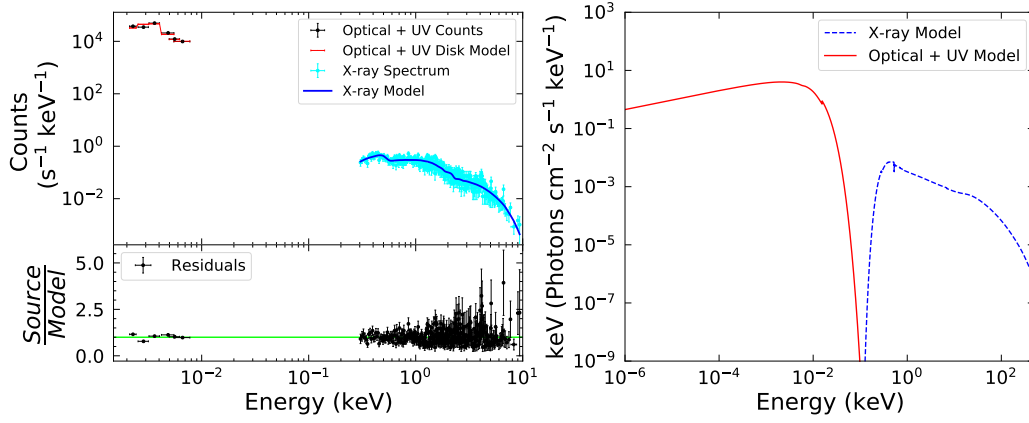
SWIFTJ1349.3-3018



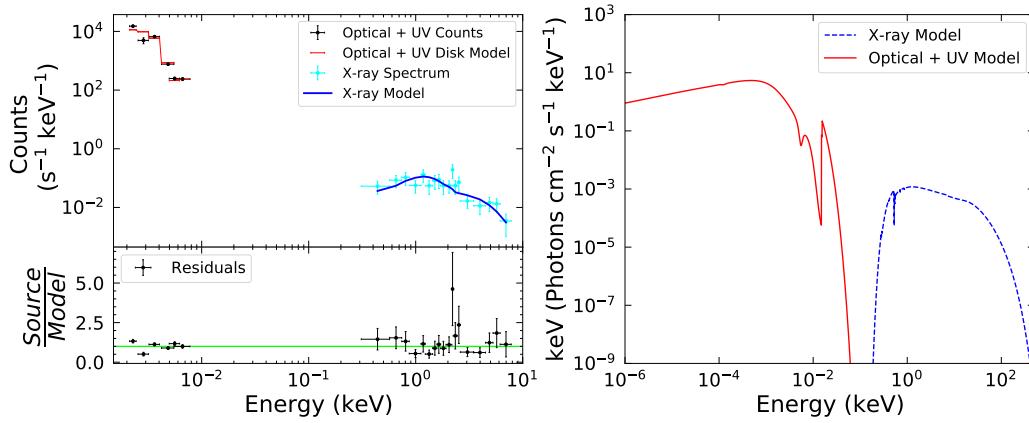
SWIFTJ1351.5-1814



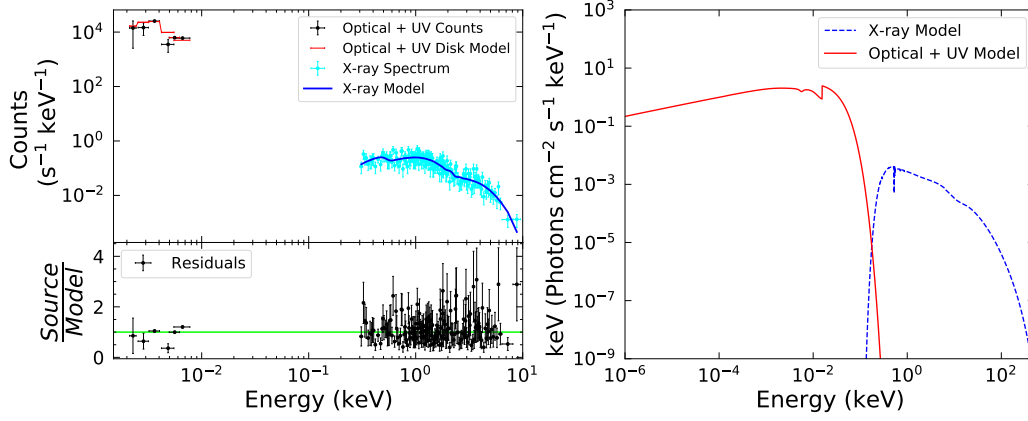
SWIFTJ1352.8+6917



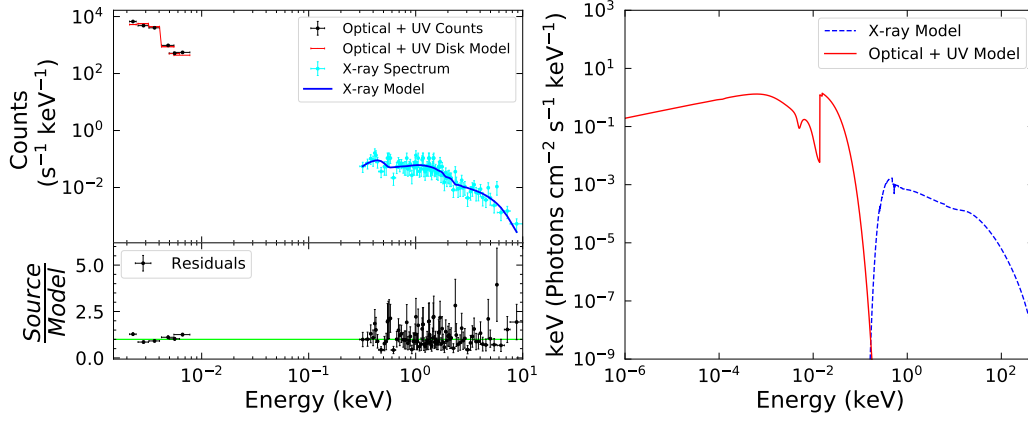
SWIFTJ1356.6-1932



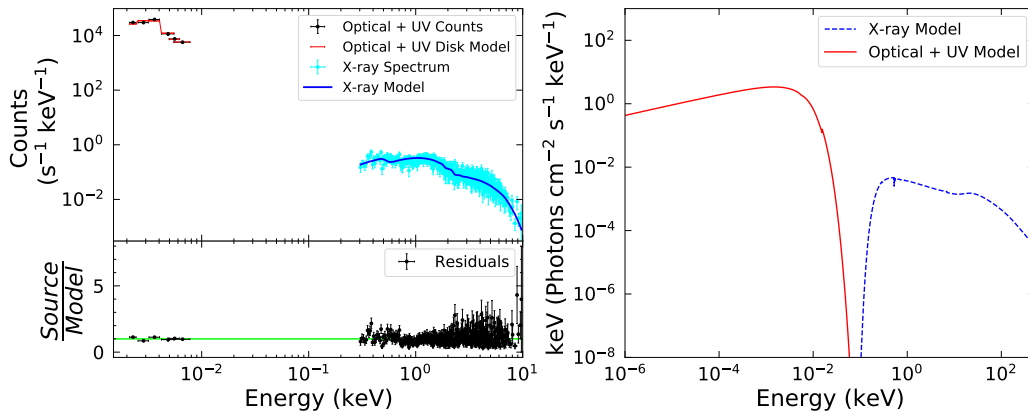
SWIFTJ1416.9-1158



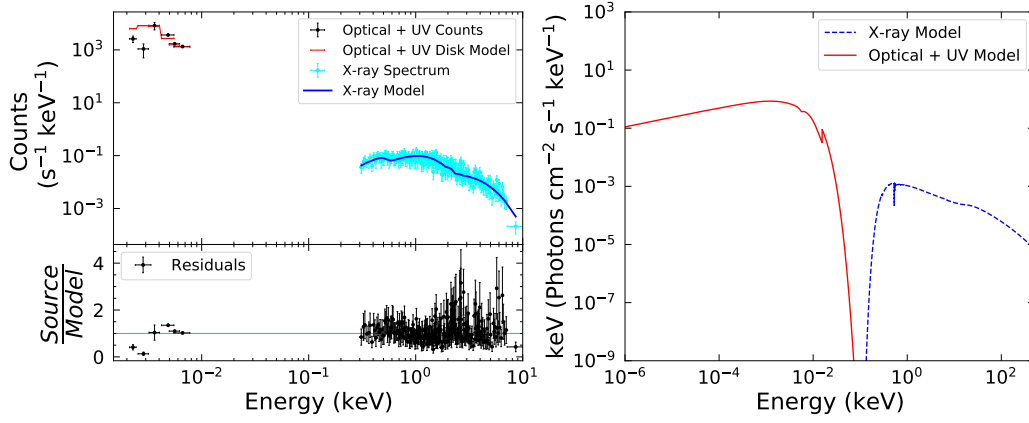
SWIFTJ1417.7+6143



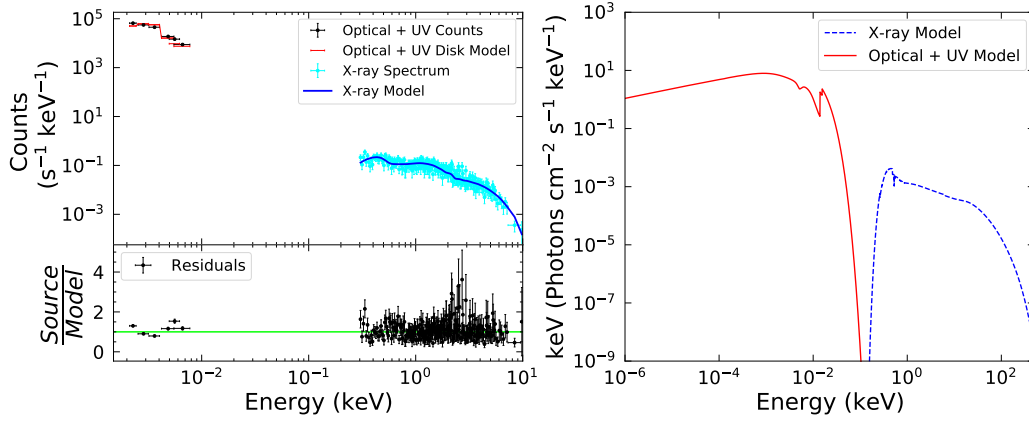
SWIFTJ1417.9+2507



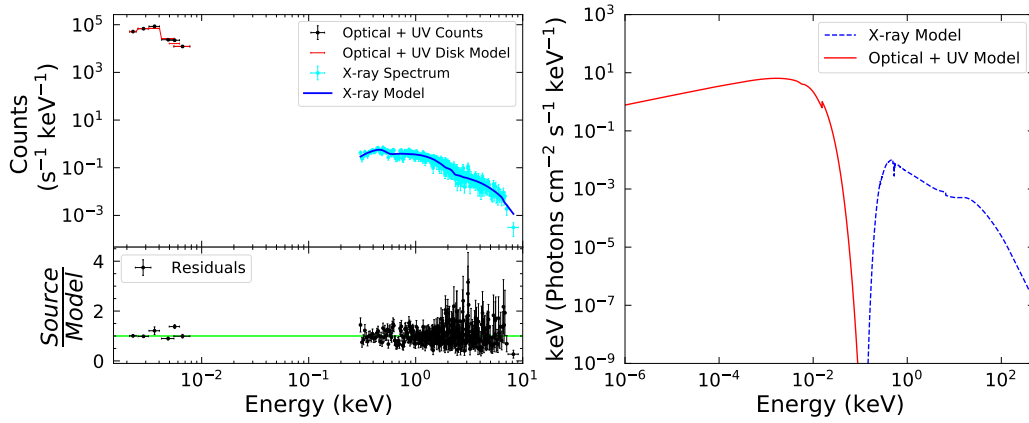
SWIFTJ1419.0-2639



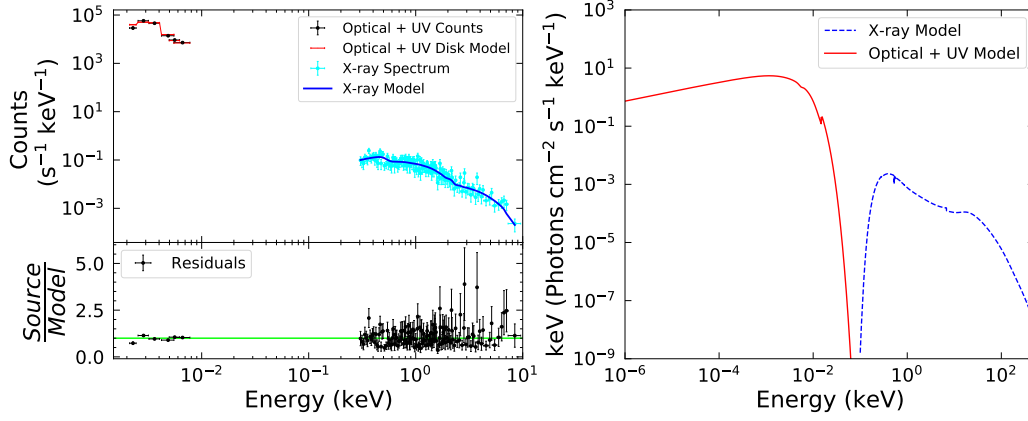
SWIFTJ1427.5+1949



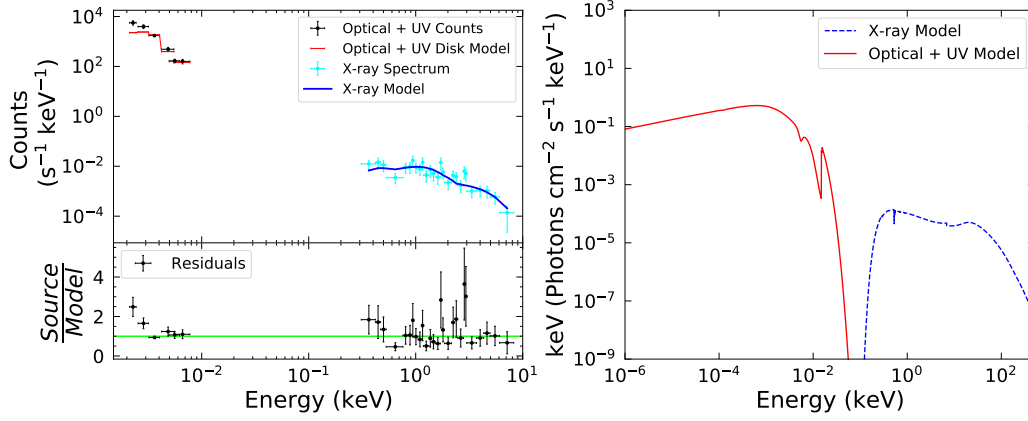
SWIFTJ1429.2+0118



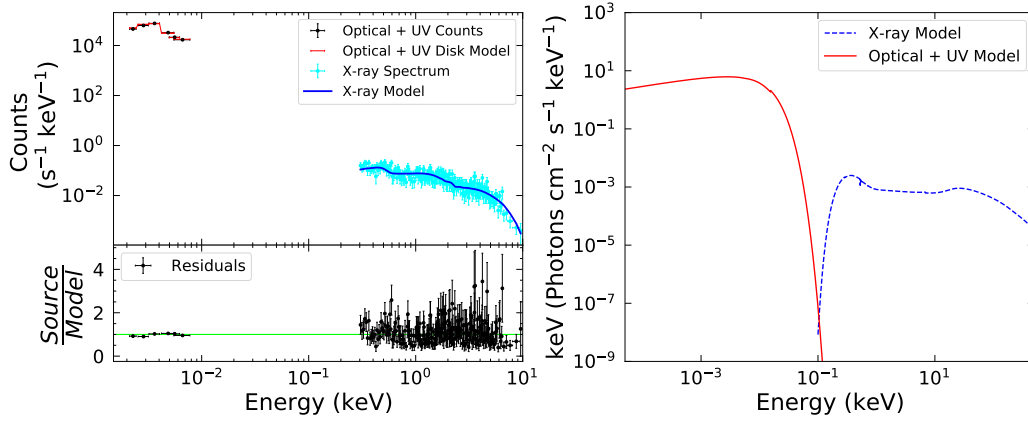
SWIFTJ1431.2+2816



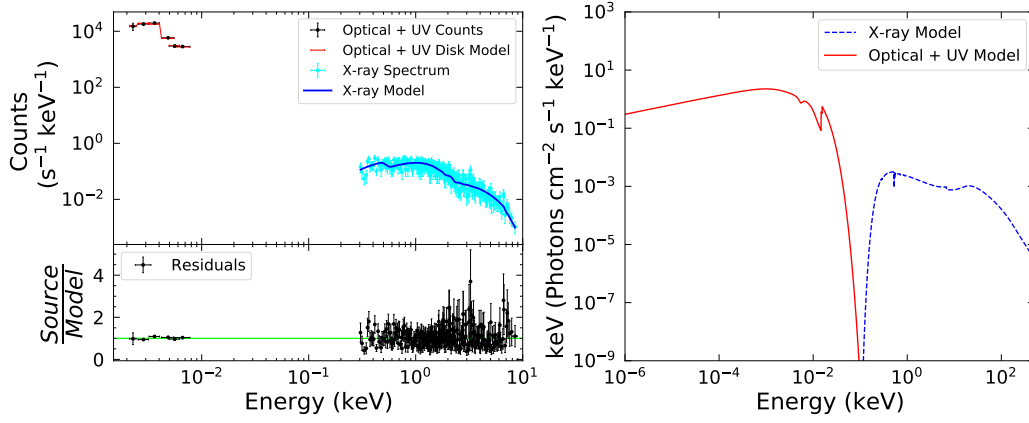
SWIFTJ1434.9+4837



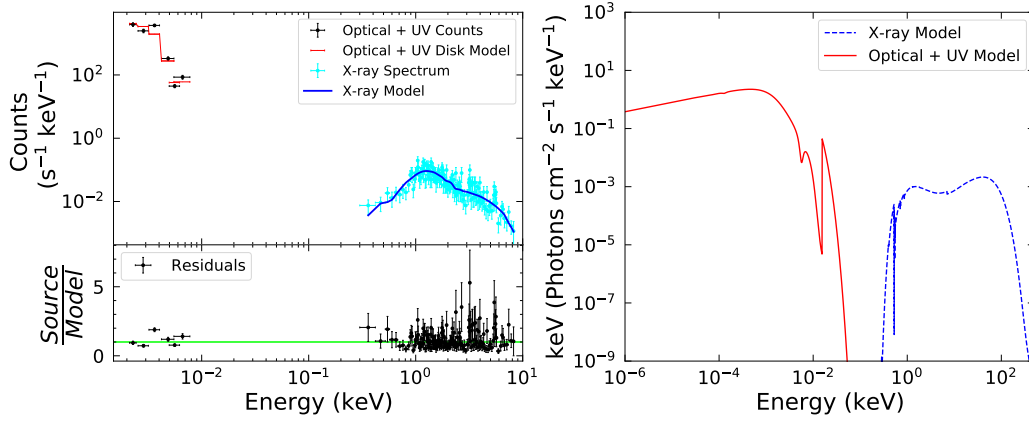
SWIFTJ1436.4+5846



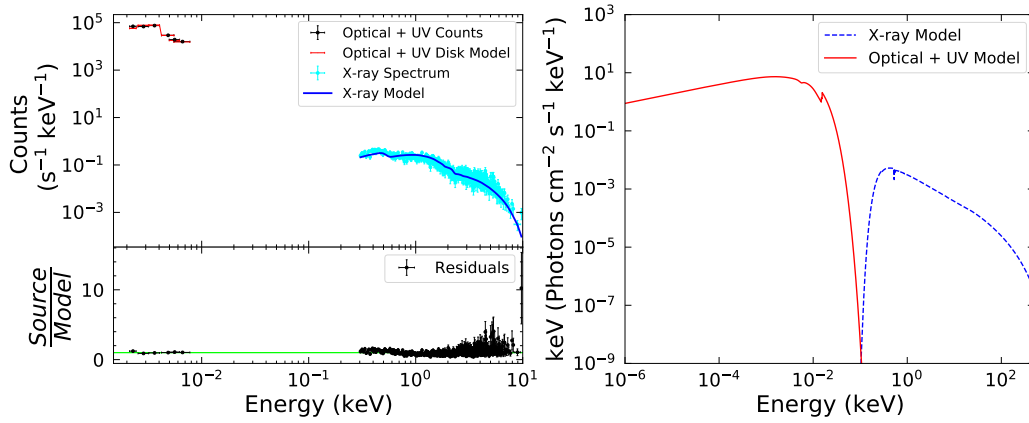
SWIFTJ1453.3+2558



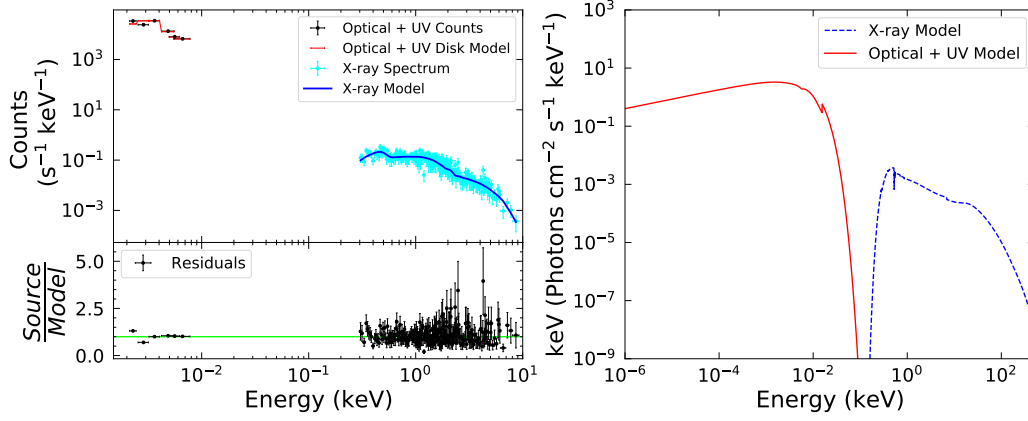
SWIFTJ1454.9-5133



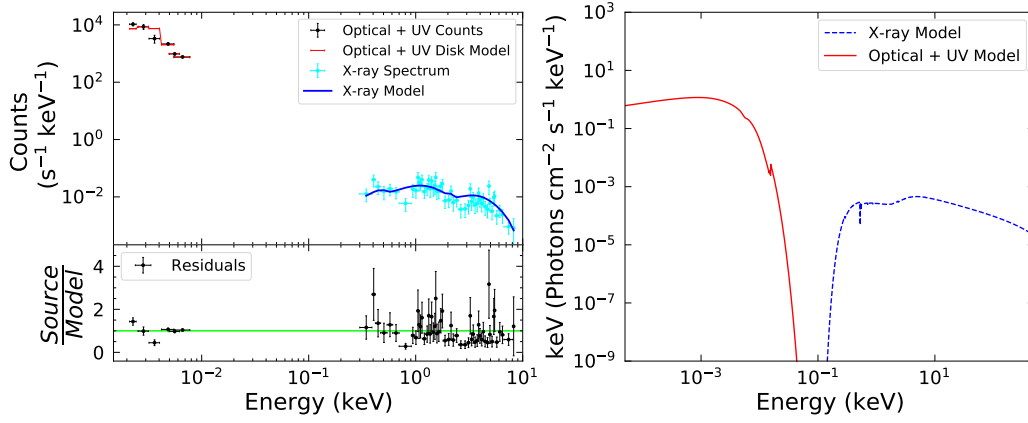
SWIFTJ1504.2+1025



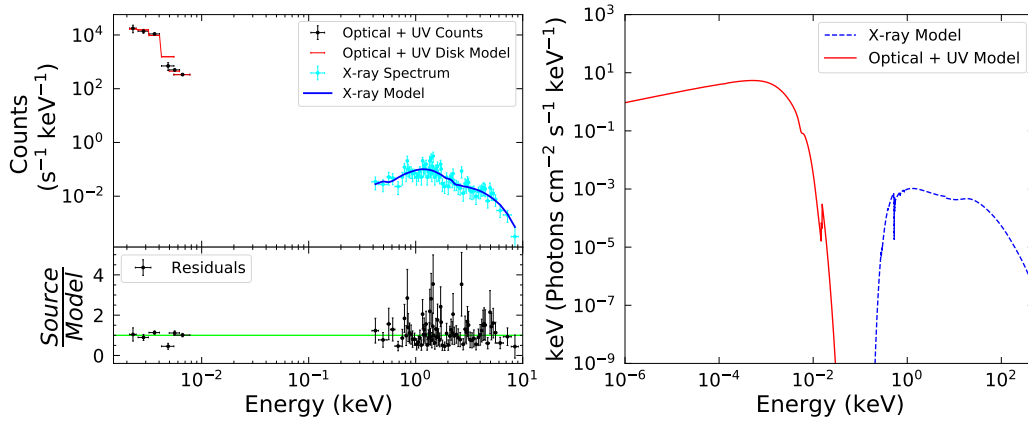
SWIFTJ1506.7+0353A



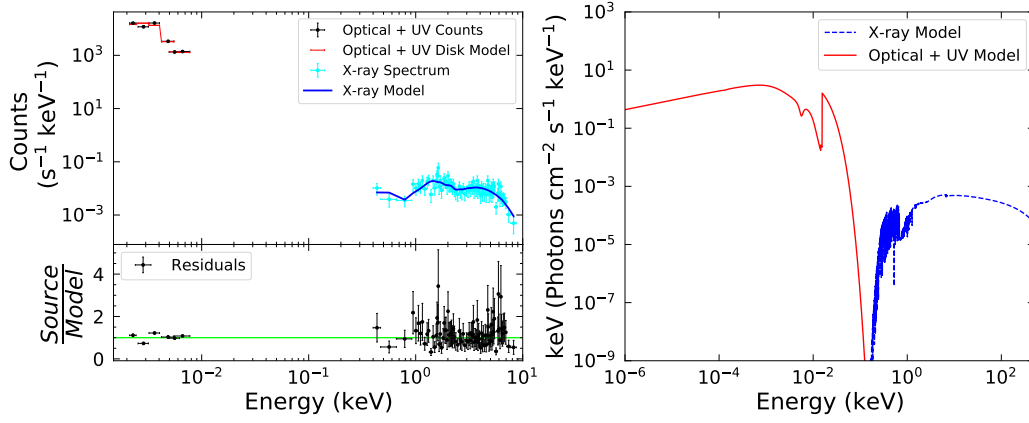
SWIFTJ1508.8-0013



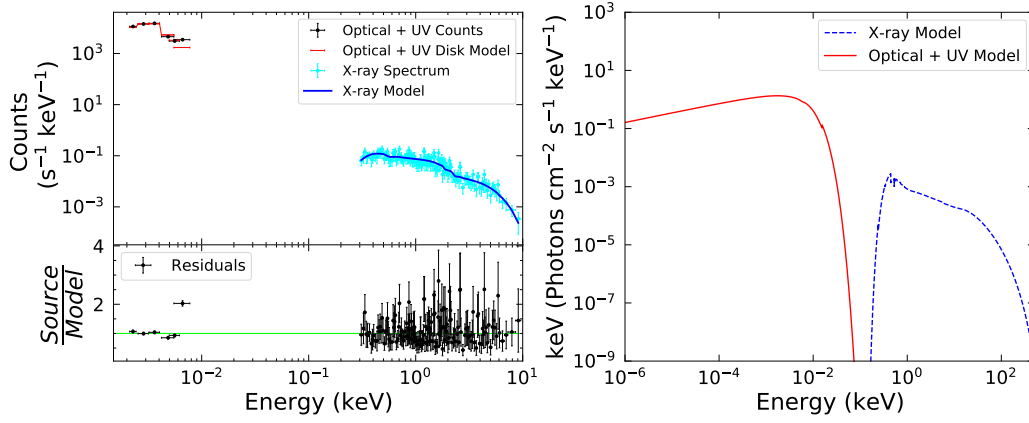
SWIFTJ1512.0-2119



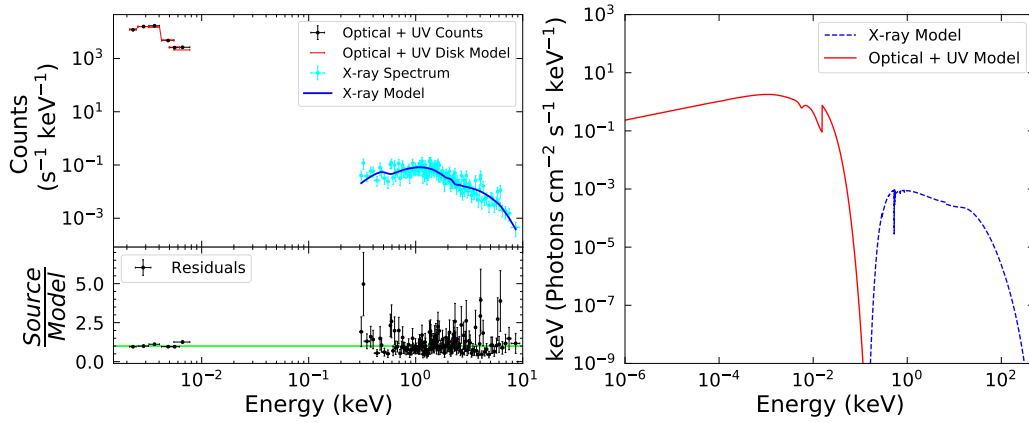
SWIFTJ1513.8-8125



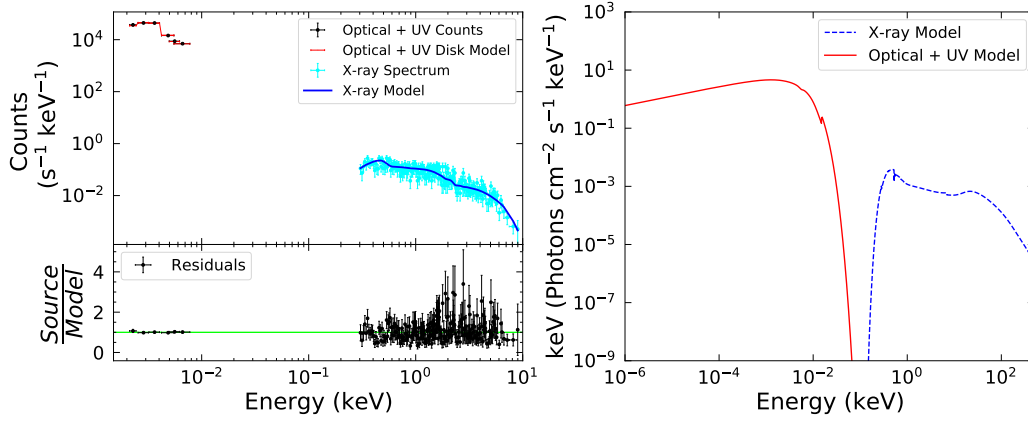
SWIFTJ1523.5+6340



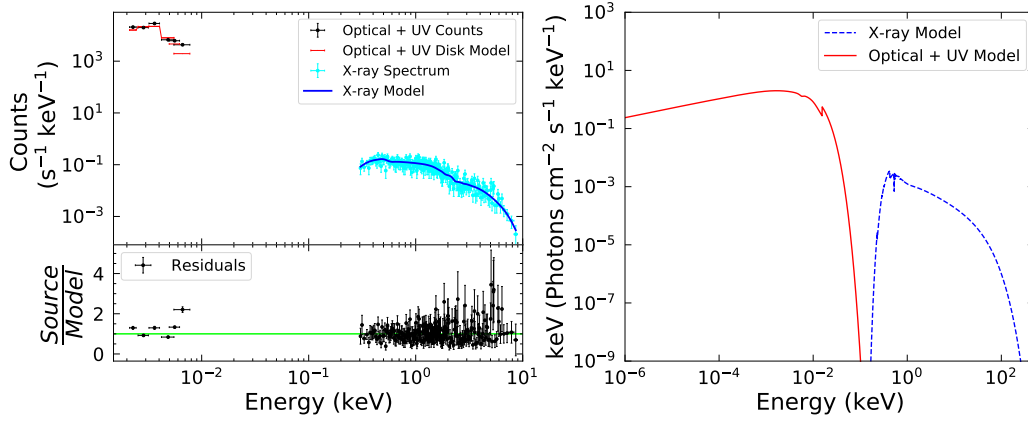
SWIFTJ1530.0-1300



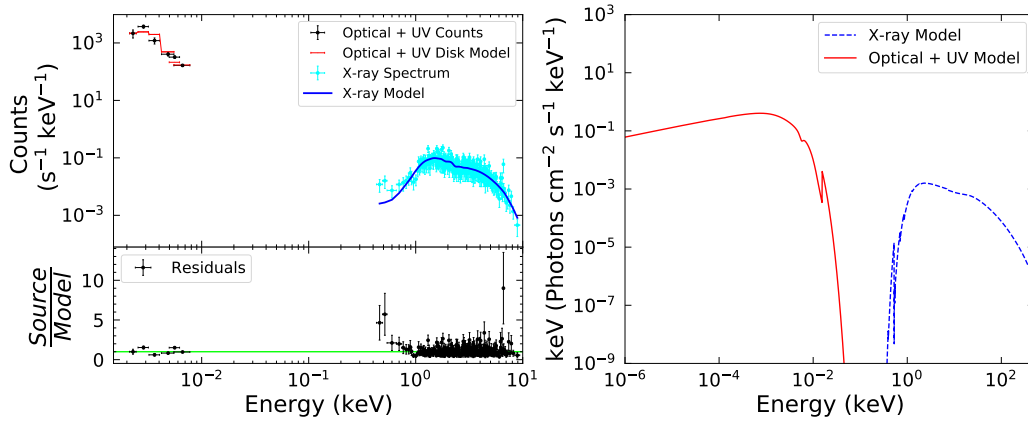
SWIFTJ1535.9+5751



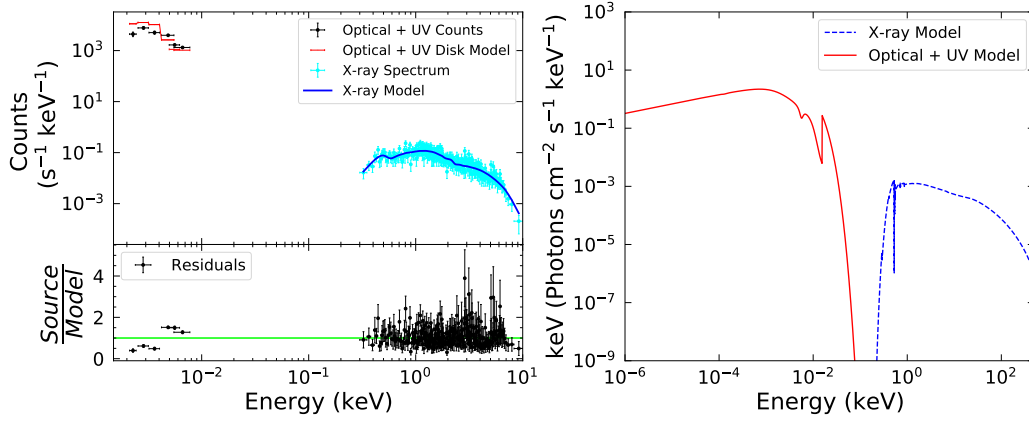
SWIFTJ1547.5+2050



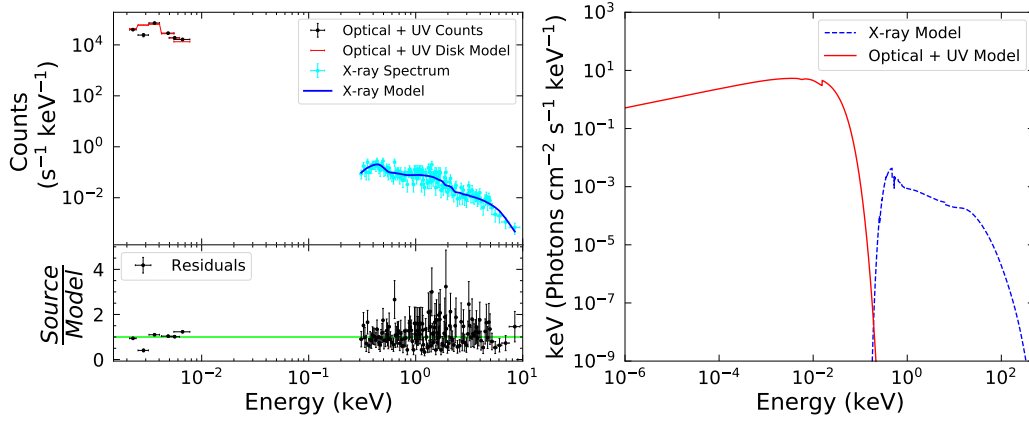
SWIFTJ1548.5-1344



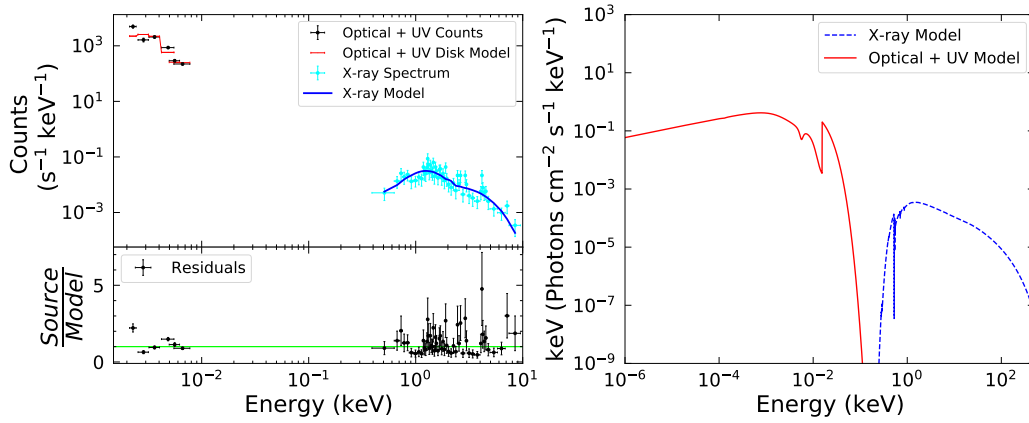
SWIFTJ1613.2-6043



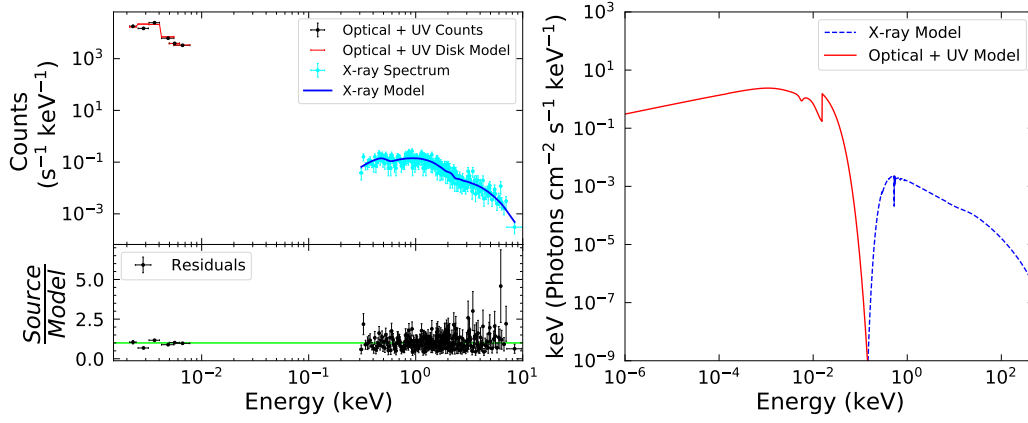
SWIFTJ1614.0+6544



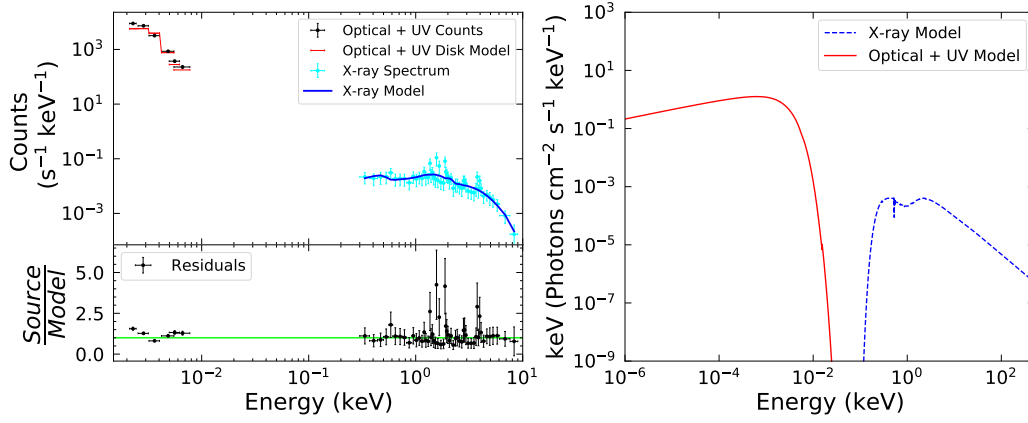
SWIFTJ1618.7-5930



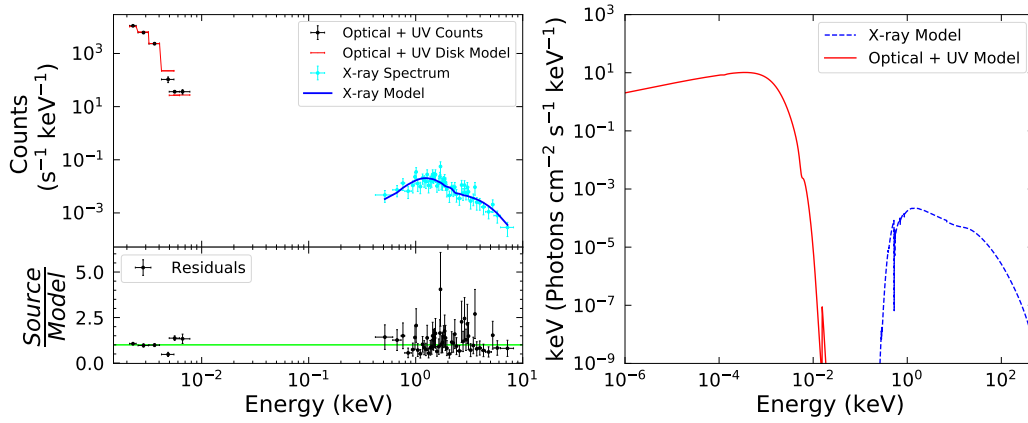
SWIFTJ1626.7+8530



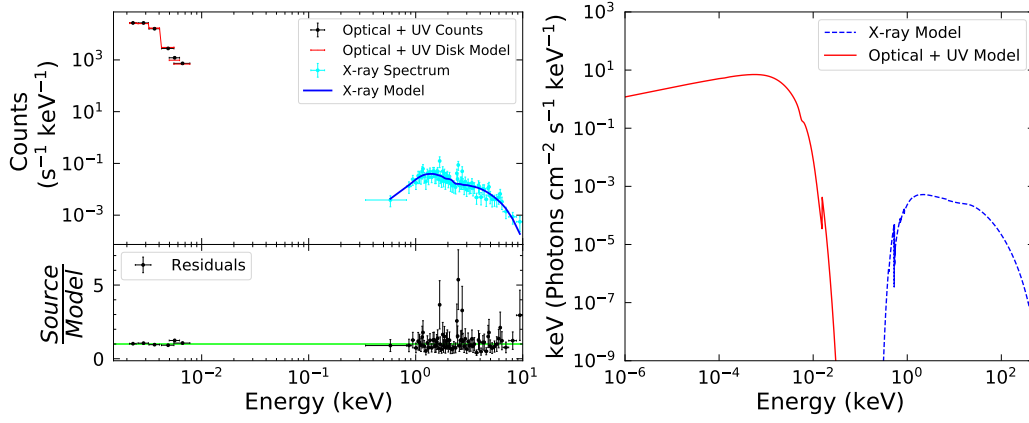
SWIFTJ1629.9+6722



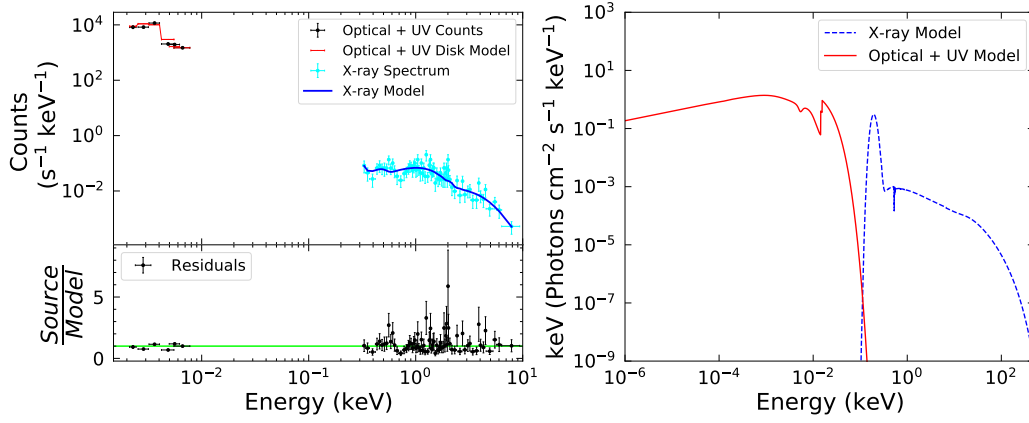
SWIFTJ1648.0-3037



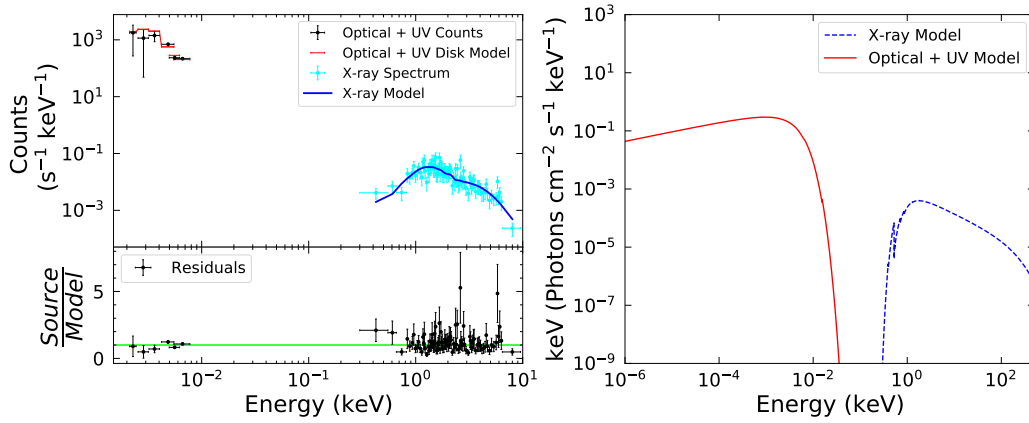
SWIFTJ1652.0-5915B



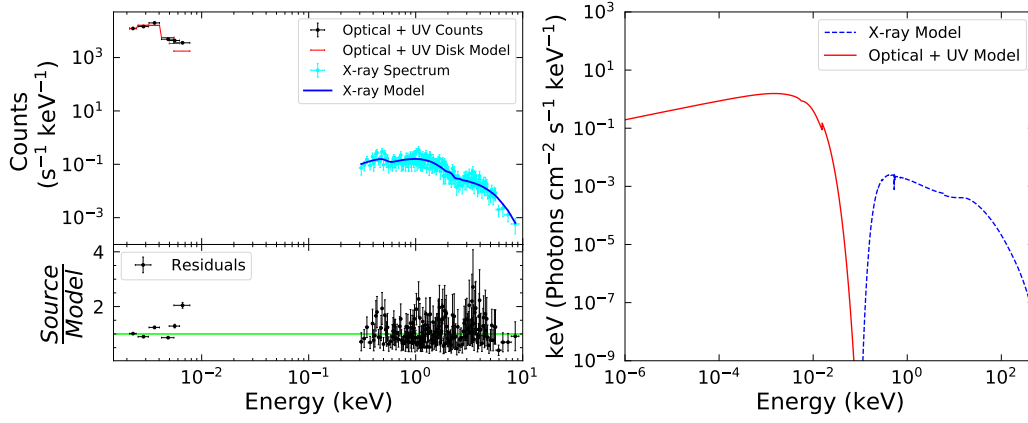
SWIFTJ1708.6+2155



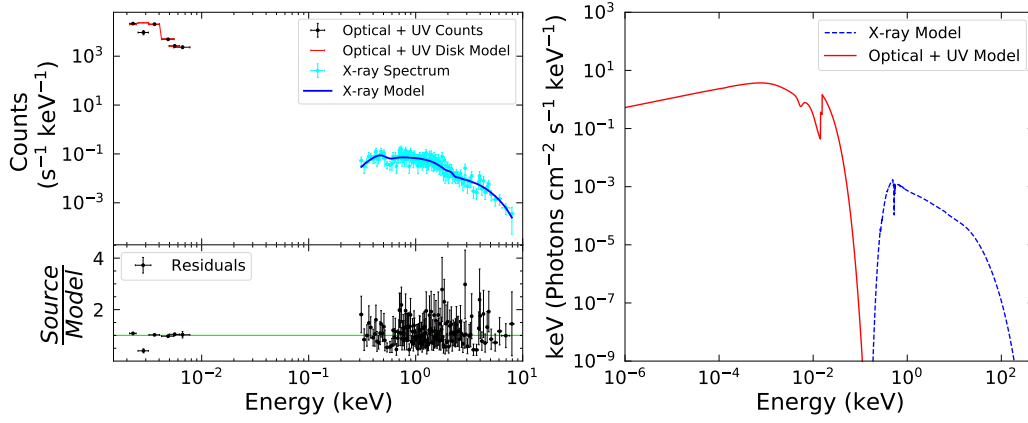
SWIFTJ1719.7+4900



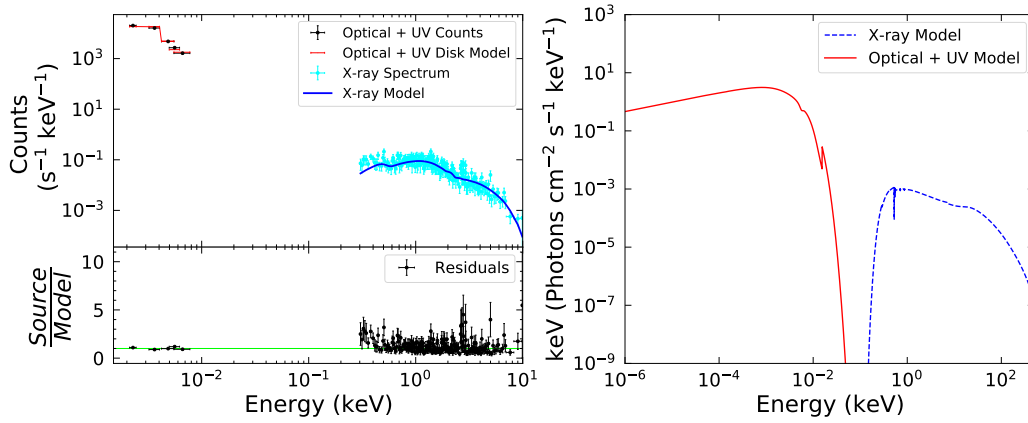
SWIFTJ1723.2+3418



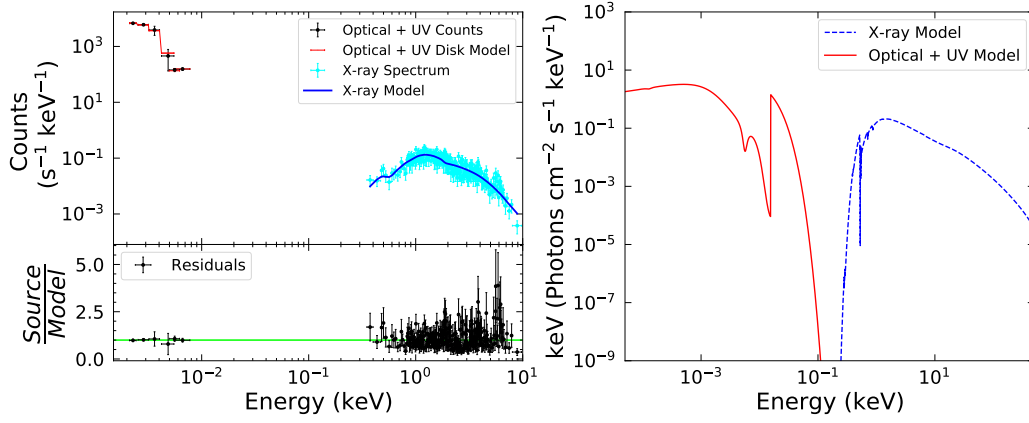
SWIFTJ1731.3+1442



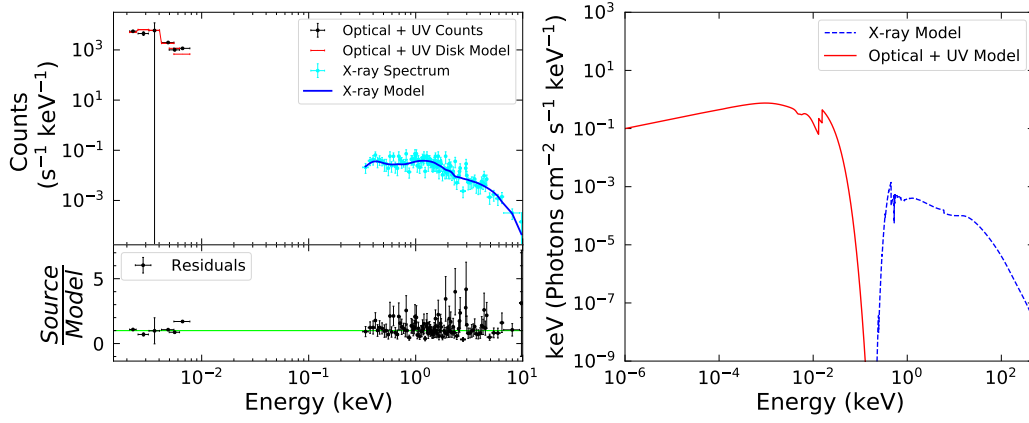
SWIFTJ1737.7-5956B



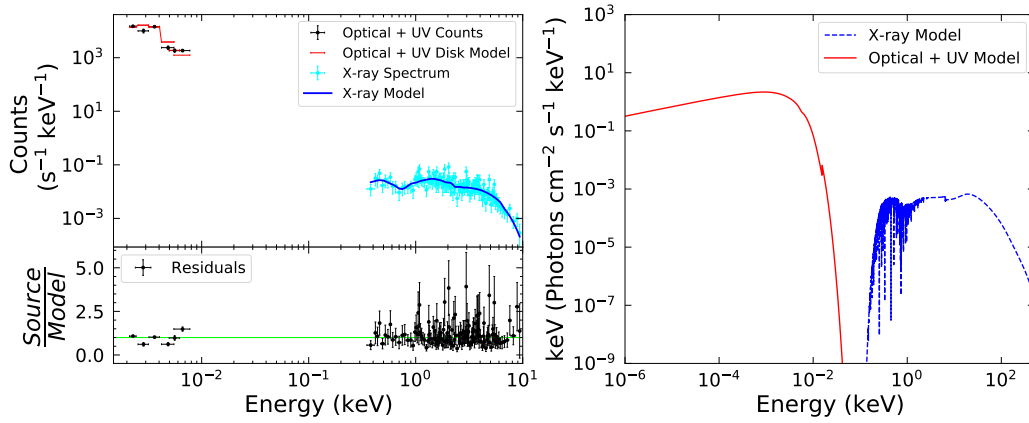
SWIFTJ1741.9-1211



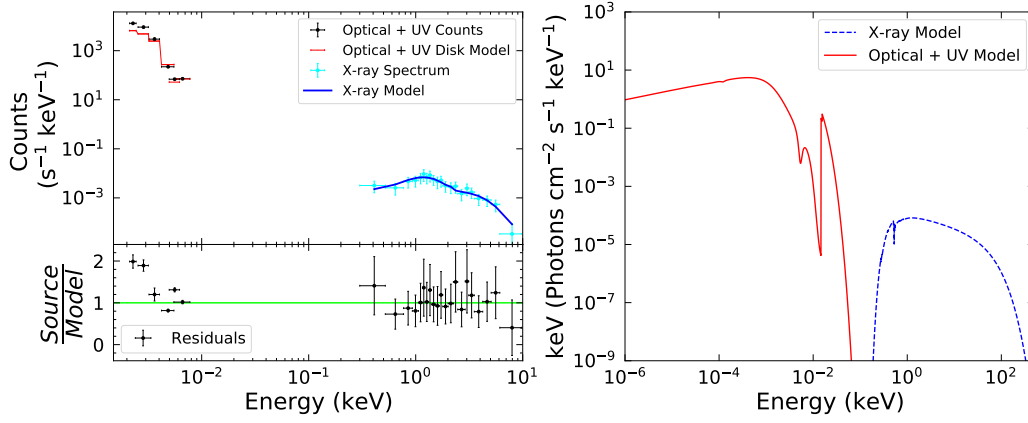
SWIFTJ1742.2+1833



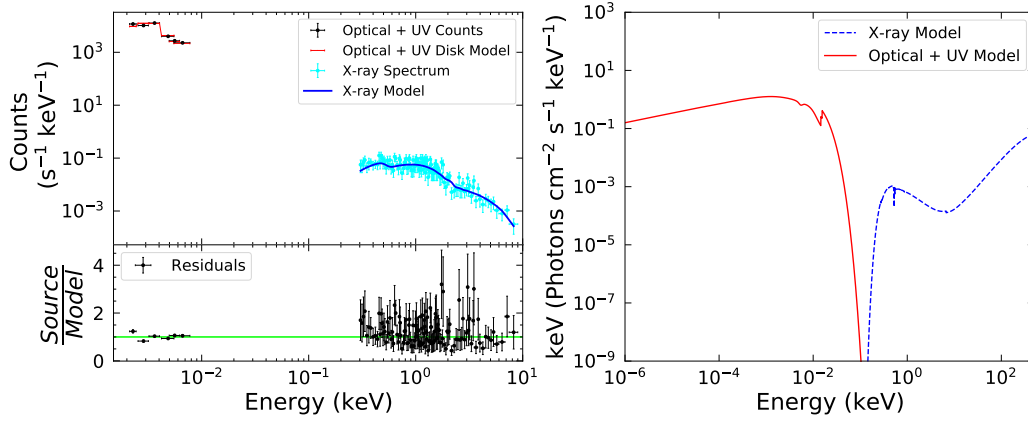
SWIFTJ1745.4+2906



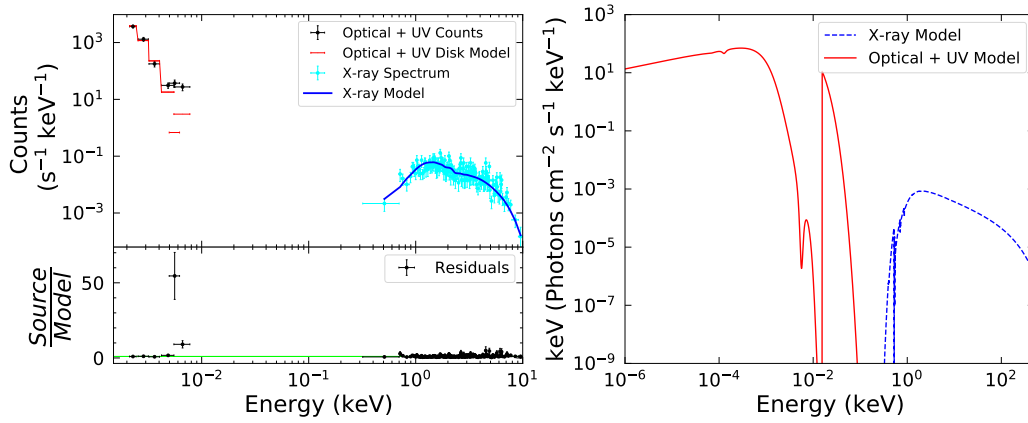
SWIFTJ1747.8+6837A



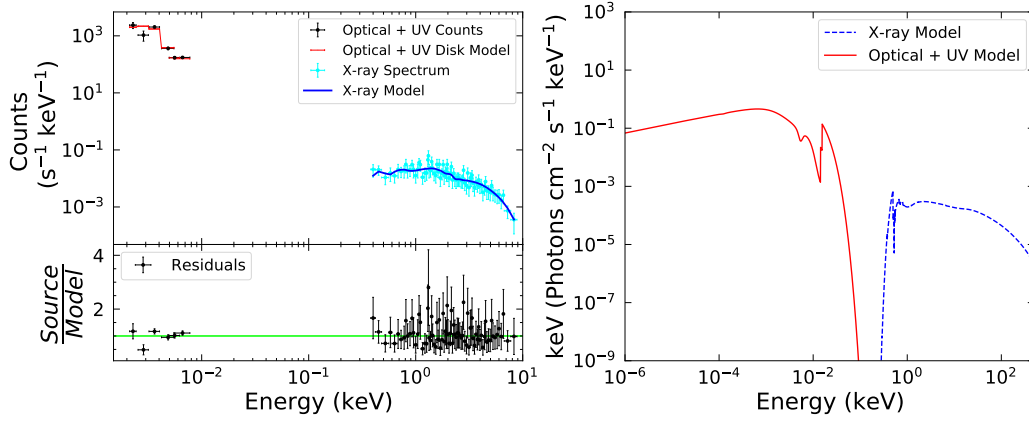
SWIFTJ1747.8+6837B



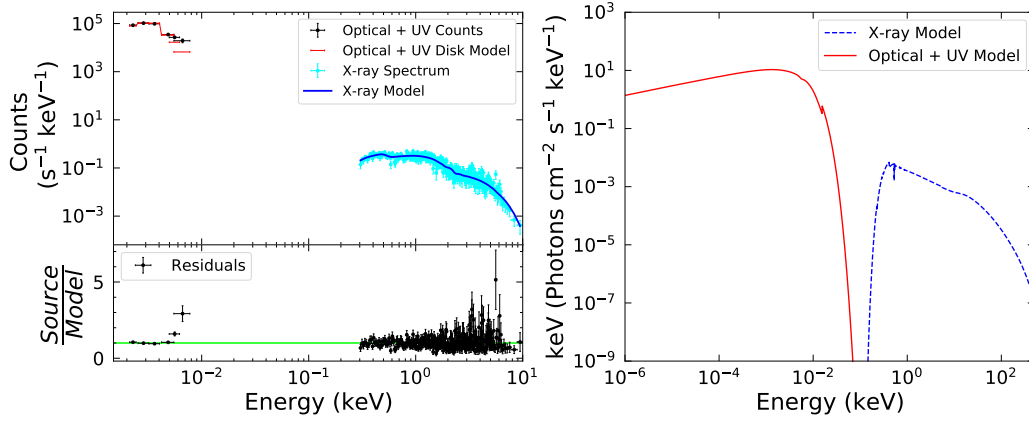
SWIFTJ1748.8-3257



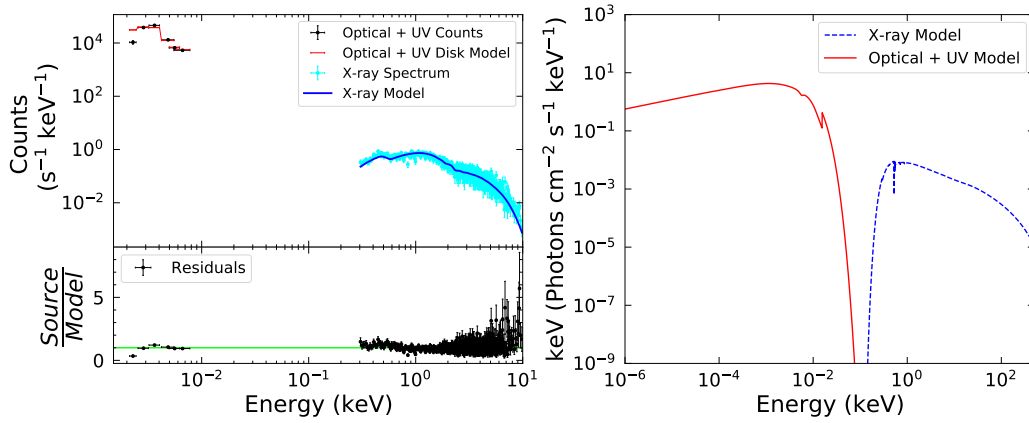
SWIFTJ1807.9+1124



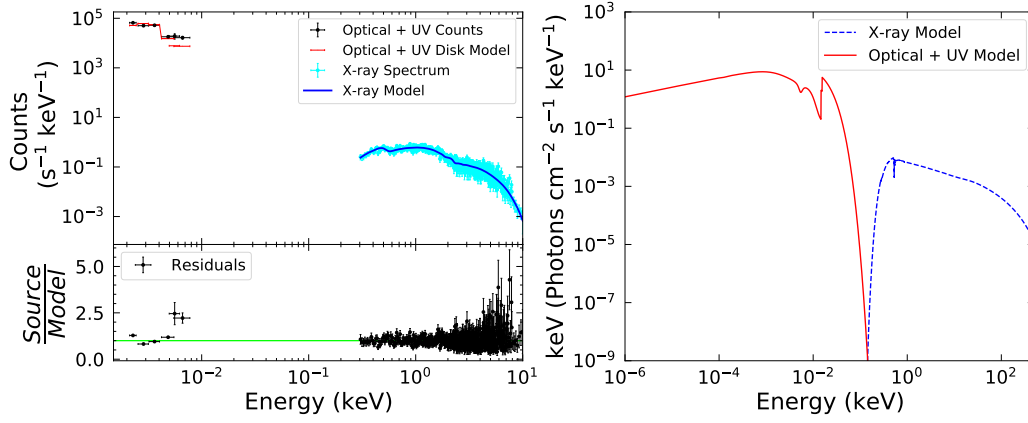
SWIFTJ1822.0+6421



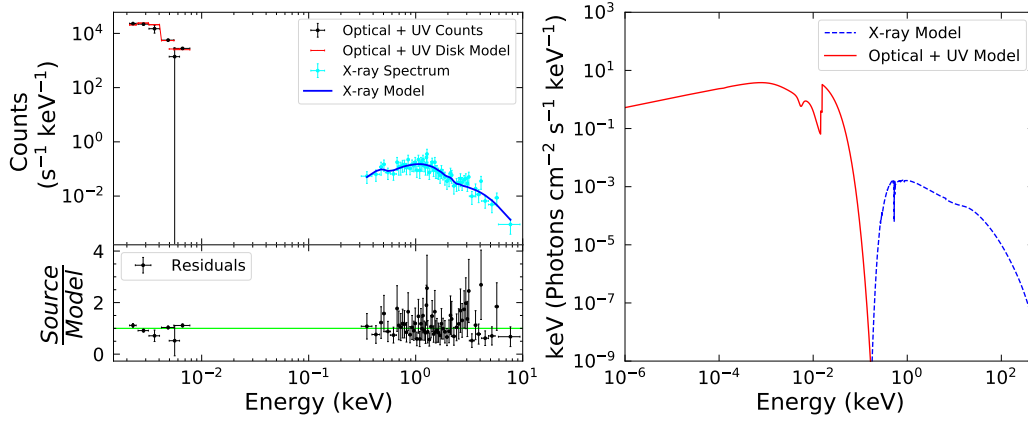
SWIFTJ1835.0+3240



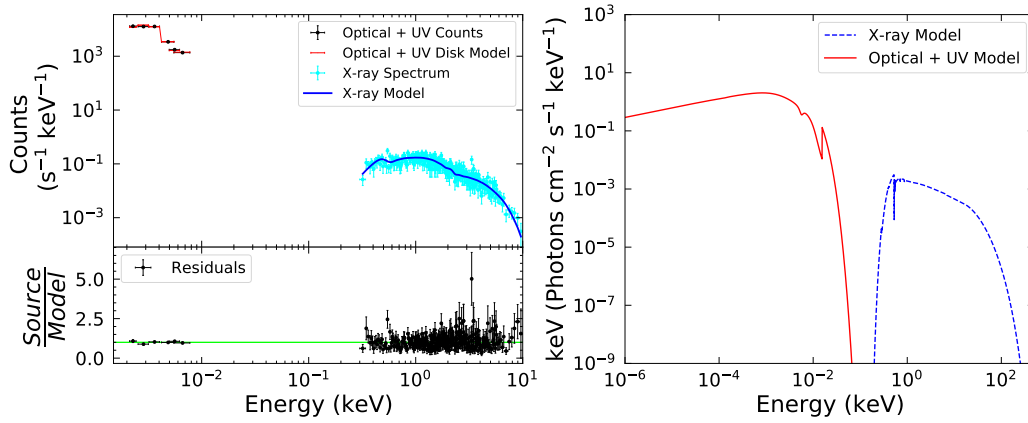
SWIFTJ1842.0+7945



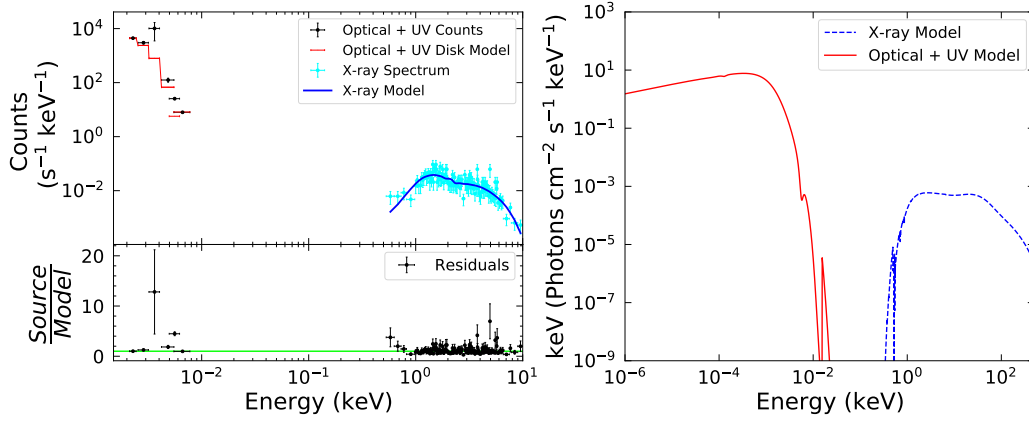
SWIFTJ1848.0-7832



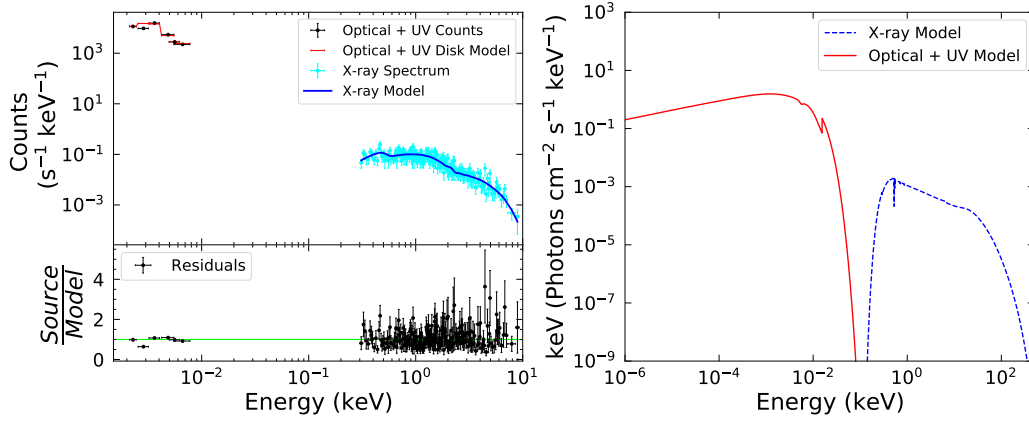
SWIFTJ1856.5-7851



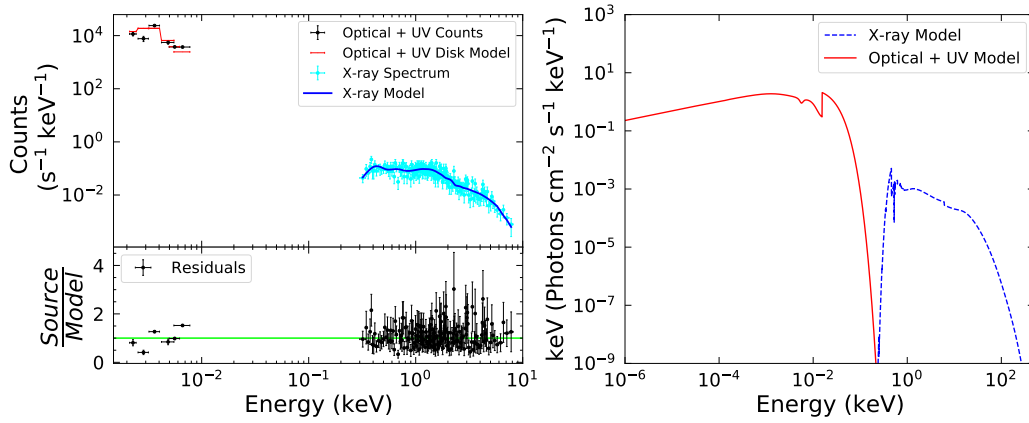
SWIFTJ1856.1+1539



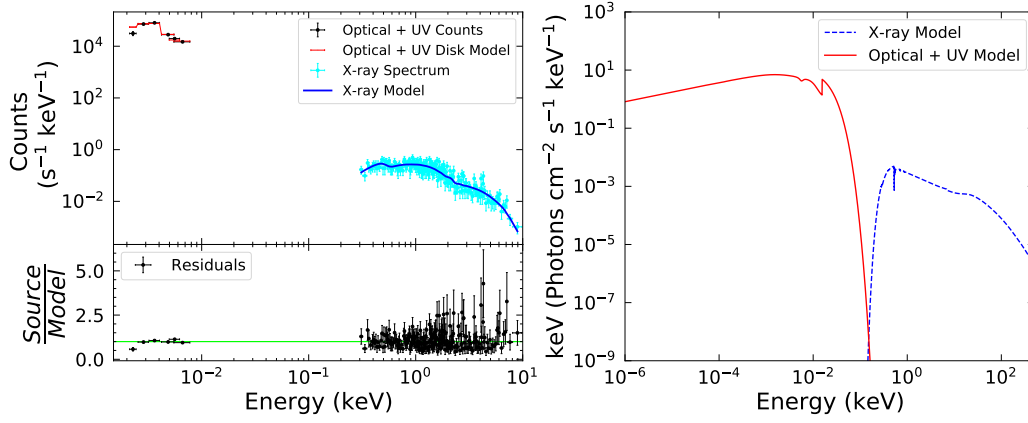
SWIFTJ1905.4+4231



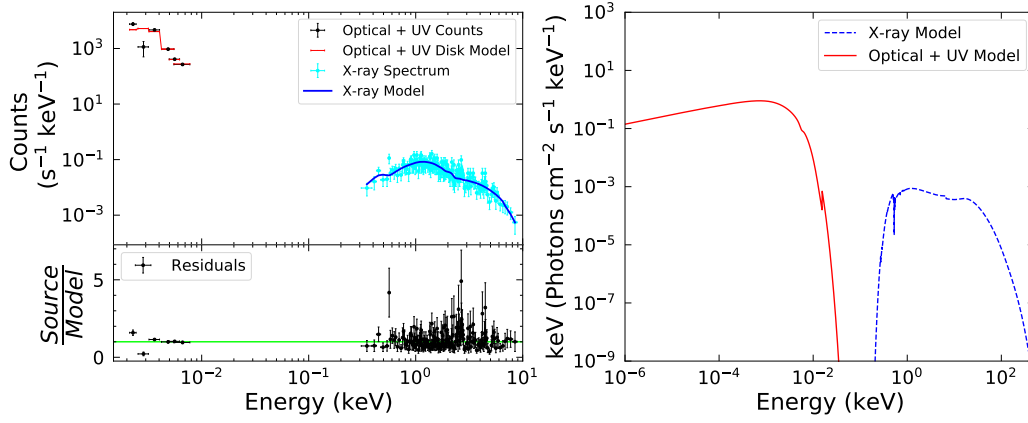
SWIFTJ1919.4-2958



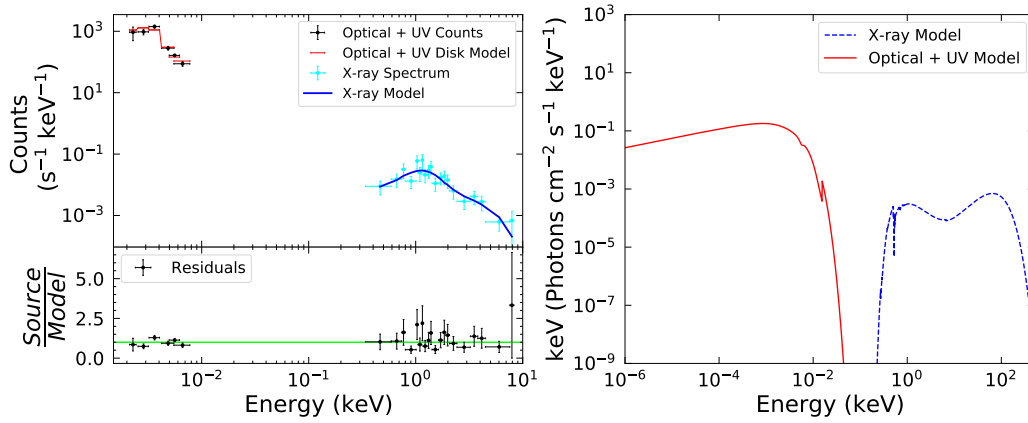
SWIFTJ1921.1-5842



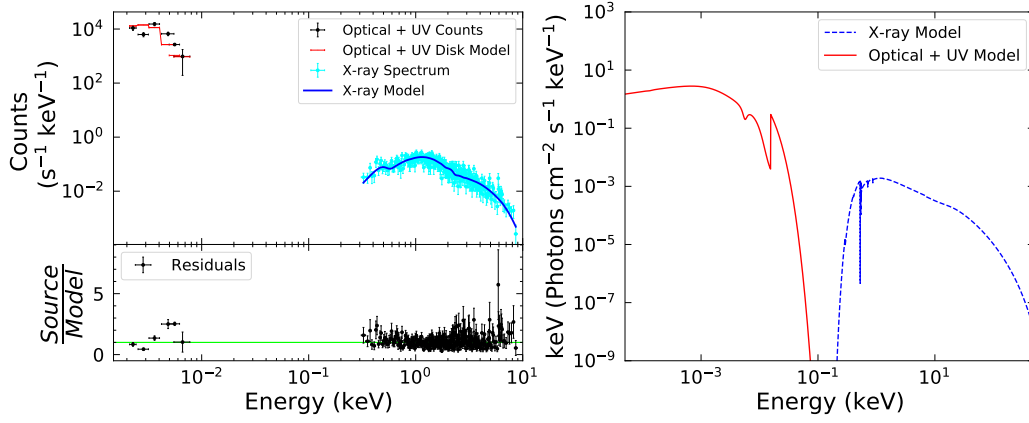
SWIFTJ1925.0+5041



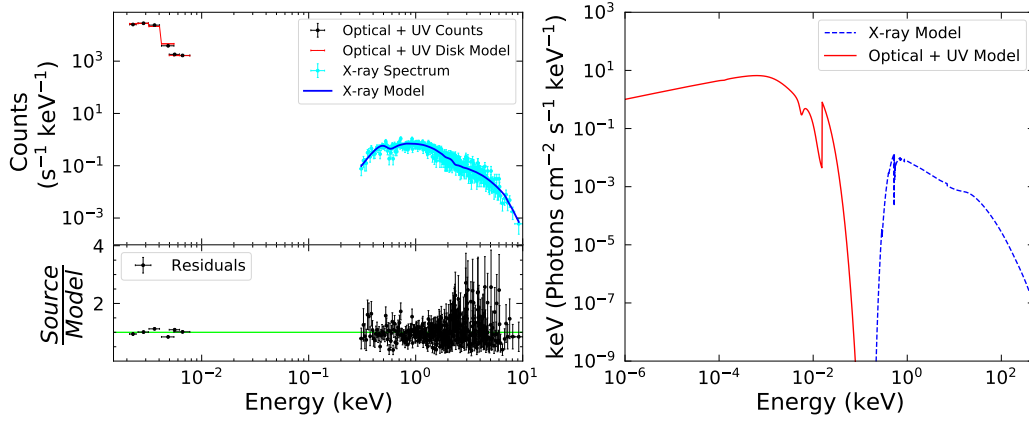
SWIFTJ1926.9+4140



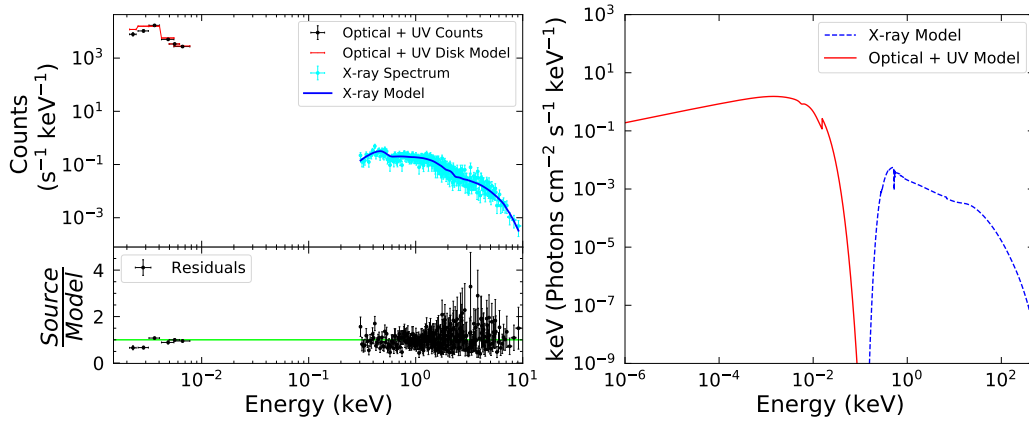
SWIFTJ1933.9+3258



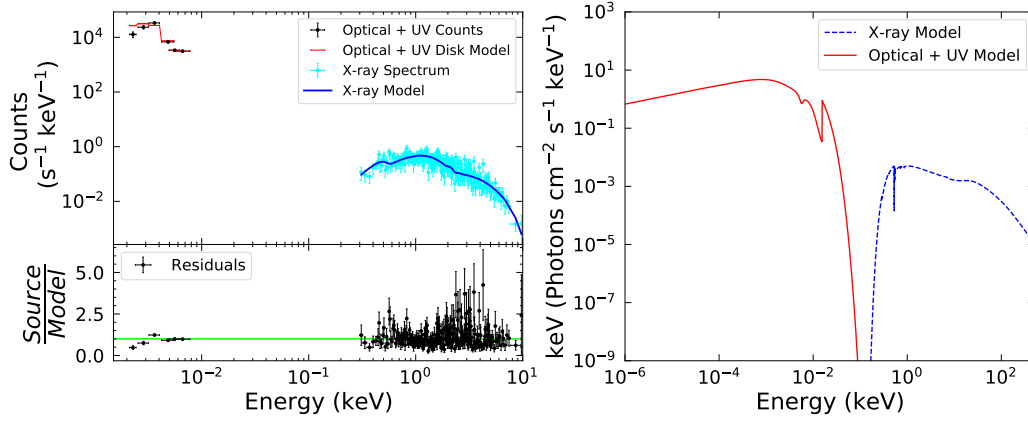
SWIFTJ1937.5-0613



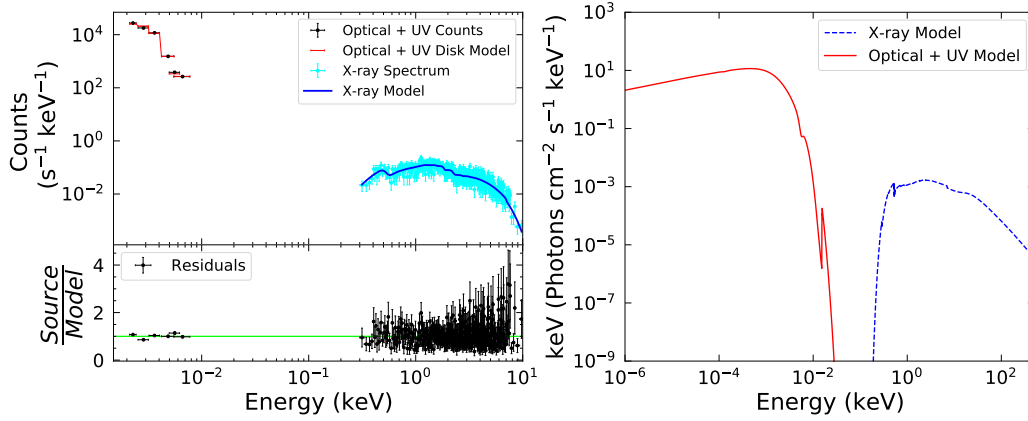
SWIFTJ1938.1-5108



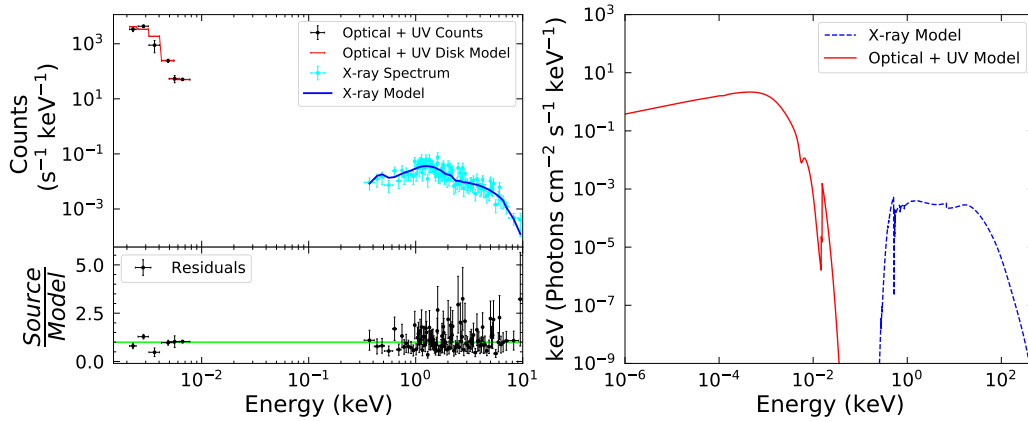
SWIFTJ1942.6-1024



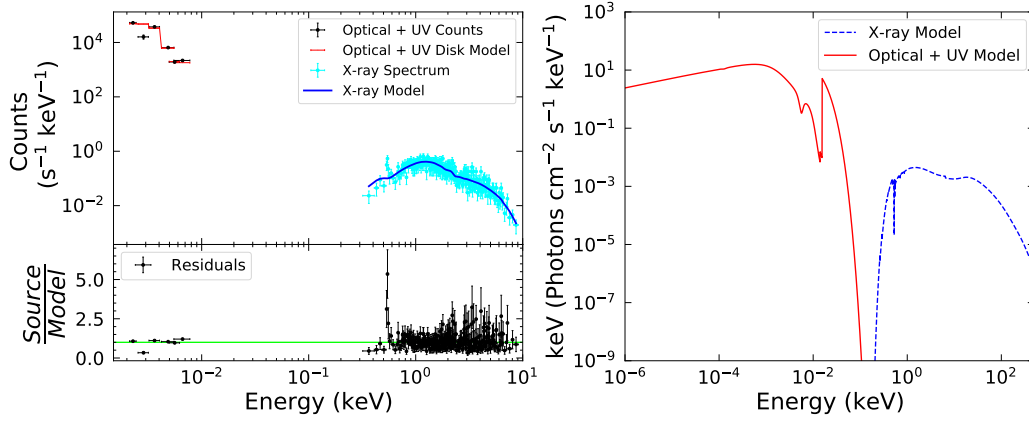
SWIFTJ2009.0-6103



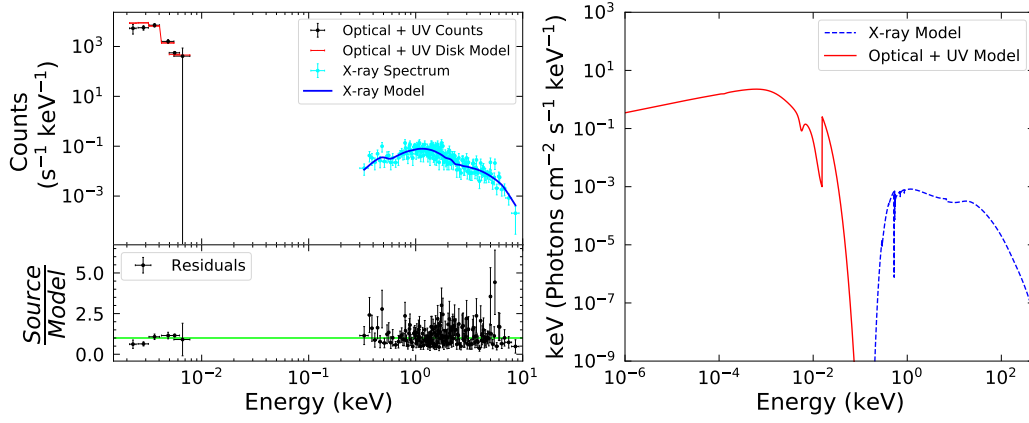
SWIFTJ2035.2+2604



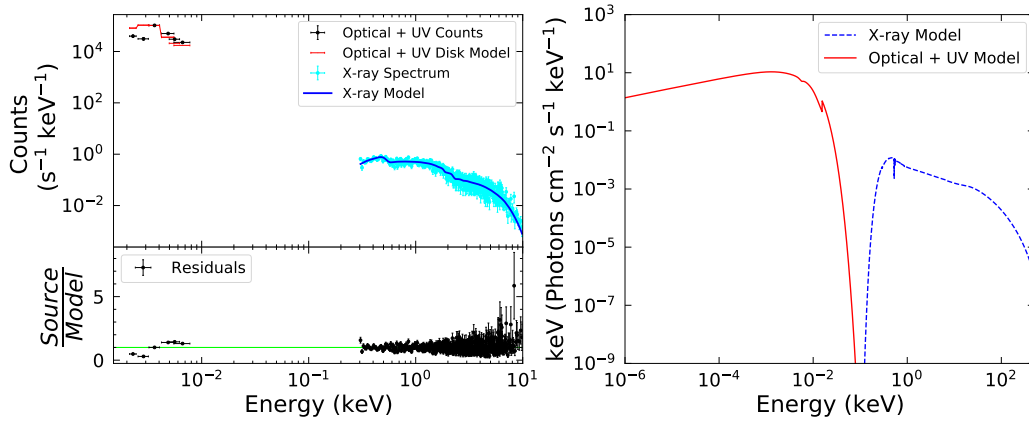
SWIFTJ2042.3+7507



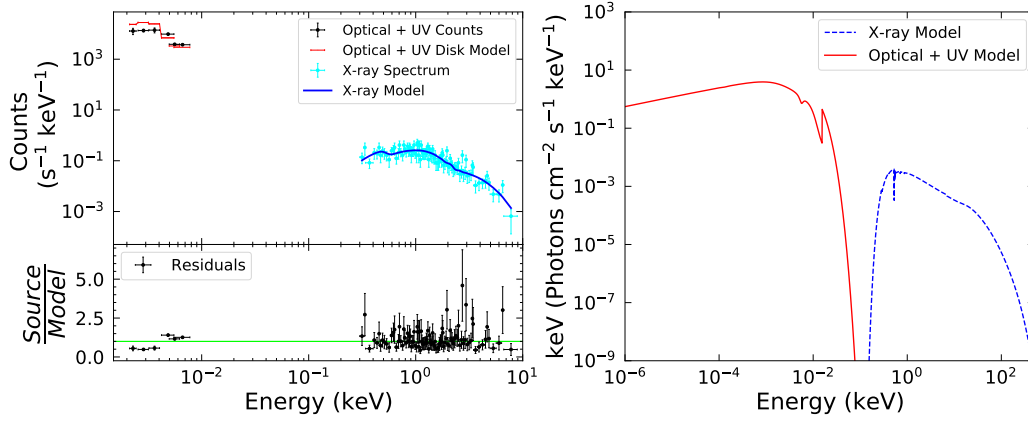
SWIFTJ2044.0+2832



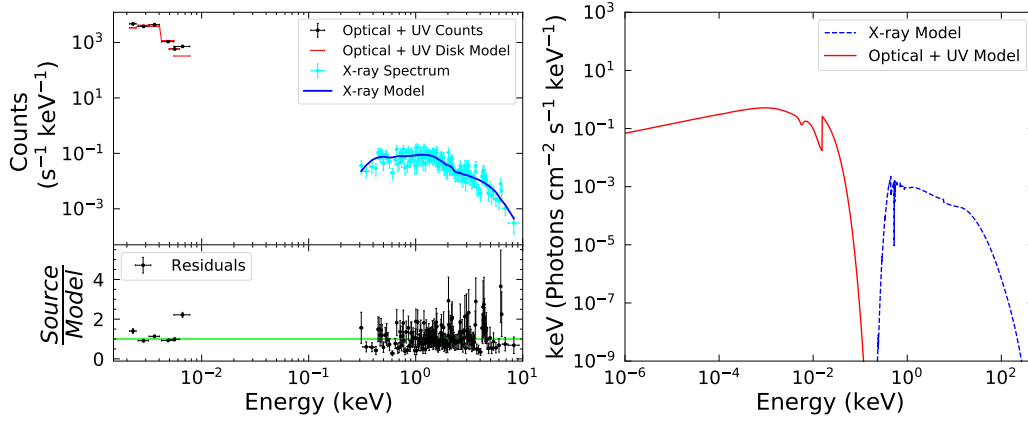
SWIFTJ2044.2-1045



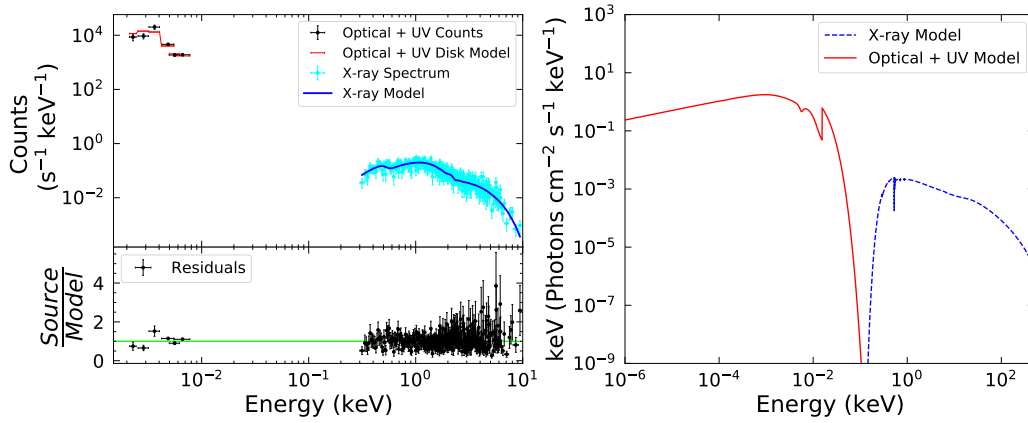
SWIFTJ2109.1-0942



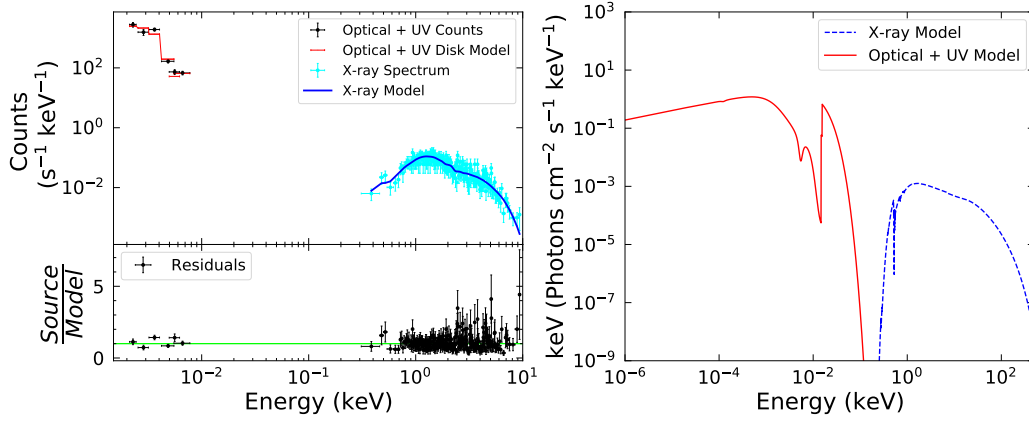
SWIFTJ2109.2+3531



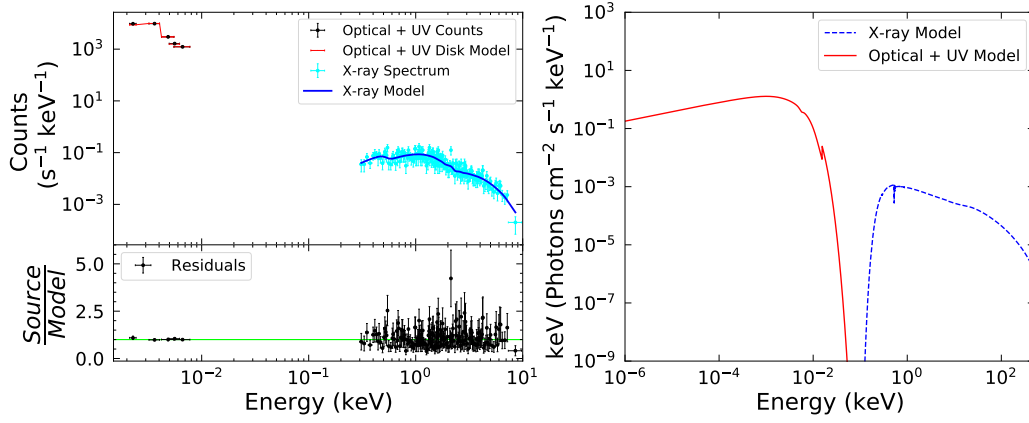
SWIFTJ2114.4+8206



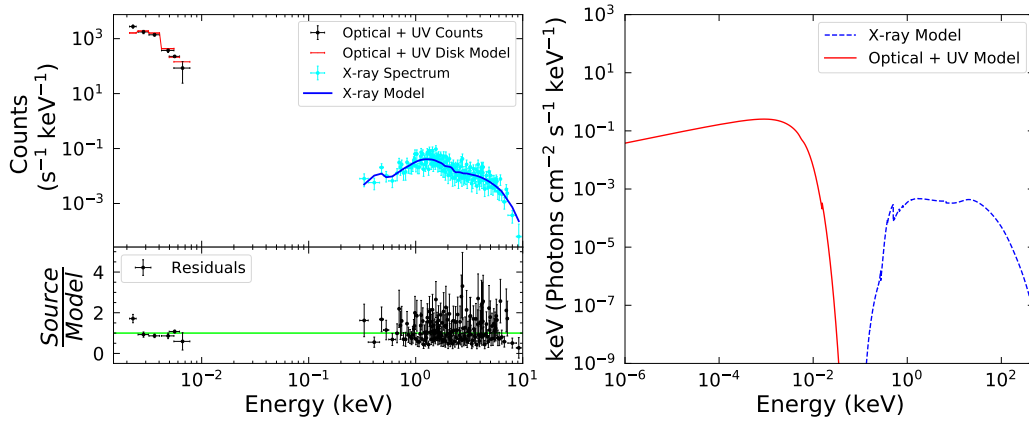
SWIFTJ2118.9+3336



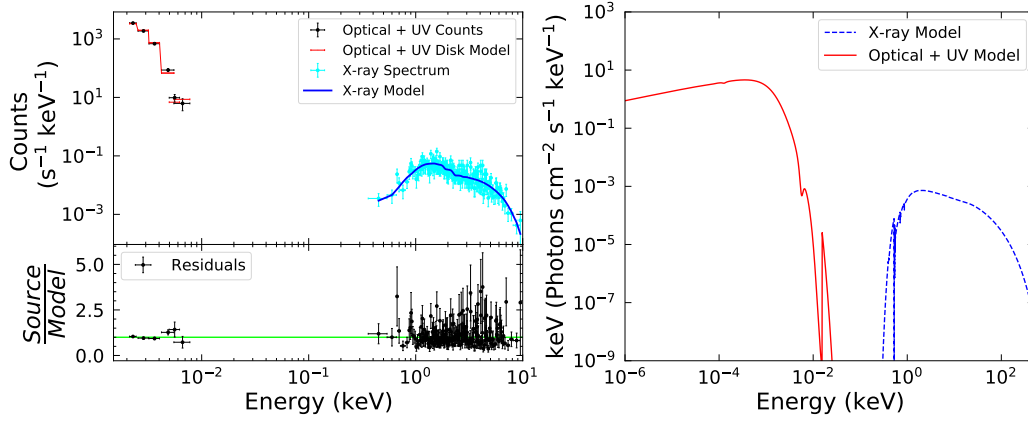
SWIFTJ2132.0-3343



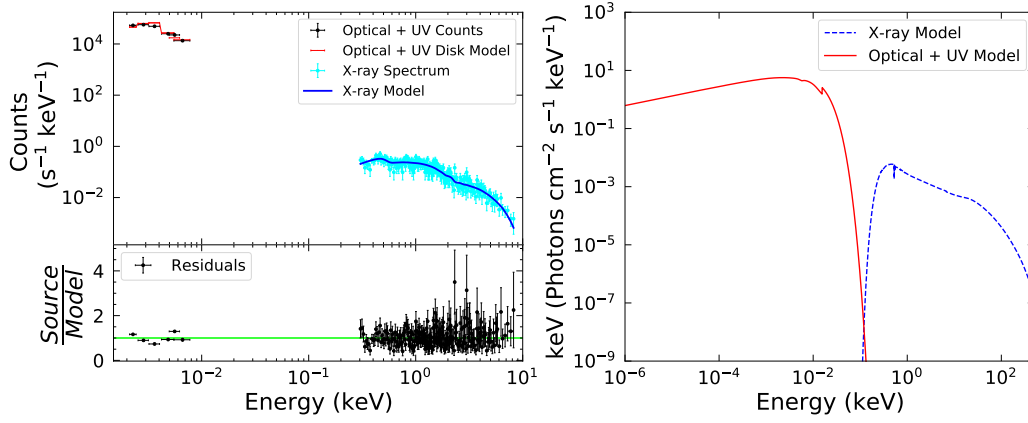
SWIFTJ2134.9-2729



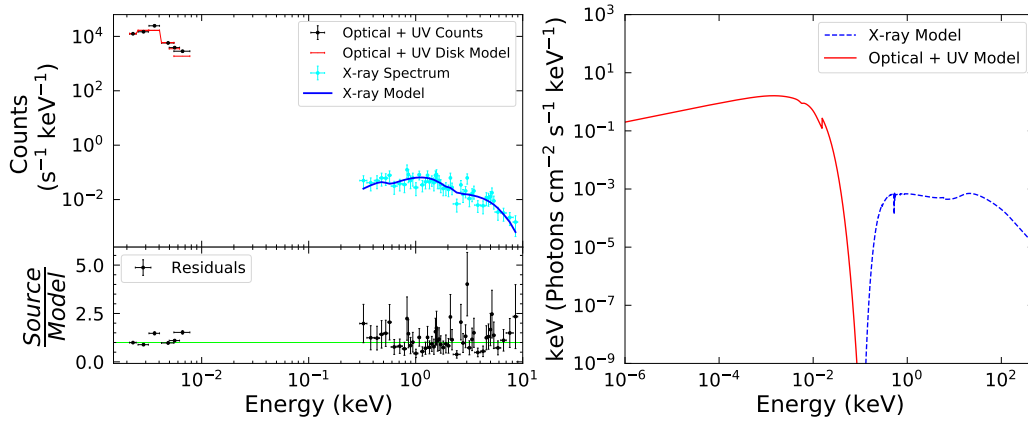
SWIFTJ2156.1+4728



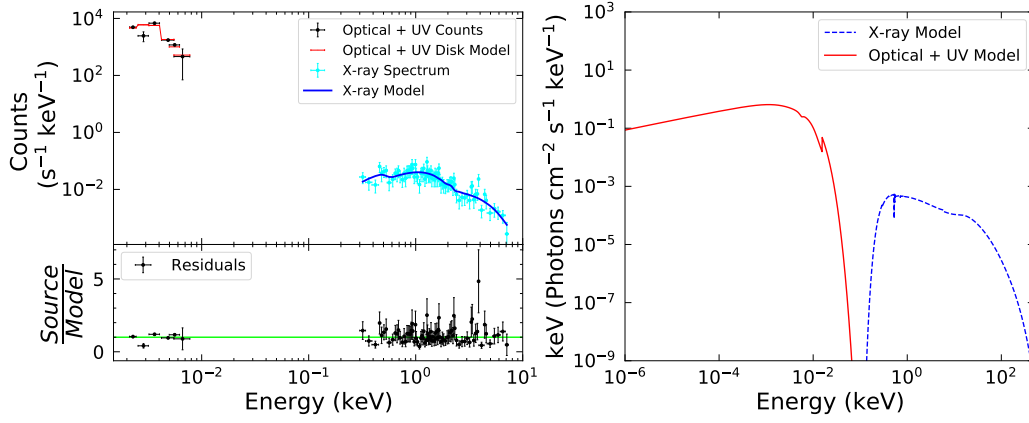
SWIFTJ2135.5-6222



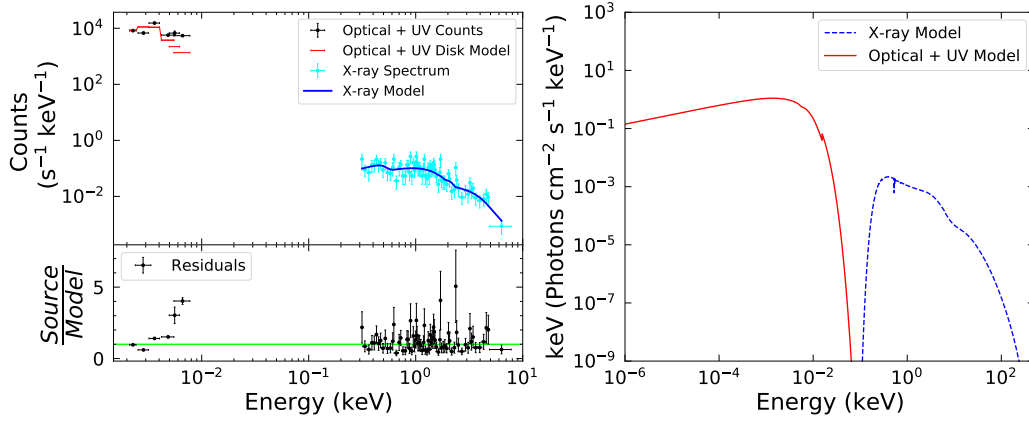
SWIFTJ2137.8-1433



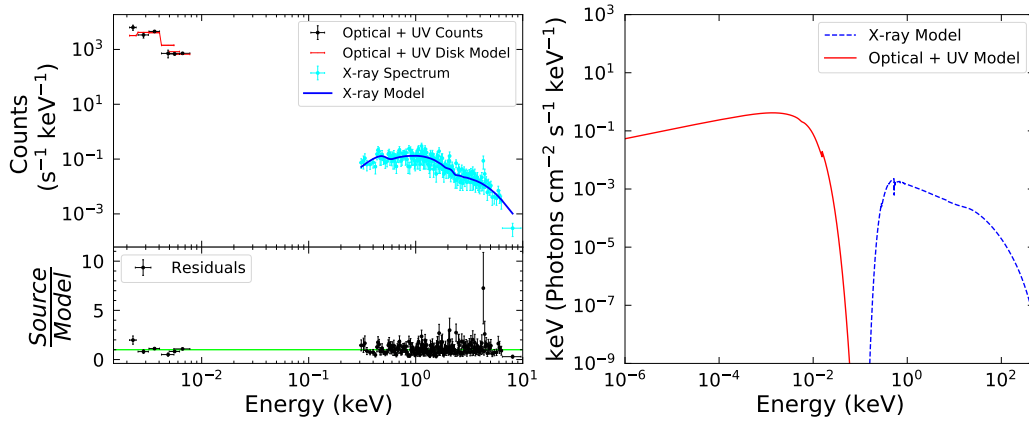
SWIFTJ2145.5+1101



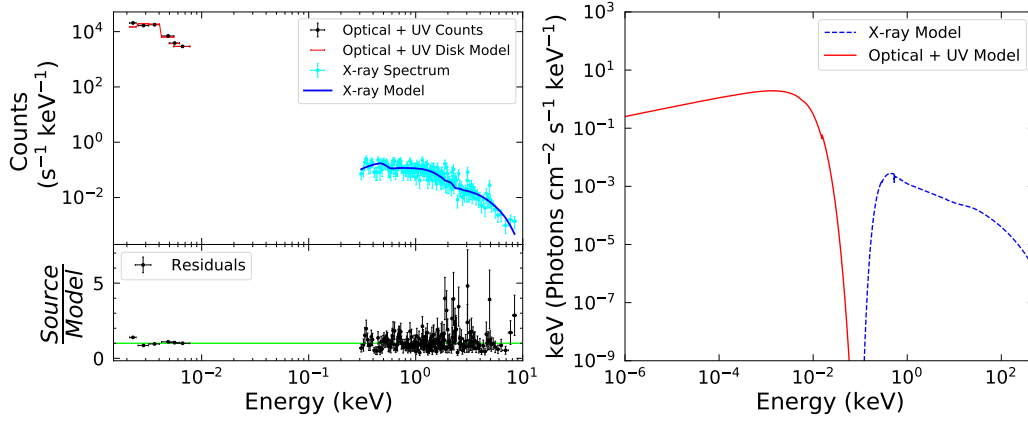
SWIFTJ2150.2-1855



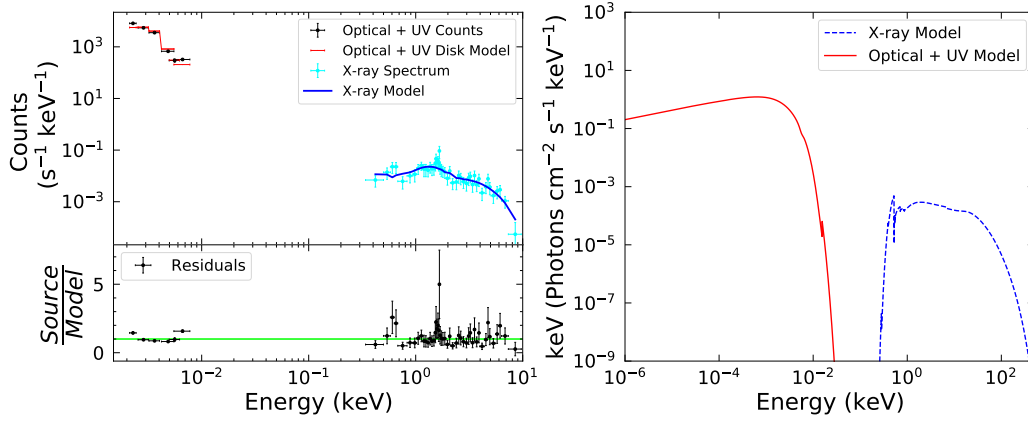
SWIFTJ2157.2-6942



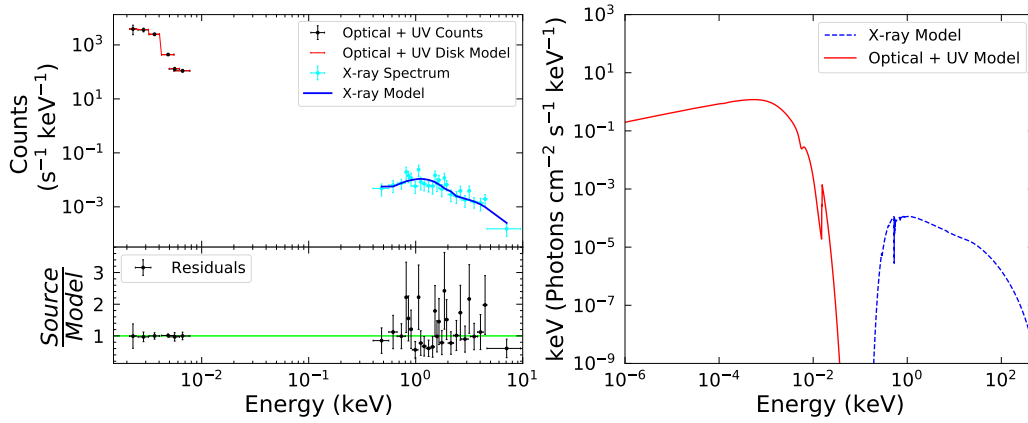
SWIFTJ2209.1-2747



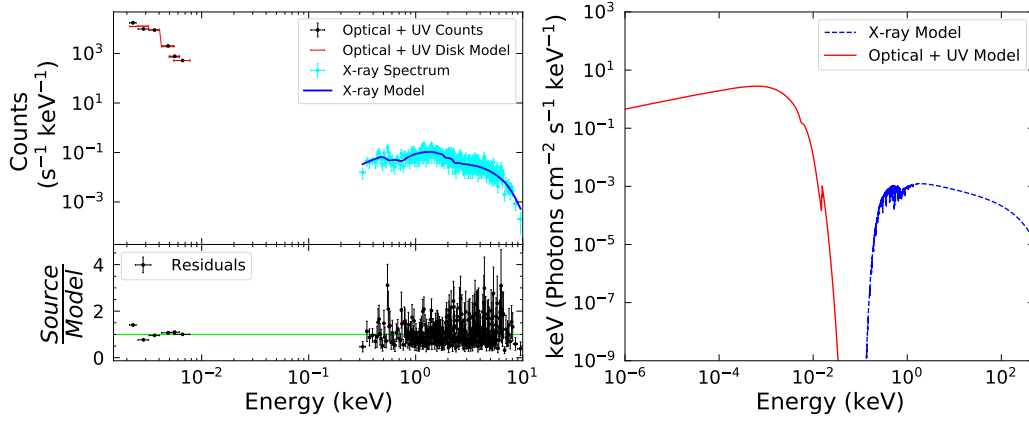
SWIFTJ2223.8+1143



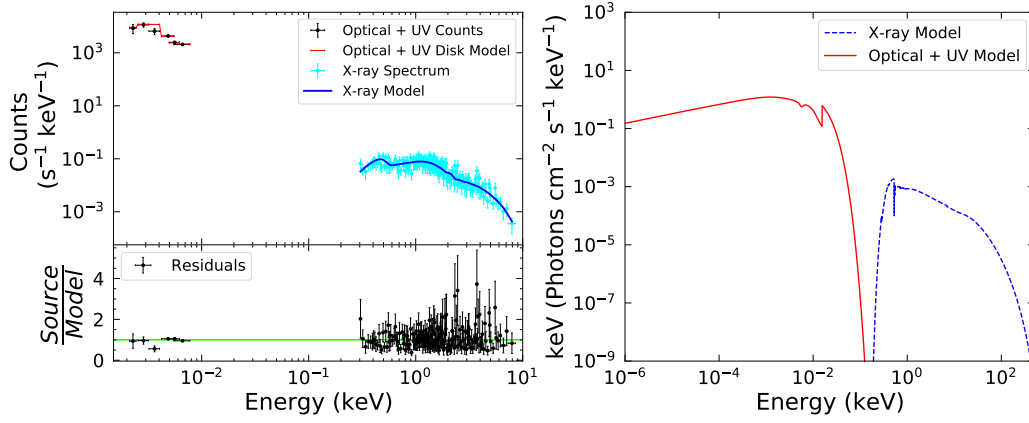
SWIFTJ2226.8+3628



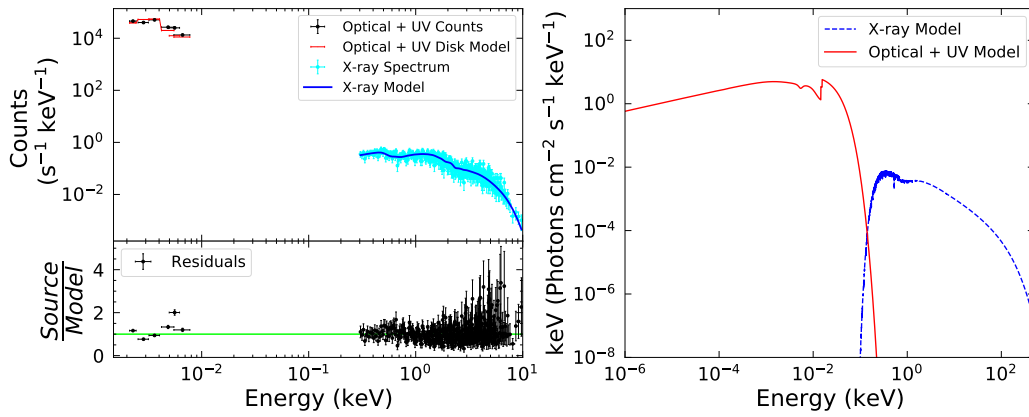
SWIFTJ2236.7-1233



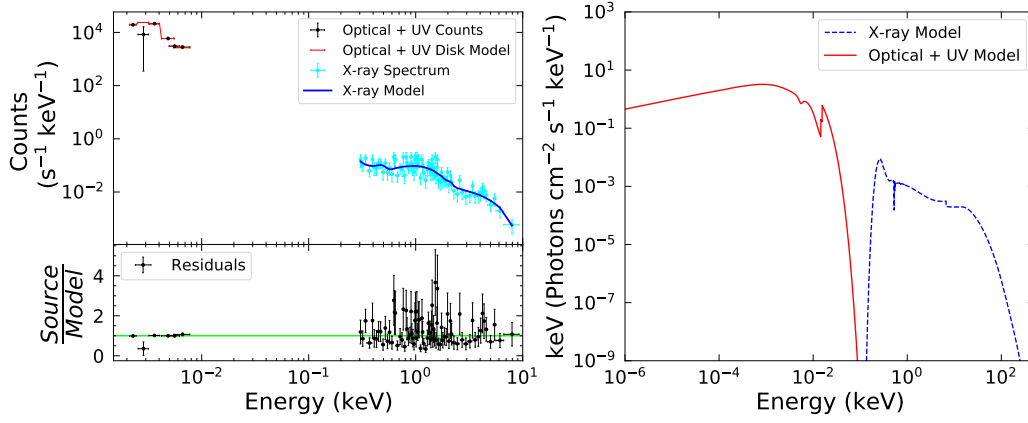
SWIFTJ2240.2+0801



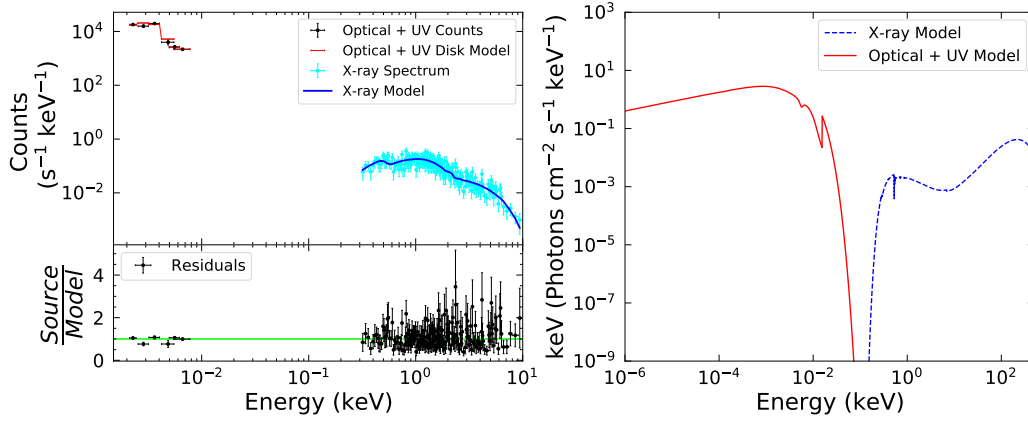
SWIFTJ2254.1-1734



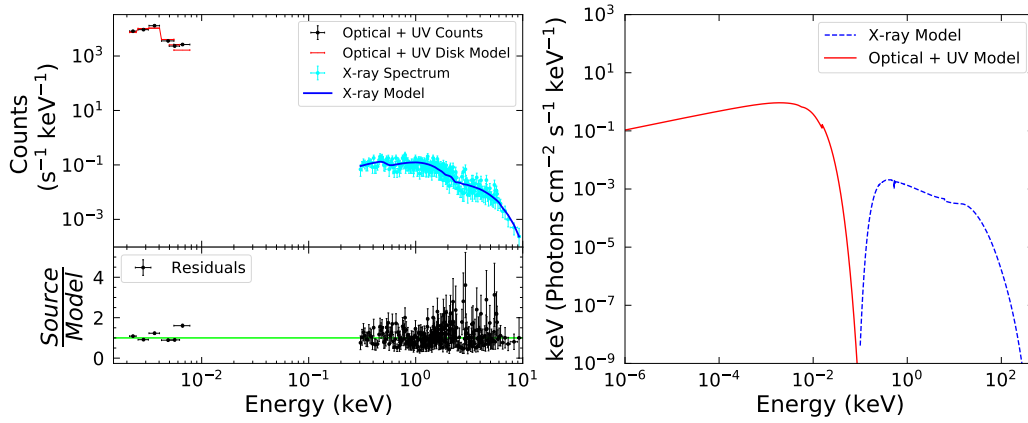
SWIFTJ2256.5+0526



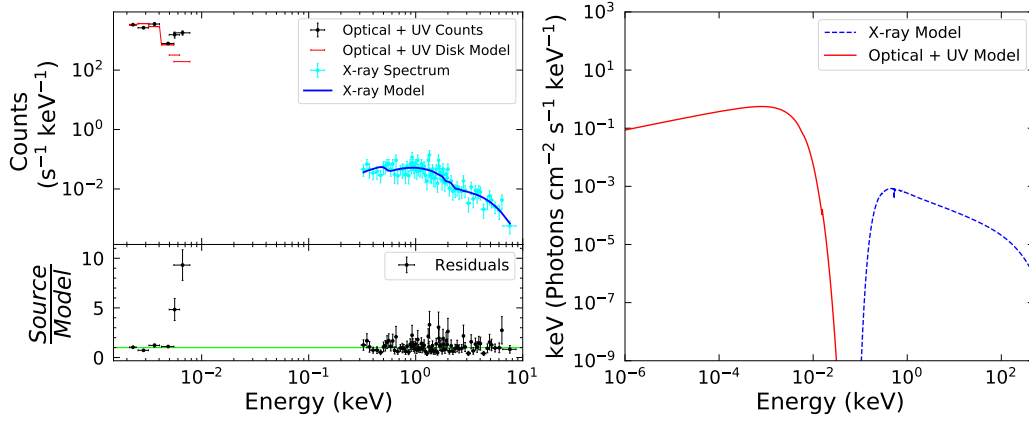
SWIFTJ2259.7+2458



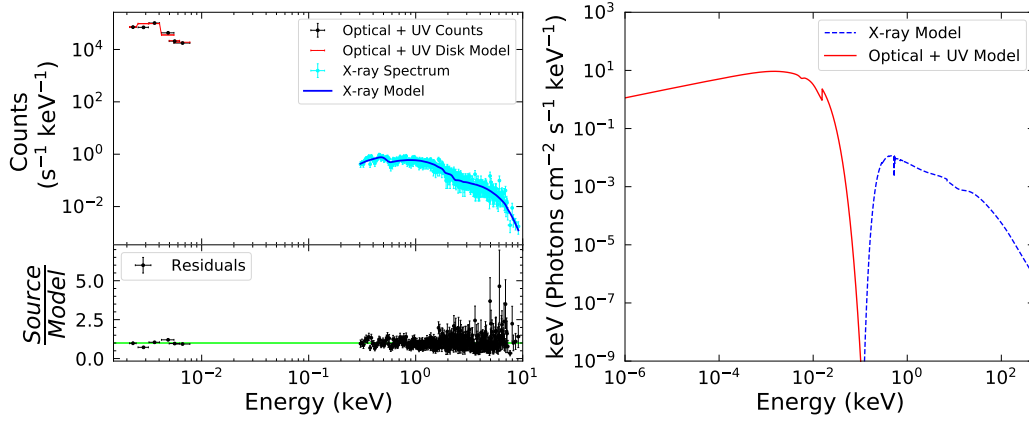
SWIFTJ2301.4-5916



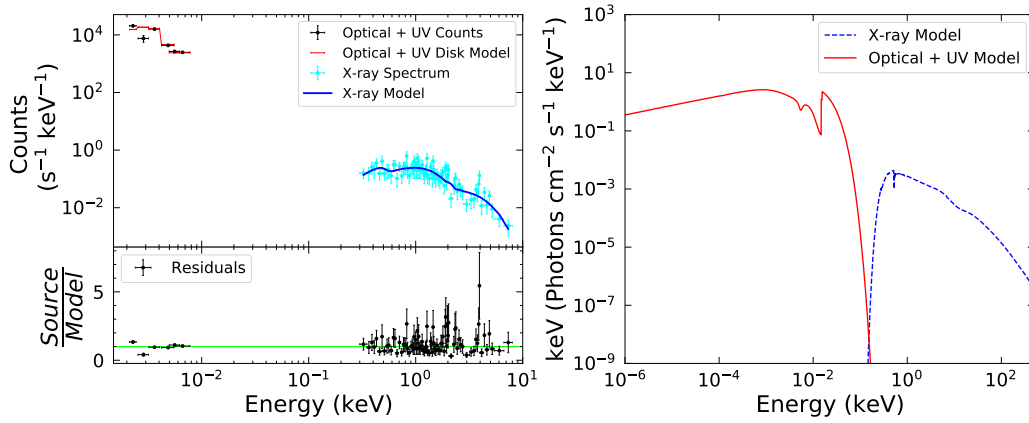
SWIFTJ2303.1-1837



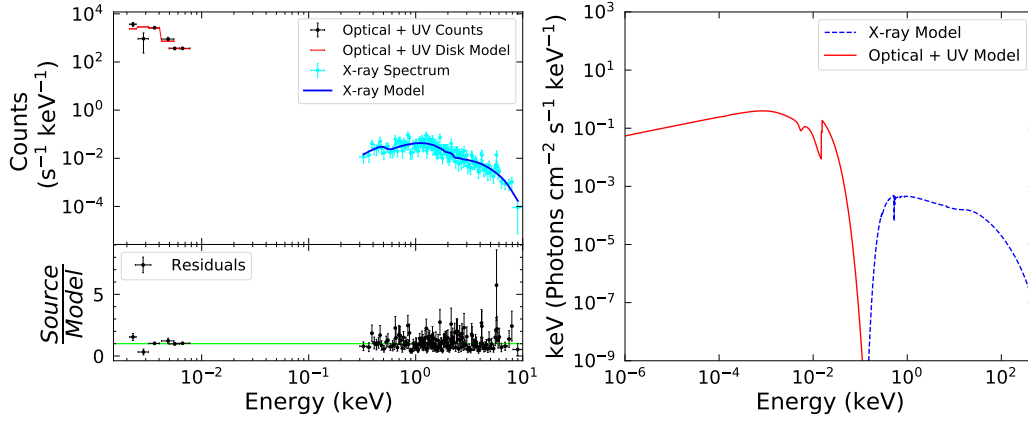
SWIFTJ2303.3+0852



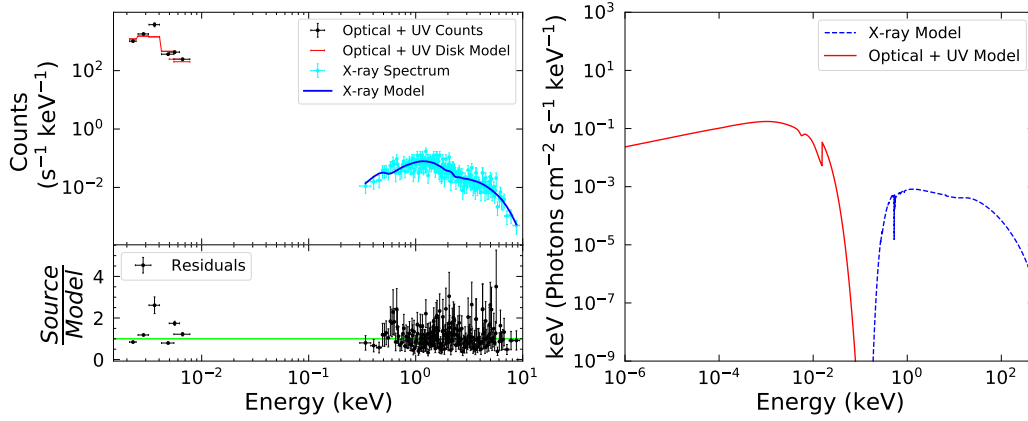
SWIFTJ2304.8-0843



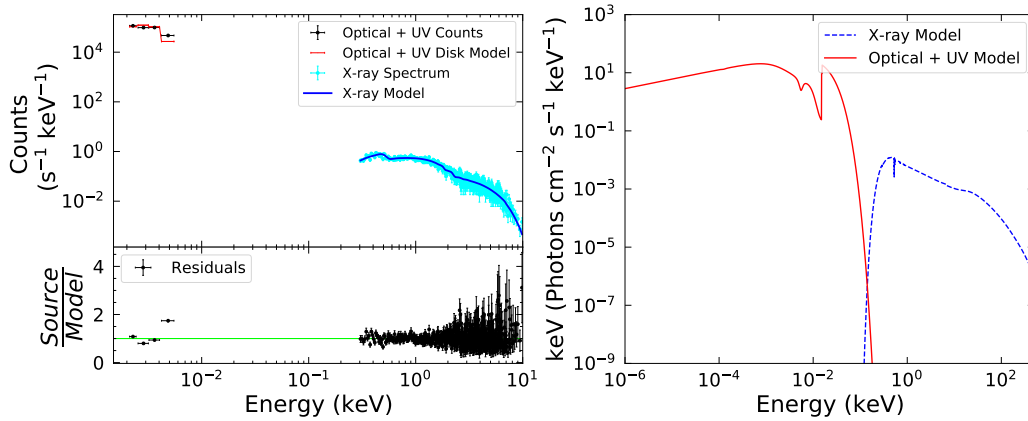
SWIFTJ2307.1+0433



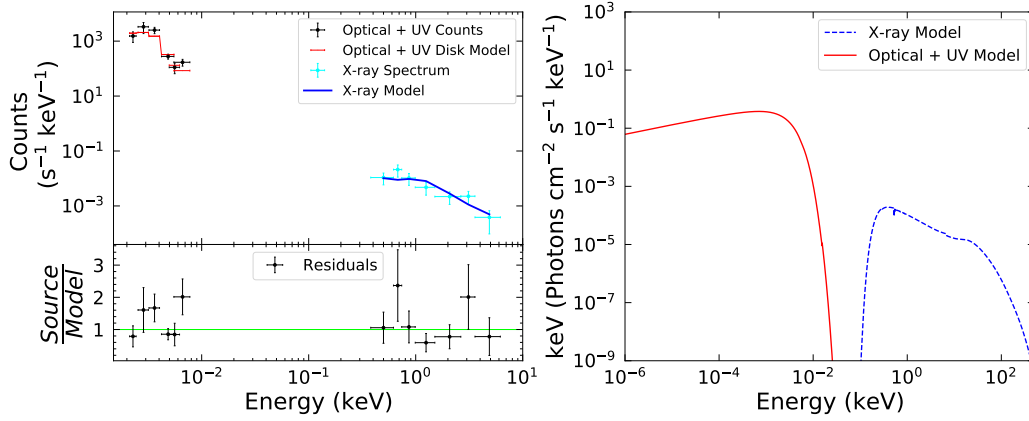
SWIFTJ2308.1+4014



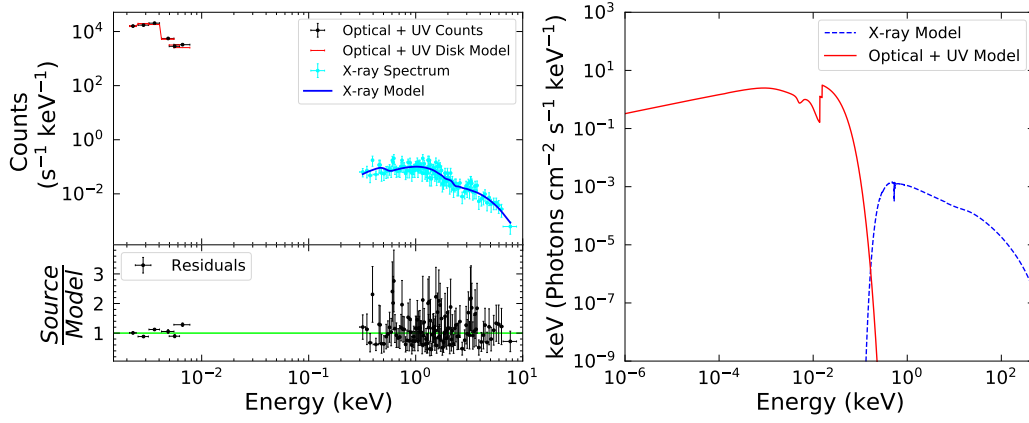
SWIFTJ2318.9+0013



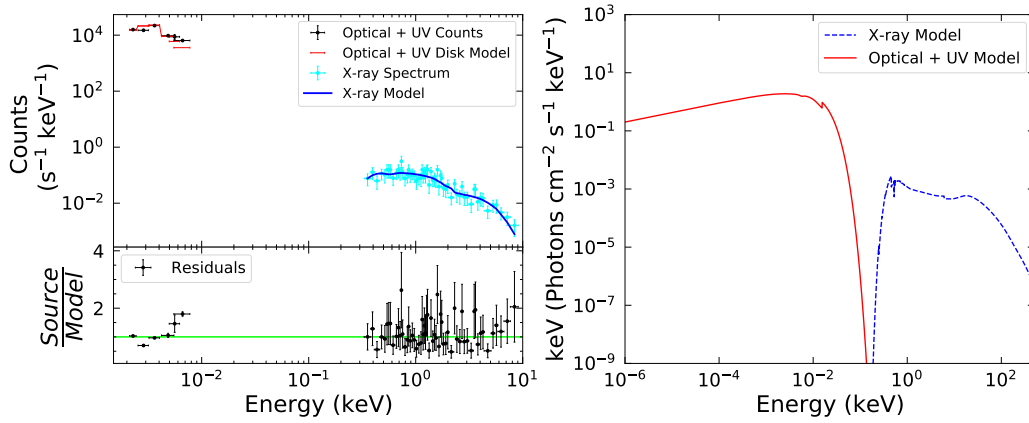
SWIFTJ2325.5-3827



SWIFTJ2325.6+2157



SWIFTJ2351.9-0109



Appendix B: Long Tables

Table 1: Full version of Table 3.2.

BAT ID	Swift ID	Counterpart Name	R.A.	Dec.	Redshift	Distance (Mpc)	$\log(N_{\text{H}}/\text{cm}^{-2})$
3	SWIFTJ0002.5+0323	NGC7811	0.6103	3.3519	0.0250	111.2	20.00
6	SWIFTJ0006.2+2012	Mrk335	1.5814	20.2029	0.0250	113.2	20.48
16	SWIFTJ0029.2+1319	PG0026+129	7.3071	13.2678	0.1420	671.7	20.00
19	SWIFTJ0034.5-7904	RHS3	8.5697	-79.0890	0.0740	335.9	20.00
34	SWIFTJ0051.6+2928	UGC524	12.8959	29.4013	0.0360	157.9	20.00
36	SWIFTJ0051.9+1724	Mrk1148	12.9782	17.4329	0.0640	287.5	20.30
39	SWIFTJ0054.9+2524	PG0052+251	13.7172	25.4275	0.1550	739.5	20.00
43	SWIFTJ0059.4+3150	Mrk352	14.9720	31.8270	0.0140	63.4	20.00
45	SWIFTJ0101.5-0308	2MASXJ01012440-0308399	15.3517	-3.1445	0.0690	313.2	20.00

BAT ID	Swift ID	Counterpart Name	R.A.	Dec.	Redshift	Distance (Mpc)	$\log(N_{\mathrm{H}}/\mathrm{cm}^{-2})$
51	SWIFTJ0105.7-1414	RBS149	16.4117	-14.2704	0.0660	300.4	20.00
61	SWIFTJ0113.8-1450	Mrk1152	18.4586	-14.8457	0.0520	234.1	20.00
69	SWIFTJ0122.0-2818	Q0119-286	20.4646	-28.3494	0.1160	537.6	20.00
73	SWIFTJ0123.9-5846	Fairall9	20.9407	-58.8058	0.0470	203.3	20.00
77	SWIFTJ0127.5+1910	Mrk359	21.8855	19.1788	0.0170	72.8	20.61
78	SWIFTJ0128.0-1850	MCG-3-4-72	22.0280	-18.8086	0.0460	189.8	20.00
82	SWIFTJ0130.2-4552	2MASXJ01302127-4601448	22.5887	-46.0292	0.1115	517.3	20.00
85	SWIFTJ0134.8-0430	LEDA1057320	23.6901	-4.5036	0.0790	359.7	20.00
95	SWIFTJ0151.3-3610	ESO354-4	27.9244	-36.1879	0.0330	146.2	20.00
98	SWIFTJ0155.4+0228	RBS255	28.8538	2.4712	0.0820	385.9	20.00
106	SWIFTJ0206.2-0019	Mrk1018	31.5666	-0.2914	0.0420	188.5	20.00
110	SWIFTJ0208.2+4452	UGC1609	31.9649	44.8438	0.0210	94.3	21.97
113	SWIFTJ0209.7+5226	LEDA138501	32.4059	52.4443	0.0490	221.0	20.00
116	SWIFTJ0214.6-0049	Mrk590	33.6398	-0.7667	0.0260	115.7	20.00
117	SWIFTJ0214.9-6432	RBS295	33.6558	-64.5014	0.0740	335.0	20.00
122	SWIFTJ0222.3+2509	2MASXJ02223523+2508143	35.6467	25.1374	0.0620	276.2	20.00
124	SWIFTJ0225.0-2312	LEDA2823078	36.2612	-23.2133	0.2320	1158.0	20.00

BAT ID	Swift ID	Counterpart Name	R.A.	Dec.	Redshift	Distance (Mpc)	$\log(N_{\mathrm{H}}/\mathrm{cm}^{-2})$
127	SWIFTJ0226.4-2821	AM0224-283	36.6072	-28.3497	0.0590	268.0	20.57
129	SWIFTJ0228.1+3118	Mrk1040	37.0603	31.3115	0.0160	70.7	21.09
130	SWIFTJ0230.2-0900	Mrk1044	37.5230	-8.9981	0.0160	75.0	20.00
134	SWIFTJ0234.6-0848	NGC985	38.6578	-8.7881	0.0430	190.3	20.92
135	SWIFTJ0235.3-2934	ESO416-2	38.8061	-29.6048	0.0590	265.1	20.00
138	SWIFTJ0238.8-4039	LEDA74091	39.7041	-40.6439	0.0610	274.8	20.41
141	SWIFTJ0241.6+0711	Mrk595	40.3953	7.1872	0.0270	119.4	20.92
147	SWIFTJ0244.8+6227	Q0241+622	41.2404	62.4685	0.0490	197.9	20.92
161	SWIFTJ0259.9+4419	2MASXJ02593756+4417180	44.9064	44.2883	0.0310	137.2	20.00
164	SWIFTJ0308.5-7251	ESO31-8	46.8973	-72.8341	0.0270	121.5	20.30
167	SWIFTJ0311.5-2045	HE0309-2057	47.8284	-20.7717	0.0670	299.5	20.82
175	SWIFTJ0325.0-4154	LEDA12773	51.2595	-41.9049	0.0580	263.0	20.00
185	SWIFTJ0334.4-1515	LEDA2816367	53.6021	-15.2278	0.0340	153.0	20.00
191	SWIFTJ0347.0-3027	HE0345-3033	56.7729	-30.3969	0.0950	434.1	20.00
194	SWIFTJ0351.7-4030	Fairall1116	57.9237	-40.4665	0.0580	262.5	20.00
197	SWIFTJ0354.2+0250	HE0351+0240	58.5394	2.8252	0.0360	156.4	20.00
207	SWIFTJ0405.3-3707	Fairall1119	61.2570	-37.1875	0.0550	245.1	20.00

BAT ID	Swift ID	Counterpart Name	R.A.	Dec.	Redshift	Distance (Mpc)	$\log(N_{\mathrm{H}}/\mathrm{cm}^{-2})$
214	SWIFTJ0418.3+3800	3C111	64.5887	38.0266	0.0480	221.1	21.87
216	SWIFTJ0420.0-5457	NGC1566	65.0017	-54.9380	0.0050	17.9	20.00
220	SWIFTJ0426.2-5711	RBS542	66.5030	-57.2005	0.1040	480.5	20.00
228	SWIFTJ0436.3-1022	Mrk618	69.0929	-10.3761	0.0350	152.2	20.95
229	SWIFTJ0437.4-4713	HE0436-4717	69.3673	-47.1915	0.0530	229.0	20.00
234	SWIFTJ0441.2-2704	IRAS04392-2713	70.3439	-27.1387	0.0830	383.2	20.74
244	SWIFTJ0452.2+4933	LEDA168563	73.0199	49.5458	0.0290	124.0	21.23
252	SWIFTJ0502.1+0332	LEDA75258	75.5377	3.5305	0.0160	68.9	21.04
256	SWIFTJ0504.6-7345	2MASXJ05043414-7349269	76.1428	-73.8243	0.0450	198.9	21.91
266	SWIFTJ0516.2-0009	Ark120	79.0475	-0.1498	0.0320	143.0	20.00
268	SWIFTJ0516.4-1034	MCG-2-14-9	79.0884	-10.5615	0.0280	122.7	20.70
269	SWIFTJ0501.9-3239	ESO362-18	79.8992	-32.6578	0.0120	53.9	20.00
270	SWIFTJ0519.5-4545	PictorA	79.9572	-45.7788	0.0350	153.8	20.49
280	SWIFTJ0528.1-3933	LEDA17320	82.0086	-39.5791	0.0360	161.7	21.68
310	SWIFTJ0554.8+4625	UGC3374	88.7234	46.4393	0.0200	87.7	20.46
314	SWIFTJ0559.8-5028	Q0558-504	89.9475	-50.4478	0.1370	648.6	20.00
316	SWIFTJ0602.2+2829	IRAS05589+2828	90.5436	28.4721	0.0330	145.3	20.81

BAT ID	Swift ID	Counterpart Name	R.A.	Dec.	Redshift	Distance (Mpc)	$\log(N_{\mathrm{H}}/\mathrm{cm}^{-2})$
333	SWIFTJ0626.6+0729	LEDA136513	96.6126	7.4579	0.0432	187.7	20.00
335	SWIFTJ0630.7+6342	UGC3478	98.1966	63.6737	0.0120	55.0	21.18
342	SWIFTJ0640.4-2554	ESO490-26	100.0487	-25.8953	0.0240	110.2	21.48
347	SWIFTJ0651.9+7426	Mrk6	103.0513	74.4270	0.0180	82.7	20.76
348	SWIFTJ0654.6+0700	2MASSJ06543417+0703210	103.6424	7.0558	0.0240	104.2	21.32
378	SWIFTJ0736.9+5846	Mrk9	114.2376	58.7704	0.0390	176.0	20.46
382	SWIFTJ0742.5+4948	Mrk79	115.6368	49.8097	0.0220	96.3	20.00
395	SWIFTJ0753.1+4559	LEDA2272950	118.1842	45.9493	0.0510	229.9	20.00
397	SWIFTJ0756.3-4137	2MASXJ07561963-4137420	119.0818	-41.6284	0.0210	92.0	21.77
398	SWIFTJ0759.8-3844	2MASSJ07594181-3843560	119.9243	-38.7322	0.0400	176.4	20.00
402	SWIFTJ0801.9-4946	ESO209-12	120.4916	-49.7784	0.0400	176.9	21.18
409	SWIFTJ0810.9+7602	PG0804+761	122.7444	76.0451	0.1000	454.4	20.64
414	SWIFTJ0819.2-2259	LEDA80921	124.7405	-22.8767	0.0340	150.3	20.00
420	SWIFTJ0832.5+3703	RBS707	128.1056	37.1267	0.0910	421.2	20.00
423	SWIFTJ0838.4-3557	Fairall1146	129.6282	-35.9926	0.0310	139.6	20.00
425	SWIFTJ0839.6-1213	3C206	129.9608	-12.2429	0.1970	967.4	20.00
431	SWIFTJ0845.0-3531	1RXSJ084521.7-353048	131.3391	-35.5067	0.1370	647.1	20.00

BAT ID	Swift ID	Counterpart Name	R.A.	Dec.	Redshift	Distance (Mpc)	$\log(N_{\mathrm{H}}/\mathrm{cm}^{-2})$
432	SWIFTJ0845.3+1420	SDSSJ084518.51+142034.1	131.3271	14.3428	0.0600	272.1	21.85
447	SWIFTJ0917.2-6221	IRAS09149-6206	139.0390	-62.3249	0.0570	254.7	20.00
449	SWIFTJ0918.5+1618	Mrk704	139.6083	16.3055	0.0290	129.0	20.00
458	SWIFTJ0925.0+5218	Mrk110	141.3035	52.2862	0.0350	154.9	20.00
460	SWIFTJ0926.2+1244	Mrk705	141.5136	12.7344	0.0290	125.3	20.00
471	SWIFTJ0945.6-1420	NGC2992	146.4252	-14.3264	0.0070	38.0	21.72
473	SWIFTJ0947.7+0726	3C227	146.9381	7.4224	0.0850	392.7	20.00
477	SWIFTJ0955.5+6907	M81	148.8882	69.0653	0.0000	3.7	19.95
481	SWIFTJ0959.9+1303	NGC3080	149.9827	13.0438	0.0350	155.7	20.00
482	SWIFTJ0959.7-3112	LEDA154502	149.9277	-31.2162	0.0370	164.6	20.00
485	SWIFTJ1003.4-3726	ESO374-25	150.8483	-37.3958	0.0230	99.7	20.00
487	SWIFTJ1007.4+6534	1RXSJ100712.6+653511	151.8071	65.5836	0.1260	593.0	20.00
496	SWIFTJ1021.7-0327	Ark241	155.4177	-3.4538	0.0400	181.0	20.00
497	SWIFTJ1023.5+1952	NGC3227	155.8774	19.8651	0.0030	22.9	20.95
501	SWIFTJ1031.9-1418	HE1029-1401	157.9763	-14.2809	0.0860	388.2	20.00
521	SWIFTJ1051.2-1704B	LEDA32573	162.9061	-17.1247	0.0180	80.6	21.51
529	SWIFTJ1105.7+5854B	2MASXJ11053754+5851206	166.4068	58.8558	0.1910	932.2	20.00

BAT ID	Swift ID	Counterpart Name	R.A.	Dec.	Redshift	Distance (Mpc)	$\log(N_{\mathrm{H}}/\mathrm{cm}^{-2})$
530	SWIFTJ1106.5+7234	NGC3516	166.6977	72.5687	0.0080	38.9	20.00
531	SWIFTJ1110.6-2832	ESO438-9	167.7000	-28.5010	0.0240	103.9	20.00
532	SWIFTJ1113.6+0936	Mrk732	168.4573	9.5863	0.0290	128.2	20.00
537	SWIFTJ1119.5+5132	SBS1116+518	169.9084	51.5543	0.1070	495.8	-
542	SWIFTJ1125.6+5423	Arp151	171.4006	54.3825	0.0210	89.7	20.48
549	SWIFTJ1132.9+1019A	IC2921	173.2053	10.2965	0.0430	193.5	21.52
556	SWIFTJ1139.1+5913	LEDA36114	174.7874	59.1985	0.0600	274.3	20.00
557	SWIFTJ1139.0-2323	HE1136-2304	174.7125	-23.3598	0.0270	118.8	21.30
558	SWIFTJ1139.0-3743	NGC3783	174.7571	-37.7386	0.0090	38.5	20.49
561	SWIFTJ1141.3+2156	PG1138+222	175.3173	21.9393	0.0630	283.7	20.00
562	SWIFTJ1142.2+1021	NGC3822	175.5463	10.2778	0.0200	84.7	20.00
565	SWIFTJ1144.1+3652	KUG1141+371	176.1245	36.8857	0.0380	168.7	21.40
566	SWIFTJ1143.7+7942	UGC6728	176.3164	79.6815	0.0060	25.7	20.00
567	SWIFTJ1145.6-1819	HE1143-1810	176.4186	-18.4542	0.0320	143.2	20.00
572	SWIFTJ1148.3+0901	RBS1035	176.9795	9.0413	0.0680	310.7	20.00
574	SWIFTJ1149.3-0414	LEDA1060433	177.3278	-4.2808	0.0840	383.5	20.00
576	SWIFTJ1152.1-1122	PG1149-110	178.0148	-11.3734	0.0490	215.7	20.79

BAT ID	Swift ID	Counterpart Name	R.A.	Dec.	Redshift	Distance (Mpc)	$\log(N_{\mathrm{H}}/\mathrm{cm}^{-2})$
579	SWIFTJ1157.8+5529	NGC3998	179.4839	55.4536	0.0030	15.3	20.66
583	SWIFTJ1201.2-0341	Mrk1310	180.3098	-3.6781	0.0190	84.6	20.00
585	SWIFTJ1203.0+4433	NGC4051	180.7900	44.5313	0.0020	11.0	20.00
587	SWIFTJ1204.8+2758	PG1202+282	181.1755	27.9033	0.1650	794.6	20.00
589	SWIFTJ1205.8+4959	LED A2359832	181.4834	49.9990	0.0630	283.3	20.00
594	SWIFTJ1210.1-4637	CSRG644	182.5169	-46.6075	0.0310	137.2	20.00
604	SWIFTJ1213.9-0531	HE1211-0513	183.4775	-5.5054	0.0660	308.5	20.78
607	SWIFTJ1217.3+0714	NGC4235	184.2912	7.1916	0.0080	26.6	21.26
608	SWIFTJ1218.5+2952	NGC4253	184.6105	29.8129	0.0120	55.9	20.32
611	SWIFTJ1222.4+7520	Mrk205	185.4336	75.3106	0.0700	316.9	20.00
613	SWIFTJ1223.7+0238	Mrk50	185.8506	2.6790	0.0230	103.3	20.00
616	SWIFTJ1202.5+3332	NGC4395	186.4536	33.5469	0.0010	4.8	21.04
622	SWIFTJ1232.0-4802	2MASXJ12313717-4758019	187.9048	-47.9672	0.0270	122.6	20.59
623	SWIFTJ1232.1+2009	Mrk771	188.0151	20.1582	0.0630	286.7	20.00
631	SWIFTJ1239.6-0519	NGC4593	189.9143	-5.3442	0.0090	37.2	20.00
634	SWIFTJ1240.9-3331	ESO381-7	190.1957	-33.5700	0.0550	243.9	20.00
636	SWIFTJ1241.6-5748	LED A166252	190.3574	-57.8343	0.0240	108.7	21.12

BAT ID	Swift ID	Counterpart Name	R.A.	Dec.	Redshift	Distance (Mpc)	$\log(N_{\mathrm{H}}/\mathrm{cm}^{-2})$
641	SWIFTJ1252.3-1323	NGC4748	193.0519	-13.4148	0.0140	61.2	20.00
644	SWIFTJ1255.0-2657	CTS18	193.7348	-26.9505	0.0590	264.3	20.00
651	SWIFTJ1302.9+1620	Mrk783	195.7449	16.4077	0.0670	301.5	20.78
652	SWIFTJ1303.8+5345	MCG+9-21-96	195.9979	53.7916	0.0290	132.0	20.00
658	SWIFTJ1306.4-4025B	ESO323-81	196.8003	-40.4077	0.0171	70.2	20.00
663	SWIFTJ1313.1-1108	HE1310-1051	198.2741	-11.1284	0.0340	152.0	20.00
664	SWIFTJ1313.6+3650A	RXJ1313.8+3653	198.4540	36.8994	0.0660	301.2	-
665	SWIFTJ1313.6+3650B	NGC5033	198.3647	36.5936	0.0020	19.1	20.00
667	SWIFTJ1316.9-7155	2MASXJ13165424-7155270	199.2263	-71.9242	0.0700	317.0	20.00
678	SWIFTJ1334.8-2328D2	LEDA47848	203.6652	-23.4465	0.0340	150.5	21.65
680	SWIFTJ1335.8-3416	MCG-6-30-15	203.9740	-34.2956	0.0070	30.4	20.85
686	SWIFTJ1341.9+3537	NGC5273	205.5349	35.6542	0.0030	16.6	20.59
688	SWIFTJ1345.5+4139	NGC5290	206.3298	41.7124	0.0080	34.5	21.96
694	SWIFTJ1349.3-3018	IC4329A	207.3303	-30.3095	0.0160	69.3	21.52
696	SWIFTJ1351.5-1814	CTS103	207.8729	-18.2295	0.0120	52.2	20.18
697	SWIFTJ1352.8+6917	Mrk279	208.2643	69.3082	0.0300	132.1	20.43
704	SWIFTJ1356.6-1932	ESO578-9	209.1530	-19.5291	0.0350	153.8	20.95

BAT ID	Swift ID	Counterpart Name	R.A.	Dec.	Redshift	Distance (Mpc)	$\log(N_{\mathrm{H}}/\mathrm{cm}^{-2})$
713	SWIFTJ1416.9-1158	LEDA126226	214.2083	-11.9828	0.0980	455.9	20.00
715	SWIFTJ1417.7+6143	SDSSJ141742.94+614152.5	214.4289	61.6979	0.1180	552.9	20.00
717	SWIFTJ1417.9+2507	NGC5548	214.4981	25.1368	0.0170	72.4	20.69
719	SWIFTJ1419.0-2639	ESO511-30	214.8434	-26.6448	0.0220	100.0	20.00
722	SWIFTJ1421.4+4747	LEDA140305	215.3739	47.7901	0.0720	327.1	20.00
726	SWIFTJ1427.5+1949	Mrk813	216.8544	19.8312	0.1100	513.4	20.85
728	SWIFTJ1429.2+0118	Mrk1383	217.2774	1.2850	0.0860	391.7	20.00
730	SWIFTJ1431.2+2816	Mrk684	217.7699	28.2873	0.0460	203.9	20.00
734	SWIFTJ1434.9+4837	NGC5683	218.7186	48.6619	0.0360	160.6	20.00
735	SWIFTJ1436.4+5846	Mrk817	219.0920	58.7943	0.0310	136.8	20.00
748	SWIFTJ1453.3+2558	SDSSJ145307.92+255433.0	223.2830	25.9092	0.0490	215.8	20.00
750	SWIFTJ1454.9-5133	LEDA3076910	223.8230	-51.5709	0.0160	69.8	20.92
753	SWIFTJ1504.2+1025	Mrk841	226.0050	10.4377	0.0360	161.2	20.00
754	SWIFTJ1506.7+0353A	Mrk1392	226.4856	3.7073	0.0360	158.5	20.00
757	SWIFTJ1508.8-0013	Mrk1393	227.2248	-0.1969	0.0540	242.5	20.28
760	SWIFTJ1512.0-2119	IRAS15091-2107	227.9992	-21.3171	0.0440	196.9	21.28
765	SWIFTJ1513.8-8125	2MASXJ15144217-8123377	228.6748	-81.3939	0.0680	309.5	20.00

BAT ID	Swift ID	Counterpart Name	R.A.	Dec.	Redshift	Distance (Mpc)	$\log(N_{\mathrm{H}}/\mathrm{cm}^{-2})$
770	SWIFTJ1523.5+6340	LEDA2821626	230.9411	63.6567	0.2040	1003.8	20.00
771	SWIFTJ1530.0-1300	LEDA944345	232.4929	-13.0110	0.1030	479.4	20.00
774	SWIFTJ1535.9+5751	Mrk290	233.9683	57.9026	0.0290	133.2	20.00
779	SWIFTJ1547.5+2050	3C323.1	236.9314	20.8713	0.2640	1342.9	20.00
783	SWIFTJ1548.5-1344	NGC5995	237.1040	-13.7576	0.0250	108.3	21.97
795	SWIFTJ1613.2-6043	LEDA2793282	242.9641	-60.6320	0.0150	66.8	20.00
797	SWIFTJ1614.0+6544	Mrk876	243.4882	65.7194	0.1290	606.1	20.00
801	SWIFTJ1618.7-5930	LEDA3078020	244.6519	-59.4548	0.0350	150.9	20.00
810	SWIFTJ1626.7+8530	VIIZw653	246.3581	85.4949	0.0630	292.0	20.58
815	SWIFTJ1629.9+6722	Mrk885	247.4516	67.3783	0.0250	118.1	20.00
833	SWIFTJ1648.0-3037	2MASXJ16481523-3035037	252.0635	-30.5844	0.0310	138.3	21.40
838	SWIFTJ1652.0-5915B	NGC6221	253.1930	-59.2169	0.0050	11.9	21.15
862	SWIFTJ1708.6+2155	SDSSJ170859.13+215308.1	257.2464	21.8856	0.0720	327.6	20.00
876	SWIFTJ1719.7+4900	ARP102B	259.8104	48.9804	0.0240	108.5	21.32
882	SWIFTJ1723.2+3418	4C+34.47	260.8366	34.2994	0.2060	1013.1	20.00
888	SWIFTJ1731.3+1442	2MASXJ17311341+1442561	262.8058	14.7155	0.0827	374.3	20.00
898	SWIFTJ1737.7-5956B	ESO139-12	264.4128	-59.9407	0.0170	73.4	20.00

BAT ID	Swift ID	Counterpart Name	R.A.	Dec.	Redshift	Distance (Mpc)	$\log(N_{\mathrm{H}}/\mathrm{cm}^{-2})$
905	SWIFTJ1741.9-1211	1RXSJ174155.3-121157	265.4802	-12.1991	0.0370	165.7	21.40
907	SWIFTJ1742.2+1833	Q1739+184	265.5289	18.4558	0.1860	902.4	20.00
912	SWIFTJ1745.4+2906	1RXSJ174538.1+290823	266.4094	29.1395	0.1100	511.1	20.00
924	SWIFTJ1747.8+6837A	Mrk507	267.1601	68.7045	0.0550	245.6	20.00
925	SWIFTJ1747.8+6837B	2XMMJ174659.4+683631	266.7481	68.6084	0.0630	286.4	20.00
929	SWIFTJ1748.8-3257	2MASSJ17485512-3254521	267.2297	-32.9145	0.0200	89.9	21.38
950	SWIFTJ1807.9+1124	LEDA2808003	271.9580	11.3470	0.0800	354.6	21.54
967	SWIFTJ1822.0+6421	Q1821+643	275.4885	64.3434	0.2970	1533.7	20.00
984	SWIFTJ1835.0+3240	3C382	278.7641	32.6963	0.0570	258.9	20.00
994	SWIFTJ1842.0+7945	3C390.3	280.5375	79.7714	0.0560	248.4	20.85
1002	SWIFTJ1848.0-7832	LEDA89032	281.7612	-78.5304	0.0740	334.4	20.00
1009	SWIFTJ1856.5-7851	Fairall189	283.6678	-78.8984	0.0280	123.8	20.00
1013	SWIFTJ1856.1+1539	SSTSL2J185600.55+153758.4	284.0023	15.6329	0.0840	384.5	21.36
1021	SWIFTJ1905.4+4231	Z229-15	286.3581	42.4610	0.0270	120.5	20.76
1031	SWIFTJ1919.4-2958	LEDA2829969	289.8668	-29.9689	0.1660	801.6	20.00
1032	SWIFTJ1921.1-5842	ESO141-55	290.3089	-58.6703	0.0360	163.2	20.00
1036	SWIFTJ1925.0+5041	2E1923.7+5037	291.2591	50.7205	0.0670	304.2	20.70

BAT ID	Swift ID	Counterpart Name	R.A.	Dec.	Redshift	Distance (Mpc)	$\log(N_{\mathrm{H}}/\mathrm{cm}^{-2})$
1037	SWIFTJ1926.9+4140	2MASXJ19263018+4133053	291.6259	41.5514	0.0710	323.6	20.49
1041	SWIFTJ1933.9+3258	2MASSJ19334715+3254259	293.4465	32.9072	0.0570	262.5	20.00
1042	SWIFTJ1937.5-0613	LEDA90334	294.3876	-6.2180	0.0100	44.7	20.85
1043	SWIFTJ1938.1-5108	CTS61	294.5183	-51.1637	0.0400	176.4	20.00
1046	SWIFTJ1942.6-1024	NGC6814	295.6691	-10.3236	0.0050	22.8	20.97
1064	SWIFTJ2009.0-6103	NGC6860	302.1954	-61.0999	0.0140	63.6	21.08
1084	SWIFTJ2035.2+2604	2MASXJ20350566+2603301	308.7735	26.0583	0.0480	216.0	21.30
1088	SWIFTJ2042.3+7507	4C+74.26	310.6555	75.1340	0.1040	484.9	21.36
1089	SWIFTJ2044.0+2832	1RXSJ204404.0+283303	311.0177	28.5526	0.0500	218.9	21.15
1090	SWIFTJ2044.2-1045	Mrk509	311.0406	-10.7235	0.0340	152.5	20.00
1099	SWIFTJ2109.1-0942	H2106-099	317.2915	-9.6708	0.0260	117.0	21.20
1100	SWIFTJ2109.2+3531	1RXSJ210932.5+353245	317.3828	35.5493	0.2020	985.4	20.00
1102	SWIFTJ2114.4+8206	S52116+81	318.5049	82.0801	0.0840	378.7	20.00
1106	SWIFTJ2118.9+3336	2MASXJ21192912+3332566	319.8714	33.5491	0.0500	226.4	21.57
1114	SWIFTJ2132.0-3343	CTS109	323.0092	-33.7149	0.0290	131.5	20.70
1116	SWIFTJ2134.9-2729	2MASXJ21344509-2725557	323.6881	-27.4321	0.0670	300.7	21.43
1117	SWIFTJ2156.1+4728	2MASXJ21355399+4728217	323.9751	47.4727	0.0250	112.5	21.28

BAT ID	Swift ID	Counterpart Name	R.A.	Dec.	Redshift	Distance (Mpc)	$\log(N_{\mathrm{H}}/\mathrm{cm}^{-2})$
1118	SWIFTJ2135.5-6222	LEDA89176	324.0963	-62.4001	0.0580	263.2	20.00
1120	SWIFTJ2137.8-1433	Q2135-147	324.4383	-14.5488	0.2000	980.2	20.00
1125	SWIFTJ2145.5+1101	1RXSJ214532.2+110255	326.3868	11.0486	0.2090	1027.6	20.00
1128	SWIFTJ2150.2-1855	LEDA2831062	327.4920	-18.9899	0.1580	752.0	20.00
1131	SWIFTJ2157.2-6942	ESO75-41	329.2749	-69.6899	0.0280	122.4	20.00
1141	SWIFTJ2209.1-2747	NGC7214	332.2819	-27.8095	0.0230	98.8	20.00
1150	SWIFTJ2223.8+1143	MCG+2-57-2	335.9376	11.8359	0.0290	130.1	20.00
1152	SWIFTJ2226.8+3628	UGC12040	336.7740	36.3616	0.0210	90.7	20.00
1161	SWIFTJ2236.7-1233	Mrk915	339.1937	-12.5452	0.0240	104.4	20.00
1162	SWIFTJ2240.2+0801	UGC12138	340.0711	8.0538	0.0250	108.8	20.00
1172	SWIFTJ2254.1-1734	MR2251-178	343.5245	-17.5821	0.0640	289.7	20.00
1176	SWIFTJ2256.5+0526	RBS1917	344.1519	5.4214	0.0660	296.5	20.00
1178	SWIFTJ2259.7+2458	LEDA70195	344.8871	24.9183	0.0340	148.1	20.00
1179	SWIFTJ2301.4-5916	RBS1931	345.4010	-59.2225	0.1490	713.2	20.73
1181	SWIFTJ2303.1-1837	PKS2300-18	345.7624	-18.6905	0.1280	601.3	20.26
1182	SWIFTJ2303.3+0852	NGC7469	345.8153	8.8737	0.0160	69.4	20.53
1183	SWIFTJ2304.8-0843	Mrk926	346.1812	-8.6857	0.0460	211.9	20.00

BAT ID	Swift ID	Counterpart Name	R.A.	Dec.	Redshift	Distance (Mpc)	$\log(N_{\mathrm{H}}/\mathrm{cm}^{-2})$
1185	SWIFTJ2307.1+0433	PG2304+042	346.7621	4.5492	0.0420	188.2	20.00
1187	SWIFTJ2308.1+4014	2MASXJ23075724+4016393	346.9886	40.2775	0.0740	328.3	21.64
1189	SWIFTJ2318.9+0013	NGC7603	349.7361	0.2439	0.0290	125.7	20.00
1194	SWIFTJ2325.5-3827	IRAS23226-3843	351.3508	-38.4470	0.0350	158.7	20.00
1195	SWIFTJ2325.6+2157	RHS61	351.4760	21.8872	0.1200	560.6	20.00
1206	SWIFTJ2351.9-0109	PG2349-014	357.9838	-1.1537	0.1740	839.6	20.00

Table 2: Full version of Table 4.2.

BAT ID	Swift ID	$\log(L_{2500\text{\AA}})$	$\log(L_{2\text{keV}})$	$\log(L_{\text{bol}})$	$\log(M_{\text{BH}}/M_{\odot})$	α_{ox}	$\kappa_{4400\text{\AA}}$	κ_{2-10}	$\log(\lambda_{\text{Edd}})$
3	SWIFTJ0002.5+0323	43.07	42.35	43.68	6.70	-1.28	5.59	10.09	-1.20
6	SWIFTJ0006.2+2012	43.99	43.11	44.57	7.23	-1.34	5.86	22.26	-0.84
16	SWIFTJ0029.2+1319	45.49	44.32	46.16	8.49	-1.45	8.12	49.53	-0.50
19	SWIFTJ0034.5-7904	44.26	43.78	44.95	8.02	-1.19	6.56	10.70	-1.25
34	SWIFTJ0051.6+2928	43.96	42.49	44.44	7.62	-1.56	4.63	53.75	-1.36
36	SWIFTJ0051.9+1724	44.43	43.91	45.15	7.75	-1.20	7.38	8.66	-0.77
39	SWIFTJ0054.9+2524	45.36	44.28	46.08	8.46	-1.42	9.13	32.70	-0.56
43	SWIFTJ0059.4+3150	42.69	41.96	43.42	7.56	-1.28	8.96	14.26	-2.32
45	SWIFTJ0101.5-0308	43.90	42.75	44.38	8.13	-1.44	4.19	23.78	-1.93
51	SWIFTJ0105.7-1414	44.30	43.48	45.03	7.88	-1.32	8.37	16.79	-1.03
61	SWIFTJ0113.8-1450	43.42	43.42	44.71	8.33	-1.00	14.59	8.40	-1.79
69	SWIFTJ0122.0-2818	45.38	43.70	46.29	8.18	-1.64	15.07	194.03	-0.07
73	SWIFTJ0123.9-5846	44.67	43.88	45.55	8.30	-1.31	13.47	24.47	-0.93
77	SWIFTJ0127.5+1910	43.02	42.46	43.78	6.05	-1.22	9.66	13.30	-0.45
78	SWIFTJ0128.0-1850	44.05	43.29	44.63	7.03	-1.29	4.31	12.30	-0.57

BAT ID	Swift ID	$\log(L_{2500\text{\AA}})$	$\log(L_{2\text{keV}})$	$\log(L_{\text{bol}})$	$\log(M_{\text{BH}}/M_{\odot})$	α_{ox}	$\kappa_{4400\text{\AA}}$	κ_{2-10}	$\log(\lambda_{\text{Edd}})$
82	SWIFTJ0130.2-4552	44.26	43.39	44.97	7.90	-1.33	8.60	25.81	-1.11
85	SWIFTJ0134.8-0430	43.56	43.42	44.76	8.40	-1.06	13.56	10.12	-1.82
95	SWIFTJ0151.3-3610	42.88	42.77	43.85	7.89	-1.04	6.08	9.59	-2.22
98	SWIFTJ0155.4+0228	43.83	43.62	44.77	8.29	-1.08	4.13	6.40	-1.70
106	SWIFTJ0206.2-0019	43.81	43.33	44.63	7.81	-1.18	9.15	9.72	-1.35
110	SWIFTJ0208.2+4452	43.71	42.31	44.15	7.74	-1.54	3.73	34.22	-1.76
113	SWIFTJ0209.7+5226	43.94	43.52	44.96	8.01	-1.16	14.23	12.40	-1.22
116	SWIFTJ0214.6-0049	42.59	42.11	43.31	7.57	-1.19	5.17	6.05	-2.43
117	SWIFTJ0214.9-6432	44.46	43.39	44.91	8.07	-1.41	3.71	21.02	-1.33
122	SWIFTJ0222.3+2509	45.11	43.27	45.53	8.07	-1.71	3.57	53.60	-0.71
124	SWIFTJ0225.0-2312	44.92	44.35	45.82	8.88	-1.22	11.37	12.38	-1.24
127	SWIFTJ0226.4-2821	43.26	43.45	44.67	7.98	-0.93	7.63	9.11	-1.49
129	SWIFTJ0228.1+3118	42.89	42.64	44.24	7.41	-1.09	10.91	15.83	-1.34
130	SWIFTJ0230.2-0900	43.46	42.21	44.04	6.45	-1.48	6.20	35.34	-0.58
134	SWIFTJ0234.6-0848	44.28	43.45	44.98	8.11	-1.32	7.86	16.55	-1.31
135	SWIFTJ0235.3-2934	43.25	42.73	44.14	8.84	-1.20	6.91	11.05	-2.87
138	SWIFTJ0238.8-4039	43.85	43.24	44.54	7.45	-1.23	5.92	10.52	-1.09

BAT ID	Swift ID	$\log(L_{2500\text{\AA}})$	$\log(L_{2\text{keV}})$	$\log(L_{\text{bol}})$	$\log(M_{\text{BH}}/M_{\odot})$	α_{ox}	$\kappa_{4400\text{\AA}}$	κ_{2-10}	$\log(\lambda_{\text{Edd}})$
141	SWIFTJ0241.6+0711	43.07	42.03	43.74	7.41	-1.40	5.64	19.95	-1.85
147	SWIFTJ0244.8+6227	43.82	43.69	44.93	nan	-1.05	8.42	8.55	nan
161	SWIFTJ0259.9+4419	42.61	42.33	43.44	6.68	-1.11	6.75	7.95	-1.41
164	SWIFTJ0308.5-7251	43.42	42.74	44.10	6.70	-1.26	7.66	19.02	-0.78
167	SWIFTJ0311.5-2045	44.51	43.55	45.21	7.79	-1.37	8.30	20.50	-0.76
175	SWIFTJ0325.0-4154	44.28	43.26	45.34	7.70	-1.39	21.92	70.36	-0.53
185	SWIFTJ0334.4-1515	43.48	42.57	44.03	7.08	-1.35	4.84	14.29	-1.22
191	SWIFTJ0347.0-3027	43.44	42.99	44.18	7.55	-1.17	3.57	8.89	-1.54
194	SWIFTJ0351.7-4030	44.47	43.37	45.03	8.09	-1.42	5.85	30.96	-1.24
197	SWIFTJ0354.2+0250	43.99	43.13	44.70	7.18	-1.33	6.34	18.19	-0.65
207	SWIFTJ0405.3-3707	42.82	42.78	43.80	8.57	-1.02	9.01	7.03	-2.94
214	SWIFTJ0418.3+3800	44.66	43.96	45.68	8.45	-1.27	13.50	19.61	-0.95
216	SWIFTJ0420.0-5457	42.76	41.26	43.49	6.83	-1.58	9.52	74.17	-1.52
220	SWIFTJ0426.2-5711	45.14	44.37	45.91	8.34	-1.29	9.86	16.55	-0.61
228	SWIFTJ0436.3-1022	43.84	42.92	44.51	7.72	-1.35	7.68	20.51	-1.39
229	SWIFTJ0437.4-4713	44.44	43.28	45.16	7.87	-1.45	9.17	42.61	-0.89
234	SWIFTJ0441.2-2704	44.15	43.78	44.93	8.04	-1.14	6.89	8.05	-1.28

BAT ID	Swift ID	$\log(L_{2500\text{\AA}})$	$\log(L_{2\text{keV}})$	$\log(L_{\text{bol}})$	$\log(M_{\text{BH}}/M_{\odot})$	α_{ox}	$\kappa_{4400\text{\AA}}$	κ_{2-10}	$\log(\lambda_{\text{Edd}})$
244	SWIFTJ0452.2+4933	44.60	43.61	45.19	7.88	-1.38	5.24	18.30	-0.87
252	SWIFTJ0502.1+0332	42.35	42.39	43.84	7.02	-0.98	59.25	10.69	-1.36
256	SWIFTJ0504.6-7345	43.92	42.58	44.51	7.93	-1.51	5.31	32.11	-1.60
266	SWIFTJ0516.2-0009	44.45	43.54	45.02	8.07	-1.35	5.03	14.47	-1.22
268	SWIFTJ0516.4-1034	43.96	42.69	44.53	7.02	-1.49	6.04	37.18	-0.67
269	SWIFTJ0501.9-3239	43.35	42.55	44.12	7.11	-1.31	9.55	16.56	-1.16
270	SWIFTJ0519.5-4545	43.17	43.19	44.51	6.77	-0.99	27.20	9.15	-0.44
280	SWIFTJ0528.1-3933	44.36	42.26	44.77	7.34	-1.81	3.47	119.80	-0.75
310	SWIFTJ0554.8+4625	43.82	43.35	44.85	6.61	-1.18	13.71	13.49	0.07
314	SWIFTJ0559.8-5028	45.35	44.45	46.11	7.62	-1.35	10.00	36.08	0.31
316	SWIFTJ0602.2+2829	44.32	43.27	45.06	8.00	-1.40	6.75	23.25	-1.12
333	SWIFTJ0626.6+0729	43.61	43.21	44.46	7.80	-1.15	9.63	9.08	-1.52
335	SWIFTJ0630.7+6342	42.32	42.02	43.26	6.06	-1.12	4.20	8.37	-0.97
342	SWIFTJ0640.4-2554	43.19	43.04	44.30	7.15	-1.06	12.24	8.26	-1.02
347	SWIFTJ0651.9+7426	43.38	42.83	44.63	8.10	-1.21	8.53	24.58	-1.64
348	SWIFTJ0654.6+0700	43.36	42.76	44.22	6.74	-1.23	9.40	12.95	-0.70
378	SWIFTJ0736.9+5846	44.05	42.51	44.45	7.60	-1.59	3.11	34.20	-1.33

BAT ID	Swift ID	$\log(L_{2500\text{\AA}})$	$\log(L_{2\text{keV}})$	$\log(L_{\text{bol}})$	$\log(M_{\text{BH}}/M_{\odot})$	α_{ox}	$\kappa_{4400\text{\AA}}$	κ_{2-10}	$\log(\lambda_{\text{Edd}})$
382	SWIFTJ0742.5+4948	43.65	42.84	44.36	7.61	-1.31	7.01	14.34	-1.43
395	SWIFTJ0753.1+4559	42.79	42.95	44.17	8.66	-0.94	22.19	7.84	-2.67
397	SWIFTJ0756.3-4137	43.41	41.86	44.07	7.89	-1.59	1.77	73.43	-2.00
398	SWIFTJ0759.8-3844	44.36	43.45	45.00	8.82	-1.35	5.83	16.91	-2.00
402	SWIFTJ0801.9-4946	43.42	43.33	44.51	7.82	-1.03	7.13	8.18	-1.48
409	SWIFTJ0810.9+7602	44.94	44.22	45.50	8.73	-1.27	5.02	11.81	-1.40
414	SWIFTJ0819.2-2259	42.85	42.65	43.87	7.85	-1.08	15.43	8.46	-2.15
420	SWIFTJ0832.5+3703	44.58	43.74	45.12	9.00	-1.32	4.75	11.18	-2.06
423	SWIFTJ0838.4-3557	42.86	43.07	44.20	8.32	-0.92	12.70	6.68	-2.29
425	SWIFTJ0839.6-1213	45.24	44.75	46.04	8.58	-1.19	10.01	8.05	-0.72
431	SWIFTJ0845.0-3531	44.54	43.98	45.49	8.93	-1.21	10.81	13.68	-1.61
432	SWIFTJ0845.3+1420	42.57	43.27	44.72	8.64	-0.73	17.58	12.74	-2.10
447	SWIFTJ0917.2-6221	45.06	43.80	45.64	8.63	-1.48	6.08	34.89	-1.17
449	SWIFTJ0918.5+1618	43.75	42.88	44.47	8.24	-1.34	4.54	14.25	-1.95
458	SWIFTJ0925.0+5218	44.16	43.56	45.11	7.29	-1.23	15.14	15.15	-0.35
460	SWIFTJ0926.2+1244	43.87	43.02	44.51	7.08	-1.32	6.73	17.15	-0.75
471	SWIFTJ0945.6-1420	43.83	41.26	44.22	7.97	-1.99	3.27	304.70	-1.93

BAT ID	Swift ID	$\log(L_{2500\text{\AA}})$	$\log(L_{2\text{keV}})$	$\log(L_{\text{bol}})$	$\log(M_{\text{BH}}/M_{\odot})$	α_{ox}	$\kappa_{4400\text{\AA}}$	κ_{2-10}	$\log(\lambda_{\text{Edd}})$
473	SWIFTJ0947.7+0726	44.02	43.91	45.45	8.91	-1.04	28.15	13.91	-1.64
477	SWIFTJ0955.5+6907	40.19	39.85	41.02	7.90	-1.13	7.07	7.86	-5.05
481	SWIFTJ0959.9+1303	43.30	42.47	43.99	6.84	-1.32	8.07	15.77	-1.03
482	SWIFTJ0959.7-3112	44.14	42.99	44.64	7.25	-1.44	4.57	22.74	-0.79
485	SWIFTJ1003.4-3726	43.35	42.03	43.77	7.33	-1.51	3.53	29.52	-1.74
487	SWIFTJ1007.4+6534	44.25	43.70	44.90	8.01	-1.21	5.34	7.60	-1.29
496	SWIFTJ1021.7-0327	44.11	43.21	44.62	8.19	-1.34	3.89	21.20	-1.75
497	SWIFTJ1023.5+1952	42.06	41.87	43.49	6.77	-1.07	15.33	16.33	-1.45
501	SWIFTJ1031.9-1418	45.42	44.08	45.93	8.85	-1.52	4.85	32.18	-1.09
521	SWIFTJ1051.2-1704B	42.46	42.02	43.31	8.48	-1.17	2.74	13.75	-3.34
529	SWIFTJ1105.7+5854B	44.96	43.74	45.66	8.44	-1.47	3.69	37.72	-0.96
530	SWIFTJ1106.5+7234	43.04	42.33	44.05	7.39	-1.27	15.83	20.39	-1.52
531	SWIFTJ1110.6-2832	43.24	42.40	43.78	6.87	-1.32	3.44	11.74	-1.27
532	SWIFTJ1113.6+0936	42.99	42.84	44.24	6.59	-1.06	16.38	10.33	-0.53
537	SWIFTJ1119.5+5132	44.67	43.83	45.53	8.40	-1.32	13.08	32.00	-1.05
542	SWIFTJ1125.6+5423	42.40	41.94	43.42	6.67	-1.18	19.09	16.96	-1.43
549	SWIFTJ1132.9+1019A	42.79	42.41	44.29	7.70	-1.14	3.99	28.46	-1.58

BAT ID	Swift ID	$\log(L_{2500\text{\AA}})$	$\log(L_{2\text{keV}})$	$\log(L_{\text{bol}})$	$\log(M_{\text{BH}}/M_{\odot})$	α_{ox}	$\kappa_{4400\text{\AA}}$	κ_{2-10}	$\log(\lambda_{\text{Edd}})$
556	SWIFTJ1139.1+5913	44.35	43.66	45.03	7.85	-1.26	6.74	12.25	-0.99
557	SWIFTJ1139.0-2323	43.97	42.65	44.54	7.84	-1.51	6.17	40.52	-1.48
558	SWIFTJ1139.0-3743	43.35	42.73	43.97	7.37	-1.24	5.59	11.52	-1.58
561	SWIFTJ1141.3+2156	44.30	43.60	45.15	7.39	-1.27	12.73	19.58	-0.42
562	SWIFTJ1142.2+1021	42.18	42.24	43.55	7.43	-0.98	9.13	9.32	-2.06
565	SWIFTJ1144.1+3652	43.88	43.03	44.44	8.11	-1.33	4.49	12.62	-1.85
566	SWIFTJ1143.7+7942	41.97	41.34	42.65	5.55	-1.24	5.26	10.97	-1.07
567	SWIFTJ1145.6-1819	44.06	43.32	44.92	7.39	-1.28	10.47	16.42	-0.64
572	SWIFTJ1148.3+0901	44.33	42.60	44.75	8.24	-1.66	3.26	61.81	-1.67
574	SWIFTJ1149.3-0414	44.17	43.41	44.75	8.56	-1.29	4.10	12.35	-1.99
576	SWIFTJ1152.1-1122	43.45	42.49	44.02	7.68	-1.37	4.28	10.71	-1.83
579	SWIFTJ1157.8+5529	40.99	41.11	42.90	8.93	-0.96	4.96	28.14	-4.21
583	SWIFTJ1201.2-0341	42.26	42.09	43.41	6.21	-1.06	12.95	7.02	-0.98
585	SWIFTJ1203.0+4433	41.61	40.98	42.30	6.13	-1.24	5.13	11.37	-2.00
587	SWIFTJ1204.8+2758	45.03	44.35	45.78	8.10	-1.26	9.35	13.99	-0.49
589	SWIFTJ1205.8+4959	43.76	42.89	44.39	8.32	-1.33	2.79	15.43	-2.11
594	SWIFTJ1210.1-4637	44.15	42.56	44.53	6.92	-1.61	3.10	39.94	-0.56

BAT ID	Swift ID	$\log(L_{2500\text{\AA}})$	$\log(L_{2\text{keV}})$	$\log(L_{\text{bol}})$	$\log(M_{\text{BH}}/M_{\odot})$	α_{ox}	$\kappa_{4400\text{\AA}}$	κ_{2-10}	$\log(\lambda_{\text{Edd}})$
604	SWIFTJ1213.9-0531	42.94	43.42	44.62	8.29	-0.82	5.99	8.92	-1.84
607	SWIFTJ1217.3+0714	42.92	41.37	43.35	7.28	-1.60	3.61	34.45	-2.11
608	SWIFTJ1218.5+2952	43.24	42.15	43.68	6.82	-1.42	2.55	21.03	-1.32
611	SWIFTJ1222.4+7520	44.56	43.67	45.08	8.57	-1.34	4.26	16.85	-1.67
613	SWIFTJ1223.7+0238	43.30	42.78	44.11	7.42	-1.20	8.42	10.85	-1.48
616	SWIFTJ1202.5+3332	40.10	40.49	41.46	5.45	-0.85	19.94	7.82	-2.17
622	SWIFTJ1232.0-4802	43.43	42.63	43.97	6.82	-1.31	4.69	13.85	-1.03
623	SWIFTJ1232.1+2009	44.46	43.37	44.95	7.76	-1.42	4.55	21.23	-0.99
631	SWIFTJ1239.6-0519	42.56	42.16	43.47	6.88	-1.15	7.62	8.57	-1.59
634	SWIFTJ1240.9-3331	43.35	43.08	44.38	7.78	-1.11	11.46	9.54	-1.58
636	SWIFTJ1241.6-5748	43.76	43.12	44.73	8.79	-1.25	12.61	15.95	-2.24
641	SWIFTJ1252.3-1323	43.15	42.30	43.67	6.41	-1.33	4.26	15.58	-0.91
644	SWIFTJ1255.0-2657	44.09	43.12	45.39	8.15	-1.38	22.16	53.80	-0.94
651	SWIFTJ1302.9+1620	43.10	43.30	45.05	7.30	-0.92	11.01	21.87	-0.43
652	SWIFTJ1303.8+5345	43.46	43.27	44.54	7.67	-1.07	13.54	7.39	-1.31
658	SWIFTJ1306.4-4025B	41.89	41.19	42.75	6.52	-1.27	4.67	15.21	-1.95
663	SWIFTJ1313.1-1108	43.88	42.94	44.42	7.49	-1.36	5.10	18.19	-1.25

BAT ID	Swift ID	$\log(L_{2500\text{\AA}})$	$\log(L_{2\text{keV}})$	$\log(L_{\text{bol}})$	$\log(M_{\text{BH}}/M_{\odot})$	α_{ox}	$\kappa_{4400\text{\AA}}$	κ_{2-10}	$\log(\lambda_{\text{Edd}})$
664	SWIFTJ1313.6+3650A	43.83	42.98	44.32	7.74	-1.33	3.70	15.89	-1.60
665	SWIFTJ1313.6+3650B	41.30	40.58	42.22	7.75	-1.28	2.47	23.81	-3.71
667	SWIFTJ1316.9-7155	44.02	43.40	45.09	9.29	-1.24	13.42	19.43	-2.37
678	SWIFTJ1334.8-2328D2	42.69	42.85	44.09	8.01	-0.94	31.97	8.59	-2.09
680	SWIFTJ1335.8-3416	41.42	42.16	43.46	6.60	-0.72	42.48	8.41	-1.31
686	SWIFTJ1341.9+3537	42.48	41.50	42.99	6.66	-1.37	4.15	14.75	-1.85
688	SWIFTJ1345.5+4139	43.23	41.64	43.77	7.83	-1.61	4.68	49.41	-2.24
694	SWIFTJ1349.3-3018	43.60	43.20	44.93	7.65	-1.16	6.26	20.25	-0.90
696	SWIFTJ1351.5-1814	42.97	42.33	43.66	6.11	-1.25	6.48	11.73	-0.62
697	SWIFTJ1352.8+6917	43.79	43.15	44.57	7.43	-1.24	9.08	12.70	-1.04
704	SWIFTJ1356.6-1932	44.02	43.03	44.78	7.61	-1.38	6.82	23.92	-1.00
713	SWIFTJ1416.9-1158	44.77	44.06	45.71	8.12	-1.27	16.11	28.78	-0.58
715	SWIFTJ1417.7+6143	44.85	43.75	45.60	8.68	-1.42	10.01	36.04	-1.26
717	SWIFTJ1417.9+2507	43.12	42.74	44.31	7.72	-1.14	19.29	13.91	-1.59
719	SWIFTJ1419.0-2639	42.87	42.46	43.82	7.23	-1.16	11.97	10.43	-1.59
722	SWIFTJ1421.4+4747	44.98	43.69	45.97	8.42	-1.49	18.54	80.75	-0.62
726	SWIFTJ1427.5+1949	45.42	44.03	45.97	8.51	-1.53	5.53	40.14	-0.72

BAT ID	Swift ID	$\log(L_{2500\text{\AA}})$	$\log(L_{2\text{keV}})$	$\log(L_{\text{bol}})$	$\log(M_{\text{BH}}/M_{\odot})$	α_{ox}	$\kappa_{4400\text{\AA}}$	κ_{2-10}	$\log(\lambda_{\text{Edd}})$
728	SWIFTJ1429.2+0118	44.97	44.05	45.51	9.01	-1.35	5.05	16.12	-1.68
730	SWIFTJ1431.2+2816	44.21	42.74	44.61	6.78	-1.56	3.04	37.76	-0.35
734	SWIFTJ1434.9+4837	43.02	41.84	43.56	7.69	-1.45	4.07	19.51	-2.31
735	SWIFTJ1436.4+5846	44.03	42.76	44.67	7.59	-1.49	6.86	32.45	-1.10
748	SWIFTJ1453.3+2558	44.05	43.41	44.83	8.48	-1.25	8.87	9.97	-1.83
750	SWIFTJ1454.9-5133	42.93	42.29	43.51	7.55	-1.25	4.16	9.41	-2.21
753	SWIFTJ1504.2+1025	44.30	43.23	44.84	8.16	-1.41	5.33	23.97	-1.50
754	SWIFTJ1506.7+0353A	43.91	42.94	44.42	7.87	-1.37	4.77	16.46	-1.62
757	SWIFTJ1508.8-0013	43.51	43.30	44.82	8.40	-1.08	18.81	13.47	-1.76
760	SWIFTJ1512.0-2119	43.52	43.17	44.61	6.94	-1.13	6.01	11.72	-0.50
765	SWIFTJ1513.8-8125	44.60	43.40	45.66	8.74	-1.46	18.45	53.24	-1.26
770	SWIFTJ1523.5+6340	45.16	44.35	45.85	8.98	-1.31	7.28	15.11	-1.30
771	SWIFTJ1530.0-1300	44.72	43.78	45.43	8.23	-1.36	8.27	20.51	-0.97
774	SWIFTJ1535.9+5751	43.77	42.77	44.45	7.28	-1.38	5.87	17.10	-1.01
779	SWIFTJ1547.5+2050	45.67	44.79	46.38	8.88	-1.34	8.21	22.60	-0.68
783	SWIFTJ1548.5-1344	42.40	43.04	44.20	7.77	-0.76	62.12	7.12	-1.74
795	SWIFTJ1613.2-6043	42.99	42.36	43.88	6.95	-1.24	10.76	14.46	-1.24

BAT ID	Swift ID	$\log(L_{2500\text{\AA}})$	$\log(L_{2\text{keV}})$	$\log(L_{\text{bol}})$	$\log(M_{\text{BH}}/M_{\odot})$	α_{ox}	$\kappa_{4400\text{\AA}}$	κ_{2-10}	$\log(\lambda_{\text{Edd}})$
797	SWIFTJ1614.0+6544	45.38	43.96	46.16	8.34	-1.55	10.86	81.71	-0.36
801	SWIFTJ1618.7-5930	43.11	42.51	43.93	7.77	-1.23	10.57	13.24	-2.02
810	SWIFTJ1626.7+8530	44.43	43.46	45.10	7.57	-1.37	7.84	24.84	-0.65
815	SWIFTJ1629.9+6722	42.31	42.63	43.64	7.29	-0.88	8.32	8.02	-1.83
833	SWIFTJ1648.0-3037	42.47	42.23	44.00	5.94	-1.10	4.23	33.67	-0.11
838	SWIFTJ1652.0-5915B	41.21	40.56	42.25	6.72	-1.25	5.28	20.17	-2.65
862	SWIFTJ1708.6+2155	44.31	43.31	45.01	8.23	-1.38	8.39	26.25	-1.40
876	SWIFTJ1719.7+4900	42.13	42.34	43.53	8.00	-0.92	20.17	7.91	-2.65
882	SWIFTJ1723.2+3418	45.22	44.63	45.98	8.30	-1.23	8.33	10.27	-0.50
888	SWIFTJ1731.3+1442	44.85	43.40	45.35	7.56	-1.56	5.07	60.35	-0.38
898	SWIFTJ1737.7-5956B	42.96	42.17	43.66	7.11	-1.30	4.93	13.94	-1.63
905	SWIFTJ1741.9-1211	44.10	43.24	44.78	8.03	-1.33	7.47	16.96	-1.43
907	SWIFTJ1742.2+1833	44.98	44.05	45.64	9.23	-1.36	7.73	21.32	-1.77
912	SWIFTJ1745.4+2906	44.45	43.85	45.36	8.41	-1.23	7.48	10.78	-1.23
924	SWIFTJ1747.8+6837A	44.53	42.27	44.90	6.08	-1.87	2.97	175.09	0.65
925	SWIFTJ1747.8+6837B	44.07	42.98	44.61	7.43	-1.42	5.46	27.65	-1.00
929	SWIFTJ1748.8-3257	44.87	42.55	45.23	8.02	-1.89	3.15	232.79	-0.96

BAT ID	Swift ID	$\log(L_{2500\text{\AA}})$	$\log(L_{2\text{keV}})$	$\log(L_{\text{bol}})$	$\log(M_{\text{BH}}/M_{\odot})$	α_{ox}	$\kappa_{4400\text{\AA}}$	κ_{2-10}	$\log(\lambda_{\text{Edd}})$
950	SWIFTJ1807.9+1124	43.89	43.26	44.94	8.74	-1.24	17.17	18.35	-1.98
967	SWIFTJ1822.0+6421	46.46	45.30	46.94	9.23	-1.44	4.32	22.91	-0.47
984	SWIFTJ1835.0+3240	44.40	44.19	45.53	8.01	-1.08	18.42	10.31	-0.65
994	SWIFTJ1842.0+7945	44.88	44.08	45.79	8.64	-1.31	13.54	21.14	-1.03
1002	SWIFTJ1848.0-7832	44.82	43.69	45.49	8.34	-1.44	8.07	37.25	-1.03
1009	SWIFTJ1856.5-7851	43.43	42.97	44.42	7.13	-1.18	12.24	14.08	-0.89
1013	SWIFTJ1856.1+1539	43.99	43.64	45.42	8.86	-1.13	7.91	22.08	-1.62
1021	SWIFTJ1905.4+4231	43.31	42.59	44.02	6.91	-1.28	7.11	13.24	-1.07
1031	SWIFTJ1919.4-2958	45.28	44.39	46.13	8.85	-1.34	12.71	34.74	-0.90
1032	SWIFTJ1921.1-5842	44.37	43.27	45.04	7.99	-1.42	8.08	28.98	-1.12
1036	SWIFTJ1925.0+5041	43.42	43.46	44.70	8.06	-0.99	13.88	7.33	-1.54
1037	SWIFTJ1926.9+4140	43.04	42.95	43.99	8.09	-1.04	9.28	8.37	-2.27
1041	SWIFTJ1933.9+3258	44.30	43.62	44.91	8.30	-1.26	5.48	11.87	-1.57
1042	SWIFTJ1937.5-0613	43.09	42.54	43.75	6.61	-1.21	6.03	10.76	-1.04
1043	SWIFTJ1938.1-5108	43.64	43.19	44.44	7.33	-1.17	9.14	9.34	-1.07
1046	SWIFTJ1942.6-1024	42.41	41.91	43.31	7.04	-1.19	11.20	10.80	-1.91
1064	SWIFTJ2009.0-6103	42.72	42.78	43.88	7.71	-0.98	5.59	8.33	-2.00

BAT ID	Swift ID	$\log(L_{2500\text{\AA}})$	$\log(L_{2\text{keV}})$	$\log(L_{\text{bol}})$	$\log(M_{\text{BH}}/M_{\odot})$	α_{ox}	$\kappa_{4400\text{\AA}}$	κ_{2-10}	$\log(\lambda_{\text{Edd}})$
1084	SWIFTJ2035.2+2604	43.59	42.86	44.21	7.18	-1.28	3.09	8.08	-1.14
1088	SWIFTJ2042.3+7507	45.72	44.51	46.32	9.83	-1.47	6.17	25.65	-1.68
1089	SWIFTJ2044.0+2832	44.06	43.11	44.61	8.32	-1.36	4.78	13.81	-1.89
1090	SWIFTJ2044.2-1045	44.34	43.54	45.13	8.05	-1.30	8.49	16.61	-1.09
1099	SWIFTJ2109.1-0942	43.71	42.95	44.28	7.51	-1.29	5.02	13.28	-1.41
1100	SWIFTJ2109.2+3531	44.88	44.53	45.72	8.04	-1.14	11.51	9.26	-0.50
1102	SWIFTJ2114.4+8206	44.50	43.95	45.41	8.91	-1.21	12.62	13.01	-1.68
1106	SWIFTJ2118.9+3336	43.95	43.45	44.90	7.63	-1.19	14.14	13.41	-0.91
1114	SWIFTJ2132.0-3343	43.12	42.66	44.13	7.84	-1.18	11.06	12.78	-1.89
1116	SWIFTJ2134.9-2729	42.94	43.26	44.85	6.94	-0.88	66.78	16.25	-0.26
1117	SWIFTJ2156.1+4728	42.92	42.65	44.23	7.40	-1.11	7.85	16.19	-1.35
1118	SWIFTJ2135.5-6222	44.62	43.63	45.31	7.35	-1.38	7.91	23.02	-0.22
1120	SWIFTJ2137.8-1433	45.25	44.34	46.19	9.10	-1.35	13.16	21.61	-1.09
1125	SWIFTJ2145.5+1101	44.85	44.06	45.54	8.17	-1.30	6.85	13.87	-0.81
1128	SWIFTJ2150.2-1855	44.77	43.91	45.29	8.25	-1.33	4.53	19.29	-1.13
1131	SWIFTJ2157.2-6942	42.67	42.75	43.97	8.07	-0.97	24.75	8.20	-2.28
1141	SWIFTJ2209.1-2747	43.10	42.47	43.88	7.44	-1.24	7.12	12.03	-1.73

BAT ID	Swift ID	$\log(L_{2500\text{\AA}})$	$\log(L_{2\text{keV}})$	$\log(L_{\text{bol}})$	$\log(M_{\text{BH}}/M_{\odot})$	α_{ox}	$\kappa_{4400\text{\AA}}$	κ_{2-10}	$\log(\lambda_{\text{Edd}})$
1150	SWIFTJ2223.8+1143	42.51	42.37	43.92	7.81	-1.05	12.34	14.65	-2.07
1152	SWIFTJ2226.8+3628	42.52	41.47	43.13	8.05	-1.40	3.02	24.00	-3.10
1161	SWIFTJ2236.7-1233	42.94	42.77	44.56	7.93	-1.06	27.26	21.82	-1.55
1162	SWIFTJ2240.2+0801	43.23	42.49	43.93	7.08	-1.28	8.18	16.05	-1.33
1172	SWIFTJ2254.1-1734	44.79	44.19	45.71	8.19	-1.23	15.19	19.66	-0.66
1176	SWIFTJ2256.5+0526	44.50	43.24	44.96	7.70	-1.48	4.15	23.46	-0.92
1178	SWIFTJ2259.7+2458	43.76	43.03	44.36	6.87	-1.28	5.41	11.00	-0.68
1179	SWIFTJ2301.4-5916	44.70	44.22	45.58	8.64	-1.19	11.61	10.57	-1.23
1181	SWIFTJ2303.1-1837	43.86	43.71	45.13	8.74	-1.06	13.72	11.70	-1.79
1182	SWIFTJ2303.3+0852	43.63	42.76	44.20	6.96	-1.34	5.51	16.07	-0.94
1183	SWIFTJ2304.8-0843	44.23	43.38	44.94	7.98	-1.33	8.82	24.71	-1.21
1185	SWIFTJ2307.1+0433	43.26	42.71	44.29	8.09	-1.21	17.22	15.67	-1.97
1187	SWIFTJ2308.1+4014	43.32	43.53	45.14	7.61	-0.92	96.80	15.20	-0.65
1189	SWIFTJ2318.9+0013	44.69	43.33	45.34	8.59	-1.52	7.61	51.99	-1.43
1194	SWIFTJ2325.5-3827	42.20	41.74	43.06	7.83	-1.18	3.45	11.03	-2.95
1195	SWIFTJ2325.6+2157	45.11	43.94	45.95	8.39	-1.45	12.58	53.54	-0.61
1206	SWIFTJ2351.9-0109	45.21	44.35	46.00	8.70	-1.33	10.41	16.73	-0.88

Bibliography

Abramowicz M. A., Czerny B., Lasota J. P., Szuszkiewicz E., 1988, , [332](#), [646](#)

Alloin D., Pelat D., Phillips M., Whittle M., 1985, , [288](#), [205](#)

Ananna T. T., Treister E., Urry C. M., Ricci C., Hickox R. C., Padmanabhan N., Marchesi S., Kirkpatrick A., 2020, , [889](#), [17](#)

Anderson J. M., Ulvestad J. S., Ho L. C., 2004, , [603](#), [42](#)

Antonucci R., 1993, , [31](#), [473](#)

Antonucci R. R. J., Miller J. S., 1985, , [297](#), [621](#)

Arnaud K. A., 1996, XSPEC: The First Ten Years. p. 17

Astropy Collaboration et al., 2022, [apj](#), [935](#), [167](#)

Awaki H., Kunieda H., Tawara Y., Koyama K., 1991, , [43](#), [L37](#)

Azadi M., Wilkes B., Kuraszkiewicz J., Ashby M., Willner S. P., 2022, [arXiv e-prints](#), p. [arXiv:2204.12697](#)

Baek J., et al., 2019, [MNRAS](#), [488](#), [4317](#)

Barthelmy S. D., et al., 2005, , [120](#), [143](#)

Baumgartner W. H., Tueller J., Markwardt C. B., Skinner G. K., Barthelmy S., Mushotzky R. F., Evans P. A., Gehrels N., 2013, , [207](#), [19](#)

Bechtold J., et al., 2003, , [588](#), [119](#)

Beckmann V., et al., 2009, , [505](#), [417](#)

- Begelman M. C., 1978, [Monthly Notices of the Royal Astronomical Society](#), 184, 53
- Beloborodov A. M., 1999, in Poutanen J., Svensson R., eds, Astronomical Society of the Pacific Conference Series Vol. 161, High Energy Processes in Accreting Black Holes. p. 295 ([arXiv:astro-ph/9901108](#)), [doi:10.48550/arXiv.astro-ph/9901108](#)
- Bentz M. C., Katz S., 2015, , [127](#), [67](#)
- Bentz M. C., Peterson B. M., Netzer H., Pogge R. W., Vestergaard M., 2009, , [697](#), [160](#)
- Berney S., et al., 2015, [MNRAS](#), [454](#), [3622](#)
- Bianchi S., Guainazzi M., Chiaberge M., 2006, , [448](#), [499](#)
- Bianchi S., Chiaberge M., Evans D. A., Guainazzi M., Baldi R. D., Matt G., Piconcelli E., 2010, [MNRAS](#), [405](#), [553](#)
- Bietenholz M. F., Bartel N., Rupen M. P., 2000, , [532](#), [895](#)
- Bisogni S., Marconi A., Risaliti G., 2017, [MNRAS](#), [464](#), [385](#)
- Blandford R. D., Königl A., 1979, , [232](#), [34](#)
- Bradley L., et al., 2021, astropy/photutils: 1.1.0, Zenodo, [doi:10.5281/zenodo.4624996](#)
- Braitto V., Reeves J. N., Bianchi S., Nardini E., Piconcelli E., 2017, , [600](#), [A135](#)
- Breeveld A. A., et al., 2010, [MNRAS](#), [406](#), [1687](#)
- Brightman M., et al., 2017, , [844](#), [10](#)
- Brinkman A. C., Kaastra J. S., van der Meer R. L. J., Kinkhabwala A., Behar E., Kahn S. M., Paerels F. B. S., Sako M., 2002, , [396](#), [761](#)
- Burrows D. N., et al., 2005, , [120](#), [165](#)
- Calzetti D., Armus L., Bohlin R. C., Kinney A. L., Koornneef J., Storchi-Bergmann T., 2000, , [533](#), [682](#)
- Cappi M., et al., 2006, , [446](#), [459](#)
- Cardelli J. A., Clayton G. C., Mathis J. S., 1989, , [345](#), [245](#)

- Cash W., 1979, , [228](#), [939](#)
- Collier S., Peterson B. M., 2001, , [555](#), [775](#)
- Comastri A., Setti G., Zamorani G., Hasinger G., 1995, , [296](#), [1](#)
- Dadina M., 2007, , [461](#), [1209](#)
- Dadina M., 2008, , [485](#), [417](#)
- Dadina M., Guainazzi M., Cappi M., Bianchi S., Vignali C., Malaguti G., Comastri A., 2010, , [516](#), [A9](#)
- Di Matteo T., Fabian A. C., 1997, [MNRAS](#), [286](#), [L50](#)
- Duras F., et al., 2020, , [636](#), [A73](#)
- Edelson R. A., Malkan M. A., 1986, , [308](#), [59](#)
- Eguchi S., Ueda Y., Terashima Y., Mushotzky R., Tueller J., 2009, , [696](#), [1657](#)
- Elitzur M., 2012, , [747](#), [L33](#)
- Elvis M., et al., 1994, , [95](#), [1](#)
- Elvis M., et al., 2012, , [759](#), [6](#)
- Esin A. A., McClintock J. E., Narayan R., 1997, , [489](#), [865](#)
- Fabbiano G., Paggi A., Karovska M., Elvis M., Maksym W. P., Wang J., 2018, , [865](#), [83](#)
- Fabian A. C., Rees M. J., 1995, [MNRAS](#), [277](#), [L55](#)
- Fabian A. C., Iwasawa K., Reynolds C. S., Young A. J., 2000, , [112](#), [1145](#)
- Fabian A. C., Celotti A., Erlund M. C., 2006, [MNRAS](#), [373](#), [L16](#)
- Fabian A. C., Vasudevan R. V., Gandhi P., 2008, [MNRAS](#), [385](#), [L43](#)
- Fabian A. C., Vasudevan R. V., Mushotzky R. F., Winter L. M., Reynolds C. S., 2009, [MNRAS](#), [394](#), [L89](#)
- Falcke H., Markoff S., 2000, , [362](#), [113](#)

- Falcke H., Nagar N. M., Wilson A. S., Ulvestad J. S., 2000, , [542](#), [197](#)
- Feigelson E. D., Nelson P. I., 1985, , [293](#), [192](#)
- Fukazawa Y., et al., 2011, , [727](#), [19](#)
- Gehrels N., et al., 2004, , [611](#), [1005](#)
- George I. M., Fabian A. C., 1991, [MNRAS](#), [249](#), [352](#)
- Ghisellini G., Haardt F., Matt G., 1994, [MNRAS](#), [267](#), [743](#)
- Gilli R., Comastri A., Hasinger G., 2007, , [463](#), [79](#)
- Gómez-Guijarro C., González-Martín O., Ramos Almeida C., Rodríguez-Espinosa J. M., Gallego J., 2017, [MNRAS](#), [469](#), [2720](#)
- Greene J. E., Ho L. C., 2005, , [630](#), [122](#)
- Greene J. E., Pooley D., Zakamska N. L., Comerford J. M., Sun A.-L., 2014, , [788](#), [54](#)
- Grier C. J., et al., 2012, , [744](#), [L4](#)
- Guainazzi M., Bianchi S., 2007, [MNRAS](#), [374](#), [1290](#)
- Gupta K. K., et al., 2021, [MNRAS](#), [504](#), [428](#)
- HI4PI Collaboration et al., 2016, , [594](#), [A116](#)
- Haardt F., Maraschi L., 1991, , [380](#), [L51](#)
- Harrison C., 2014, PhD thesis, Durham University
- Herrnstein J. R., Greenhill L. J., Moran J. M., Diamond P. J., Inoue M., Nakai N., Miyoshi M., 1998, , [497](#), [L69](#)
- Hönig S. F., Gandhi P., Asmus D., Mushotzky R. F., Antonucci R., Ueda Y., Ichikawa K., 2014, [MNRAS](#), [438](#), [647](#)
- Hopkins P. F., Richards G. T., Hernquist L., 2007, , [654](#), [731](#)
- Ichikawa K., Ueda Y., Terashima Y., Oyabu S., Gandhi P., Matsuta K., Nakagawa T., 2012, , [754](#), [45](#)

-
- Ichikawa K., et al., 2019a, , [870](#), [31](#)
- Ichikawa K., et al., 2019b, , [883](#), [L13](#)
- Ichimaru S., 1977, , [214](#), [840](#)
- Jansen F., et al., 2001, , [365](#), [L1](#)
- Kaspi S., Smith P. S., Netzer H., Maoz D., Jannuzi B. T., Givon U., 2000, , [533](#), [631](#)
- Kaspi S., Maoz D., Netzer H., Peterson B. M., Vestergaard M., Jannuzi B. T., 2005, , [629](#), [61](#)
- Katz J. I., 1977, , [215](#), [265](#)
- Kawamuro T., Ueda Y., Tazaki F., Ricci C., Terashima Y., 2016, , [225](#), [14](#)
- Kellermann K. I., Sramek R., Schmidt M., Shaffer D. B., Green R., 1989, , [98](#), [1195](#)
- Kewley L. J., Groves B., Kauffmann G., Heckman T., 2006, [MNRAS](#), [372](#), [961](#)
- Kinkhabwala A., et al., 2002, , [575](#), [732](#)
- Koratkar A., Blaes O., 1999, , [111](#), [1](#)
- Kormendy J., Ho L. C., 2013, , [51](#), [511](#)
- Koss M. J., et al., 2016, , [825](#), [85](#)
- Koss M., et al., 2017, , [850](#), [74](#)
- Koss M. J., et al., 2018, , [563](#), [214](#)
- Koss M. J., et al., 2020, arXiv e-prints, p. [arXiv:2010.15849](#)
- Koss M. J., et al., 2022a, , [261](#), [1](#)
- Koss M. J., et al., 2022b, , [261](#), [2](#)
- Koss M. J., et al., 2022c, , [261](#), [6](#)
- Kraemer S. B., Crenshaw D. M., 2000, , [544](#), [763](#)
-

- Krawczyk C. M., Richards G. T., Mehta S. S., Vogeley M. S., Gallagher S. C., Leighly K. M., Ross N. P., Schneider D. P., 2013, , [206](#), [4](#)
- Krimm H. A., et al., 2013, , [209](#), [14](#)
- Krolik J. H., Begelman M. C., 1988, , [329](#), [702](#)
- Krolik J. H., Madau P., Zycki P. T., 1994, , [420](#), [L57](#)
- Kumar S., Dewangan G. C., Singh K. P., Gandhi P., Papadakis I. E., Tripathi P., Mallick L., 2023, [arXiv e-prints](#), p. [arXiv:2303.11882](#)
- Kuraszkiewicz J. K., et al., 2003, , [590](#), [128](#)
- Lamperti I., et al., 2017, [MNRAS](#), [467](#), [540](#)
- Lawrence A., 2012, [MNRAS](#), [423](#), [451](#)
- Levenson N. A., Krolik J. H., Życki P. T., Heckman T. M., Weaver K. A., Awaki H., Terashima Y., 2002, , [573](#), [L81](#)
- Lightman A. P., White T. R., 1988, , [335](#), [57](#)
- Lusso E., Risaliti G., 2016, , [819](#), [154](#)
- Lusso E., et al., 2010, , [512](#), [A34](#)
- Lusso E., et al., 2012, [MNRAS](#), [425](#), [623](#)
- Maddox N., 2018, [MNRAS](#), [480](#), [5203](#)
- Magdziarz P., Zdziarski A. A., 1995, [MNRAS](#), [273](#), [837](#)
- Maiolino R., Salvati M., Bassani L., Dadina M., della Ceca R., Matt G., Risaliti G., Zamorani G., 1998, , [338](#), [781](#)
- Makishima K., Maejima Y., Mitsuda K., Bradt H. V., Remillard R. A., Tuohy I. R., Hoshi R., Nakagawa M., 1986, , [308](#), [635](#)
- Malkan M. A., 1983, , [268](#), [582](#)

- Malkan M. A., Sargent W. L. W., 1982, , [254](#), [22](#)
- Maraschi L., Ghisellini G., Celotti A., 1992, , [397](#), [L5](#)
- Marchese E., Della Ceca R., Caccianiga A., Severgnini P., Corral A., Fanali R., 2012, , [539](#), [A48](#)
- Marchesi S., Ajello M., Marcotulli L., Comastri A., Lanzuisi G., Vignali C., 2018, , [854](#), [49](#)
- Marconi A., Risaliti G., Gilli R., Hunt L. K., Maiolino R., Salvati M., 2004, in Storchi-Bergmann T., Ho L. C., Schmitt H. R., eds, IAU Symposium Vol. 222, The Interplay Among Black Holes, Stars and ISM in Galactic Nuclei. pp 49–52 ([arXiv:astro-ph/0409542](#)), [doi:10.1017/S1743921304001437](#)
- Markoff S., Falcke H., Fender R., 2001, , [372](#), [L25](#)
- Marshall A., Auger-Williams M. W., Banerji M., Maiolino R., Bowler R., 2022, [MNRAS](#), [515](#), [5617](#)
- Massaro E., Giommi P., Leto C., Marchegiani P., Maselli A., Perri M., Piranomonte S., Sclavi S., 2009, , [495](#), [691](#)
- Mateos S., et al., 2016, , [819](#), [166](#)
- Matt G., Perola G. C., Piro L., 1991, , [247](#), [25](#)
- Mejía-Restrepo J. E., Trakhtenbrot B., Lira P., Netzer H., Capellupo D. M., 2016, [MNRAS](#), [460](#), [187](#)
- Mejía-Restrepo J. E., et al., 2022, , [261](#), [5](#)
- Mitsuda K., et al., 1984, , [36](#), [741](#)
- Mitsuda K., et al., 2007, , [59](#), [S1](#)
- Mushotzky R. F., Done C., Pounds K. A., 1993, , [31](#), [717](#)
- Nandra K., Pounds K. A., 1994, [MNRAS](#), [268](#), [405](#)
- Narayan R., 2005, , [300](#), [177](#)
- Narayan R., Yi I., 1994, , [428](#), [L13](#)
- Narayan R., Yi I., 1995, , [452](#), [710](#)
- Narayan R., Yi I., Mahadevan R., 1995, , [374](#), [623](#)

- Nenkova M., Ivezić Ž., Elitzur M., 2002, , [570](#), [L9](#)
- Netzer H., 2013, *The Physics and Evolution of Active Galactic Nuclei*
- Netzer H., 2019, [MNRAS](#), [488](#), [5185](#)
- Noguchi K., Terashima Y., Awaki H., 2009, , [705](#), [454](#)
- Noguchi K., Terashima Y., Ishino Y., Hashimoto Y., Koss M., Ueda Y., Awaki H., 2010, , [711](#), [144](#)
- Novikov I. D., Thorne K. S., 1973, in *Black Holes (Les Astres Occlus)*. pp 343–450
- Nucita A. A., Guainazzi M., Longinotti A. L., Santos-Lleo M., Maruccia Y., Bianchi S., 2010, , [515](#), [A47](#)
- Oh K., Sarzi M., Schawinski K., Yi S. K., 2011, , [195](#), [13](#)
- Oh K., Yi S. K., Schawinski K., Koss M., Trakhtenbrot B., Soto K., 2015, , [219](#), [1](#)
- Oh K., et al., 2017, [MNRAS](#), [464](#), [1466](#)
- Oh K., et al., 2022, , [261](#), [4](#)
- Osterbrock D. E., 1978, [Proceedings of the National Academy of Science](#), [75](#), [540](#)
- Page K. L., Reeves J. N., O’Brien P. T., Turner M. J. L., 2005, [MNRAS](#), [364](#), [195](#)
- Paliya V. S., et al., 2019, , [881](#), [154](#)
- Paltani S., Ricci C., 2017, , [607](#), [A31](#)
- Panagiotou C., Walter R., 2019, , [626](#), [A40](#)
- Pei Y. C., 1992, , [395](#), [130](#)
- Peng C. Y., Ho L. C., Impey C. D., Rix H.-W., 2002, , [124](#), [266](#)
- Peng C. Y., Ho L. C., Impey C. D., Rix H.-W., 2010, , [139](#), [2097](#)
- Peterson B. M., 2006, in Alloin D., ed., , Vol. 693, *Physics of Active Galactic Nuclei at all Scales*. p. 77, [doi:10.1007/3-540-34621-X_3](#)

-
- Ponti G., et al., 2013, , [549](#), [A72](#)
- Poole T. S., et al., 2008, [MNRAS](#), [383](#), [627](#)
- Ramos Almeida C., Ricci C., 2017, [Nature Astronomy](#), [1](#), [679](#)
- Reeves J. N., Turner M. J. L., 2000, [MNRAS](#), [316](#), [234](#)
- Reeves J., Done C., Pounds K., Terashima Y., Hayashida K., Anabuki N., Uchino M., Turner M., 2008, [MNRAS](#), [385](#), [L108](#)
- Reynolds C. S., Di Matteo T., Fabian A. C., Hwang U., Canizares C. R., 1996, [MNRAS](#), [283](#), [L111](#)
- Ricci C., Walter R., Courvoisier T. J. L., Paltani S., 2011, , [532](#), [A102](#)
- Ricci C., Ueda Y., Paltani S., Ichikawa K., Gandhi P., Awaki H., 2014, [MNRAS](#), [441](#), [3622](#)
- Ricci C., Ueda Y., Koss M. J., Trakhtenbrot B., Bauer F. E., Gandhi P., 2015, [The Astrophysical Journal](#), [815](#), [L13](#)
- Ricci C., et al., 2017a, , [233](#), [17](#)
- Ricci C., et al., 2017b, , [549](#), [488](#)
- Ricci C., et al., 2018, [MNRAS](#), [480](#), [1819](#)
- Ricci C., et al., 2021, , [255](#), [7](#)
- Ricci F., et al., 2022, , [261](#), [8](#)
- Richards G. T., et al., 2006, , [166](#), [470](#)
- Risaliti G., Elvis M., 2004, A Panchromatic View of AGN. p. 187, [doi:10.1007/978-1-4020-2471-9_6](#)
- Risaliti G., Maiolino R., Salvati M., 1999, , [522](#), [157](#)
- Risaliti G., Salvati M., Marconi A., 2011, [MNRAS](#), [411](#), [2223](#)
- Rojas A. F., et al., 2020, [MNRAS](#), [491](#), [5867](#)
- Runnoe J. C., Brotherton M. S., Shang Z., 2012a, [MNRAS](#), [422](#), [478](#)

- Runnoe J. C., Brotherton M. S., Shang Z., 2012b, [MNRAS](#), **426**, 2677
- Rybicki G. B., Lightman A. P., 1986, *Radiative Processes in Astrophysics*
- Saccheo I., et al., 2023, , [671](#), A34
- Sako M., Kahn S. M., Paerels F., Liedahl D. A., 2000, , [543](#), L115
- Sanders D. B., Phinney E. S., Neugebauer G., Soifer B. T., Matthews K., 1989, , [347](#), 29
- Sarzi M., et al., 2006, [MNRAS](#), **366**, 1151
- Schawinski K., Koss M., Berney S., Sartori L. F., 2015, [MNRAS](#), **451**, 2517
- Schlegel D. J., Finkbeiner D. P., Davis M., 1998, , [500](#), 525
- Schurch N. J., Warwick R. S., Griffiths R. E., Kahn S. M., 2004, [MNRAS](#), **350**, 1
- Shakura N. I., Sunyaev R. A., 1973, , [500](#), 33
- Shang Z., et al., 2005, , [619](#), 41
- Shang Z., et al., 2011, , [196](#), 2
- Shen X., Hopkins P. F., Faucher-Giguère C.-A., Alexander D. M., Richards G. T., Ross N. P., Hickox R. C., 2020, [MNRAS](#), **495**, 3252
- Shields G. A., 1978, , [272](#), 706
- Shimizu T. T., Mushotzky R. F., Meléndez M., Koss M. J., Barger A. J., Cowie L. L., 2017, [MNRAS](#), **466**, 3161
- Shu X. W., Yaqoob T., Wang J. X., 2010, , [187](#), 581
- Smith K. L., et al., 2020, [MNRAS](#), **492**, 4216
- Steffen A. T., Strateva I., Brandt W. N., Alexander D. M., Koekemoer A. M., Lehmer B. D., Schneider D. P., Vignali C., 2006, , [131](#), 2826
- Strateva I. V., Brandt W. N., Schneider D. P., Vanden Berk D. G., Vignali C., 2005, , [130](#), 387
- Sun W.-H., Malkan M. A., 1989, , [346](#), 68

- Svoboda J., Beuchert T., Guainazzi M., Longinotti A. L., Piconcelli E., Wilms J., 2015, , [578](#), [A96](#)
- Tanaka Y., Inoue H., Holt S. S., 1994, , [46](#), [L37](#)
- Tananbaum H., et al., 1979, , [234](#), [L9](#)
- Tanimoto A., Ueda Y., Kawamuro T., Ricci C., Awaki H., Terashima Y., 2018, , [853](#), [146](#)
- Temple M. J., Hewett P. C., Banerji M., 2021, [MNRAS](#), [508](#), [737](#)
- Thorne K. S., 1974, , [191](#), [507](#)
- Trakhtenbrot B., Netzer H., 2012, [MNRAS](#), [427](#), [3081](#)
- Turner T. J., George I. M., Nandra K., Mushotzky R. F., 1997, , [113](#), [23](#)
- Ueda Y., Akiyama M., Ohta K., Miyaji T., 2003, , [598](#), [886](#)
- Ueda Y., et al., 2007, , [664](#), [L79](#)
- Ueda Y., Akiyama M., Hasinger G., Miyaji T., Watson M. G., 2014, , [786](#), [104](#)
- Ueda Y., et al., 2015, , [815](#), [1](#)
- Ulvestad J. S., Ho L. C., 2001, , [562](#), [L133](#)
- Urry C. M., Padovani P., 1995, , [107](#), [803](#)
- Vanden Berk D. E., et al., 2001, , [122](#), [549](#)
- Vasudevan R. V., Fabian A. C., 2007, [MNRAS](#), [381](#), [1235](#)
- Vasudevan R. V., Fabian A. C., 2009, [MNRAS](#), [392](#), [1124](#)
- Vasudevan R. V., Mushotzky R. F., Winter L. M., Fabian A. C., 2009, [MNRAS](#), [399](#), [1553](#)
- Vasudevan R. V., Fabian A. C., Gandhi P., Winter L. M., Mushotzky R. F., 2010, [MNRAS](#), [402](#), [1081](#)
- Veilleux S., Osterbrock D. E., 1987, , [63](#), [295](#)
- Vestergaard M., Peterson B. M., 2006, , [641](#), [689](#)
- Vietri G., et al., 2018, , [617](#), [A81](#)

- Vignali C., Comastri A., Cappi M., Palumbo G. G. C., Matsuoka M., Kubo H., 1999, , [516](#), [582](#)
- Ward M., Elvis M., Fabbiano G., Carleton N. P., Willner S. P., Lawrence A., 1987, , [315](#), [74](#)
- Weisskopf M. C., Tananbaum H. D., Van Speybroeck L. P., O'Dell S. L., 2000, Chandra X-ray Observatory (CXO): overview. pp 2–16, [doi:10.1117/12.391545](#)
- Winter L. M., Mushotzky R. F., Reynolds C. S., Tueller J., 2009, , [690](#), [1322](#)
- Yamada S., Ueda Y., Tanimoto A., Oda S., Imanishi M., Toba Y., Ricci C., 2020, , [897](#), [107](#)
- Yaqoob T., Padmanabhan U., 2004, , [604](#), [63](#)
- Young A. J., Wilson A. S., Shopbell P. L., 2001, , [556](#), [6](#)
- Yuan F., Narayan R., 2014, , [52](#), [529](#)
- Yuan W., Siebert J., Brinkmann W., 1998, , [334](#), [498](#)
- Yuan F., Markoff S., Falcke H., 2002, , [383](#), [854](#)
- Zappacosta L., et al., 2018, , [854](#), [33](#)
- Zdziarski A. A., Johnson W. N., Magdziarz P., 1996, [MNRAS](#), [283](#), [193](#)
- Zhao X., Marchesi S., Ajello M., Cole D., Hu Z., Silver R., Torres-Albà N., 2021, , [650](#), [A57](#)
- Życki P. T., Done C., Smith D. A., 1999, [MNRAS](#), [309](#), [561](#)
- den Brok J. S., et al., 2022, , [261](#), [7](#)